Charge Transport in Metal-Organic Frameworks

by

Brian Michael Wiers

A dissertation submitted in partial satisfaction of the

requirements for the degree of

Doctor of Philosophy

in

Chemistry

in the

Graduate Division

of the

University of California, Berkeley

Committee in charge:

Professor Jeffrey R. Long, Chair
Professor Kenneth N. Raymond
Professor Nitash P. Balsara

Spring 2015

Abstract

Charge Transport in Metal-Organic Frameworks

by

Brian Michael Wiers

Doctor of Philosophy in Chemistry

University of California, Berkeley

Professor Jeffrey R. Long, Chair

This dissertation documents efforts to synthesize and measure ionically and electronically conductive porous, three-dimensional metal-organic frameworks. Chapter 1 introduces concepts of conductivity, mixed-valency, measurement techniques and gives a survey of charge-transport in metal-organic and covalent-organic frameworks. Concepts that directed the work detailed in this thesis is given, as is a perspective on possible future avenues to generate conductive metal-organic frameworks and possible applications. Chapter 2 details the attainment of a solid lithium fast-ion conductor by post-synthetic grafting of lithium alkoxides to a metal-organic framework with open metal-sites, Mg_2(DOBDC). Chapter 3 shows the synthesis of a novel metal-organic framework $Fe_2(BDP)_3$, and its chemical reduction to obtain the compositional series $K_xFe_2(BDP)_3$ that displays porosity and tunable charge transport as demonstrated by contactless microwave measurements. Chapter 4 investigates this system further and shows the first 4-point and field effect transistor measurements of a metal-organic framework. FET measurements show the effects of sequential reduction on a single crystal device and high electron mobilities. Mössbauer spectroscopy and solid state cyclic voltammetry confirm the high degree of electronic delocalization in the partially reduced material. Chapter 5 shows a new chalcogen-based metal organic framework Fe_2(DSBDC)(*N*,*N*-DMF)$_2$, isostructural with the known and heavily investigated series of metal-organic frameworks, M_2(DOBDC)(SOLVENT)$_2$. Contactless microwave measurements reveal high charge mobilities and pressed pellet measurements indicate intrinsic conductivity, that increases upon oxidation, indicative of *p*-type conduction. Appendix A shows five novel dipyrazole ligands and five novel dipyrazolate metal-organic frameworks.

This dissertation is dedicated to my parents John Wayne and Susan Gayle (neé Beaudry) Wiers.

Table of Contents

List of Figures

Chapter 1

Chapter 2

Chapter 4

Chapter 5

List of Tables

Acknowledgements

I first acknowledge my teachers. First among those is Professor Jeff Long, my advisor. His support, guidance and patience these past years have made this work possible. Not only has he taught me so much about how to think about chemistry and science, he has taught me about how to communicate science. I still have further to go in those regards, and as I work to improve, I will measure myself against his standard. In addition to these roles as an academic advisor and primary investigator, it must be noted that he has created a wonderful group to work in, who I will further acknowledge below. While he sets an awesome example as a scientist and a leader I am also impressed with his fundamental kindness, decency and generosity. Jeff always believed in me, even when I didn't believe in myself. I must also thank his wife Jen, whose warmth and hospitality are a boon to all in Jeff's group. They throw the best holiday party I have ever been to, where they share fine food, drink, and later in the evening, Jeff's love of gangsta rap. I thank Professor Ken Raymond for reading this dissertation, serving as my qualifying exam chair and teaching me crystallography. I also thank Professor Nitash Balsara for reading this dissertation, serving on my qualifying exam committee and teaching me much about batteries and ionic conductivity, the topic of Chapter 2 of this dissertation. Professors Angelica Stacy and Peidong Yang both served on my qualifying exam committee and Professor Yang contributed to the work in Chapter 4 of this dissertation. In high school I had a phenomenal chemistry teacher, Patricia Vance, who sparked an interest in this discipline and instilled in me a lifelong appreciation of dimensional analysis. I am not sure if I would have pursued chemistry without her introduction to the subject. In undergrad I had the privilege of working for Professor Paul G. Rasmussen, who cultivated a passion for research and chemistry, made room for me in his group, and found funding for me to work as a research assistant one summer. It was in his group that I got my first taste for materials chemistry and conductivity (H^+). Professor Robert Kennedy taught me analytical chemistry, was always approachable and wrote me a letter of recommendation. Professors Fernande Grandjean and Gary Long have been immensely helpful to me and I have learned much from them about Mössbauer spectroscopy and being a good scientist in general. Though I did not study physical organic chemistry or mechanistic chemistry in my graduate research, Professor Bob Bergmann's course may be one of the most useful I had ever taken for the way it changed my thinking about and approach to chemistry. Mary Kay Glazek taught me much about writing and loving English, and gave me the lifetime limit of seven exclamation marks - I have ~~five~~ four left! Mary Grace Campbell and Dave Crawford had a strong impact in the way I think about the world and my place in it.

I would not be writing this were it not for my parents, John and Susan Wiers. This is because: a.) I could not write a dissertation if I did not exist and b.) the love, support, and encouragement that they have selflessly given to me my entire life. I will never be able to express the gratitude I have for the sacrifices that they have made for me and my education. The examples they set for the values of hard work, education, integrity, morality, and fair-mindedness have served as guidance in my pursuit of a PhD and in my life as a whole. It is to them that I dedicate this work. I would say I am the luckiest person in the world to have parents like them; but there is another who shares that privilege. My

sister Ashley was a wonderful person to grow up with, a few childhood conflicts and the infamous fishpond incident notwithstanding. Though she is my younger sister, she is far more savvy than I, and I value her counsel and advice.

I have the good fortune to have grown up surrounded and loved by a tightly knit extended family that all lived in very close geographic proximity. I did not understand well into adulthood, that when asked about one's family, the question is typically being posed about one's parents and siblings (if any). To this day, when asked about my family, my immediate instinct is to begin to describe the following people: Grandmas and Grandpas Wiers and Beaudry; Great Uncles Lanny and George; Great Aunt Joanne, Uncles Mike, Mark, Tom, and Ed; Aunts Sharon, Shelley, Marilyn, and Theresa; my Godson Mitchell, Cousins Hunter, Logan, Jordan, Nicholas, Gavin, and Alyssa.[1] It was hard moving 2,500 miles from Romeo, Michigan, but being able to pause and think about this group of people who I love, and who love me is always a source of comfort and perspective. I have been blessed with wonderful grandparents. Thank you Grandma Beaudry and Grandma Wiers for everything. My grandfathers Ward Wiers and Allen Beaudry, were always very kind to me and indulgent in answering my questions, I am grateful to have known them. I wish to make them proud.

Kevin has been a great friend, teacher and mentor. I would be a much different person had I not known Kevin, certainly a much duller person. Dan and I have known each other for over 2/3 of our lives. We do not talk nearly as often as we should, but no matter what time elapses between our conversations, we pick up again as if one of us had left the room for only a moment. In college and Ann Arbor I met a great group of people who I am lucky to call friends; Ian, Dax, Paul, Stefan, Chuck, Adam, rgEddie, Chris, Nicole, Graham, Joel, Tarek, Justin, Tristan, Sarah, Carlie, and Colin. Paul and I have travelled the world together. He has nursed me back to health as I was delirious with a fever in the Andes, and throughout our journeys we only had one argument, in the middle of Mongolia. Ian and I met at East Quad, lived together in the Stefan T. Vail Student Co-operative and rekindled our friendship in San Francisco. I am lucky to count his wife Natalya as a friend too and I am so happy that they have generated a new friend: Naomi. Dax has been a stalwart friend and is great at keeping in touch, something I am awful at. It is always a pleasure when he visits. Jen was a great girlfriend and I am happy to see we remain close friends. Getting to know Ohnmar Khin these past four years has been very special to me. The friendship and bike rides with Brian Coyne and Lily Janiak have been a great part of my California experience. At Nanocerox, Inc. I met Lela Liu (now Lee), who has confessed she recommended that I not be hired. Fortunately, no one listened to her and we later became friends. It was fun covertly applying to grad schools with her. David Lawrence introduced me to rock-climbing and later in California, surfing. Dr. Tony Sutorik was great to work for and I thank him for writing a letter of recommendation and encouraging me to go to graduate school. He has been a great mentor and has an infectious passion for materials research.

[1] Cousins of degree > 1 and/or removal > 0 and family friends are listed in a supplemental appendix.

I joined the Long Group in 2008 with Zoey Herm, Tom McDonald, Curtis Wray, and Lily Huang. a great group to start with. Curtis is the most civic-minded person I know, and deeply impresses me with his interest and knowledge about politics from the national to the municipal level. Now that he has left the Bay Area I do not know how to vote on anything. Tom has been a partner in crime, organizer of outings to the Capay Tomato Festival, traveling companion to Santa Rosa and a host of "The Wire" viewing parties. Zoey has become a close friend and confidant. After I talk to her about any problem or situation that seems intractable and daunting, I feel I can handle it.

It was great to join the group with a great cadre of senior students, visting scholars and post-docs. While a very nice person in general, I still have anxiety dreams about getting in trouble with Hemamala Karunadasa for breaches of glove box procedure. Leslie Murray was great to learn organic synthesis from and generously hosted parties with a view of the Bay and a hot tub at his and Sofia's place. Joe Zadrozny has a warped sense of humor and a willingness to enjoy the absurd and strange, while Kenji Sumida, himself being absurd and strange, played for me the Bob Dylan Christmas album, in July. Yoji Kobayashi and Deanna D'Alessandro taught me much about solid state physics and how to probe electron transfer. Maw Lin Foo was great to talk science with. Kentaro Tamaki was very GOOOOOOOOOOOOOD to me. Aude Demessence, Matt Hill, Bettina Bechlars, and Satoshi Hiroke were great fun and I got a taste of polyoxometallate synthesis with Maheswaran Shanmugam. Though I only saw him give a group meeting Navid Solheina deserves mention as a founding father of the Long group conductivity project. Hye Jin was very knowledgeable and helpful and I am delighted I get to work with her again. A former student of Jeff's, Professor Mircea Dinca, has profoundly molded my thinking about conductivity with his work in his independent career and through discussions with him.

The year after I joined, Eric Bloch, Dana Levine and Katie Meihaus signed on. Eric and his wife Lynn were founding members of the Super Fun Adventure Group® and I enjoyed many trips in Northern California with them and Valentina Colombo. Katie Meihaus is always good for a discussion/heated debate that is rooted in mutual respect and friendship. Dana Levine is truly kind and is a pillar of the Long Group social life. Jarad Mason has been an immeasurable help with powder x-ray diffraction, David Zee asks probing questions about science and is unwilling to take a sloppy answer, and Jordan laughs readily and freely. Miguel Gonzalez is a formidable crystallographer and has been immensely helpful in this work. Lucy Darago has taught me a lot about magnetism and helped keep me sane my last few years of grad school. I thank Dianne Xiao for not getting too mad at me and Douglas Reed for his friendliness. Phil Bunting is one alright thing to come out of Ohio and Matt Kapelweski is great to talk about science and laugh with. Mercedes Taylor, Julia Oktawiec, Rebecca Siegelman, Jon Bachmann and Kristen Colwell are great additions to the group and will contribute to the Long group's tradition of scientific and interpersonal excellence. Maryanne, Kaitlin, Sunmin, Nicholas, Jo, David Gygi, and Ruixuan Gao have been great undergrads to work with.

I have not mentioned Jeff Rinehart, Xiaowen Feng, Dave Harris and Danna Freedman, as they go in this section reserved for residents of 3001 Ellis St., Apt. C. Long

walks home (sometimes punctuated by a stop at a watering hole) with Jeff Rinehart were opportunities so learn about the Nazi sympathies of Johannes Stark, analog cryptography and the electronic structure of lanthanides. Dave Harris was always there to motivate me to "play like a champion" by saying a "few words" or by his example. He was also lot kinder than he had to be in my GRS introduction. In spite of her better judgement, Danna Freedman stayed with us for three weeks while in transit to Boston. We would talk late into the night, something I am happy we continue on Google chat today. Xiaowen Feng has been an excellent roommate and is a great cook. I have also lived with people I do not work with. Watching Daniel Montiel's ongoing campaign to scare Jeff Rinehart was entertaining and he took time to help me get settled in Berkeley when I first moved out here. Alex Gura and Ben were good to live with as well. I thank Nawaf for late night discussions over tea and coffee and his Arabic language instruction !شـكـراً

Will Hudson was the first student of Jeff's to work on batteries and charge transport and is a pioneer. I do not know anyone who thinks as deeply about science as Mike Aubrey does. In addition to science he has a great love for bluegrass and intriguing characters. Rodi and I share two passions: conductive metal-organic frameworks and geographical trivia. Raymond Yu is a tremendously hard worker and a great chemist. I am excited to see him flourish in grad school. Keith, Rob Ameloot, Jeff Van Humbeck, Aravind and Farshid were great post-docs to study conductivity with. I am very happy I got to work closely with and learn from these people.

Michael Nippe was always there for encouragement and to make me laugh. I had great fun with Paulina Gomoa-Figueroa, Elizabeth Montalvo and their respective plus ones, Diego and Carlos. David Rogow and I bonded over mycology and West Coast counter-culture figures. Stephen Geier as a Canadian was able to enjoy references to Don Cherry and the Tragically Hip. Selly was a great companion in lab at 1 AM. Wendy Queen, Tae-Hyun, Ming-Lee, Shuao Wang, Pierre Dechambenoit, Zach Mensinger and Zach Smith, Minyoung Yoon and Alex were great colleagues and I got help and advice from every single one of them.

Jeff Long has hosted many visiting scholars and students, some of whom have been already mentioned. I enjoyed watching movies and surfing with Professor Jeremy Smith and learning about South African slang and charge transfer salts from Professor Delia Haynes. Hopefully I can see Finisterre and Professor Socorro Castro-García sometime soon. I give a special Hi to Wooram Lee. I enjoyed the company of Professor Jinxing Ye, Professor Wei Shi, Yaoqi, Konrad Hindelgang, Anna Aulisio, Aurel Tabacaru, Chiara Otelli, Josefin Åkerstedt, Xiaofei Li, Fuxing, Tess Fahem, Chen-Wei Lu, Emily Mensforth, Tadao, Celia, Gregoire, Professor Xavier Roman, Professor Kitty Nijmeijer, Professor Bob Pike, Professor Kajal Rajak, Professor Rajamani Krishna, Professor Chang Seop Hong, and Professor Shane Telfer. I am pleased that Henry Jiang, after his stay with us, will join the Berkeley chemistry department this coming fall.

Professor Shu Seki and Dr. Tsuneaki Sakurai did FP-TRMC measurements for me and Doctors Craig Brown and Matt Hudson did neutron diffraction studies on $Fe_2(BDP)_3$ as well as Professor Norberto Masciocchi for sharing his powder diffraction expertise. Professors Rajamani Krishna, Pawel Zajdel and Dr. Jasper M. van Baten did

computational studies of $Fe_2(BDP)_3$ as did Dr. Kyuho Lee and Professor Jeff Neaton. I thank Dr. Mark Allendorf for fruitful discussions and an opportunity to serve at the Materials Research Society 2011 San Francisco conference.

Kathy Bean and Shela Deguzman deserve special note for administrative help and support and generally keeping me on track in terms of deadlines and paperwork these past seven years, as well as bailing me out of trouble. Although she is not in the Long Group, I here acknowledge Lynn Keithlin for all her help at the departmental level. I do not know if I would have finished without the aid of those three.

The College of Chemistry as a whole is a great place to do research. I enjoyed collaborating with Sean C. Andrews, a true artist with an electron beam and an all around great guy. Annie was quite helpful with the Mössbauer spectrometer. Shrayesh Patel, Alex Teran and Scott Mullin were very helpful in teaching me about impedance spectroscopy and measurements. Meg Fasulo, Geoff and Dan were great to play softball with. I thank Jim Breen, the machine shop, Phil Simon, Kinfe Lita, Antonio DiPasquale, Chris Canlas, Elena Kreimer and the QB3 Mass Spec Facility for the good work they do. The woodshop plays an often forgotten but crucial role. They made some terrifying moves of glove boxes possible and chatting with Jody and Bob was always a nice break. The custodial staff kept my workplace nice to work in and I am grateful for talks with John Lane about everything under the sun.

Thank you to everyone who made my dissertation possible and kept me sane these past seven years. Please know that even if you are not on these pages, you are in my heart.

Chapter 1: Charge Transport in Metal-Organic Frameworks and Related Porous Materials

1.1 Introduction

Metal-organic frameworks (MOFs) are a relatively new class of highly porous crystalline materials, built up from zero- or one-dimensional inorganic clusters or chains linked together in three dimensions by multitopic organic ligands.[1] The canonical metal-organic framework, $Zn_4O(BDC)_3$ or MOF-5, is built of zero-dimensional zinc-oxygen tetrahedral clusters (the basic zinc acetate structure - $Zn_4O(OAc)_6$) linked by the 1,4-benzenedicarboxylate linker (= BDC^{2-}) and has the formula $Zn_4O(BDC)_3$.[2] Another heavily investigated metal-organic framework referred to as MOF-74, with the formula $M_2(DOBDC)$ where $DOBDC^{4-}$ = 2,5-dioxido-1,4-benzenedicarboxylate and M = Zn^{2+}, Mg^{2+}, Mn^{2+}, Fe^{2+}, Ni^{2+}, Co^{2+}, and Cu^{2+}.[3-9] It is built of infinite chains of edge sharing metal-oxygen octahedra as shown in Figure 1.2 In this thesis, investigations of metal-organic frameworks of this structure type will be described: ionic conductivity demonstrated in $Mg_2(DOBDC)$ is the focus of Chapter 2, and the electronic conductivity of $Fe_2(DSBDC)$, a sulfur substituted analogue of $Fe_2(DOBDC)$, is the focus of Chapter 5. Metal-organic frameworks have been studied extensively for their high permanent porosities and surface areas, properties that have been exploited in investigations into their possible implementation in gas storage[10] and separation[11] applications. More recently metal-organic frameworks have been investigated for sensing,[12] catalysis,[13] drug delivery[14] and optical applications.[15] However, charge transport in metal-organic frameworks in the form of ion transport through the pores and electron conduction through the framework remains largely unexplored, even though ionic and electronic conductivity in metal-organic frameworks could lead to their implementation in areas such as electrochemical energy storage, photovoltaics, thermoelectrics, photocatalysis, and electrocatalysis. In addition to metal-organic frameworks, covalent-organic frameworks, or COFs, have recently been demonstrated.[16] These materials are built from symmetric organic molecules that cross-link via reversible, covalent bond-forming reactions to yield crystalline extended structures. The charge transport properties of covalent-organic frameworks are discussed below.

Ion conduction in inorganic solids has been intensively investigated since the discovery of the remarkably high conductivities of sodium beta-alumina[17] and silver rubidium iodide.[18] Proposed and implemented applications of solid ionic conductors include sensors, fuel cells, and batteries. Metal-organic frameworks have the advantage of being highly designable due to the flexibility in combining metal ions with organic linkers of different size and/or bearing different functional groups, enabling rational control of the pore dimensions and functionalization of the pore surface, a degree of tunability not available in completely inorganic solids. In addition to the possibility of generating completely novel metal-organic framework electrolytes, the ability to alter pore size in a controlled manner allows for systematically probing the behavior of ions in an environment very different from what would be expected or possible in bulk solution phases.[19] Nanoconfinement has been demonstrated in systems other than metal-organic frameworks to strongly influence ionic transport.[20]

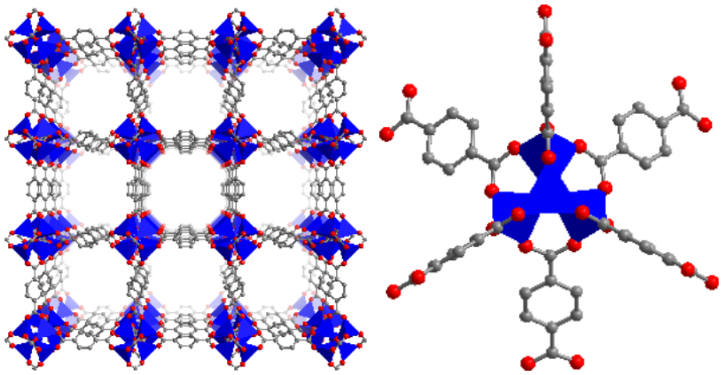

Figure 1.1 (Left) Structure of $Zn_4O(BDC)_3$ (Right) Zn_4O nodes attached to six terephthalates in an octahedral arrangement. Gray and red spheres represent carbon and oxygen atoms and the blue tetrahedral represent the nearest-neighbor coordination environments of zinc ions. Hydrogen atoms are omitted for clarity.

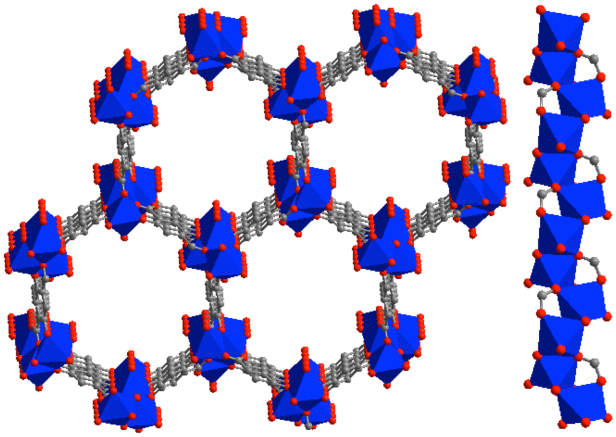

Figure 1.2 Structure of $M_2(DOBDC)$ and the one-dimensional chains of edge sharing M^{2+} octahedra. Gray and red spheres represent carbon and oxygen atoms and the blue tetrahedral represent the nearest-neighbor coordination environments of zinc ions. Hydrogen atoms and non-oxygen atoms of the coordinating solvent molecules are omitted for clarity.

One of the first known extended coordination compounds, Prussian blue,[21] with the idealized formula of $Fe_4[Fe(CN)_6]_3$ is a Class II mixed-valence compound and a known semiconductor[22] that displays permanent porosity.[23] However, theoretical studies have shown most metal-organic frameworks to possess large band gaps, with minimal band dispersion and therefore act as electronic insulators.[24,25] There are several reasons for this. Firstly, the metals typically used (e.g. Ln^{3+}, Zn^{2+} and Cu^{2+}) are not present in a redox-active form. Secondly, bridging ligands used are not conducive to electron transfer between metal centers;[26] hard ligands such as carboxylates are typically used for metal-organic framework syntheses forming bonds ionic in character, minimizing metal-ligand orbital overlap and electronic communication. Electronically conductive metal-organic frameworks could open a wide range of potential applications. Notably, in power storage applications, porous electrodes should have greater ionic diffusivity, allowing for more rapid cell charge and discharge and improved gravimetric power densities. A porous,

high-surface area material that is conductive and features catalytically active sites would open up the possibility of utilizing metal-organic frameworks to catalyze reactions that consume or release electrons. Porous materials, such as porous oxides and carbon nanotubes, have further demonstrated sensing via conductivity changes upon exposure to analytes.[27] A porous, conductive metal-organic framework could display similar behavior, with an extraordinary degree of tunability to optimize sensor selectivity and sensitivity. In addition to enabling the potential applications listed above, access to novel microporous solids, with rigidly held three-dimensional structures with high electrical conductivity are an interesting avenue to fundamentally explore exciting new physical phenomena associated with spatially constrained correlated-electron systems[28] as well as structure property relationships in ways not possible with other conductive systems such as traditional inorganic semiconductors, nor organic molecular conductors and conductive polymers. This chapter reviews the terms of conductivity, some simple models of conductivity for well-studied systems, and methods to measure conductivity. Mixed-valency is discussed, as many of its concepts are useful in considering charge-transport in metal-organic frameworks and related systems. Then, proton and ionic conduction in metal-organic frameworks is discussed as well as successful approaches to demonstrate electronic (including hole and electron) transport in metal-organic frameworks.

1.2 Definition of Terms and Overview of Conductivity

Conductance is defined as the inverse of resistance, the derivative of voltage with respect to current as per Ohm's law:

$$R = \frac{\partial V}{\partial I}; g = \frac{\partial I}{\partial V} \quad (1)$$

Its unit is the Siemen (S), defined as the inverse Ohm (Ω^{-1}). Both resistance and conductance are extrinsic properties. To normalize for sample geometry and dimension the resistivity of a sample is defined by:

$$R = \rho \frac{l}{A} \ , \quad (2)$$

where l is the length of a sample, and A is the cross-sectional area of the sample. P has the units ohms cm. Its inverse, conductivity, σ, has the units $ohm^{-1}cm^{-1}$. Using this quantity it is possible to re-write Ohm's law in the following form:

$$\boldsymbol{J} = \sigma \boldsymbol{E}, \quad (3)$$

where $\boldsymbol{J}$ is the current density vector at a given location in a material and $\boldsymbol{E}$ is the electric field vector in that location. In an isotropic system it will be a scalar quantity, however in an anisotropic system it will be a tensor quantity. Mobility is defined by the following relation between the drift velocity of charge carrier in a material and the mobility of a charge carrier in an applied electric field:

$$\boldsymbol{v_d} = \mu \boldsymbol{E} \quad (4)$$

The total conductivity of material is the sum of the product of each charge carrier's mobility, μ, fundamental charge, q, and volumetric density, n:

$$\sigma = \sum \mu q n \tag{5}$$

In ionic conductivity, the charge carrier is an ion, such as a H^+ proton in proton conductors, or a Li^+ ion in the case of lithium-ion conductors. The diffusion D, of a mobile ionic species is thermally activated:

$$D = D_0 e^{\left(\frac{-E_a}{RT}\right)} \tag{6}$$

Using the Nernst-Einstein equation,

$$\frac{\sigma}{D} = \frac{Ne^2}{kT} \tag{7}$$

it is possible to relate the product of conductivity, σ, and temperature:[29]

$$\sigma T = \sigma_0 e^{\left(\frac{-E_a}{RT}\right)} \tag{8}$$

This relation enables determination of energy of activation, E_a by the slope of a plot of $\log(\sigma T)$ vs. $1/T$. Solid ionic conductors with energies of activation of less than 0.4 eV are classified as superionic conductors.[30]

In electronic conductivity the charge carriers may be electrons, holes, or both. How the movement of an electron generates a current requires little explanation or imagination to appreciate. Why a band filled with electrons is an insulator and how holes behave as positive charge carriers requires further explanation. To better understand hole conduction, consider a filled band with N electrons occupying N states, each with its own momentum k, and velocity v. For each ith electron with a momentum k_i and velocity v_i, there will be another electron with an opposite momentum $-k_i$ and velocity $-v_i$. If we multiply the charge of an electron by the sum of the velocities of the electrons, the current density J, will equal zero:

$$J = (-e)\sum_{i}^{N} v_i = 0 \tag{9}$$

This is why filled bands do not conduct electrons. If the jth electron is removed from the band to form a hole, the current density will become nonzero:

$$J = (-e)\sum_{i}^{N} v_i - (e)v_j = +ev_j \tag{10}$$

Because the first term of the right hand side of equation 10 is zero, the current density will then equal $+ev_j$. As such, the absence of the electron, the hole, will then behave as a positively charged particle with a velocity v_j of the missing electron.[31] A partially filled

band will have available, empty states for electrons to occupy upon application of an electric field, allowing net movement of charge in the band.

In band theory, an electronic insulator has a filled (valence) band separated from a higher energy empty (conduction) band by a band-gap such that thermal population of the conduction band does not occur to an appreciable degree. In an intrinsic semiconductor, the band gap is sufficiently small so that thermal population of the conduction band from the valence band does occur. The temperature dependence of conductivity of an intrinsically doped semiconductor with a bandgap, E_g, is related to the thermal generation of hole and electron pairs in the following form:

$$\sigma = \sigma_0 e^{-(\frac{E_g}{2kT})} \qquad (11)$$

In an extrinsic semiconductor, dopants that can be either low-lying acceptor states above the valence band, or high energy donor states just below the conduction band, serve to create either holes in the valence band or donate free electrons in the conduction band. In a metal there is either a partially filled band, or a filled band that overlaps with an empty band, allowing free movement of electrons (Fig. 1.3). In a metal, there is an inverse relation between conductivity and temperature as phonons scatter the hole or electron charge carriers with increasing temperature.[32]

These are simple models of conduction that apply to traditional inorganic semiconductors and metals. More complicated models are necessary to describe electronic conduction in systems such as organic molecular and polymeric conductors, amorphous semiconductors and many oxides. For example, in heavily investigated conductive polymers, such as polyacetylene and polythiophene, as well as some conducting oxides, light doping does not in fact directly generate holes or electrons in valence and conduction bands, respectively. Rather reduction or oxidation creates a localized state where the geometry is distorted from the polymer's equilibrium geometry. This distortion propagates along with the charge carrier in charge transport and is referred to a polaron.[33] As the concentration of polarons increase in a system, polarons may pair, thus lowering their total energy by sharing the a distortion of the lattice sufficiently to overcome their Coulombic repulsion to form bipolarons, which themselves may behave as charge carriers. As the concentration of bipolarons increase they can overlap to form bipolaron band states responsible for conduction. Bipolaron conduction is implicated in systems such as vanadium bronzes.[34] Other materials may display Nernst-Einstein behavior by diffusion of the charge carriers.[35] Inter-site hopping may be the dominant conduction mechanism,[36] with a variety of ranges of hops with differing energies of activation.[37] Conductivity in a material may have other, more complicated mechanisms with different temperature dependencies of conduction as well as multiple modes of conduction.[38]

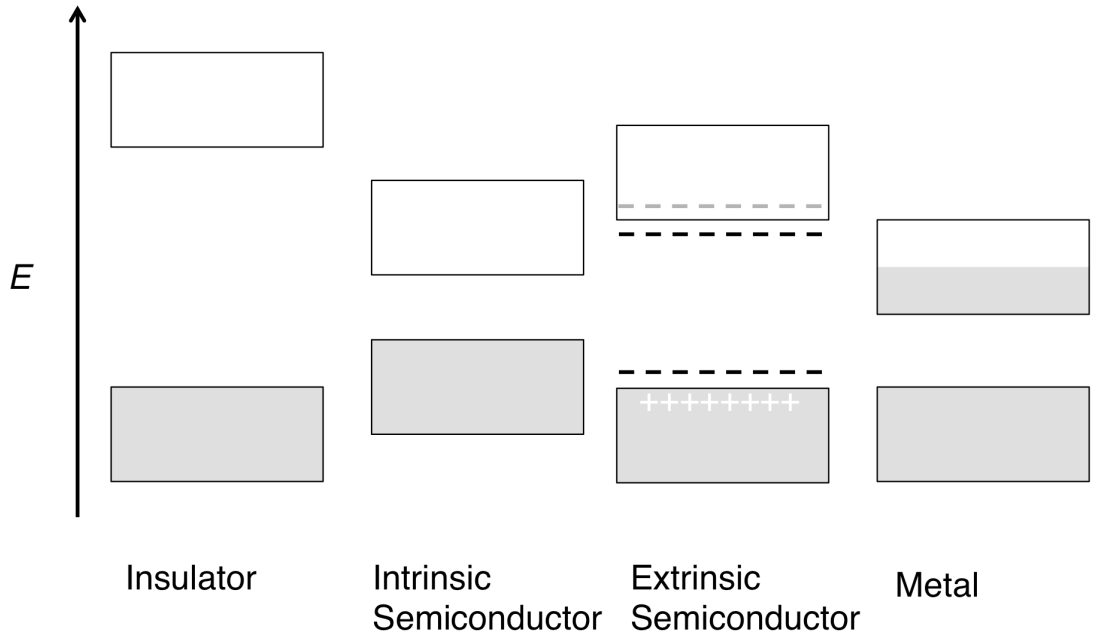

Figure 1.3 Band model treatments of insulators, intrinsic semiconductors, extrinsic semiconductors and metals formed by partially filled bands as well as overlapping filled and unfilled bands. Adapted from ref. 32.

1.3 Techniques for Evaluation of Charge Transport in Metal-Organic Frameworks

Because the techniques used to evaluate charge transport in metal-organic frameworks are not frequently encountered by chemists, this section will discuss the techniques used in this thesis. A discussion of measurements performed on other systems (such as Hall effect measurements,[39] thermopower measurements,[40] time of flight measurements[41] and diode conductivity measurements[42]) is out of the scope of this introduction. The same material measured by different techniques can display drastically different conductivities and mobilities, as such it is important to specify the measurement technique used to evaluate the charge transport of any conductive material.

1.3.1 Two-point and Four-point Direct Current Measurements

In two-point direct current (DC) measurements the sample (a single crystal, a pressed pellet, or a thin film) is contacted between electrodes and a direct current potential is applied. The current through the sample is then measured. Pellet conductivities are a poor measurement of intrinsic conductivity, as grain contacts may dominate conduction,[43] and in highly anisotropic systems random spatial orientations of crystallites will weight the measured conductivities to the least conductive crystal directions.[44] If the sample obeys Ohm's Law, a linear relation between current and applied voltage will be observed. Accounting for the geometry of the measurement, it is possible to obtain a conductivity that shows the scaling of conductance (inverse resistance) with sample extension. Poor contacts, the interface between metallic electrodes and a semiconducting material, degradation of the sample during measurement and intrinsic material properties can all conspire to create samples that do not show

ohmic conductivity.[45] Many semiconductors and low-dimensional conductors do not show ohmic conductivity and some metals even display non-ohmic conductivity at different current and voltage regimes.[46] Contact resistances between the electrodes and the sample may be much higher than the intrinsic resistance of the material, masking the true conductivity of the sample. To measure the conductivity of the sample without interfacial resistances, four-point conductivity measurements can be utilized. In this technique a known current from a constant current sources is applied between two electrodes placed onto the sample. In between the two outer electrodes an inner pair of electrodes is attached to the sample and the potential drop between the two inner electrodes is measured. Because a known current is being passed through the material, and it is possible to measure voltage without drawing current, it is possible to divide the voltage drop across the inner electrodes by the applied current to obtain the resistance of the sample.[45] In this instance the measured voltage is plotted against the applied current. Again, a linear relation should be observed between voltage and current if the sample is an ohmic conductor. In instances where it is difficult to get electrodes in a line on a sample, arrangements of electrodes with specific sequences of measurement allow determination of sample resistances independent of exact sample geometry.[47]

1.3.2 AC Impedance Spectroscopy

One commonly utilized technique to measure both ionic and electrical conductivity is alternating current (AC) impedance spectroscopy.[30a,48] In this technique a sample is contacted with two electrodes and a periodic potential is applied. Direct current measurements of ionic conductors with blocking electrodes (i.e., electrodes that will not absorb or release the charge carriers in the sample) will lead to cell polarizations as mobile charge carriers diffuse to different electrodes, continually increasing resistance. If an alternating potential is applied, the periodically reversal of electric field prevents the development of long range polarizations. In the measurement, current as a function of time is measured as a periodic potential is applied to the sample. In an AC circuit, the voltage as function of time is related to the current as a function of time by the following relation:

$$V(t) = Z(\omega)I(t) \tag{12}$$

The quantity Z, impedance, is analogous to resistance in Ohm's law and is dependent on the angular frequency ω. It has both real and imaginary components. The impedance of a circuit can be decomposed into single circuit elements with their own contributions to the total impedance. For the most trivial case, the impedance of a resistor is simply its resistance, which does not vary with frequency and has only a real component:

$$Z_R = R \tag{13}$$

The impedance of a capacitor with capacitance C, is given by the following relation:

$$Z_C = \frac{-i}{C\omega} \tag{14}$$

where i is $\sqrt{-1}$. While the impedance of an inductor L, is given by:

$$Z_L = i\omega L \tag{15}$$

In addition to the more familiar resistors, capacitors and inductors, constant phase elements (CPEs) and Warburg elements are used to model electrolytes and electrochemical cells. The impedance of a constant phase element, Z_{CPE}, is given by the following expression:

$$Z_{CPE} = \frac{1}{Q_o \omega^n} e^{\frac{\pi}{2} ni}, \tag{16}$$

where Q_o and n are frequency independent quantities fit from the data. For n = 1, a constant phase element has the impedance of an ideal capacitor, whereas for n = 0 the expression reduces to that of a pure resistor. The impedance of a Warburg diffusion element is given by the following expression:

$$Z_W = \frac{A_W}{\sqrt{\omega}} + \frac{A_W}{i\sqrt{\omega}} \tag{17}$$

where A_W is a diffusion coefficient of ions in solution.

It is possible to model a system measured by AC impedance spectroscopy as a circuit composed of multiple circuit elements of the type described above to determine the frequency dependent impedance. Many electronics and specialist electrochemical software packages allow the ready modeling of circuits and fitting of data, without the need of the user to explicitly solve the differential equations describing the voltage and current relations of the model circuit.[49,50] In addition to measuring conductivity of materials, AC impedance spectroscopy is also used to study a diverse array of electrochemical phenomena such as ion-insertion, corrosion, and surface reactivity at electrodes, by modeling these processes with equivalent circuits. Figure 1.4 shows the AC impedance spectra of a solid electrolyte fit as an equivalent circuit, shown below it.

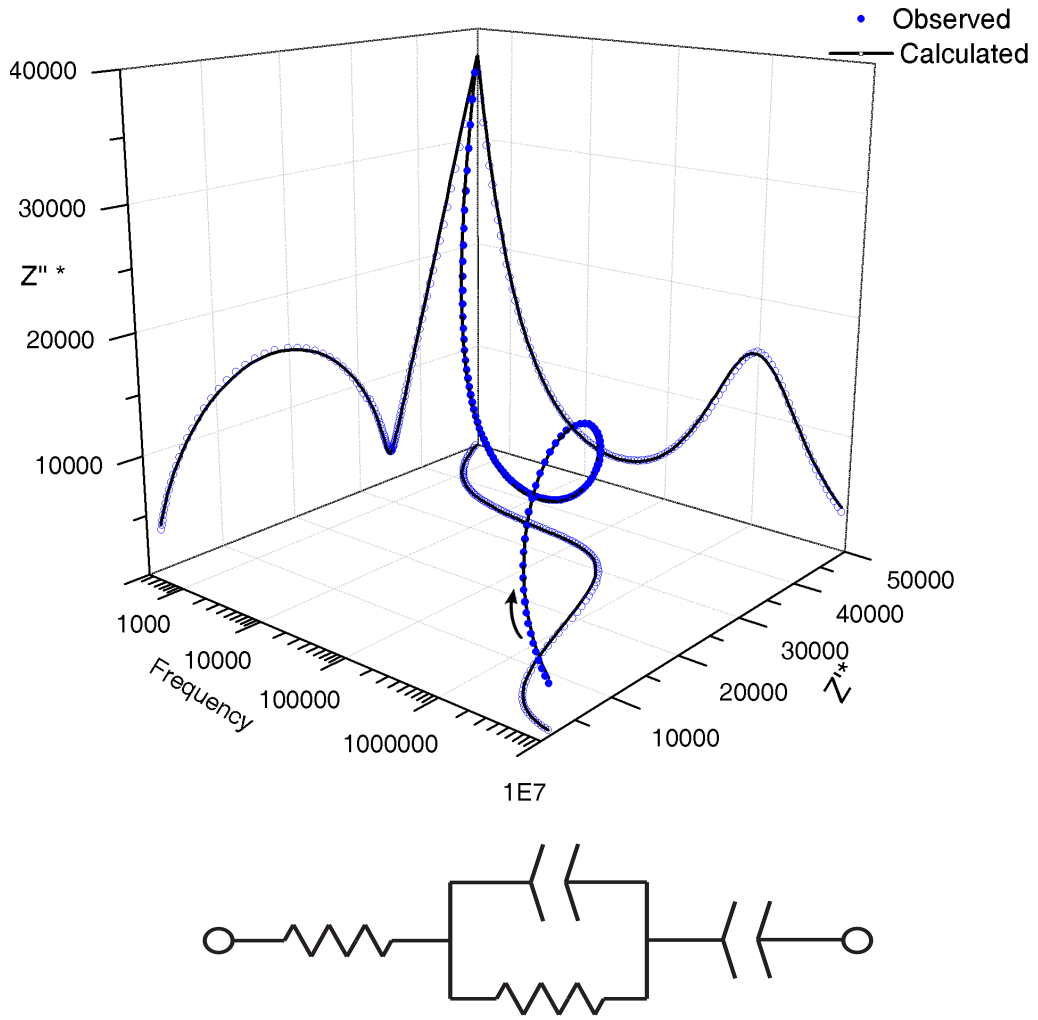

Figure 1.4 Three-dimensional representation of an AC impedance measurement. The arrow points to the direction of decreasing frequency. The projection of the relation between frequency and real impedance is called a Bode plot and is shown as the projection of the data on the bottom of the plot. Regions where the real impedance plateaus are in frequency regimes where only real resistance contributes to impedance. The projection of the complex conjugate of imaginary impedance as a function of frequency is shown on the right of the plot. In systems with negligible inductance, minima in this plot correspond to frequency domains where imaginary reactance vanishes and only real resistance contributes to the impedance. Conversely, maxima correspond to regions of maximal capacitive reactance. The projection of imaginary impedance versus real impedance on the left is referred to as a Nyquist plot. Minima here show frequency regimes where the impedance is resistive in origin. Below it is the circuit used to model the data. The left resistance was taken to represent the ionic resistance of the sample, and the constant phase element in parallel with the resistor was used to model the inhomogeneity of the sample. The rightmost constant phase element was used to model the double layer capacitance.

1.3.3 Flash Photolysis Time-Resolved Microwave Conductivity (FP-TRMC) Measurements

In this technique a sample is placed inside a resonant microwave cavity; a chamber with a standing microwave. The sample is then irradiated with a laser pulse, generating hole/electron pairs. The electric field of the microwave will then do electrical work to move the charge carriers, attenuating the power of the reflected microwave in the cavity, which is measured as a function of time in a FP-TRMC experiment.[51,52] A schematic of this experiment is shown in Figure 1.5

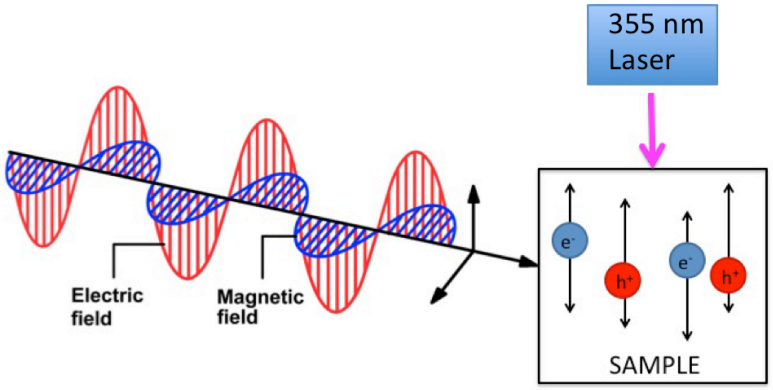

Figure 1.5 Schematic of the FP-TRMC experiment.

The following expression gives the relation between the attenuation of power of the reflected microwave in the resonant cavity, $\Delta P_r/P_r$, to the change in conductivity of the sample $\Delta\sigma$:

$$< \Delta\sigma > = \frac{1}{A}\frac{\Delta P_r}{P_r} \qquad (18)$$

where A is a sensitivity factor determined by the geometry of the resonant cavity, the ratio of incident to reflected microwave power, the resonant frequency of the cavity, and a dielectric constant. Using the Lambert-Beer's law and the relation between conductivity, mobility, and charge carrier population, it is possible to relate the transient conductivity with by the following expression:[52]

$$< \Delta\sigma > = \phi \sum \mu = \frac{1}{eAI_0F}\frac{\Delta P_r}{P_r} \qquad (19)$$

where ϕ is the quantum efficiency of charge carrier generation, $\Sigma\mu$ the total charge carrier mobility, e the charge of an electron, I_0 is the incident photon density, and F a filling factor. The transient conductivity decays with time as a 2nd order rate law as charge carriers recombine, and a plot of a conductivity transient as a function of time will show a peak at illumination followed by a decay (Figure 1.6). Taking the conductivity transient peak it is possible to estimate relate the product of the quantum efficiency of charge carrier generation and the total mobility of charge carriers. Either transient absorption spectroscopy[53] or transient photocurrent measurements[54] or can be used to evaluate the

number of charge carrier pairs generated per photon pulse and thus the quantum efficiency of charge carrier generation. In samples where it is difficult to directly measure either time of flight photoconductivity measurements or transient absorption spectra, photocurrent integrations of the sample after illumination with a pulse of light can be compared to a standard of a sample where the quantum efficiency of charge carrier generation has been previously determined by transient-absorption spectroscopy.[55] Once quantum efficiency has been determined it is possible to then determine the total charge carrier mobility, $\Sigma\mu$.

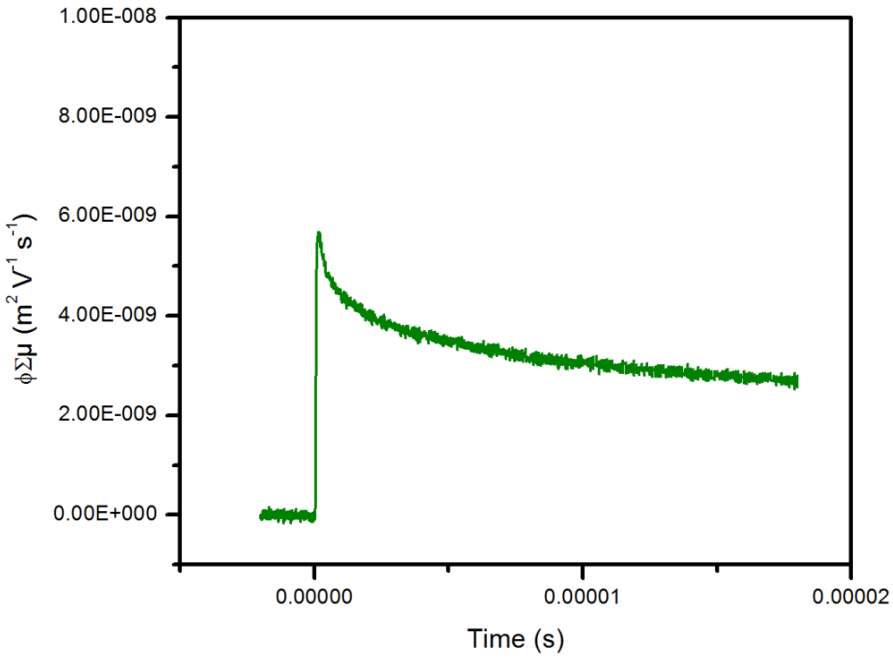

Figure 1.6 A FP-TRMC conductivity transient. Irradiation with a laser pulse occurs at time = 0 seconds. From this work.

1.3.4 Field Effect Transistor (FET) Measurements

In a field-effect transistor (FET) measurement,[32] the sample, which could be in addition to the planar wafers of the semiconductor industry, a single crystal[56] or a thin film[57] is contacted with two electrodes – a source electrode from which electrons will flow from and a drain that electrons will flow into during the operation of the FET device. Between the two electrodes a dielectric is contacted to the sample, and a potential is applied to dielectric via another electrode referred to as the gate electrode. When a positive gate voltage is applied to the dielectric negative charge carriers accumulate at the junction of the dielectric and sample, while lowering the conduction band (or LUMO states of a molecular conductor) into resonance with the Fermi levels of the source and drain electrodes to form a conductive channel in an *n*-type transistor. Conversely, in a *p*-type transistor, a negative gate voltage will accumulate positive charge carriers at the junction of the sample and the dielectric while raising the valence band (or HOMO states of a molecular conductor) into resonance of the Fermi levels of the source and drain electrodes. Figure 1.7 schematically shows the operation of a field effect transistor.

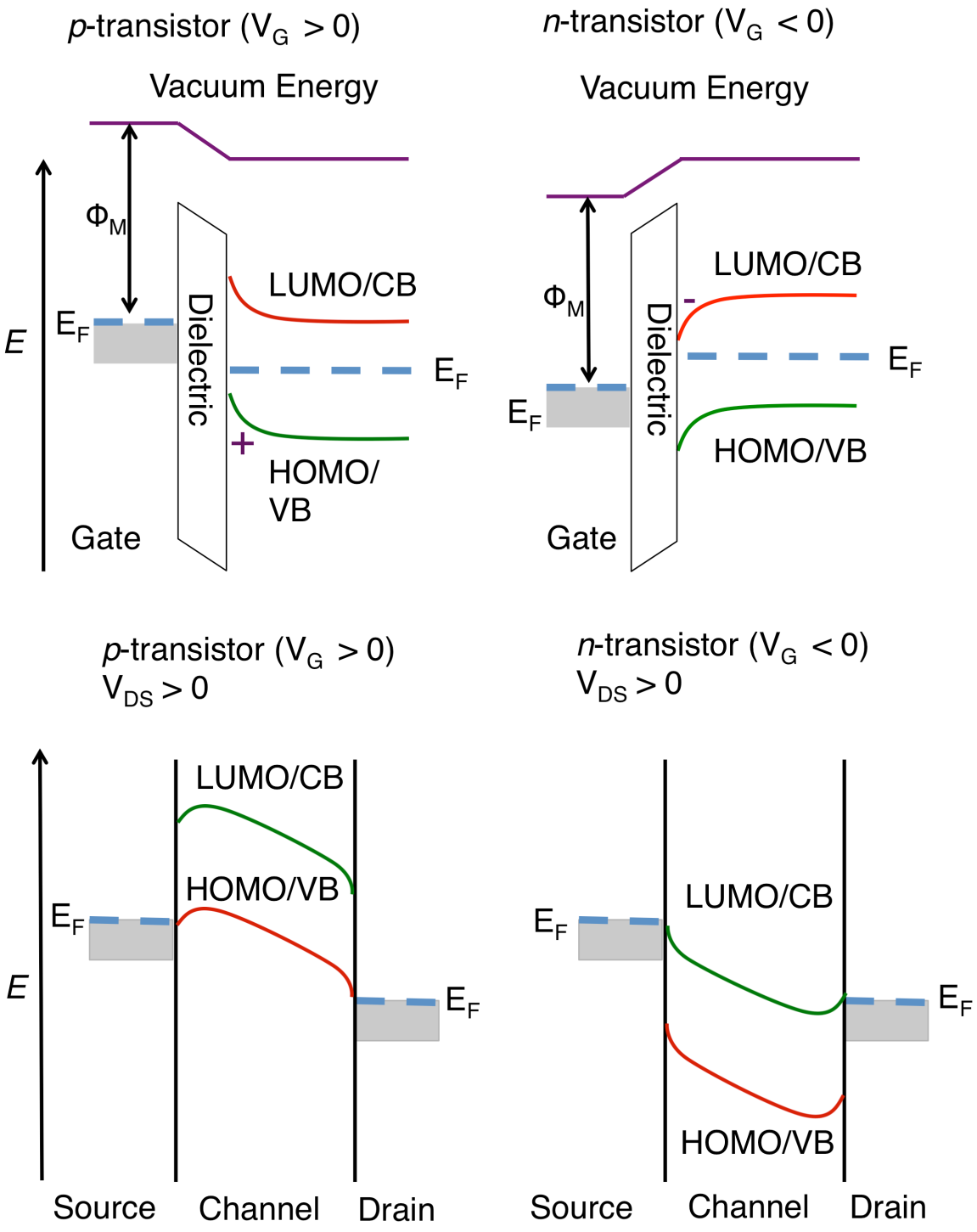

Figure 1.7 Diagram of the energy levels of a FET device. LUMO or conduction band states responsible for *n*-type mobility are shown in green and HOMO or valence band states responsible for *p*-type mobility are shown in red. The top diagrams show the accumulation of charge carriers for *p*-type (left) and *n*-type transistors (right). The bottom diagrams show the energy level diagrams of the electronic states responsible for charge-transport in *p*-type (left) and *n*-type (right) transistors. Adapted from reference 57b.

The left of Figure 1.8 plots the source-drain current (transcurrent) $I_{SD,}$ as a function of gate voltage, V_G, for an *n*-type conductor. For a *p*-type conductor the behavior would be the same with the trends in transcurrent occurring with increasingly negative gate voltages. In an ambipolar conductor the trends in transcurrent will be observed at both negative and positive gate voltages (although not necessarily symmetrically, depending on differences in hole and electron mobilities in the material and matching of the valence band/HOMO states or conduction band/LUMO states with the Fermi levels of the source and drain electrodes). Plots of transcurrent as a function of gating voltage are referred to as transfer curves. Initially at $V_G = 0$, minimal current flows (in highly conductive samples there will be current flow at any gate voltage). Not all accumulated charge goes to forming a conductive channel. First, charge injected fills deep trap states, and no appreciable increase in current is observed below the threshold voltage, V_{th}. When $V_G > V_{th}$, the source drain current will begin increase, and is described by the following equation:

$$I_{SD} = \frac{W}{L}\mu V_{SD} C_i (V_G - V_{th}) \tag{20}$$

where L is the length of the channel, W is its width, C_i is the capacitance of the dielectric layer and $V_D < V_G$. If I_{SD} is directly proportional to V_G, as it is in the linear regime the mobility in the linear regime can be extracted with the following relation:

$$\mu = \frac{\partial I_{SD}}{\partial V_G}\frac{L}{W C_i V_{DS}} \tag{21}$$

When $V_D \geq V_G$, the channel will saturate, to a good approximation I_{SD} will no longer depend on V_D and will instead apply only will have the following dependence on V_G:

$$I_{SD} = \frac{\mu C_i W}{2L}(V_G - V_{th})^2 \tag{22}$$

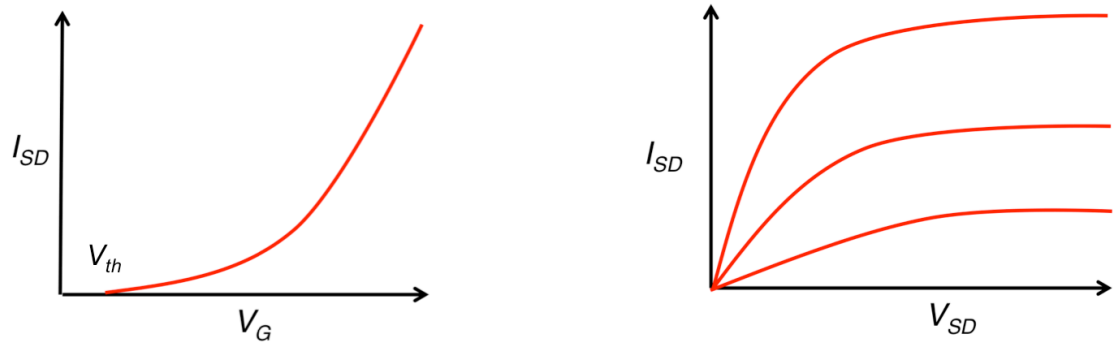

Figure 1.8 Left: Source-drain current, I_{SD}, as a function of gate voltage, V_G (transfer curve). Right: I_{SD} as a function of source-drain voltage, V_{SD} (output curve). The traces of increasing saturation current are are for increasing V_G above the threshold voltage, V_{th}.

1.3.5 Miscellaneous Measurements

In addition to direct measurements of charge transport properties, Tauc plots[58] can be used to determine band-gaps from diffuse reflectance or thin film absorbance data in metal-organic frameworks that may display a band structure, and diffuse reflectance measurements of metal-organic frameworks can elucidate mixed-valence behavior.[59] FT-IR features typical of highly conductive systems[60] are observed in the conductive metal-organic framework system discussed in Chapter 3. BET fits of adsorption isotherms, typically of N_2 measured at 77 K are used to evaluate the porosity and surface area of metal-organic frameworks.[61] Biased photocurrent measurements can be used to determine the sign of the majority charge carrier in metal-organic frameworks.[62] NMR experiments may also be used to determine diffusivity and relaxation times of mobile ionic charge carriers.[63] In Chapter 4, solid-state slow-scan cyclic voltammetry[64] is used to determine the comproportionation constant K_c of the framework $K_xFe_2(BDP)_3$ to gain insight into the degree of electron communication and delocalization in this material.

1.4 Mixed-valency

A mixed-valence compound is one in which the same element (or molecule) is present in two formally different oxidation states. Robin and Day published a landmark review of mixed-valence compounds, proposing a tripartite classification scheme where classes I, II, and III refer to decreasing degrees of electronic localization on individual sites.[65] At the same time Hush and co-workers developed a two-site formalism for the treatment of mixed-valence systems.[66] These classifications and models are discussed below.

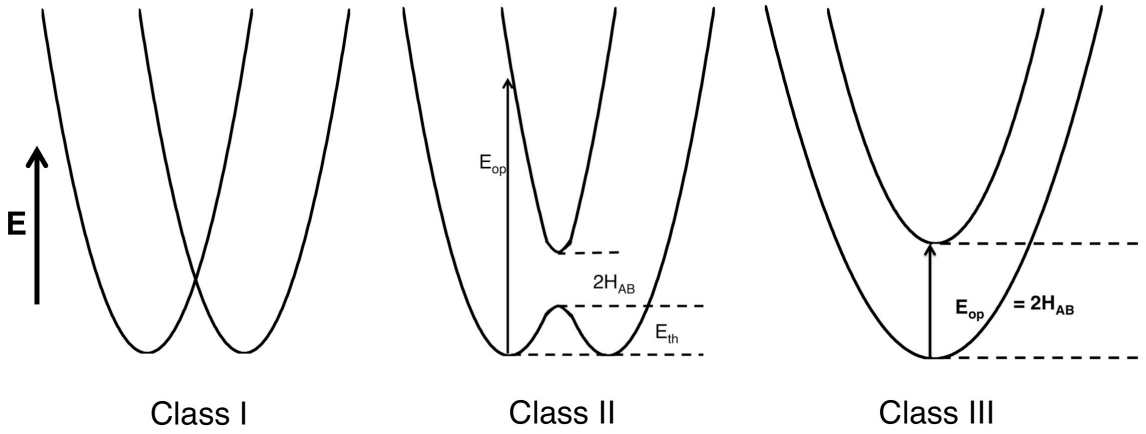

Figure 1.9 Potential energy curves for Class I, II, and III mixed-valence systems. The ordinate is energy while the abscissa is the electron transfer coordinate. E_{op} is photon energy, E_{th} is the thermal barrier to electron-transfer and H_{AB} is an electronic interaction parameter showing the strength of inter-site electronic coupling.

Class I mixed-valence compounds have distinct sites with different oxidation states where electron transfer and interconversion between oxidation states does not

occur. This can be because of a lack of connectivity between the sites, or because the sites are in environments so different that electron transfer is prohibited. The potential energy of the ions can be thought of as two non-interacting parabola as shown in Figure 1.9. Class I compounds are electronic insulators, and their spectroscopic properties are simply the summation of the spectra of their constituent chromophores. Figure 1.10 shows Pb_3O_4 or lead (II, IV) oxide, also known by the common name, red lead.[67] Its structure features trigonal pyramidal Pb(II) sites and Pb(IV) octahedral sites. The trigonal pyramidal geometry of Pb(II) sites is explained as a consequence of the inert-pair effect.[68] These significantly different coordination environments prevent Pb^{2+} and Pb^{4+} interconversion. As ready electron transfer is precluded, Pb_3O_4 is an insulator, and from the standpoint of electronic conductivity it, along with other Class I mixed-valence compounds is uninteresting. However, this compound is interestingly tied to the etymology of the word miniature A casual reader of a dictionary may be mystified by the following etymology : "fr. L. *miniatus*, past. Part. of *miniāre*, to color with cinnabar or red lead."[69] Pliny the Elder refers to red pigments as *minium*, a term he seemingly applies to HgS, Pb_3O_4, and Cu_2O in his *Natural History*.[70] *Miniāre* came to refer to paint with any red mineral pigment, while *minium* came to refer specifically to red and orange lead oxide pigments.[71] In the medieval era, manuscripts were illustrated with small drawings, often painted with minium, and were referred to as miniatures. Eventually miniature became an adjective meaning diminutive.[72] Red lead is also used to check planarity in hand scraping, a process used to make very flat metal surfaces.[73] Another compound used for this purpose is Prussian Blue (referred to in the metal-working trade as Engineer's Blue),[74] an intensely blue-colored Class II mixed-valence compound discussed below and shown in Figure 1.10.

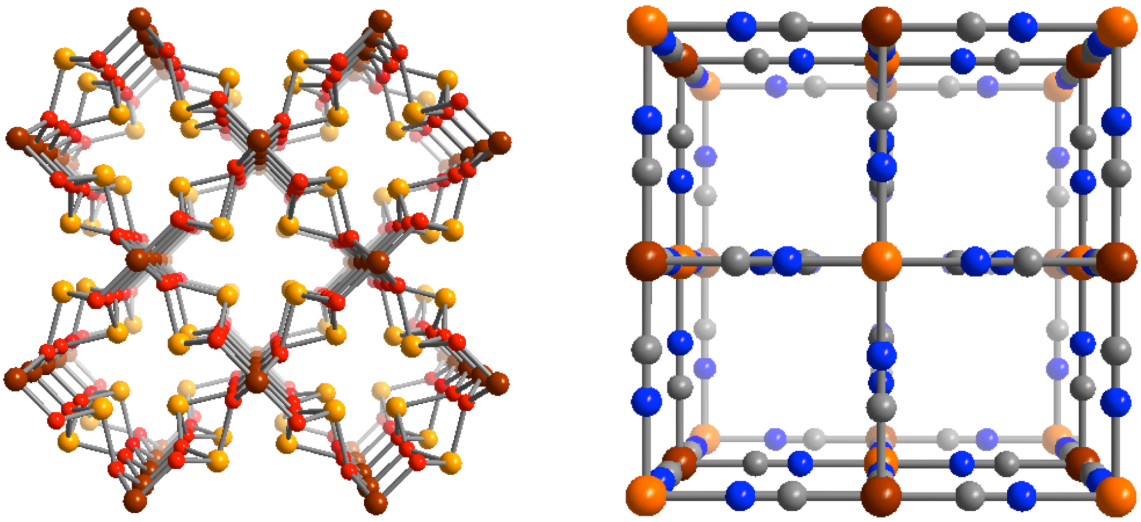

Figure 1.10 Left: Ball and stick representation of Pb_3O_4, a Class I mixed-valence compound. Burgundy, yellow and red spheres represent octahedral Pb^{4+}, trigonal pyramidal Pb^{2+} and O^{2-} ions respectively. Right: The structure of Prussian Blue. Dark orange, light orange, blue, and gray spheres represent Fe^{3+} ions, Fe^{2+} ions, nitrogen atoms, and carbon atoms. The fractional occupancy of the $Fe(CN)_6$ sites are not represented.

In Class II compounds, electron transfer is possible between elements of different oxidation states. In Hush's model, the electron can be transferred over a thermal barrier, E_{th}, or can be optically excited by a photon of sufficient energy. The degree of interaction between the two sites is related by the H_{AB}, an energy of the stabilization of the interaction between the two sites. As H_{AB} increases, E_{th} decreases (Figure 1.9). In addition to the spectroscopic properties of the constituents of the Class II mixed-valence system, an intervalence charge transfer band is observed. Hush theory predicts it to be symmetric and with a half-width equal to the square root of the energy of the peak maximum (in wavenumbers):

$$\Delta\overline{\nu}_{1/2} = \sqrt{2310\overline{\nu}_{max}} \qquad (23)$$

With the peak intensity ε_{max} and a known inter-site distance R, it is possible to directly extract the energy of electronic coupling, H_{AB}:

$$H_{AB} = \frac{2.05 \times 10^{-2}\sqrt{\varepsilon_{max}\overline{\nu}_{max}\Delta\overline{\nu}_{1/2}}}{r} \qquad (24)$$

Because of thermally activated electron transfer between ions, extended solids of Class II compounds are semiconductors. Prussian blue, with the idealized formula $Fe^{III}_4[Fe^{II}(CN)_6]_3 \bullet 14H_2O$ assembles into a face-centered cubic structure, where the low spin Fe^{2+} ions are coordinated by the carbon atoms of the cyanide ligand, and the high spin Fe^{3+} ions are coordinated by the cyanide's nitrogen atoms. To have a charge balanced structure with the idealized stoichiometry, ¼ of the $[Fe(CN)_6]^{4-}$ groups in the structure shown in Figure 1.10 must be vacant, and water completes the coordination sphere of the Fe^{3+} ions.[75] Electron transfer from the Fe^{2+} to the Fe^{3+} sites is possible, enabling long-range, activated charge transport. The intense blue of Prussian blue due to an absorption band at 14,000 cm^{-1} from intervalence charge transfer between Fe^{2+} and Fe^{3+} sites.[76] By substitution of ruthenium, with its greater orbital extension, it is possible to obtain the analagous ruthenium framework, $K_{1.2}Ru_{3.6}[(Ru(CN)_6]_3 \bullet 16H_2O$, with a 300 K four-point pressed pellet conductivity of 5.7×10^{-3} S/cm, two orders of magnitude greater than that of Prussian Blue, 5.5×10^{-5} S/cm.[77]

Another measure of electronic interaction between metal sites is the comproportionation constant K_c. Consider a symmetrical system with an element M in two sites A and B with two possible oxidation states M^{n+} and $M^{(n+1)+}$. There are four possible states, two homovalent: $\{M_A{}^{n+}, M_B{}^{n+}\}$, $\{M_A{}^{(n+1)+}, M_B{}^{(n+1)+}\}$ and two equivalent mixed-valence states: $\{M_A{}^{(n+1)+}, M_B{}^{n+}\}$ and $\{M_A{}^{n+}, M_B{}^{(n+1)+}\}$. A comproportionation/disproportionation equilibrium can then be written:

$$\{M_A^{n+}, M_B^{n+}\} + \{M_A^{(n+1)+}, M_B^{(n+1)+}\} \rightleftharpoons 2\{M_{A,B}^{n+}, M_{B,A}^{(n+1)+}\} \qquad (25)$$

with a comproportionation constant K_c:

$$K_c = \frac{[M_{A,B}^{n+}, M_{B,A}^{(n+1)+}]^2}{[M_A^{n+}, M_B^{n+}][M_A^{(n+1)+}, M_B^{(n+1)+}]} \quad (26)$$

When there is no electronic interaction between the metal sites, the value of K_c will equal 4, the statistical value. As electronic interaction between the sites increases the comproportionation constant will increase. Class II compounds have K_c's on the order of 4 to 1,000.[78] The K_c of Class III compounds can be as high as 10^{14}.[79]

Using the Nernst equation it is possible to electrochemically measure the comproportionation constant by measuring the difference in the redox potentials of the reduction potentials of the fully reduced and oxidized states with respect to the mixed-valence state.[80]

$$\{M_A^{(n+1)+}, M_B^{(n+1)+}\} + e^- \rightleftharpoons \{M_{A,B}^{n+}, M_{B,A}^{(n+1)+}\} \quad E_1^\circ \quad (27)$$

$$\{M_{A,B}^{n+}, M_{B,A}^{(n+1)+}\} + e^- \rightleftharpoons \{M_A^{n+}, M_B^{n+}\} \quad E_2^\circ \quad (28)$$

such that:

$$\frac{RT}{\mathfrak{F}} \ln K_c = E_1^\circ - E_2^\circ \quad (29)$$

where R is the ideal gas constant, T is temperature and $\mathfrak{F}$ is Faraday's constant.

In a Class III mixed-valence compound, $2H_{AB}$ increases until E_{th} disappears. The two sites are no longer distinguishable; rather than a double well the potential energy of the electron is located in a well with only one minimum (Figure 1.10). Electron transfer can no longer be discussed in a meaningful manner, as the electron is already delocalized between sites. Extended solids of this nature show high, quite often metallic conductivities. Inspection of Figure 1.10 reveals that even through there is no more intervalence charge transfer, optical absorption between delocalized ground and excited state occurs, with a photon energy $E_{op} = 2H_{AB}$. These absorption features are highly intense and asymmetric.[81] It should be noted that the optically excited state of a Class II mixed valence compound is itself a delocalized Class III mixed-valence system, as shown by Figure 1.10; it is in this way that electron transfer between the two sites is possible.

In the symmetric Creutz-Taube ion (shown in Figure 1.11), in the ground state of the molecule, the oxidation state of the ruthenium ions are considered as $Ru^{2.5+}$ instead of Ru^{2+}/Ru^{3+}. This compound is the canonical Class III mixed-valence molecule.[82] In molecular systems analogous to the Creutz-Taube ion, perturbations of the bridging ligand and the metal sites have been carefully tuned and studied to study electron transfer and mixed-valency.[83] However, the Creutz-Taube ion may be better described as a system at the borderline between Class II and Class III,[84] along with many other molecular systems with properties that are neither described by the extreme cases of the Hush two-site treatment of the Class II system, nor the completely delocalized Class III model. Additionally, the diagrams in Figure 1.9 are of mixed-valence systems with two sites for the location of the transferred electron. In fact, in many systems there is

considerable localization of charge on the bridging ligand. As such, three-site models that account for where there is electronic localization on the bridging ligand, give much more applicable descriptions of these systems.[85] In Chapter 3 of this work, Mössbauer spectroscopy indicates that reduction electrons are not significantly localized on iron-based orbitals of the investigated framework, but instead may be heavily localized on ligand-based orbitals.

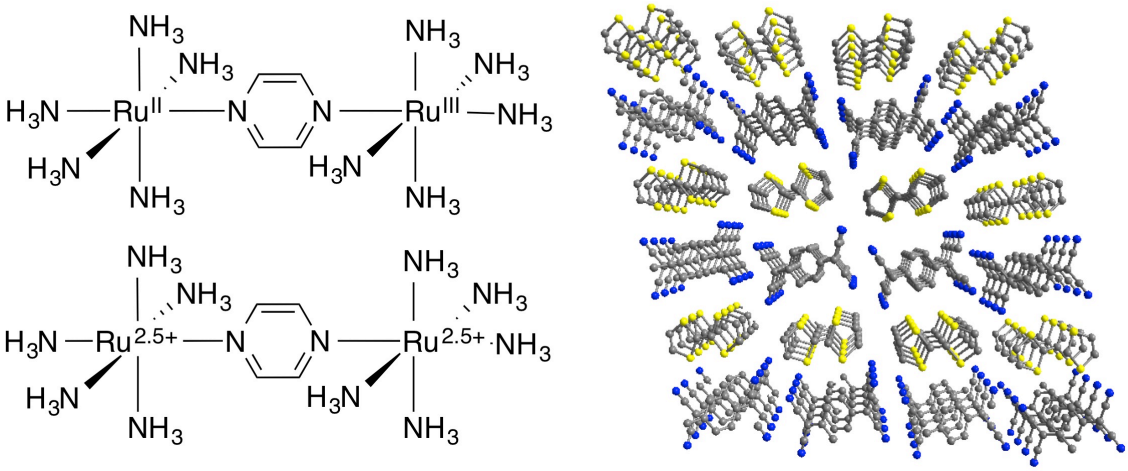

Figure 1.11 Left: The structure of the mixed-valence Creutz-Taube complex with valence trapped (top) and de-trapped (bottom) representations of the ruthenium oxidation states. Right: Ball and stick representation of TTF-TCNQ. Yellow, blue, and gray spheres represent sulfur, nitrogen, and carbon atoms. Hydrogen atoms have been admitted for clarity.

In 1973, it was discovered that 1:1 mixtures of tetrathiafulvalene (TTF) and 7,7',8,8'-tetracyanoquinidomethane (TCNQ) display metallic conductivity above 58 K.[86] In the solid state TTF-TCNQ crystallizes in the solid state as parallel stacks of TTF and TCNQ molecules[87] (Figure 1.11). The TTF partially oxidizes TCNQ (~ 0.6 e^- from TTF to TCNQ).[88] The excess electrons are delocalized over the TCNQ stacks, forming a partially filled band. As such TTF-TCNQ can be considered Class III with respect to TCNQ and the high degree of electronic delocalization of the partially reduced TCNQ is responsible for this compound's metallic conductivity. Mixed-valence π-stacked charge-transfer salts of TTF, TCNQ and related compounds also yield conductive charge transfer salts.[89-91] The use of donor and acceptor molecules such as TTF and TCNQ have been employed to form conductive metal-organic and covalent-organic frameworks, and partially oxidized stacks of planar platinum complexes yield conductive one-dimensional inorganic chains as will be discussed below.

1.5 Conductive Covalent-Organic and Metal-Organic Frameworks

Below I describe the current state of the art in conductive metal-organic frameworks and covalent-organic frameworks, describing progress in proton conduction, metal-organic frameworks that display conduction of other ions, and electronic (hole and electron) transport measured in metal-organic frameworks.

1.5.1 Proton Conducting Metal-Organic Frameworks

To date there has been an extensive number of investigations of metal-organic frameworks that display proton-conductivity. Most systems rely upon proton conduction pathways through adsorbed water. Water adsorbed in the pores of a metal-organic framework are conductive via transfer of protons through a concerted Grotthuss mechanism, where proton transport is due to bond isomerization in clusters of closely spaced water molecules instead of diffusion of protons (Figure 1.12).[92] Exposed metal sites on a metal-organic framework can serve as Lewis acids activating the protons on water molecules coordinating to metal sites, increasing its acidity.[93] In systems where proton-conductivity is water dependent it is necessary to specify the percent relative humidity that the measurement is performed at. $Ni_2(DOBDC)(H_2O)_2 \bullet 6H_2O$, the hydrated form of $Ni_2(DOBDC)$ (structure shown in Figure 1.2) showed a conductivity of 5.3×10^{-5} S/cm at 25 ºC and 95% RH.[94] By soaking the material in aqueous solutions with pH ranging from 5.4-1.8 the conductivity (measured at 25 ºC, 95% RH) increased from 1.9×10^{-4} S/cm at pH = 5.4 to 1.1×10^{-2} S/cm at pH = 1.8. Because variable temperature conductivity measurements of this material demonstrate extremely low energies of activation (0.12-0.19 eV) and FT-IR spectroscopy showed red-shifted O-H stretching frequencies, the authors attribute the high proton conductivities to a Grotthuss mechanism.

Another approach to increase proton-conductivity is to add acidic groups to the organic linker. The M(OH)(BDC) ($M = Fe^{3+}$, Al^{3+}, Cr^{3+})[95-97] or MIL-53 structure type is formed of vertex sharing μ^2-OH bridged interconnected by 1,4-benzenedicarboxylate to form a three-dimensional framework with open diamond shaped channels (Figure 1.9). It is possible to obtain isoreticular frameworks, with varied substituents on the phenylene ring of the organic linker. By adding increasingly acidic substituents it is possible to increase the conductivity at 25 ºC and 95% RH from 2.3×10^{-8} S/cm to 2.9×10^{-6} S/cm, while decreasing the energy of activation from 0.47 eV to 0.20 eV.[98]

Anhydrous proton-conduction is of interest as it allows the operation of fuel cells at temperatures greater than 100°C. Imidazole exists in tautomeric forms that support a proton-transport pathway not unlike the Grotthuss mechanism. Imidazole can be incorporated into the pores of Al(OH)(BDC) and Al(OH)(NDC) (NDC^{2-} = 1,4-naphthalenedicarboxylate), a compound with a very similar structure to Al(OH)(BDC) (Figure 1.9).[99] Al(OH)(BDC)⊃0.6Im (Im = imidazole) displays a room-temperature anhydrous proton conductivity of 10^{-10} S/cm that increased to 1.8×10^{-7} S/cm at 120ºC under anhydrous conditions, with an E_a of 0.6 eV. Al(OH)(NDC)⊃1.3Im, with its greater imidazole content, displayed an anhydrous room temperature conductivity of 5.5×10^{-7} S/cm that increases to 2.2×10^{-5} S/cm at 120 ºC with an E_a of 0.6 eV.[100] It should be noted that imidazole is molten at 120 ºC (m.p. = 89-91 ºC). Here, loading of imidazole in the metal-organic framework pores allowed the access of molten proton-conductivities in a solid material. Incorporation of histamine, an amphoteric nitrogenous base with three sites for proton transfer into Al(OH)(NDC) yielded an inclusion compound with an anhydrous proton-conductivity of 1.7×10^{-3} S/cm at 150 ºC,[101] and incorporation of 1,2,3-triazole (m.p. = 23-25 ºC) into a framework with free phosphonic acid groups gave an

anhydrous proton conductor with a conductivity of 5×10^{-4} S/cm at 150 ºC, with an activation energy of 0.34 eV for temperatures between 90 ºC and 150 ºC.[102]

A complete overview of all of the strategies to engender proton-conductivity in metal-organic frameworks is out of the scope of this work. However, more exhaustive treatments of proton-conducting metal-organic frameworks are given in reviews and perspectives on this topic.[103-105]

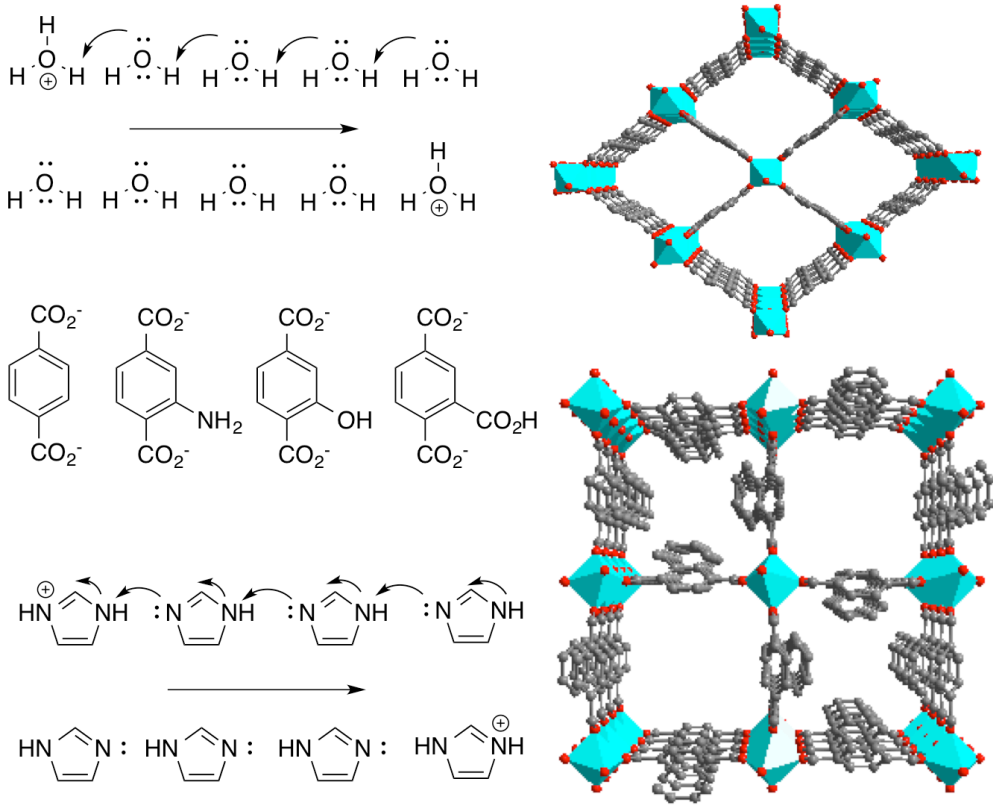

Figure 1.12 Top left: Grotthuss mechanism of proton transfer. Middle Left: Terephthalic acid derivatives with increasingly acidic functional side groups. Bottom Left: Grotthus-type proton transfer mechanism for imidazole. Top right: Polyhedral representation of the M(OH)(BDC) structure M (= Fe^{3+}, Al^{3+}, Cr^{3+}). Bottom right: Polyhedral representation of the Al(OH)(NDC) structure. Gray, and red spheres represent carbon and oxygen atoms, respectively. The teal octahedra represent the nearest neighbor coordination environment of the metal atom. Hydrogen atoms omitted for clarity.

1.5.2 Ionically Conductive Metal-Organic Frameworks

Chapter 2 of this dissertation demonstrates lithium ion conductivity in metal-organic frameworks via post-synthetic modification of a framework with open metal sites, Mg_2(DOBDC), with lithium alkoxides to form a metal-organic framework solid electrolyte with ionic conductivities of 3.3×10^{-4} S/cm (Figure 1.13) and a low energy of

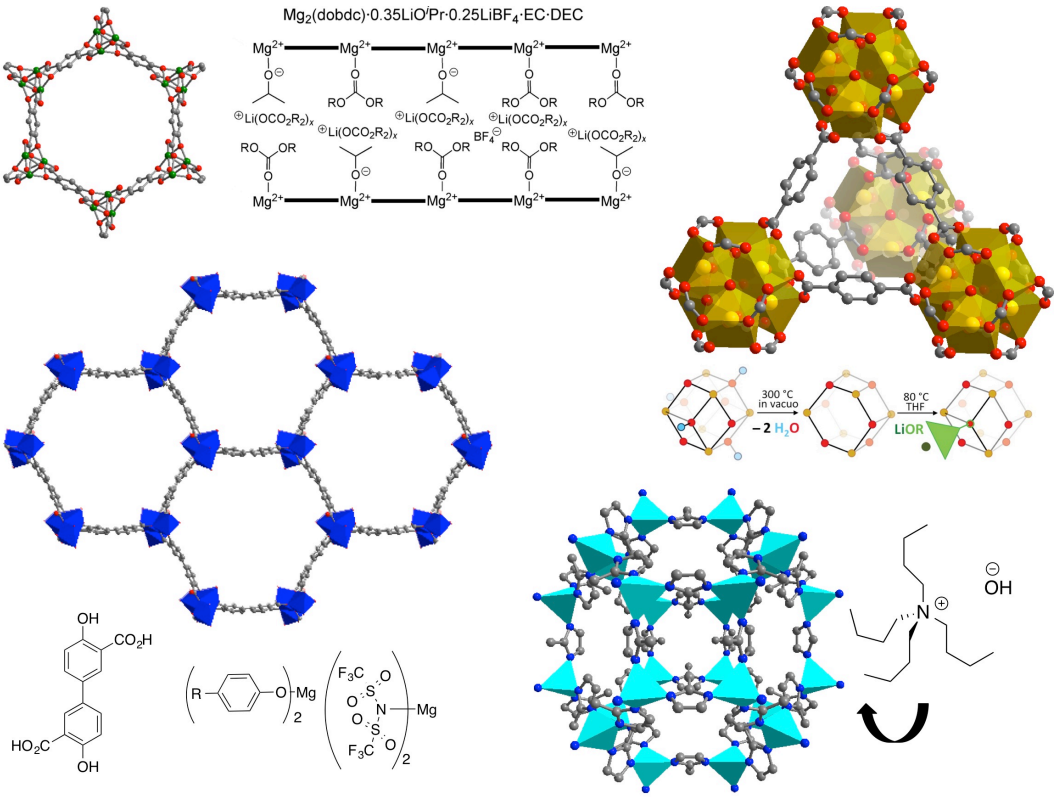

Figure 1.13 Ion conducting metal-organic frameworks. Top left: Mg_2(DOBDC) grafted with lithium isopropoxide. Top right: Zr_6(OH)8(BDC) grafted with lithium isopropoxide. Bottom lfet: Mg(DOBPDC) grafted with Mg-TFSI and phenoxides. The expanded linker is shown at bottom left. Bottom right: ZIF-8 structure with tetra-*n*-butylammonium hydroxide.

activation of 0.14 eV.[106] Our group has subsequently demonstrated lithium ion conductivity by substitution of alkoxides from lithium alkoxide salts for hydroxides in the $Zr_6O_4(OH)_4(O_2C)_{12}$ building units of the metal-organic framework $Zr_6O_4(OH)_4(BDC)_{12}$ (referred to as UiO-66)[107] to yield a framework with a lithium ion conductivity of 10^{-4} S/cm[108] (Figure 1.13). Magnesium ion conductivity has been demonstrated in our group by expansion of the pores of the Mg_2(DOBDC) framework by use of the expanded linker 2,2'-dihydroxy-4,4'-biphenyldicarboxylic acid to yield the framework Mg_2(DOBPDC).[109] By post-synthetic grafting of magnesium phenoxides and magnesium bistrifluoromethanesulfonate to Mg_2(DOBPDC), it was possible to obtain a novel series of solid magnesium conductors[110] (Figure 1.13). Electron-donating substituents decreased uptake of the phenoxides into the framework, while electron-withdrawing substituents on the phenoxides increased the uptake of the phenoxide into the pores of the framework, increasing the conductivity, whilst decreasing the energy of activation. The most-conductive formulation, $Mg_2(DOBPDC)\bullet 0.21Mg(OC_6H_4CF_3)_2\bullet 0.46Mg(TFSI)_2$ had a room temperature conductivity of 0.25 $\times 10^{-4}$ S/cm and an activation of 0.11 eV.

Polyethers have been investigated as solid lithium conductors after they were shown to solvate lithium ions in the 1970s.[111] However, as solids at room temperature they have conductivities too low for practical use.[112] Zn_2(1,4-benzenedicarboylate)(triethylamine), a framework with one-dimensional square (0.75 ×

0.75 nm^2) pores, was loaded with $LiBF_4$ dissolved in 600 Da polyethylene glycol. NMR relaxation measurements showed a liquid-like lithium ion mobility.[113] It was postulated that the nano-confinement of the polymer chains in he pores of the framework in inhibited crystalline ordering, as previous studies showed confinement of polyethylene glycol in nanopores increased the glass transition temperature.[114]

While in most solid state ion-conductors the mobile ion is cationic, solid anion conductors such as the F^- conductor PbF_2,[115] and the high temperature ($T \geq 1000$ ºC) O^{2-} conductor yttria-stabilized zirconia (YSZ),[116] have been studied. By loading a framework, ZIF-8, noted for its stability with the formula $Zn(2\text{-mim})_2$ (2-mim^{-1} = 2-methylimiazolate^{-1}) with a sodalite topology (Figure 1.13) with bulky and immobile quarternary alkylammonium hydroxides, a hydroxide-ion conductor was obtained.[117] At 99% RH the material showed a room temperature conductivity of 2.3×10^{-8} S/cm (in comparison to a conductivity of 3.8×10^{-12} S/cm of the bare, hydrated framework) with an energy of activation of 0.7 eV. Ion exchange experiments indicated that the hydroxide ions were mobile, whereas the tetrabutylammonium ions were immobile in the pores of the framework.

1.5.3 Electronically Conductive Covalent-Organic Frameworks with π-Stacked Groups

The discovery of conductivity in tetrathiafulvalene (TTF)[118] and tetracyanoquinodimethane (TCNQ)[85a,117] and dicyanoquinodiimine (DCNQ)[120] salts (see Figure 17) in the 1970s has created the burgeoning and very active field of organic electronics.[121] These systems quite often display fascinating physics, for instance, the charge transfer salt $(TMTSF)_2PF_6$ (TMTSF = tetramethyltetraselenafulvalene) is a quasi-one-dimensional superconductor.[122] In these materials, π-stacked organic donor or acceptor units are partially oxidized or reduced, generating a partly filled conduction band to enable electronic conductivity. In addition to two-dimensional metal-organic frameworks generated by the reaction of a metal-precursor and a planar bridging ligand that will be discussed below, covalent-organic frameworks built by the reaction of planar organic molecules that π-stack have demonstrated considerable charge mobility. Systems constructed of two-dimensional stacked TTF groups linked through enamine linkages displaying a porosity of 720 m^2/g as demonstrated by BET fits of 77 K N_2 adsorption isotherms.[123] It is possible to oxidize the TTF stacks with oxidants such as TCNQ or I_2 to obtain a mixed-valence covalent-organic framework with a two-point thin film conductivity of 2.8×10^{-3} S/cm at room temperature. EPR spectroscopy confirmed that oxidation of the framework generated a radical located on the TTF-groups.

It is possible to obtain conductive covalent-organic frameworks built of π-stacks of conjugated macrocycles analogous to conductive π-stacked macrocycles[124] In one reported series of metalloporphyrin based covalent-organic framework, by changing the central metal atom from zinc, to copper, to the free acid it is possible to change the mobility (as measured by FP-TRMC) from ambipolar ($\mu_h = 0.032$ $cm^2/V{\cdot}s$, $\mu_e = 0.016$ $cm^2/V{\bullet}s$), to electron ($\mu_e = 0.19$ $cm^2/V{\cdot}s$) to hole ($\mu_e = 3.5$ $cm^2/V{\cdot}s$) with BET surface areas of 1893, 1713, and 1724 m^2/g (N_2, 77 K), respectively.[125] To effect this discrimination the mobility was measured in a chamber with argon and with sulfur hexafluoride (SF_6). Sulfur hexafluoride is an electron acceptor, so measuring the mobility

in an SF_6 atmosphere should yield the hole mobility alone, as the SF_6 acts as an electron scavenger. This value was subtracted from the total mobility measured in Ar to obtain the electron mobility. Another group reported tremendously high hole and electron mobilities with free porphyrin stacks of 8.1 and 3.0 cm/V·s for two frameworks COF-366 and COF-66 respectively.[126] COF-366 has a BET surface area of 735 m^2/g and COF-66 has a surface area of 360 m^2/g (N_2, 77 K). In an analogous design principle to the organic charge transfer salts such as TTF-TCNQ, a covalent-organic framework built of planar triphenylene acceptor and 1,2,5-benzothiadiazole donor groups linked by boronic ester linkages referred to by the authors as DA-COF, has been reported.[127] FP-TRMC of this material shows respective hole and electron mobilities of $\mu_h = 0.01$ and $\mu_e = 0.04$ $cm^2/V \cdot s$ while displaying a BET surface area of 2021 m^2/g (N_2, 77 K).

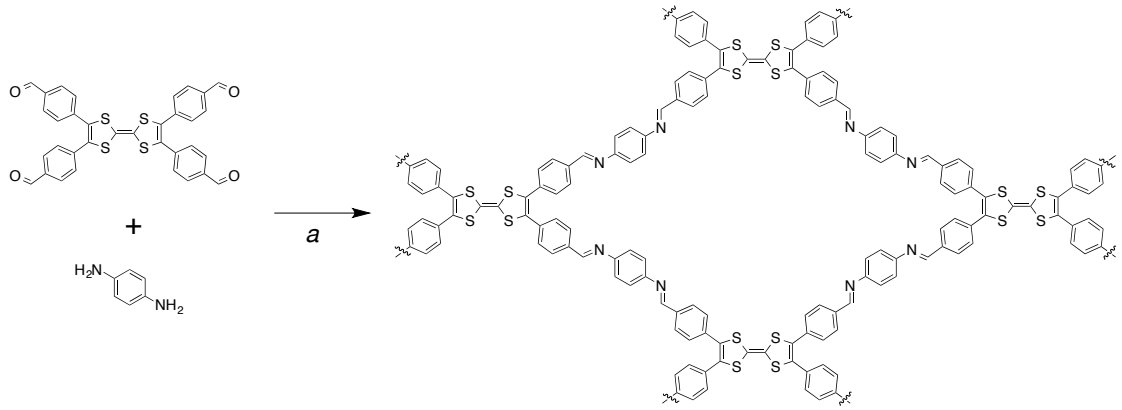

Figure 1.14 Synthesis of TTF-COF by reacting a benzaldehyde derivative of TTF with *p*-diaminobenzene to yield a covalent-organic framework built of two-dimensional sheets that form a three-dimensional structure by forming eclipsed stacks. *a*: Mesitylene, acetic acid, 120ºC, 3d.

1.5.4 Electronically Conductive Metal-Organic Frameworks with π-Stacked Moieties

It is possible to exploit the conductivity of redox-active π-stacked groups to generate conductive metal-organic architectures. The reaction divalent metal salts (Cu^{2+}, Ni^{2+}, and Co^{2+}) with 2,3,6,7,10,11-hexahydroxytriphenylene (HHTP) forms an extended structure referred to as M-CAT-1 (M = Cu^{2+}, Co^{2+}, Ni^{2+}).[128] Single-crystal x-ray diffraction of Co-CAT-1 reveals a structure of two-dimensional sheets of cobalt-bridged HHTP groups that are interlayered with trinuclear complexes of the formula $Co_3(HHTP)$-$(H_2O)_{12}$, with a π-stacking distance of 3.63 Å. EPR of Co-CAT-1 indicated a ligand centered radical with a near symmetric signal of $g = 2.105$. 87 K Ar adsorption isotherms of Co-CAT-1 and Ni-CAT-1, displayed a BET surface areas of 490 and 425 m^2/g respectively. Single crystals of the copper analogue of this material, Cu-CAT-1, displayed 4-point conductivities of $1.8\text{-}2.1 \times 10^{-1}$ S/cm. Conductivities of Co-CAT-1 and Ni-CAT-1 were not reported, nor was the surface area of Cu-CAT-1.

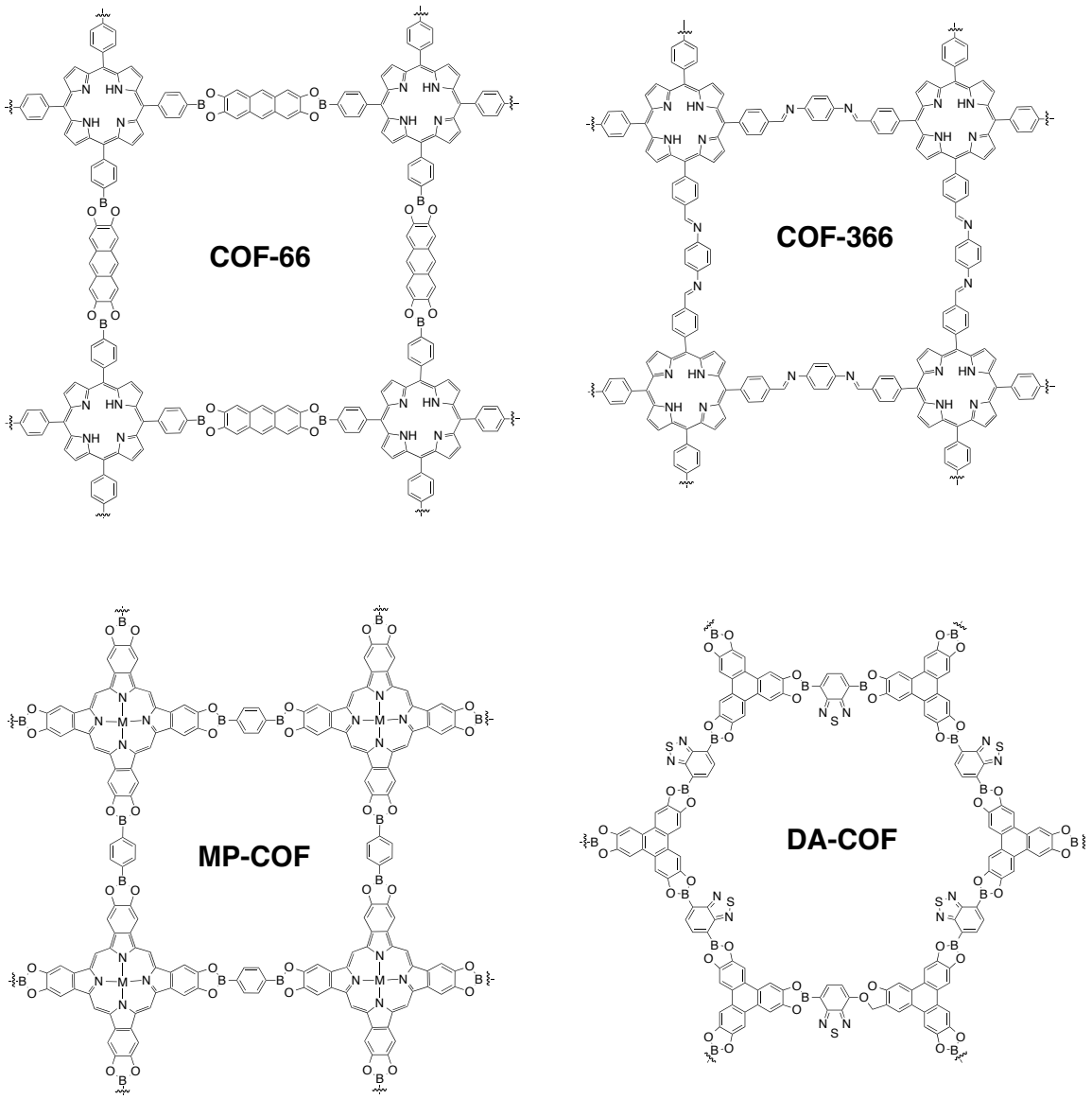

Figure 1.15 Structure of the two-dimensional sheets of four conductive covalent-organic frameworks, COF-66, COF-366, MP-COF (M=Zn^{2+}, Cu^{2+}, and $2H^{+}$) and DA-COF. In these covalent-organic frameworks the sheets form nearly eclipsed stacks.

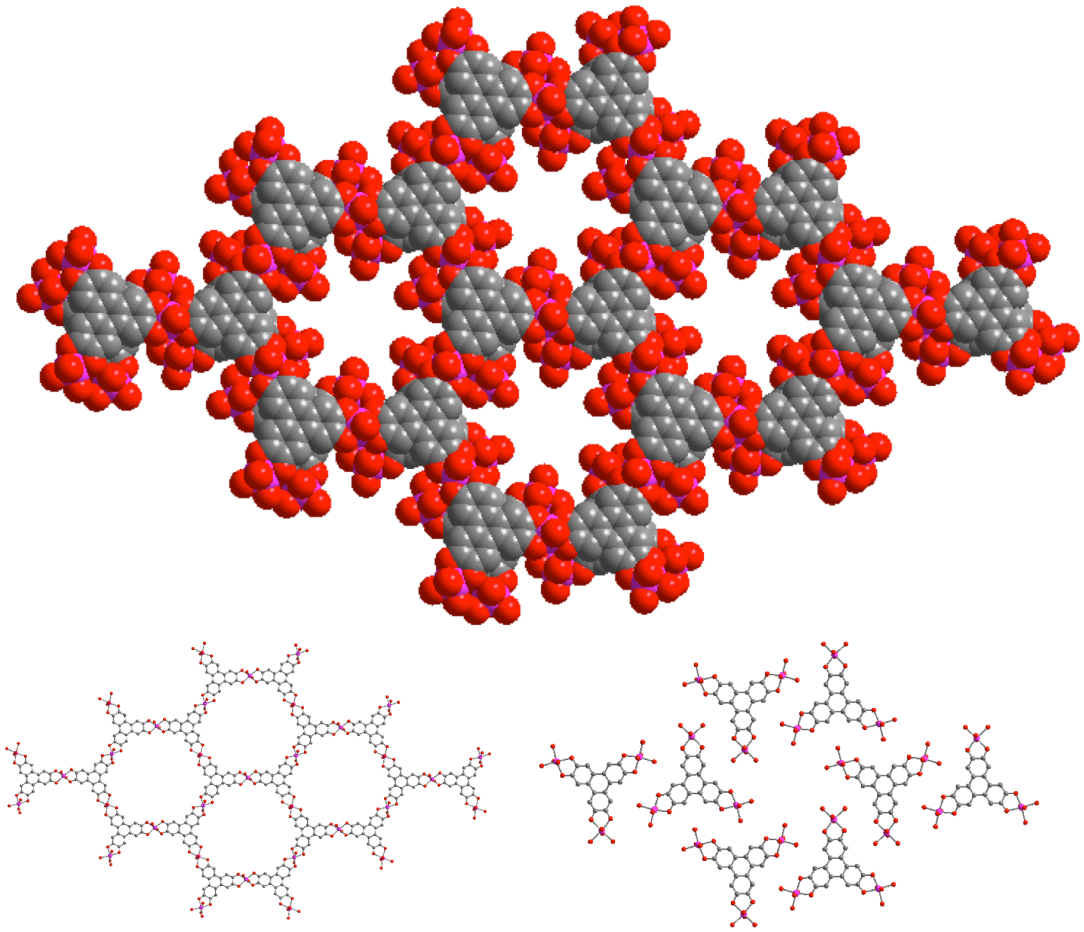

Figure 1.16 Space filling diagram of the crystal structure of Co-CAT-1. Below on the left is a ball-and stick model of the extended two-dimensional layers that are interleaved with the discrete $Co_3HHTP(H_2O)_{12}$ molecules shown on the bottom right. Gray, red, and pink spheres, represent carbon, oxygen, and cobalt atoms, respectively. Non-coordinating water molecules and hydrogen atoms have been omitted for clarity.

Reaction of $NiCl_2 \cdot 6H_2O$ with the ligand 2,3,6,7,10,11-hexaiminotriphenylne (HITP) yields the compound $Ni_3(HITP)_2$, built of two-dimensional stacked sheets (Figure 1.17).[129] This material has a pressed pellet conductivity of 2 S/cm and thin-film conductivity of 40 S/cm (room temperature). For comparison TTF-TCNQ shows a pressed pellet conductivity of 10 S/cm.[43] Because the material was conductive and reported analogues have partial biradical character[130] the authors suggest that there may be significant radical character on the ligands. The high conductivity of this material suggests the ligand is probably open shell. However, no magnetism or EPR spectroscopy confirms this.

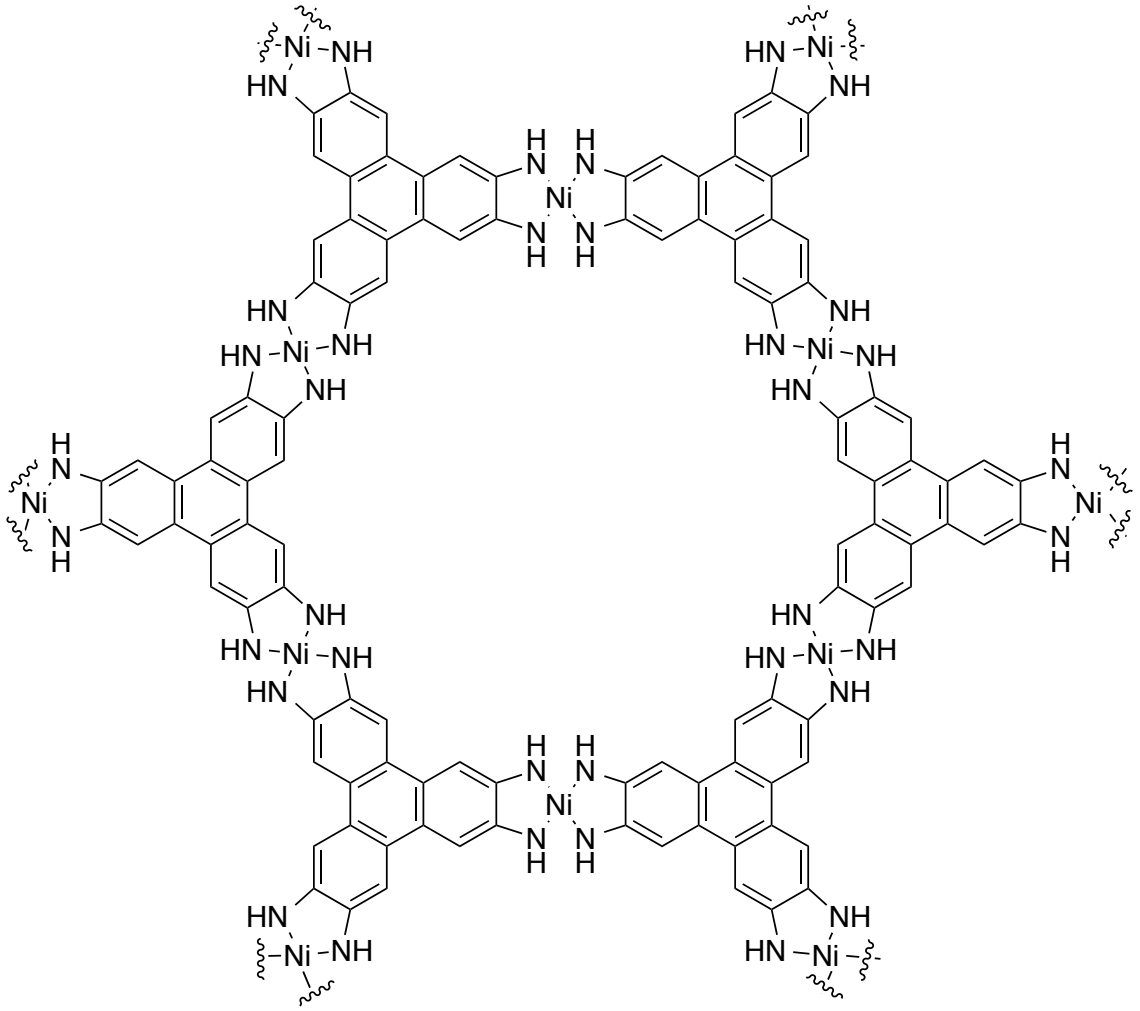

Figure 1.17 A two-dimensional sheet of $Ni_3(HITP)_2$. In the three dimensional structure of this material, these sheets form slightly offset stacks out of the plane of the paper.

The above structures are built from stacks of two-dimensional metal-organic sheets held together by van der Waals forces. A fascinating three-dimensional structure containing π-stacked motifs is Zn_2(TTF-TBA) (TTF-TBA^{4-} is tetrathiafulvalene-tetrabenzoate).[131] This structure has one-dimensional stacks of the TTF-TBA bridging ligand held into a three-dimensional network by parallel chains of carboxylate bridged zinc atoms (Figure 1.18). BET fits of 77 K N_2 adsorption isotherms show the material is microporous with a surface area of 662 m^2/g. FP-TRMC demonstrates a mobility of 0.2 $cm^2/V{\cdot}s$. EPR showed an organic radical with a g = 2.006 attributed to the partial oxidation of the TTF, engendering conductivity in the structure.

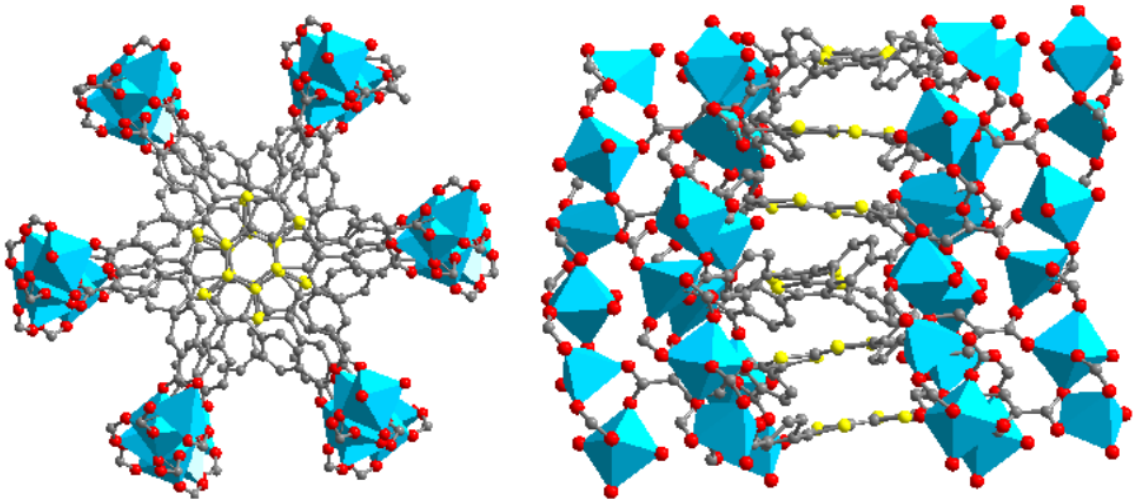

Figure 1.18. Views of Zn_2(TTF-TBA) looking down the TTF stacks and zinc chains (right) and normal to the TTF stacking direction. Gray, red, and sulfur spheres represent carbon, oxygen, and sulfur atoms. The teal polyhedra represent the nearest neighbor coordination environments of the octahedrally and tetrahedrally coordinated zinc atoms of the structure.

The properties of π-stacked charge-transfer salts are highly dependent on crystal packing; subtle variations in distances and angles between the organic units can drastically alter conductivity.[132] Charge-transfer salts also quite often display polymorphism, with numerous crystal phases displaying a variety of different physical properties.[133] These factors complicate fundamental studies of the physics of these systems, and limit the tunability and optimization of these systems. Furthermore, it is difficult to integrate these functionalities into robust materials for possible applications in sensing, surface modification, or electrochemical switching.[134] Metal-organic frameworks may offer a route to address these challenges. It is possible to take known organic donor and acceptor units and elaborate their structures with ligating groups such as carboxylates and pyrazolates to form new electroactive ligands. Here, the metal-organic framework assembly process may control the packing of these organic units, allowing the orientation and spacing of the organic donor or acceptor moieties to be tuned. The inorganic building units of the frameworks can further act as an inorganic acceptor or donor unit. Using a mixed ligand approach, it may be possible create frameworks with both organic donors and acceptors. Additionally, it may be possible to use the inorganic building units with appropriate redox couples as an electron donor or acceptors with organic acceptor or donor stacks. This approach may enable electronic communication between the inorganic and organic building units, increasing the dimensionality of charge transfer.

In addition to being able to alter the organic ligand systematically without changing the crystal structure, other opportunities for even more sophisticated manipulation of material properties. For example, other groups have used "chemical pressure" to obtain physics normally found in materials at high pressures at ambient conditions.[135] Here, metal-organic frameworks may serve as a platform to allow for the implementation of this strategy. If a framework with π-stacked acceptor moieties is obtained, the metal-organic framework structure could prevent expansion of the material upon partial

reduction of the acceptor stacks, creating a material with π-stacking distances found typically at high pressures at ambient conditions.

1.5.5 Electronic Conductivity in Metal-Organic Framework/Guest Composite Materials

There are two reports that demonstrate, through the addition of small molecules to intrinsically insulating metal-organic frameworks, that that it is possible to generate electronically-conductive metal-organic framework based composite materials. The first is a report of the addition of iodine to the framework $Zn_3(D,L\text{-lac})_2(pybz)_2$ (D,L-lac = D,L-lactate^{2-}, pybz = 4-pyridylbenzoate).[136] This framework is built of chains of zinc tetrahedra coordinated by lactates, benzoates and pyridines. These chains are linked into a three-dimensional structure by alternating 4-pyridylbenzoate molecules. (Figure 1.19) The framework has a BET surface area of 763 m^2/g (77 K N_2 adsorption isotherm). It demonstrates a tremendous capacity for the uptake of iodine from solution (3.03 I_2 per formula unit by thiosulfate titration). Upon iodine uptake, single crystal 4-point measurements show conductivities of $Zn_3(D,L\text{-lac})_2(pybz)_2 \supset 3.03I_2$ to be 3.42×10^{-3} and 1.65×10^{-4} S/cm (parallel and normal to the channels, respectively, 298 K), greater than the conductivity of I_2 – 7.69×10^{-6} S/cm. The authors attribute the conductivity, and the I_2 uptake to the formation of a charge transfer complex between iodine and the framework.

It is possible to grow thin films of an insulating metal-organic framework, $Cu_3(BTC)_2$, (BTC^{3-} = 1,3,5-benzenetricarboxylate^{3-}) also referred to as HKUST-1,[137] a well known metal-organic framework built of copper paddlewheel units, (Fig 1.19) on a Pt electrode microarray.[138] Upon uptake of TCNQ, the composite material of composition was shown to be a semiconductor with an ohmic room temperature 0.07 S/cm by room temperature two-point DC conductivity measurements on TCNQ infiltrated thin films. Variable temperature conductivity measurements revealed an E_a of 41 meV. TCNQ infiltration of the bulk framework with TCNQ afforded a material of composition $Cu_3(BTC)_2 \supset TCNQ_{0.5}$ with a decreases in BET surface area from 1844 m^2/g to 214 m^2/g (N_2, 77 K). This group did not report conductivities of the bulk material, nor single crystals. *Ab initio* calculations indicated the possibility that the nitrogen atoms of the TCNQ nitrile groups bridge the copper paddlewheel units at the axial sites creating a continuous path for electron transfer, but there was no experimental demonstration of the arrangement of TCNQ molecules in the framework. FT-IR demonstrated partial electron transfer to the TCNQ, however XPS indicated that the copper ions were Cu^{2+} indicating that the transferred electrons were not from the copper ions. The authors did not suggest the possibility that a thin film of partially reduced TCNQ on the surface of the metal-organic framework thin film was responsible for the observed conductivity.

In-situ polymerization of metal-organic frameworks has been demonstrated,[139] while confinement of polymers in framework pores leads to altered physical properties.[114] It is easy to imagine the templated polymerization of a conductive polymer in a metal-organic framework to create a conductive composite material. The confinement of the conductive polymer may create new phenomena, and synergistic interactions of the framework with the conducting polymer may lead to new phenomena. For instance,

confinement of conductive polypyrrole in a zeolite creates a composite material with giant magnetoresistance.[140]

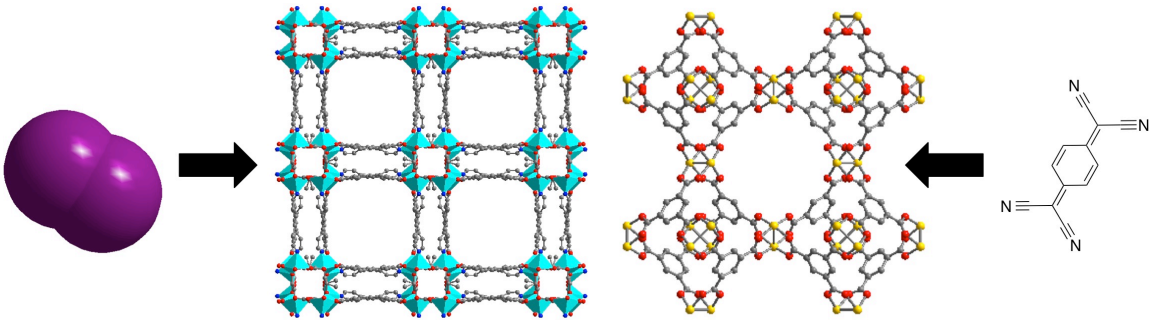

Figure 1.19 Left: The Zn_3(D,L-ac)(pybz) structure that shows conductivity upon uptake of I_2. Gray, red, and blue spheres represent carbon, oxygen, and nitrogen atoms, respectively, and the turquoise tetrahedra show the nearest neighbor coordination environments of zinc ions. Hydrogen atoms omitted for clarity. Right: A ball-and-stick representation of the structure of Cu_3(1,3,5-benzenetricarboxylate)$_2$, where yellow, red and gray spheres represent copper, oxygen and carbon atoms, respectively. Hydrogen atoms omitted for clarity. TCNQ infiltrated into the framework is shown to the right.

1.5.6 Conduction through the Metal-Ligand Bond in Metal-Organic Frameworks

Inorganic chemists are perhaps most naturally interested in conductive systems where the metal-ion plays a key role in conduction. Having a metal-ion directly participate in electronic conduction offers many possible avenues for applications and investigations. In the case of energy storage, electronically accessible metal-ions enable the realization of charge storage by metal-centered reduction or oxidation. Electronically accessible metal centers with open coordination sites could enable sensing by analyte modulated conductivity upon coordination of the analyte to the metal. A porous, conductive metal-organic framework could serve as a high surface area electrocatalyst where the metal center directly participates in catalysis. To date, achieving conductivity through the metal-ligand bond has been limited by the traditional use of hard Lewis base oxo-donor sets and hard acid, redox-inactive metals such as Zn^{2+}, Zr^{4+}, Al^{3+}, and Ln^{3+} that form ionic bonds.[25] To form bonds of greater covalency, the use of more electropositive donors with frontier orbitals that form a closer energy match with transition metals as well greater orbital extension should be sought. A ready way to implement this strategy is the replacement of oxygen with elements such as sulfur and selenium. Coordination polymers built with chalcogenide ligands quite often display interesting conductivity and electron transfer properties.[141] As described above, the use of π-acid N-donor molecules has been exploited to form mixed-valence multinuclear compounds that display mixed-valency. Studies in electron delocalization in mixed-valence bimetallic complexes with bridging organic ligands has demonstrated the best delocalization with metals that have $d^{5/6}$ electron configurations with an octahedral coordination geometry.[78,80,83,142] This situation maximizes metal-ligand π-orbital overlap, providing an efficient electron transfer pathway, and minimizes the differences in bond distances for the two redox states, thereby ensuring a low reorganization energy. As such, Fe^{2+}/Fe^{3+} and Ru^{2+}/Ru^{3+} couples are particularly interesting. Redox couples from $d^{0/1}$ and $d^{2/3}$ are also favorable

and have been used to make highly-delocalized mixed-valence extended structures and molecular complexes.[143] Second and third row transition metals are interesting because of their greater-orbital extension, and in the case of octahedral $d^{5/6}$ couples, as in the case of ruthenium and osmium compounds, electron-transfer would be between non-bonding orbital manifolds thus minimizing structural rearrangement for electron transfer. However, the vast majority of reported metal-organic frameworks are built of 1st row transition metals, as the substitutional inertness of second and third row transition metals presumably precludes the self-correction necessary for the self-assembly of crystalline three-dimensional framework materials.

Figure 1.20 shows the structure of Cu[Cu(pdt)], synthesized by the reaction of CuI and $Na[Cu(pdt)_2]$.[59] On the basis of the Cu-S and Cu-N bond distances The material displayed pressed pellet conductivity of 6×10^{-4} S/cm with an energy of activation of 44 meV. The authors assigned the conductivity to disproportionation of the Cu^{2+}, that would allow electron transfer by the following equilibrium: $Cu^{II}[Cu^{II}(pdt)_2]$ to $Cu^{I}[Cu^{III}(pdt)_2]$ $Cu^{III}Cu(pdt)$. FT-IR spectra showed an broad absorption band at an energy of 0.7 eV that was attributed to intervalence charge transfer between the $Cu^{II}[Cu^{II}(pdt)_2]$ to $Cu^{I}[Cu^{III}(pdt)_2]$ states. This material displayed no permanent porosity. An isostructural analogue of $Cu[Cu(pdt)_2]$ is $Cu[Ni(pdt)_2]$.[62] As synthesized, a thin film of this material demonstrates a conductivity of 10^{-8} S/cm that increases to 10^{-4} S/cm upon oxidation with I_2 vapor. The amount of iodine necessary to effect this 10,000-fold increase in conductivity was not measurable by weight change. This suggests sub-stoichiometric doping, or the creation of a conductive pathway at the surface of the metal-organic framework thin film is responsible for the increase in conductivity.

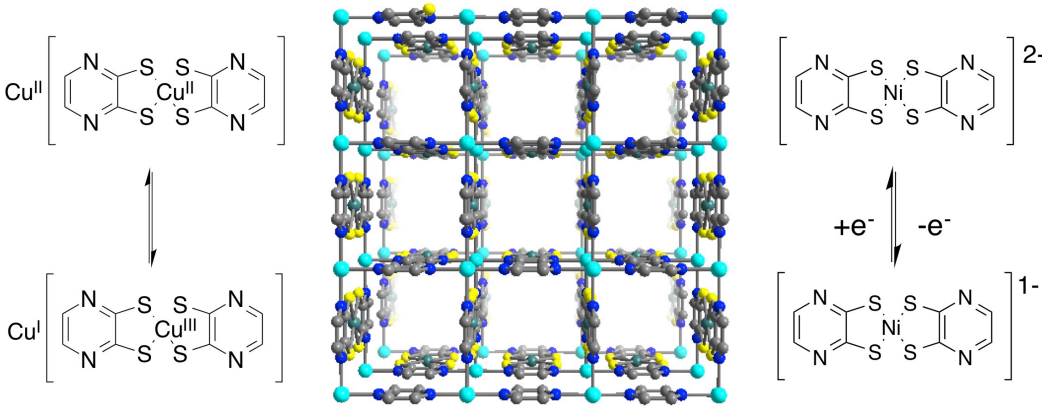

Figure 1.20. Left: Electronic bistability of $Cu[Cu(pdt)_2]$. Middle: Ball-and-stick representation of the structure of $Cu[Cu(pdt)_2]$ and $Cu[Ni(pdt)_2]$. Teal, green, yellow, blue, and gray spheres represent copper, copper or nickel, sulfur, nitrogen, and carbon atoms, respectively. Hydrogen atoms are omitted for clarity. Right: The one-electron $Ni(pdt)^{2-/1-}$ couple.

There are many reported one-dimensional inorganic conductors.[45,144] While the permanent porosity and crystallinity of metal-organic frameworks distinguishes them, metal-organic polymers built of metal ions bridged by ligands have been studied for at least over half a century,[145] some of which show charge transport. In the Krogmann's

salts $K_2Pt(CN)_4X_{0.3}$ (X= Cl^-, Br^-) conductivity is a result of the overlapping Pt d_z^2 orbitals. Oxidation depopulates the filled d_z^2 band to form a partially filled band.[146] These can be thought of as Class III mixed-valence platinum coordination polymers

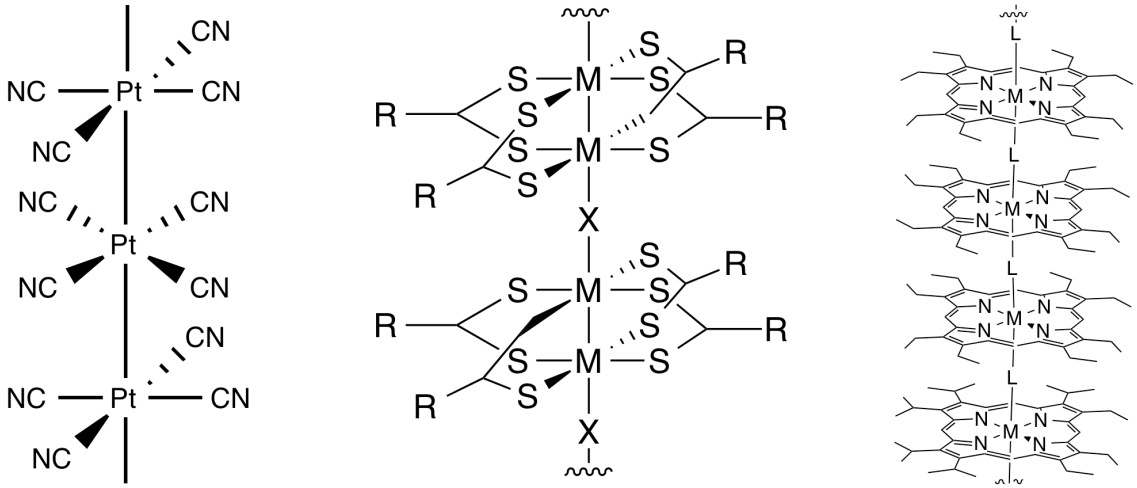

Figure 1.21 Structural motifs of one-dimensional conducting coordination polymers. Left: Pt-Pt chains of $K_2Pt(CN)_4X_{0.3}$. Middle: Halide bridged dithioacid paddlewheel polymers. Right: Ligand-bridged octaethylporphyrin "shish-kebab" polymers, L = pz, bpy, and DABCO. M = Fe^{2+}, Ru^{2+}, and Os^{2+}.

where the Pt has an oxidation state of +2.3. Single crystals of this $K_2Pt(CN)_4Br_{0.3}$ show a room temperature, 4-point, single-crystal DC conductivity of 2×10^2 S/cm when measured along the Pt···Pt axis.[147] Conductivity is reported for halide-bridged paddlewheel complexes of the structure type shown in the middle of Figure 1.21. Iodide-bridged dinuclear thioacid paddlewheel complexes of Group 8 metals show 4-point, single crystal, room temperature conductivities that range from 6.0×10^{-4} S/cm for $Ni_2(n\text{-}BuCS_2)_4I$[148] to 83 S/cm for $Pt_2(n\text{-}BuCS_2)_4I$,[149] demonstrating the effect of increased orbital extension on conductivity. For most conductive porphyrin and phthalocyanine conductors, conduction is between the π-stacks of the organic macrocycles.[124] However, in nickel tetrabenzoporphyrin iodide, the d-orbitals of the nickel ion are implicated in conduction [150] and in cobalt phtalocyanine iodide, oxidation of the filled band of created by overlapping cobalt d_z^2 to form a partially filled band gives a material with a room temperature, 4-point conductivity of 50 S/cm.[151] Octaethylporphyrinates (octaethylporphyrinate^{2-} = OEP^{2-}) of Fe^{2+}, Ru^{2+}, and Os^{2+} bridged by pyrazine (pz), 4,4'-bipyridine (bpy), and 1,4-diazabiyclo[2.2.2]octane (DABCO) have been carefully studied.[152] In this system, conductivity increases with orbital extension as the metal center varies from Fe to Ru to Os (the room temperature, pressed-pellet conductivities of $[M(OEP)(pz)]_n$ respectively increase from 1.1×10^{-10} S/cm to 1.2×10^{-8} S/cm to 3.2×10^{-7} S/cm) and as the conjugation of the bridging ligand increases (the room temperature, pressed-pellet conductivity of $[Ru(OEP)(bpy)]_n$ is 1.6×10^{-9} S/cm and of $[Ru(OEP)(DABCO)]_n$ is 2.5×10^{-10} S/cm). These trends directly implicate the ligand-bridged metal in conduction. Conductivity in these systems also increases dramatically from upon partial oxidation with iodine or ferrocinium hexafluorophosphate to achieve mixed-valency; for instance, the room temperature pressed pellet conductivity of

$[Os(OEP)(pz)(PF_6)_{0.5}]_n$ is 2.3×10^{-2} S/cm, a five order of magnitude increase in conductivity. Analogous ligand-bridged metallophthalocyanates also display conductivities that increase upon oxidation.[153] Organometallic molecular wires have been an active area of research,[154] and in the solid state, the reported conductive solids, $NbSe_3$ and $TaSe_3$ are constructed of interwoven orthogonal chains of metal-chalcogenide chains held together by van der Waals forces and as such can be considered ensembles of one-dimensional metal-chalcogenide chains.[155] Many highly conductive mixed-valence molybdenum bronzes are also built of one-dimensional chains of molybdenum and oxygen.[156]

The fact that many frameworks are constructed of one-dimensional inorganic motifs suggest the incorporation of conductive one-dimensional inorganic building units a metal-organic framework as a viable strategy to obtain charge transport in metal-organic frameworks, where the metal-ligand is part of the charge-transport pathway. $Fe(OH)_{0.8}F_{0.2}$(BDC) of the MIL-53 structure type (see Figure 1.12) is built of one-dimensional chains of trans-vertex sharing ferric octahedra. Intriguingly, it is possible to electrochemically reduce this framework with concomitant lithium ion insertion.[22] Electronic structure calculations and Mössbauer spectroscopy suggest that the electrons are highly localized, however. The M_2(DOBDC) structure (Figure 1.2) is built of helical chains of edge-sharing octahedra (square pyramids after activation). By choice of a redox-active metal such as Fe^{2+}, followed by post-synthetic oxidation, conductivity may be possible by charge transfer down the partially oxidized chain. Fe_2(DOBDC) is known, and displays redox-activity that was exploited to make an oxygen selective sorbent material.[12a] After complete activation of the material, Fe_2(DOBDC) displays electron transfer from Fe^{2+} to O_2 to form the oxygen superoxide adduct $Fe^{2+}Fe^{3+}(DOBDC)O_2^-$ below 211K. Above that temperature, electron transfer from a neighboring atom formed a superoxide ferric adduct $Fe^{3+}Fe^{3+}(DOBDC^{4-})O_2^{2-}$, demonstrating electron transfer between iron sites. Reasoning that partial substitution of oxygen with sulfur could yield a material with improved electron transfer properties, I replaced the phenols with of the 2,5-dihydroxy-1,4-benzenedicarboxlic acid (H_4DOBDC) ligand with thiophenols to obtain the with the 2,5-disulfhydryl-1,4-benzenedicarboxylic acid (H_4DSBDC) which I then reacted with $FeCl_2$ to obtain the isostructural framework Fe_2(DSBDC). Fe_2(DSBDC) displays a FP-TRMC mobility of 0.17 $cm^2/V \cdot s$, a value in the higher ranges reported for conductive polymers such as poly(3-hexylthiophene). Two-point AC impedance measurements of pressed pellets of this material demonstrated that it was intrinsically conductive and showed a 40-fold increase in conductivity upon oxidation, indicating *p*-type conduction. Chapter 5 of this thesis describes this work.

A related material is Mn_2(DSBDC)$(solv)_2$ (solv = *N*,*N*-DMF, MeOH) (Figure 1.23).[157] Like M_2(DOBDC) and Fe_2(DSBDC) this framework has a honeycomb structure of one-dimensional hexagonal channels and is built of one-dimensional chains of edge sharing octahedra, but in a different arrangement. This material has two distinct manganese sites that are bridged by sulfur and oxygen atoms of the ligand. One manganese site has two solvent molecules that can be exchanged, the other has no coordinating solvent. As synthesized, the material is coordinated by DMF, which can be exchanged with methanol and then activated to obtain a BET (N_2 77 K) surface area of 978 m^2/g. Before removal of solvent molecules, the methanol-exchanged material

displays a total mobility of 0.02 $cm^2/V \cdot s$ (measured by FP-TRMC at room temperature). After removal of solvent molecules the total mobility decreases to 0.01 $cm^2/V \cdot s$.

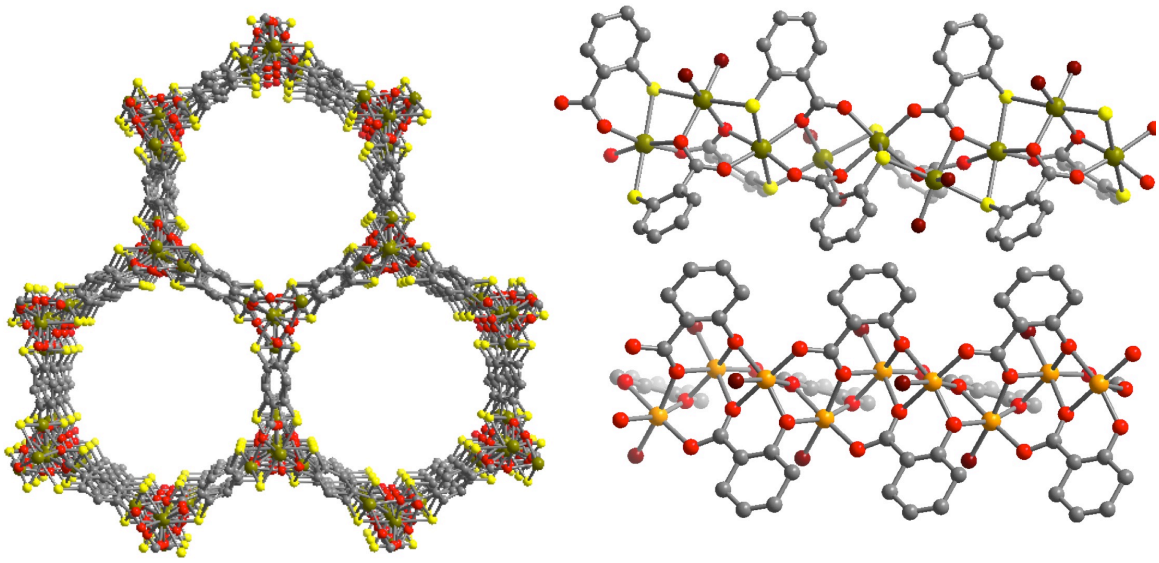

Figure 1.22 Ball and stick representations of Mn_2(DSBDC) and Fe_2(DOBDC) structures. Left: View of Mn_2(DSBDC) down its pores. Right: One-dimensional chains of Mn_2(DSBDC) (top) and one-dimensional chains of M_2(DOBDC). Gray, yellow, red, and burgundy spheres are carbon, sulfur, oxygen atoms from the organic linker and oxygen atoms from solvent ligands. The chartreuse spheres are Mn^{2+} ions, and the orange spheres are Fe^{2+} ions. Hydrogen atoms and non-oxygen atoms of the solvent molecules are omitted for clarity.

Reaction of Fe^{2+} salts with 1,2,3-triazole yields the framework Fe(1,2,3-triazaolate), an open framework with a diamondoid topology, referred to as MET-3.[158] Triazolate ligands triply bridge ferrous ions to form tetrahedral nodes. The material is porous with a BET surface area of 450 m^2/g (N_2, 77 K). This structure contains continuous networks of μ^3-1,2,3-triazolate-bridged Fe^{2+} ions, providing a three-dimensional network for electron transfer. Indeed, pressed pellets of the as-produced material demonstrates an ohmic 4-point conductivity of 7.7×10^{-4} S/cm. Upon exposure to I_2 vapor the 4-point pressed pellet conductivity increases to 10^{-3} S/cm, while remaining ohmic. The authors suggest the exposure to iodine increases the conductivity by oxidative doping to achieve mixed-valency. No probes of the oxidation state before or after reduction are given, nor is a quantification of the degree of iodine uptake. In Chapters 3 and 4 I demonstrate a three-dimensional metal-organic framework, $Fe_2(BDP)_3$,[159] built of one-dimensional chains of μ^2-pyrazolate-bridged ferric ions with a BET surface area of 1230 m^2/g (N_2, 77 K). Single crystal 4-point conductivity measurements of this compound show that it is intrinsically conductive with a room temperature conductivity of 9.6×10^{-3} S/cm. Estimated conductivities after reduction are on the order of 10^2-10^3 S/cm, within the range of metallic π-stacked organic molecular conductors. $Fe_2(BDP)_3$ can be reduced with potassium naphthalenide to obtain the compositional series $K_xFe_2(BDP)_3$. For $x > 0$, $K_xFe_2(BDP)_3$ is an *n*-type conductor. FP-TRMC and single crystal field effect transistor measurements show remarkably high electron mobilities of

0.1-0.8 $cm^2/V \cdot s$, well within the range of amorphous silicon and some of the best conductive polymers. Given the intersite spacing of the iron sites (3.56 Å), these mobility values suggest that a delocalized, band-model treatment may appropriate for this system. At the stoichiometry of peak mobility, $K_{0.9}Fe_2(BDP)_3$, the framework maintains microporosity with a BET surface area of 610 m^2/g (N_2, 77 K).

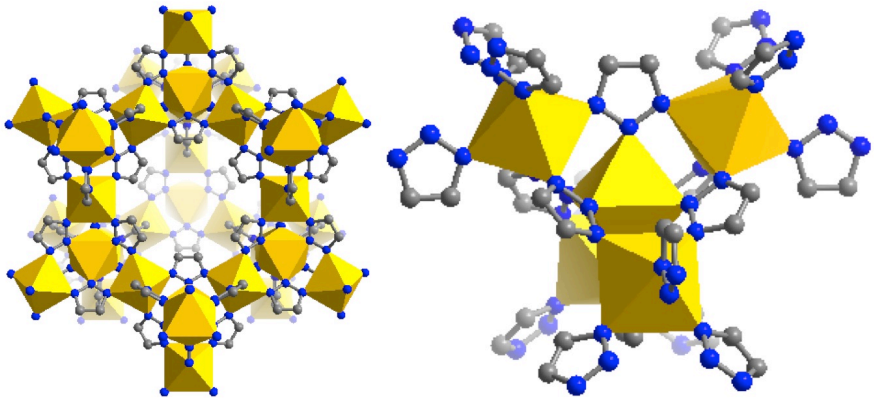

Figure 1.23 Ball and stick representations of the structure of MET-3, Fe(1,2,3-triazolate). Blue and gray spheres are nitrogen and carbon atoms and the yellow octahedra show the nearest neighbor coordination environments of Fe^{2+} atoms. Hydrogen atoms are omitted for clarity. Left: A representation of the pore volume of MET-3. Right: The tetrahedral building unit of MET-3.

1.6 Outlook

The successful approaches to create conductive metal-organic frameworks suggest other possible modes to create novel conductive metal-organic framework systems by strategies described above. The modularity of metal-organic framework self-assembly and rich diversity in structure types suggest strategies for applications for conductive metal-organic frameworks. One factor that can significantly affect electronic delocalization and communication between metal centers in mixed-valence multinuclear molecular complexes with π-acid bridges is the bridging ligand conformation. For instance the dihedral angle between the pyridine rings of a 4,4'-bipyridine bridge significantly changes the degree of electronic delocalization within the bridge and thus the electronic metal centers; lesser dihedral angles of more planar conformations display greater delocalization as measured by lower IVCT energies and greater electrochemical comproportionation constants.[160] In a rigid metal-organic framework the bridging ligand should be locked in a rigid-conformation, and judicious choice of ligand and framework structure type may enable the engineering of metal-ligand conformations that are most favorable for electron transfer. Tuning the electronics of the bridging ligand may alter the orbital energies of the bridging ligand and thus their overlap with the metal orbitals, providing a method to further alter conductivities in a conductive metal-organic frameworks with π-acid bridging ligands. Incorporation of chemically reactive functionalities into a ligand molecules may enable chemical switching of electronic delocalization, as has been demonstrated in molecular mixed-valence complexes,[142c] potentially enabling environment responsive materials and sensing applications.

Chapters 3 and 4 of this thesis detail the synthesis and characterization of an *n*-type conductive metal-organic framework. In organic molecular and polymeric systems, demonstrations of *n*-type conduction is comparatively rare in comparison to *p*-type conductors.[161] As *n*-doping in organic conductors is difficult to achieve,[162] the strategy employed to create *n*-type conductivity is to create materials with high electron affinities.[163] Unfortunately, this strategy raises the energy of the LUMOs of these materials out of the range where there can be effective energy overlap with the source and drain contacts of transistor devices.[164] One approach to deal with this issue is to use low work function electrodes such as calcium.[165] However these metals are prone to oxidation, creating challenges in substrate fabrication. By reductive doping of frameworks formed with more electropositive transition metals it may be possible to access *n*-type FET behavior while using higher work function electrodes that are easier to process.

This thesis demonstrates both ionic and electronic conductivity, as well as ion-intercalation in metal-organic frameworks. Three properties are needed in any battery electrode: ionic conduction, electronic conduction and charge storage. A metal-organic framework could demonstrate all of these functions in one material, obviating the need of added electrolyte or conductive binder.

1.7 References

(1) Yaghi, O.M.; O'Keefe, M.; Ockwig, N.W.; Chae, H. K.; Eddaoudi, M.; Kim, J. *Nature* **2005**, *423*, 705.

(2) Rosi, N. L.; Eckert, J.; Eddaoudi, M.; Vodak, D. T.; Kim, J.; O'Keeffe, M.; Yaghi, O. M. Science **2003**, *300*, 1127.

(3) Rosi, N. L.; Kim, J.; Eddaoudi, M.; Chen, B.; O'Keeffe, M.; Yaghi, O. M. *J. Am. Chem. Soc.* **2005**, *127*, 1504.

(4) Caskey, S. R.; Wong-Foy, A. G.; Matzger, A. J. *J. Am. Chem. Soc.* **2008**, *130*, 10870.

(5) Dietzel, P. D. C.; Morita, Y.; Blom, R.; Fjellvåg, H. *Angew. Chem., Int. Ed.* **2005**, *44*, 6354.

(6) Dietzel, P. D. C.; Panella, B.; Hirscher, M.; Blom, R.; Fjellvåg, H. *Chem. Commun*. **2006**, 959.

(7) Zhou, W.; Wu, J.; Yildirim, T. J. Am. Chem. Soc. **2008**, *130*, 15268.

(8) Bhattacharjee, S.; Choi, J.; Yang, S.; Choi, S. B.; Kim, J.; Ahn, W. *J. Nanosci. Nanotechnol.* **2010**, *10*, 135.

(9) R. Sanz, R.; Martínez, F.; Orcajo, G.; Wojtas, L.; Briones, D. *Dalton Trans.* **2013**, *42*, 2392

(10) (a) Sumida, K.; Rogow, D. L.; Mason, J. A.; McDonald, T. M.; Bloch, E. D.; Herm, Z. R.; Bae, T. H.; Long, J. R. *Chem. Rev.* **2012**, *112*, 724. (b) Murray, L. J.; Dinca, M.; Long, J. R. *Chem. Soc. Rev.* **2009**, *38*, 1294.

(11) (a) Bloch, E. D.; Murray, L. J.; Queen, W. L.; Chavan, S.; Maximoff, S. N.; Bigi, J. P.; Krishna, R.; Peterson, V. K.; Grandjean, F.; Long, G. J.; Smit, B.; Bordiga, S.; Brown, C. M.; Long, J. R. *J. Am. Chem. Soc.* **2011**, *133*, 14814. (b) Bloch, E. D.; Queen, W. L.; Krishna, R.; Zadrozny, J. M.; Brown, C. M.; Long, J. R. *Science* **2012**, *335*, 1606. (c) Alaerts, L.; Kirschhock, C. E. A.; Maes, M.; van der

Veen, M. A.; Finsy, V.; Depla, A.; Martens, J. A.; Baron, G. V.; Jacobs, P. A.; Denayer, J. F. M.; De Vos, D. E. *Angew. Chem.-Int. Edit.* **2007**, *46*, 4293. (d) Maes, M.; Alaerts, L.; Vermoortele, F.; Ameloot, R.; Couck, S.; Finsy, V.; Denayer, J. F. M.; De Vos, D. E. *J. Am. Chem. Soc.* **2010**, *132*, 2284.

(12) (a) Allendorf, M. D.; Houk, R. J. T.; Andruszkiewicz, L.; Talin, A. A.; Pikarsky, J.; Choudhury, A.; Gall, K. A.; Hesketh, P. J. *J. Am. Chem. Soc.* **2008**, *130*, 14404. (b) Lan, A. J.; Li, K. H.; Wu, H. H.; Olson, D. H.; Emge, T. J.; Ki, W.; Hong, M. C.; Li, J. *Angew. Chem.-Int. Edit.* **2009**, *48*, 2334. (c) Lu, G.; Hupp, J. T. *J. Am. Chem. Soc.* **2010**, *132*, 7832.

(13) (a) Garibay, S. J.; Wang, Z. Q.; Cohen, S. M. *Inorg. Chem.* **2010**, *49*, 8086. (b) Horike, S.; Dinca, M.; Tamaki, K.; Long, J. R. *J. Am. Chem. Soc.* **2008**, *130*, 5854. (c) Wu, C. D.; Hu, A.; Zhang, L.; Lin, W. B. *J. Am. Chem. Soc.* **2005**, *127*, 8940. (d) Seo, J. S.; Whang, D.; Lee, H.; Jun, S. I.; Oh, J.; Jeon, Y. J.; Kim, K. *Nature* **2000**, *404*, 982. (e) Ma, L. Q.; Abney, C.; Lin, W. B. *Chem. Soc. Rev.* **2009**, *38*, 1248. (f) Czaja, A. U.; Trukhan, N.; Muller, U. *Chem. Soc. Rev.* **2009**, *38*, 1284. (g) Wang, Z.; Chen, G.; Ding, K. L. *Chem. Rev.* **2009**, *109*, 322. (h) Lee, J.; Farha, O. K.; Roberts, J.; Scheidt, K. A.; Nguyen, S. T.; Hupp, J. T. *Chem. Soc. Rev.* **2009**, *38*, 1450. (i) Farrusseng, D.; Aguado, S.; Pinel, C. *Angew. Chem.-Int. Edit.* **2009**, *48*, 7502. (j) Cho, S. H.; Ma, B. Q.; Nguyen, S. T.; Hupp, J. T.; Albrecht-Schmitt, T. E. *Chem. Commun.* **2006**, 2563.

(14) (a) Taylor, K. M. L.; Jin, A.; Lin, W. B. *Angew. Chem.-Int. Edit.* **2008**, *47*, 7722. (b) Taylor-Pashow, K. M. L.; Della Rocca, J.; Xie, Z. G.; Tran, S.; Lin, W. B. *J. Am. Chem. Soc.* **2009**, *131*, 14261. (c) Horcajada, P.; Serre, C.; Maurin, G.; Ramsahye, N. A.; Balas, F.; Vallet-Regi, M.; Sebban, M.; Taulelle, F.; Ferey, G. *J. Am. Chem. Soc.* **2008**, *130*, 6774. (d) Miller, S. R.; Heurtaux, D.; Baati, T.; Horcajada, P.; Greneche, J. M.; Serre, C. *Chem. Commun.* **2010**, *46*, 4526. (e) Horcajada, P.; Chalati, T.; Serre, C.; Gillet, B.; Sebrie, C.; Baati, T.; Eubank, J. F.; Heurtaux, D.; Clayette, P.; Kreuz, C.; Chang, J. S.; Hwang, Y. K.; Marsaud, V.; Bories, P. N.; Cynober, L.; Gil, S.; Ferey, G.; Couvreur, P.; Gref, R. *Nat. Mater.* **2010**, *9*, 172.

(15) (a) White, K. A.; Chengelis, D. A.; Gogick, K. A.; Stehman, J.; Rosi, N. L.; Petoud, S. *J. Am. Chem. Soc.* **2009**, *131*, 18069. (b) Park, Y. K.; Choi, S. B.; Kim, H.; Kim, K.; Won, B. H.; Choi, K.; Choi, J. S.; Ahn, W. S.; Won, N.; Kim, S.; Jung, D. H.; Choi, S. H.; Kim, G. H.; Cha, S. S.; Jhon, Y. H.; Yang, J. K.; Kim, J. *Angew. Chem.-Int. Edit.* **2007**, *46*, 8230.

(16) (a) Côté. A. P.; Benin, A. I.; Ockwig, N. W.; O'keefe, M.; Matzger, A. J.; Yaghi, O. M. *Science* **2005**, *310*, 1166. (b) El-Kaderi, H. M.; Hunt, J. R.; Mendoza-Cortés, J.; Côté, A.; Taylor, R. E.; O'Keeffe, M.; Yaghi, O. M. *Science* **2007**, *316*, 268. (c) Kuhn, P.; Antonietti, M.; Thomas, A. *Angew. Chem. Int. Ed.* **2008**. *47*, 3450. (d)Uribe-Romo, F. J.; Hunt, J. R.; Furukawa, H.; Klck, C.; O'Keeffe, M.; Yaghi, O. M. *J. Am. Chem. Soc*. **2009**, *131*, 4570.

(17) Yao, Y. F. Y.; Kummer, J. T. *J. Inorg. Nuc. Chem.* **1967**, *29*, 2453.

(18) Owens, B.B. ;Christie, J. H.; Tiedeman, G. T. *J. Electrochem. Soc.* **1971**, *118*, 1144.

(19) Heinke, L.; Tzoulaki, D.; Chmelik, C.; Hibbe, F.; van Baten, J. M.; Lim, H.; Li, J.; Krishna, R.; Karger, J. *Phys. Rev. Lett.* **2009**, *102*. (b) Han, S. B.; Hermans, T.

M.; Fuller, P. E.; Wei, Y. H.; Grzybowski, B. A. *Angew. Chem.-Int. Edit.* **2012**, *51*, 2662. (c) Haldoupis, E.; Nair, S.; Sholl, D. S. *J. Am. Chem. Soc.* **2010**, *132*, 7528. (d) Chmelik, C.; Heinke, L.; Valiullin, R.; Karger, J. *Chem. Ing. Tech.* **2010**, *82*, 779.

(20) (a) Ohba, T.; Hata, K.; Kanoh, H. *J. Am. Chem. Soc.* **2012**, *134*, 17850. (b) Gao, B.; Kleinhammes, A.; Tang, X. P.; Bower, C.; Fleming, L.; Wu, Y.; Zhou, O. *Chem. Phys. Lett.* **1999**, *307*, 153. (c) Ghosal, S. *Phys. Rev. Lett.* **2007**, *98*.

(21) (a) Woodward, J. *Phil. Trans.* **1724**, *33*, 15. (b) Brown, J. *Phil. Trans.* **1724**, *33*, 17.

(22) Feldman, B. J.; Murray, R. W. *Inorg. Chem.* **1987**, *26*, 1702.

(23) Bennett, M. V.; Beauvais, L. G.; Shores, M. P.; Long, J. R. *J. Am. Chem. Soc.* **2001**, *123*, 8022.

(24) Zagorodniy, K.; Seifert, G.; Hermann, H. *Appl. Phys. Lett.* **2010**, *97*.

(25) Feng, P. L.; Perry, J. J.; Nikodemski, S.; Jacobs, B. W.; Meek, S. T.; Allendorf, M. D. *J. Am. Chem. Soc.* **2010**, *132*, 15487.

(26) Zaanen, J.; Sawatzky, G. A.; Allen, J. W. *Phys. Rev. Lett.* **1985**, *55*, 418.

(27) (a) Wang, C. X.; Yin, L. W.; Zhang, L. Y.; Xiang, D.; Gao, R. *Sensors-Basel* **2010**, *10*, 2088. (b) Li, J.; Lu, Y. J.; Ye, Q.; Cinke, M.; Han, J.; Meyyappan, M. *Nano Lett.* **2003**, *3*, 929. (c) "Comini, E.; Faglia, G.; Sberveglieri, G.; Pan, Z. W.; Wang, Z. L. *Appl. Phys. Lett.* **2002**, *81*, 1869. (d) Cao, Q. R., J.A. , in *Adv. Mater*, Vol. 21, 2008, 29. (e) Ryu, H. W.; Park, B. S.; Akbar, S. A.; Lee, W. S.; Hong, K. J.; Seo, Y. J.; Shin, D. C.; Park, J. S.; Choi, G. P. *Sensor Actuat B-Chem* **2003**, *96*, 717. (f) Wongwiriyapan, W.; Inoue, S.; Okabayashi, Y.; Ito, T.; Shimazaki, R.; Maekawa, T.; Suzuki, K.; Ishikawa, H.; Honda, S.; Mori, H.; Oura, K.; Katayama, M. *Appl Phys Express* **2009**, *2*.

(28) Seo, H.; Hotta, C.; Fukuyama, H. *Chem. Rev. (Washington, DC, U. S.)* **2004**, *104*, 5005.

(29) Linford, R. G.; Hackwood. S. *Chem. Rev.* **1981**, *81*, 327.

(30) (a) Chandra S. *Superionic Solids* North-Holland, Amsterdam, 1981. (b) Colomban, P.; Novak, A. *J. Molec. Struct.* **1988**, *177*, 277.

(31) Streetman, B.; Banerjee, *Solid State Electronic Devices 6th Ed.* Prentice Hall, New Jersey, 2005.

(32) Kittel, C. *Introduction to Solid State Physics 8th Ed.* Wiley, New York, 2004.

(33) Street, G.B.; Brédas, J.-L. *Acc. Chem. Res.* **1985**, *18*, 309.

(34) Kanai, Y.; Kagoshima, S.; Nagasawa,, S. *Synth. Met.* **1989**, *9*, 369.

(35) Brodsky, M. H., Ed. *Amorphous Semiconductors* Springer, Berlin, 1985

(36) Mott, N. F. *Phil. Mag.* **1969**, *19*, 835.

(37) Apsley, N. Hughes, H. P. *Phil. Mag.* **1974**, *30*, 963.

(38) (a) Menon, R.; Yoon, C. O.; Moses, D.; Heeger, A. J. In *Handbook of conducting polymers*; Skotheim, T. A., Elsenbaumer, R. L., Reynolds, J. R., Eds.; Marcel Dekker: New York, 1998. (b) Baranovski, S., Ed. *Charge Transport in Disordered Solids with Applications in Electronics*; Wiley: New York, 2006.

(39) Putley, E. H. *Hall Effect and Related Phenomena.* Butterworth, London, 1960.

(40) Park, Y. W.; Denenstein, A.; Chiang, C. K.; Heeger, A. J. and MacDiarmid, A. G. *Solid State Commun.* **1979**, *29*, 747.

(41) Kepler, R. G. *Phys. Rev.* **1960**, *119*, 1226.

(42) Blom, P.W.M.; de Jong, M. J. M.; Vleggaar, J. J. M. *Appl. Phys. Lett.* **1996**, *68*, 3308.
(43) Wheland, R. C.; Gillson, J. L. *J. Am. Chem. Soc.* **1976**, *98*, 3916.
(44) Wudl, F.; Bryce, M. R. *J. Chem. Educ*. **1990**, *67*, 717.
(45) Givaja, G.; Amo-Ochoa, P.; Gomez-Garcia, C. J.; Zamora, F. *Chem. Soc. Rev*. **2012**, *41*, 115.
(46) Carroll, D. R., S. , *One Dimensional Metals*, Wiley VCH, Weinheim, 2005.
(47) Van der Pauw, L. J. *Philips Technol. Rev*. **1958**, *20*, 220.
(48) Barsukov, E.; MacDonald, R. J. *Impedance Spectroscopy: Theory, Experiment, and Applications, 2nd Ed.* Springer, Berlin 2004.
(49) Quarles, T. *SPICE* [Online] v.3: http://ngspice.sourceforge.net/ Accessed Jan. 2015
(50) Bio-Logic, Inc. *EC-Lab* Claix: France, 2014.
(51) Saeki, A.; Koizumi, Y., Aidia, T.; Seki, S. *Acc. Chem. Res.* **2012**, *45*, 1193.
(52) Saeki, A.; Seki, S.; Koizumi, Y.; Tagawa, S. *J. Photochem. Photobiol. A*, **2007**, *186*, 158.
(53) Saeki, A.; Seki, S.; Sunagawa, T.; Ushida, K.; Tagawa S. *Philos. Mag.* **2006**, *86*, 1261.
(54) Minami, S.; Ide, M.; Hirano, K.; Satoh, T.; Sakurai, T.; Kato, K, Takata, M. Seki, S.; Miura, M. *Phys. Chem. Chem. Phys*. **2014**, *16*, 18805.
(55) Yasutani, Y.; Saeki, A.; Fukumatsu, T.; Koizumi, Y.; Seki, S. *Chem. Lett*. **2013**, *42*, 19.
(56) (a) Pozdorov, V.; Menard, E.; Kiryukhin V.; Rogers, J. A.; Gershenson, M. E. *Phys. Rev. Lett.* **2004**, *93*, 086602. (b) Molinari, A. S.; Alves, H.; Chen, Z. Faccheti, A. F.; Mopurgo, A. F. *J. Am. Chem. Soc.* **2009**, *131*, 2462.
(57) (a) Bao, Z.; Lovinger, A. J.; Dodabalapur, A. *App. Phys. Lett.* **1996**, *69*, 11. (b) Klauk, H. *Chem. Soc. Rev.* **2010**, *29*, 2643.
(58) Tauc, J.; Grigorovici, R; Vancu, A. *Phys. Status Solidi* **1966**, *15*, 627.
(59) Takaishi, S.; Hosoda, M.; Kajiwara, T.; Miyasaka, H.; Yamashita, M.; Nakanishi, Y.; Kitagawa, Y.; Yamaguchi, K.; Kobayashi, A.; Kitagawa, H. *Inorg. Chem.* **2009**, *48*, 9048.
(60) Torrance, J. B.; Scott, B. A.; Welber, B.; Kaufman, F. B.; Seiden, P. E. *Phys. Rev. B* **1979**, *19,* 730.
(61) Walton. K. S.; Snurr, R. Q. *J. Am. Chem. Soc.* **2007**, *129*, 8552.
(62) Kobayashi, Y.; Jacobs, B.; Allendorf, M. D.; Long, J. R. *Chem. Mater.* **2010**, *22*, 4120.
(63) Yanai, N.; Uemara, T.; Horike, S.; Shimomura, S.; Kitagawa, S. *Chem. Commun.* **2011**, *47*, 1722.
(64) Levi, M. D.; Aurbach, D. *J. Electroanal. Chem.* **1997**, *421*, 79.
(65) Robin, M. B.; Day, P. *Adv. Inorg. Chem. Radiochem.* **1967**, *10*, 247.
(66) Hush. N. S. *Prog. Inorg. Chem.,* **1967**, *8***,** 391.
(67) Gavari, J.-R., Weigel, D. *J. Sol. Stat. Chem.* **1975**, *13*, 252
(68) Walsh, A.; Watson, G. W. *J. Sol. Stat. Chem.* **2005**, *178*, 422.
(69) Babcock, P. *Webster's Third New International Dictionary of the English Language*. G. & C. Merriam Co.: Springfield, MA, USA, 1981

(70) Bailey, K. C. Ed. *The Elder Pliny's Chapters on Chemical Subjects* E. Arnold & Co., London, 1929.
(71) Fitzgurh, E. W. Red Lead and Minium. In *Artists' Pigments, v.1*, Feller, R. L., Ed.; Cambridge University Press: Cambridge, UK, 1986; pp. 109-139
(72) Thomspon, D. V. *The Materials of Medieval Painting* Yale University Press: New Haven, 1936.
(73) Yamane, Y.; Childs, T. *Manufacturing Technology Transfer: A Japanese Monozukuri View of Needs and Strategies* CRC Press: Boca Raton, FL, USA, 2013.
(74) Oberg, E.; Jones, F. D., Eds. *Machinery's Encyclopedia v. 5.* Industrial Press: New York, USA, 1917.
(75) Buser, H. J.; Schwarzenaba, D.; Petter W.; Ludi, A. *Inorg. Chem.* **1977**, *16*, 2704.
(76) Robin, M. B. *Inorg. Chem.* **1962**, *1*, 337.
(77) Behera, J.; D'Allesandro, D.; Soheilnia, N.; Long, J. R., *Chem. Mater.* **2009**, *21*, 1922.
(78) Creutz C. *Prog. Inorg. Chem.* **1983**, *30*, 1.
(79) McWhinnie, S. L. W.; Jones, C. J.; McCleverty, J. A.; Collison, D.; F. E. Mabbs, *J. Chem. Soc., Chem. Commun.* **1990**, 940.
(80) Richardson, D. E.; Taube, H. *Coord. Chem. Rev.* **1984**, *60*, 107.
(81) Parthey, M. Kaupp, M. *Chem Soc Rev.* **2014**, *43*, 5067.
(82) (a) Creutz, C.; Taube, H. *J. Am. Chem. Soc.* **1969***, 91*, 3988. (b) Creutz, C.; Taube, H. *J. Am. Chem. Soc.* **1973***, 95*, 1086.
(83) Crutchley, R. J. *Adv. Inorg. Chem.* **1994**, *41*, 273.
(84) Concepcion, J. J.; Dattelbaum, D. M.; Meyer, T. J.; Rocha, R. C. *Phil. Trans. R. Soc. A* **2007**, *366*, 163.
(85) Brunschwig, B.; Creutz, C. Sutin, N. *Chem. Soc. Rev.*, **2002**, *31*, 168.
(86) (a) Ferraris, J. P.' Cowan, D. O.; Walatka, V. V.; Perlstein, J. H. *J. Am. Chem. Soc.* **1973**, *95*, 948. (b) Coleman, L. B.; Cohen, M. J.; Sandman, D.; Yamagishi, F. G.; Garito, A. F. Heeger, A. J. *Solid State. Commun.* **1975**, *12*, 1125.
(87) Kistenmacher, T. J.; Phillips, T. E.; Cowan, D. O. *Acta Cryst.* **1974**, *B30*, 763.
(88) Coppens, P. *Phys. Rev. Lett.* **1975**, *35*, 98.
(89) Torrance, J. B.; Scott, B. A.; Kaufman, F. B. *Solid State Commun.* **1977**, *17*, 1369
(90) Saito, G.; Murata, T. *Phil. Trans. R. Soc. A* **2008**, *366*, 139.
(91) Torrance, J. B.; Mayerle, J. J.; Lee, V. Y.; Bechgaard, K. *J. Am. Chem. Soc.* **1979**, *101*, 4747.
(92) Agmon, N. *Chem. Phys. Lett.* **1995,** *244*, 456.
(93) Jeong, N. C.; Samanta, B.; Lee, C. Y.; Farha, O. K.; Hupp, J. T. *J. Am. Chem. Soc.* **2012**, *134*, 51.
(94) Phang, W. J.; Lee, W. R.; Yoo, K.; Ryu, D. W.; Kim, B. S.; Hong, C. S. Angew. Chem. Int. Ed. 2014, 53, 8383
(95) Millange, F.; Guillou, N.; Walton, R. I.; Grenèche, J.-M.; Margiolaki, I.; Férey, G. *Chem. Commmun.* **2008**, 4732.
(96) Serre, C.; Millange, F.; Thouvenot, C. ; Nogues, M.; Marsolier, G.; Louer, D.; Férey, G. *J. Am. Chem. Soc.*, **2002**, *124*, 13519.
(97) Loiseau, T.; Serre, C.; Huguenard, C.; Fink, G.; Taulelle, F.; Henry, M.; Bataille T.; Férey, G. *Chem.–Eur. J.*, **2004**, *10*, 1373.

(98) Shigematsu, A.; Yamada, T.; Kitagawa, H. *J. Am. Chem. Soc.* **2011**, *133*, 2034.
(99) Comotti, A.; Bracco, S.; Horike, S.; Matsuda, R.; Chen, J.; Takata, M.; Kubota, Y.; Kitagawa, S. *J. Am. Chem. Soc.* **2008**, *130*, 13664.
(100) Burrekaew, S.; Horike, S.; Higuchi, M.; Mizuno, M.; Kawamura, T.; Tanaka, D.; Yanai, N.; Kitagawa, S. *Nat. Mater.* **2009**, *8*, 831.
(101) Umeyama, D.; Horike, S.; Inukai, M.; Hijikata, Y.; Kitagawa, S. *Angew. Chem. Int. Ed.* **2011**, *50*, 11706.
(102) Hurd, J. A.; Vaidhyanathan, R.; Thangadurai, V.; Ratcliffe, C. I.; Moudrakovski, I. L.; Shimizu, G. K. H. *Nat. Chem.* **2009**, *1,* 705.
(103) Yoon, M.; Suh, K.; Natarajan, S.; Kim, K. *Angew. Chem. Int. Ed.* **2013***, 52*, 2688.
(104) Morozoan, A.; Jaouen, F. *Energy Environ. Sci.* **2012**, *5*, 9269.
(105) Horike, S.; Umeyama, D.; Kitagawa, S. *Acc. Chem. Res.* **2013**, *46*, 2376.
(106) Wiers, B. M.; Foo, M.-L.; Balsara, N. P.; Long, J. R. *J. Am. Chem. Soc.* **2011**, *133*, 14522.
(107) Cavka, C. H.; Jakobsen, S.; Olsbye, U.; Guillou, N.; Lamberti, C.; Bordiga, S.;K. P. Lillerud*,* K. P. *J. Am. Chem. Soc*. **2008**, *130*, 13850.
(108) Ameloot, R.; Aubrey, M.; Wiers, B. M.; Gomora-Figueroa, A. P.; Patel, S. N.; Balsara, N. P.; Long, J. R. *Chem. Eur. J.* **2013**, *19*, 5533.
(109) McDonald, T. M.; Lee, W. R.; Mason, J. A.; Wiers, B. M.; Hong, C. S.; Long, J. R. *J. Am. Chem. Soc.* **2012**, *134*, 7056.
(110) Aubrey, M. L.; Ameloot, R.; Wiers, B. M.; Long, J. R. *Energy Environ. Sci.* **2014**, *7*, 667.
(111) (a) Wright, P. V. *J. Polym Sci., Phys. Ed.* **1976**, *14*, 955. (b) Armand, M. B.; Chabango, J. M.; Duclot, M. J. In *Fast Ion Transport in Solids;* Duclot M. J.; Vashishta, P.; Mundy, J. N.; Shenoy, G .K., Eds; North Holland: Amsterdam, 1979.
(112) Gadjourova, Z.; Andreev, Y.; Tunstall, D. P.; Bruce, P. G. *Nature* **2001**, *412*, 520.
(113) Yanai, N. Uemura, T.; Horike, S.; Shimomura, S.; Kitagawa, S. *Chem. Commun.* **2011**, *47*, 1722.
(114) Uemura, T.; Yanai, N.; Watanabe, S.; Tanaka, H.; Numaguchi, R.; Miyahara, M. T.; Ohta, Y.; Nagaoka, M.; Kitagawa, S. *Nat. Commun.* **2010**, *1*, 83.
(115) Schoonman, J.; Ebert, L. B.; Hsieh, C. H.; Huggins, R. A. *J. Appl. Phys.* **1975**, *46*, 2873.
(116) Kiukkola, K.; Wagner, C. *J. Electrochem. Soc.* **1957**, *104*, 308.
(117) Sadakiyo, M.; Kasai, H.; Kato, K.; Takata, M.; Yamauchi, M. *J. Am. Chem. Soc.* **2014**, *136*, 1702.
(118) (a) Wudl, F. *Acc. Chem. Res.* **1984**, *17*, 227. (b) Wudl, F.; Wobschal.D; Hufnagel, E. J. *J. Am. Chem. Soc.* **1972**, *94*, 670.
(119) Wheland, R. C.; Gillson, J. L. *J. Am. Chem. Soc.* **1976**, *98*, 3916.
(120) (a) Hunig, S.; Erk, P. *Adv. Mater.* **1991**, *3*, 225. (b) Hunig, S. *Pure Appl. Chem.* **1990**, *62*, 395. (c) Aumuller, A.; Erk, P.; Klebe, G.; Hunig, S.; Vonschutz, J. U.; Werner, H. P. *Angew. Chem. Int. Ed.* **1986**, *25*, 740.
(121) (a) Heintz, R. A.; Zhao, H. H.; Xiang, O. Y.; Grandinetti, G.; Cowen, J.; Dunbar, K. R. *Inorg. Chem.* **1999**, *38*, 144. (b) Bendikov, M.; Wudl, F.; Perepichka, D. F. *Chem. Rev.* **2004**, *104*, 4891.

(122) Jerome, D.; Mazaud, A.; Ribault, M.; Bechgaard, K. *Cr Acad. Sci. B. Phys.* **1980**, *290*, 27.
(123) Cai, S.-L.; Zhang, Y.-B.; Pun, A. B.; He, B.; Yang, J.; Toma, F. M.; Sharp, I. D.; Yaghi, O. M.; Fan, J.; Zheng, S.-R.; Zhang, W.-G.; Liu, Y. *Chem. Sci.* **2014**, *5*, 4693.
(124) (a) Nohr, R. S.; Kuznesof, P. M.; Wynne, K. J.; Kenney, M. E.; Siebenman, P. G. *J. Am. Chem. Soc.* **1981**, *103*, 4371. (b) Diel, B. N.; Inabe, T.; Lyding, J. W.; Schoch, K. F.; Kannewurf, C. R.; Marks, T. J. *J. Am. Chem. Soc.* **1983**, *105*, 1551. (c) Dirk, C. W.; Marks, T. J. *Inorg. Chem.* **1984**, *23*, 4325. (d) Dirk, C. W.; Inabe, T.; Schoch, K. F.; Marks, T. J. *J. Am. Chem. Soc.* **1983**, *105*, 1539. (e) Marks, T. J. *Science* **1985**, *227*, 881. (f) Hoffman, B. M.; Ibers, J. A. *Acc. Chem. Res.* **1983**, *16*, 15. (g) Phillips, T. E.; Hoffman, B. M. *J. Am. Chem. Soc.* **1977**, *99*, 7734.
(125) Feng, X.; Liu, L.; Honsho, Y; Saeki, A.; Seki, S.; Irle, S.; Dong, Y.; Nagai, A.; Jiang, D. *Angew. Chem. Int. Ed.* **2012,** *51*, 2618.
(126) Wan, S.; Gándara, F.; Asano, A.; Furukawa, H.; Saeki, A.; Dey, S. K.; Liao, L.; Ambrogio, M. W.; Botros, Y. Y.; Duan, X.; Seki, S.; Stoddart, J. F.; Yaghi, O. M. *Chem. Mater.* **2011**, *23*, 4094.
(127) Feng, X.; Chen, L.; Honsho, Y.; Saengsawang, O.; Liu, L.; Wang, L.; Saeki, A.; Irle, S.; Seki, S.; Dong, Y.; Jiang, D. *Adv. Mater.* **2012**, *24,* 3026.
(128) Hmadeh, M.; Lu, Z.; Liu, Z.; Gándara, F.; Furukawa, H. Wan, S. Augustyn, V.; Chang, Y. R.; Liao, L. Zhou, F.; Perre, E.; Ozolins, V.; Suenaga, K.; Duan, X.; Dunn, B.; Yamamto, Y.; Terasaki, O.; Yaghi, O. M. *Chem. Mater.*, **2012**, *24*, 3511-3513.
(129) Sheberla, D.; Sun, L.; Blood-Forsythe, M. A.; Er, S.; Wade, C. R.; Brozek, C. K.; Aspuru-Guzik, A.; Dincā, M. *J. Am. Chem. Soc.* **2014**, *136*, 8859.
(130) Fukui, H.; Shigeta, Y.; Nakano, M.; Kubo, T.; Kamada, K.; Ohta, K.; Champagne, B.; Botek, E. *J. Phys. Chem. A* **2011**, *115*, 1117.
(131) Narayan, T. C.; Miyakai, T.; Seki, S.; Dinca, M. *J. Am. Chem. Soc.* **2012**, *134*, 12932.
(132) (a) Mori, H.; Tanaka, S.; Mori, T. *Phys. Rev. B* **1998**, *57*, 12023. (b) Kato, R.; Kobayashi, H.; Kobayashi, A. *J. Am. Chem. Soc.* **1989**, *111*, 5224.
(133) (a) Zhang, B.; Wang, Z. M.; Zhang, Y.; Takahashi, K.; Okano, Y.; Cui, H. B.; Kobayashi, H.; Inoue, K.; Kurmoo, M.; Pratt, F. L.; Zhu, D. B. *Inorg. Chem.* **2006**, *45*, 3275. (b) Zhang, B.; Kurmoo, M.; Mori, T.; Zhang, Y.; Pratt, F. L.; Zhu, D. B. *Cryst. Growth Des.* **2010**, *10*, 782. (c) Mas-Torrent, M.; Rovira, C. *Chem. Rev. (Washington, DC, U. S.)* **2011**, *111*, 4833. (d) Martin, L.; Turner, S. S.; Day, P.; Malik, K. M. A.; Coles, S. J.; Hursthouse, M. B. *Chem. Commun. (Cambridge, U. K.)* **1999**, 513.
(134) (a) Nielsen, M. B.; Lomholt, C.; Becher, J. *Chem. Soc. Rev.* **2000**, *29*, 153. (b) Bryce, M. R. *J. Mater. Chem.* **2000**, *10*, 589. (c) Schenning, A. P. H. J.; Meijer, E. W. *Chem. Commun. (Cambridge, U. K.)* **2005**, 3245. (d) Weitz, R. T.; Walter, A.; Engl, R.; Sezi, R.; Dehm, C. *Nano Lett.* **2006**, *6*, 2810. (e) Alves, H.; Molinari, A. S.; Xie, H. X.; Morpurgo, A. F. *Nat. Mater.* **2008**, *7*, 574. (f) Odom, S. A.; Caruso, M. M.; Finke, A. D.; Prokup, A. M.; Ritchey, J. A.; Leonard, J. H.; White, S. R.; Sottos, N. R.; Moore, J. S. *Adv. Funct. Mater.* **2010**, *20*, 1721.

(135) (a) Yzambart, G.; Bellec, N.; Nasser, G.; Jeannin, O.; Roisnel, T.; Fourmigue, M.; Auban-Senzier, P.; Iniguez, J.; Canadell, E.; Lorcy, D. *J. Am. Chem. Soc.* **2012**, *134*, 17138. (b) Aonuma, S.; Sawa, H.; Kato, R. *J. Chem. Soc. Perk. Trans. 2* **1996**, 1028. (c) Yoshino, H.; Murata, K.; Saito, K.; Nishikawa, H.; Kikuchi, K.; Ikemoto, I. *Phys. Rev. B* **2003**, *67*.

(136) Zeng, M.-H.; Wang, Q.-X.; Tan, Y.-X.; Hu, S.; Zhao, H.-X.; Long, L.-S.; Kurmoo, M. *J. Am. Chem. Soc.* **2010**, *132*, 2561.

(137) Chui, S. S. Y.; Lo, M. F.; Charmant, J. P. H.; Orpen, A. G.; Williams, I. D. *Science*, **1999**, *283*, 1148.

(138) Talin, A.A.; Centrone, A.; Ford, A. C.; Foster, M. E.; Stavila, V.; Haney, P.; Kinney, R. A.; Szalai, V.; El Gabaly, F.; Yoon, H. P.; Léonard, F.; Allendorf, M. D. *Science* **343**, 64-66 (2013).

(139) (a) Uemura, T.; Kitaura, R.; Ohta, Y.; Nagaoka, M.; Kitagawa, S. *Angew. Chem.-Int. Edit.* **2006**, *45*, 4112. (b) Uemura, T.; Ono, Y.; Kitagawa, K.; Kitagawa, S. *Macromolecules* **2008**, *41*, 87. (c) Uemura, T.; Yanai, N.; Kitagawa, S. *Chem. Soc. Rev.* **2009**, *38*, 1228.

(140) Mahato, R. N., Siekman, M. H.; Kersten, S. P., Bobbert, P. A.; de Jong, M. O.; van der Wiel, M. G. *Science*, **2013**, *341*, 257.

(141) (a) Szczepura, L. F.; Galloway, C. P.; Zheng, Y. F.; Han, P. D.; Rheingold, A. L.; Wilson, S. R.; Rauchfuss, T. B. *Angew Chem Int Edit* **1995**, *34*, 1890. (b) Huang, X. Y.; Li, J. *J. Am. Chem. Soc.* **2007**, *129*, 3157. (c) Che, C. M.; Li, C. H.; Chui, S. S. Y.; Roy, V. A. L.; Low, K. H. *Chem-Eur J* **2008**, *14*, 2965. (d) Feng, P. Y.; Bu, X. H.; Zheng, N. F. *Acc. Chem. Res.* **2005**, *38*, 293. (e)" Schrauzer, G. N.; Prakash, H. *Inorg. Chem.* **1975**, *14*, 1200. (f) Zhang, Z. Y.; Zhang, J.; Wu, T.; Bu, X. H.; Feng, P. Y. *J. Am. Chem. Soc.* **2008**, *130*, 15238.

(142) (a) "Mixed-Valence Properties of Ligand-Bridged Iron-Cyano Complexes" Felix, F.; Ludi, A. *Inorg. Chem.* **1978**, *17*, 1782. (b) Taube, H. *Angew. Chem.-Int. Edit.* **1984**, *23*, 329. (c) "Metal-Metal Interactions in Binuclear Complexes Exhibiting Mixed-Valency - Molecular Wires and Switches" Ward, M. D. *Chem. Soc. Rev.* **1995**, *24*, 121. (f) Astruc, D. *Acc. Chem. Res.* **1997**, *30*, 383. (d) McCleverty, J. A.; Ward, M. D. *Acc. Chem. Res.* **1998**, *31*, 842. (e) "Nelsen, S. F. *Chem-Eur J* **2000**, *6*, 581. (iKaim, W.; Klein, A.; Glockle, M. *Acc. Chem. Res.* **2000**, *33*, 755.

(143) (a) Backes-Dahmann, G. Wieghardt, K. *Inorg. Chem.*, **1985**, *24*, 4049. (b) Bechlars, B.; D'Alessandro, D. M.; Jenkins, D. J.; Iavarone, A. T.; Glover, S. D.; Kubiak, C. P.; Long, J. R. *Nat. Chem.* **2010**, *2*, 362.

(144) Shlenker, C. D., J.; Greenblatt, M. van Smaalen, S. Eds, *Physics and Chemistry of Low-Dimensional Inorganic Conductors*, Plenum Press, New York, 1996.

(145) Bailar, J. C. Jr. *Prep. Inorg. Chem.* **1964**, *1*, 1.

(146) (a) Krogmann, K. *Angew. Chem. Int. Edit.* **1969**, *8*, 35. (b) Krogmann, K.; Hausen, H. D. *Z. Anorg. Allg. Chem.* **1968**, *358*, 67.

(147) Zeller, H. R. *Adv. Solid State Phys.* **1973**, *13*, 31.

(148) Mitsumi, M.; Yoshida, Y.; Kohyama, A.; Kitagawa, Y.; Ozawa, Y.; Kobayashi, M.; Toriumi, K.; Tadokoro, M.; Ikeda, N.; Okumura, M.; Kurmoo, M. *Inorg. Chem.* **1985**, *48*, 6680.

(149) Mitsumi, M.; Umebayashi, S.; Ozawa, Y.; Toriumi, K.; Kitagawa, H.; Mitani, T. *Chem. Lett.* **2002**, *41*, 2767.

(150) Martinsen, J.; Place, L. J.; Phillips, T. E.; Hoffman, B. M.; Ibers, J. A. *J. Am. Chem. Soc.* **1982**, *104*, 83.
(151) Martinsen, J.; Stanton, J. I.; Greene, R. L.; Tanaka, J.; Hoffman, B. M.; Ibers, J. A. *J. Am. Chem. Soc.* **1985**, *107*, 6916
(152) (a) Collman, J. P.; Mcdevitt, J. T.; Leidner, C. R.; Yee, G. T.; Torrance, J. B.; Little, W. A. *J. Am. Chem. Soc.* **1987**, *109*, 4606. (b) Collman, J. P.; McDevitt, J. T.; Yee, G. T.; Leidner, C. R.; McCullough, L. G.; Little, W. A.; Torrance, J. B. *Proc. Natl. Acad. Sci.* **1986**, *83*, 4581. (c) Collman, J. P.; Mcdevitt, J. T.; Yee, G. T.; Zisk, M. B. *Synth. Met.* **1986**, *15*, 129.
(153) (a) Hanack, M.; Kobel, W.; Koch, J.; Metz, J.; Schneider, O.; Schulze, H. J. *Mol. Cryst. Liq. Cryst.* **1983**, *96*, 263.
(154) (a) Paul, F.; Lapinte, C. *Coord. Chem. Rev.* **1998**, *178*, 431. (b) Luo, L.; Benameur, A.; Brignou, P.; Choi, S. H.; Rigaut, S.; Frisbie, C. D. *J. Phys. Chem. C* **2011**, *115*, 19955. (cCummings, S. P.; Cao, Z.; Fanwick, P. E.; Kharlamova, A.; Ren, T. *Inorg. Chem.* **2012**, *51*, 7561. (d) Manna, J. J., K.D.; Hopkins, M.D., in *Adv. Organomet. Chem.*, Vol. 38, 1995, 79.
(155) (a) Monceau, P.; Peyrard, J.; Richard, J.; Molinie, P. *Phys. Rev. Lett.* **1977**, *39*, 161. (b) Bjerkelu.E; Fermor, J. H.; Kjekshus, A. *Acta Chem. Scand.* **1966**, *20*, 1836. (c) Haen, P.; Monceau, P.; Tissier, B.; Waysand, G.; Meerschaut, A.; Molinie, P.; Rouxel, J. *Ferroelectrics* **1977**, *17*, 447.
(156) (a) Schlenker, C.; Filippini, C.; Marcus, J.; Dumas, J.; Pouget, J. P.; Kagoshima, S. *J Phys-Paris* **1983**, *44*, 1757. (b) "Charge-Density-Wave Properties of Molybdenum Bronzes" Dumas, J.; Schlenker, C. *Int J Mod Phys B* **1993**, *7*, 4045. (c) Rousseau, R.; Canadell, E.; Alemany, P.; Galvan, D. H.; Hoffmann, R. *Inorg. Chem.* **1997**, *36*, 4627. (d) Adams, S.; Ehses, K. H.; Spilker, J. *Acta Crystallogr B* **1993**, *49*, 958. (e) Whangbo, M. H.; Canadell, E.; Foury, P.; Pouget, J. P. *Science* **1991**, *252*, 96. (f) Whangbo, M. H.; Canadell, E.; Schlenker, C. *J. Am. Chem. Soc.* **1987**, *109*, 6308.
(157) Sun, L.; Miyakai, T.; Seki, S. Dinca, M. *J. Am. Chem. Soc.* **2013**, *135*, 8185.
(158) Gándara, F.; Uribe-Romo, F. J.; Britt, D. K.; Furukawa, H.; Lei, L.; Cheng, R.; Duan, X. O'Keefe, M.; Yaghi, O. M. *Chem. Eur. J.* **2012**, *18,* 10595.
(159) Herm, Z. R.; Wiers, B. M.; Mason, J. A.; van Baten, J. M.; Hudson, M. R.; Zajdel, P.; Brown, C. M.; Masciocchi, N.; Krishna, R.; Long, J. R. *Science* **2013**, *340*, 960.
(160) Kim, Y. Leiber, C. M. *J. Am Chem. Soc.* **1989**, *28*, 3990.
(161) Dimitrakopoulos, C. D.; Malenfant, P. R. L. *Adv. Mat.* **2002**, *14*, 99.
(162) de Leeuw, D. M.; Simenon, M. M. J.; Brown, A. R.; Einerhand, R. E. F. *Synth. Met.* **1997**, *87*, 53.
(163) Facchetti, A.; Deng, Y.; Wang, A.; Koide, Y.; Sirringhaus, H.; Marks, T. J.Friend, R. H. Angew. Chem. Int. Ed. **2000**, *39*, 4547.
(164) Haddon, R. C.; Perel, A. S.; Morris, R. C.; Palstra, T.T.M.; Hebart, A. F.; Fleming, A. M. *Appl. Phys. Lett.* **1995**, *67*, 121.
(165) Campbell, I. H.; Kress, J. D.; Martin, R. L.; Smith, D. L.; Barashkov, N. N.; Ferraris, J. P. *Appl. Phys. Lett.* **1997**, *71*, 3528.

Chapter 2: Solid Lithium Ion Electrolytes by Post-Synthetic Grafting of Lithium Alkoxides in Metal-Organic Frameworks

2.1 Introduction

Due to their high energy density and operating potential, lithium-ion batteries have been widely adopted in portable electronics. However, to enable their implementation in traction applications, such as for electric vehicles, considerable improvements must still be made in terms of cost, energy and power density, manufacture, and safety.[1] Advances in electrode chemistries as well as the separator are needed to meet those challenges. Currently, macroporous polymer membranes swelled with lithium salts dissolved in organic carbonates are utilized as the separator in lithium-ion batteries.[2] The use of a liquid electrolyte restricts battery shape and processing, while also posing numerous safety problems, due to the potential leakage of corrosive liquids and the volatility and flammability of the electrolyte solvent.[3] Furthermore, the lack of rigidity for current battery separators precludes the use of solid lithium as an anode, because repeated cycling leads to lithium dendrites that can pierce the separator and cause cell failure.[4] In contrast, a rigid, solid separator could inhibit lithium dendrite growth and allow the use of metallic lithium as an anode.[5] Given the high theoretical capacity of lithium metal (3860 Ah/kg), and its very negative reduction potential (–3.04 V vs. SHE), such an advance would enable tremendous gains in energy capacity. Since the 1970s, salts dissolved in solid polyethers have been investigated as solid electrolyte materials.[6] However, the low conductivities of such materials at room temperature (10^{-6} S/cm) currently prevents their use in battery applications. Other solid lithium electrolytes either display total conductivities that are also too low or are poorly compatible with the battery electrodes.[7]

Metal-organic frameworks are a broad class of microporous solids that have been investigated primarily for their gas adsorption properties,[8] as well as for possible applications in sensing,[9] drug delivery,[10] catalysis,[11] and optoelectronics.[12] Recently, studies of electronic[13] and proton conductivity[14] have also been reported. While the intercalation of lithium ions into such materials has been observed,[15] and porous zeolites have been investigated as fillers in solid polymer lithium electrolyte systems,[16] as well as stand alone solid electrolytes operating at high temperatures (> 300 °C),[17] the use of metal-organic frameworks as lithium ion conductors has received scant attention. Herein, I show that the incorporation of lithium isopropoxide into a metal-organic framework with open metal cation sites can produce a solid with an ionic conductivity of greater than 10^{-4} S/cm at 300 K.

2.2 Experimental

General Considerations Unless otherwise specified all syntheses and sample manipulations were performed under the rigorous exclusion of air and moisture in either

N_2 or Ar glove boxes. All reagents and solvents were commercially available and used without further purification. Infrared spectra were collected on a Perkin Elmer Spectrum 400S FT-IR/FT-FIR spectrometer equipped with an attenuated total reflectance accessory (ATR). Powder X-ray diffraction data was collected using Cu Kα (λ = 1.5406 Å) radiation on a Bruker D8 Advance diffractometer. Carbon, hydrogen, and nitrogen analyses were obtained from the Microanalytical Laboratory of the University of California, Berkeley. Metals and halogen analyses were performed by Galbraith Laboratories in Knoxville, TN. SEM was performed at the University of California Robert D. Ogg Electron Microscope Lab on a Hitachi S-5000 SEM. TGAs were performed on TA Instruments TGA-Q500 under N_2 atmosphere at a heating rate of 0.5 °C/min.

Synthesis and activation of Zn_4OBDC (2) MOF-177 was synthesiszed as previously reported.[18] After synthesis the sample was transferred to a glove bag. The supernatant was decanted and the sample was then soaked in DMF at room temperature for 6 8-h cycles and then soaked in methylene chloride for 6 8-h cycles. The sample was transferred to a Schlenk flask, and evacuated on a Schlenk line before being brought into a glove box.

Synthesis and Activation of Cu_3BTTri (1) Cu-BTTri was synthesized and activated as previously reported.[19] The sample was transferred to a Schlenk flask, and evacuated on a Schlenk line before being brought into a glove box.

Synthesis and Activation of Mg_2(DOBDC) (3) Mg_2(DOBDC) was synthesized as previously reported.[20] The sample was then soaked in DMF at 100 °C for 6 8-h cycles and then soaked in anhydrous methanol for 6 8-h cycles. The sample was then filtered and transferred into a Schlenk flask where it was evacuated at < 10 mtorr for 12 h at 250 °C before being transferred to a glovebox.

Lithium Isopropoxide Grafting of Mg_2(DOBDC) in hexanes The activated framework was reacted with a 10-fold molar excess of 1.0 M lithium isopropoxide in hexanes in sealed vials at 80 °C for 2 weeks, after which the sample was collected by filtration and washed repeatedly with hexanes. The sample was then transferred to a Schlenk flash and evacuated on a vacuum line at < 10 mtorr for 24 h at 180 °C. Metals Analysis- Mg: 12.9%, Li: 0.970%. Molar ratio of Mg: Li- 2:0.53. Elemental analysis- Calculated C: 41.45, H: 2.05, Found C: 40.61, H: 2.90.

Mg_2(DOBDC)·0.35LiO^{i}Pr·0.25$LiBF_4$·EC·DEC The material obtained as described above was soaked for 24 h in a 1 M $LiBF_4$ solution in a 1:1 (v:v) mixture of ethylenecarbonate (EC) and diethylcarbonate (DEC). Metals and halogen analysis (weight percent)- Mg: 9.10%, Li: 0.780%, B: 0.506%, F: 3.55%. Molar ratio of Mg:Li:B:F- 2:0.6:0.25:1. Elemental analysis- Calculated (based on metals and halogen analysis) C: 39.19, H: 2.29, Found C: 37.72, H: 3.88. The obtained C, H, and N analyses poorly fit the formula calculated from the metals analysis. We believe this to be due to solvent desorption and possible uptake of other solvents in the glove box prior to analysis. Thermogravimetric analysis data of the material freshly removed from a sealed vial is consistent with the loss of one EC and one DEC molecule (45% weight loss).

Mg_2(DOBDC)·0.06LiO^{i}Pr·*x*EC·*y*DEC The activated framework was reacted with a 10-fold molar excess of 1.0 M lithium isopropoxide in tetrahydrofuran in sealed vials at 80 °C for 2 weeks, after which the sample was filtered and washed repeatedly with tetrahydrofuran. The sample was then transferred to a Schlenk flash and desolvated

by heating on a vacuum line at 180 °C and < 10 mtorr for 24 h. The material was then soaked for 24 h in a 1:1 (v:v) mixture of EC and DEC. Metals analysis (weight percent)- Mg:13.79%, Li 0.0723%. Molar ratio of Mg:Li – 2:0.06.

Mg_2(DOBDC)·0.05$LiBF_4$·*x*EC·*y*DEC An activated sample of Mg_2(dobdc) was soaked for 24 h in a 1 M $LiBF_4$ solution in a 1:1 (v:v) ethylene carbonate:diethyl carbonate solution. Metals and halogen analysis (weight percent)- Mg:11.3%, Li: 0.082%, B: 0.069%, F: 0.858%. Molar ratio of Mg:Li:B:F - 2-0.05:0.05:0.2.

Pellet Pressing Within an argon-filled glove box, the electrolyte material was placed in a Garolite washer and sandwiched between PTFE sheets. The pellet was then pressed at 5000 psi for 1 min.

Conductivity Measurements In an argon-filled glove box, AC impedance spectroscopy measurements were made using a homemade test cell on thermostatted pressed samples using a Solartron 1260 frequency response analyzer connected to a Solartron 1296 dielectric interface and blocking stainless steel electrodes. SMART (v1.1.1) software was used as control software. Measurements were made over a frequency range of 1 MHz to 1 Hz using a 100 mV (peak voltage) applied ac signal. Ten measurements were made in every frequency decade with 1 s integration times at each frequency. Variable temperature impedance spectra were collected over many temperatures using the thermostatted temperature control. Ionic conductivity σ (S/cm) was calculated as:

$$\sigma = L/(AR) \qquad (1)$$

where L is the pellet thickness and A is the area in contact with the electrodes and R is the real impedance measured from the location of the local minima between the high and low frequency arcs measured on the real axis of a Nyquist plot. We found extrapolation of the high frequency arc to the real frequency intercept did not give conductivity values significantly different from the real resistance value measured at the local minima. We also found the values to not significantly differ when obtained by finding the plateau region of the Bode plot (log |Z| vs. log f). For example the measured resistance of a pellet made of Mg_2(DOBDC)·0.35LiO^iPr·0.25$LiBF_4$·EC·DEC was 2049 Ω measuring by the local minima method, 2189 Ω by modeling the high frequency curve as a polynomial and finding the real resistance axis intercept and by finding the plateau region of the Bode plot gave a real resistance of 2010 Ω.

2.3 Results and Discussion

In our initial evaluation of metal-organic frameworks as possible lithium electrolyte materials, we tested the ionic conductivity attained upon uptake of a common electrolyte solution within MOF-177,[18] Cu-BTTri,[19] and Mg_2(DOBDC)[20] the structures of which are shown in Figure **2.**1 Each compound was soaked in a 1 M solution of $LiBF_4$ in a 1:1 mixture of ethylene carbonate (EC) and diethyl carbonate (DEC), and the resulting

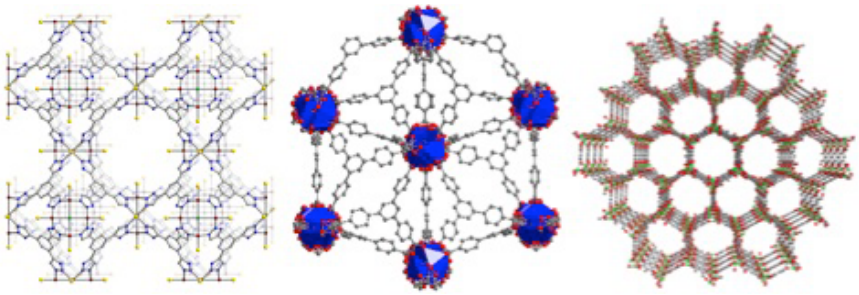

Figure 2.1 Structures of the metal-organic frameworks studied in this work. Left to right: CuBTTri, MOF-177 and Mg_2(DOBDC).

materials were dried and pressed into pellets. The pellets were then placed in a thermostatted press and their conductivities were measured via two-point ac impedance spectroscopy. A Solartron 1260 frequency response analyzer connected to a Solartron 1296 dielectric interface and blocking stainless steel electrodes were employed for this process. The conductivity of each material was obtained by measuring the real impedance of the semicircles of the Nyquist plots, and taking the geometry of the pellets into account. The impregnated frameworks showed conductivities on the order of 10^{-9} to 10^{-6} S/cm (Figure 2.2-3). The most promising material is Mg_2(DOBDC), which upon uptake of the electrolyte solution afforded a room temperature conductivity of 1.8×10^{-6} S/cm. Although the most conductive of the materials we measured, this value still lies three orders of magnitude below what is desired for a battery electrolyte (10^{-3} S/cm at ambient temperature)[4] and two orders of magnitude below what is considered the technological limit for a functional battery electrolyte (10^{-4} S/cm).[7]

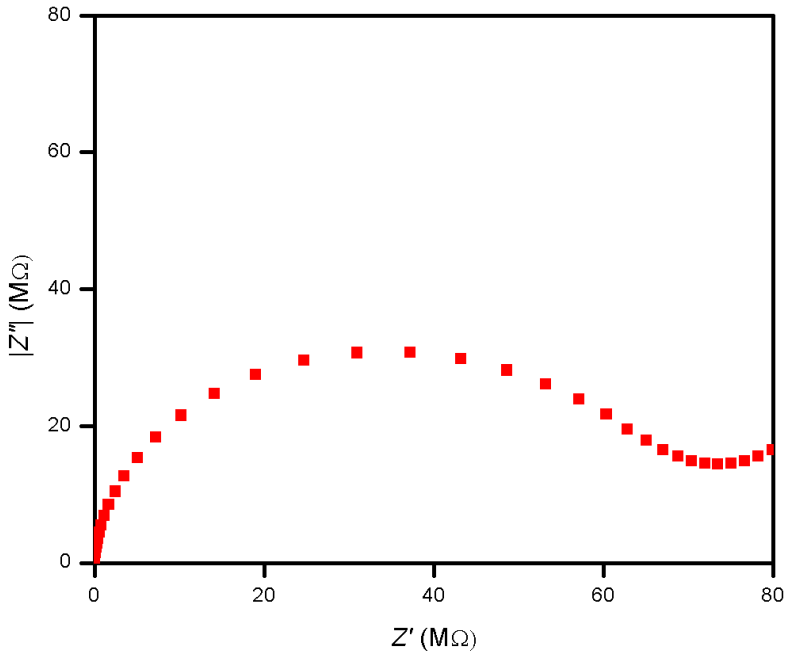

Figure 2.2 Nyquist plot of a room temperature, 2-point AC impedance measurement of a pressed pellet of CuBTTri soaked in a 1M $LiBF_4$ in 1:1 (v:v) ethylene carbonate: diethyl carbonate mixture. Conductivity is 1.5×10^{-9} S/cm.

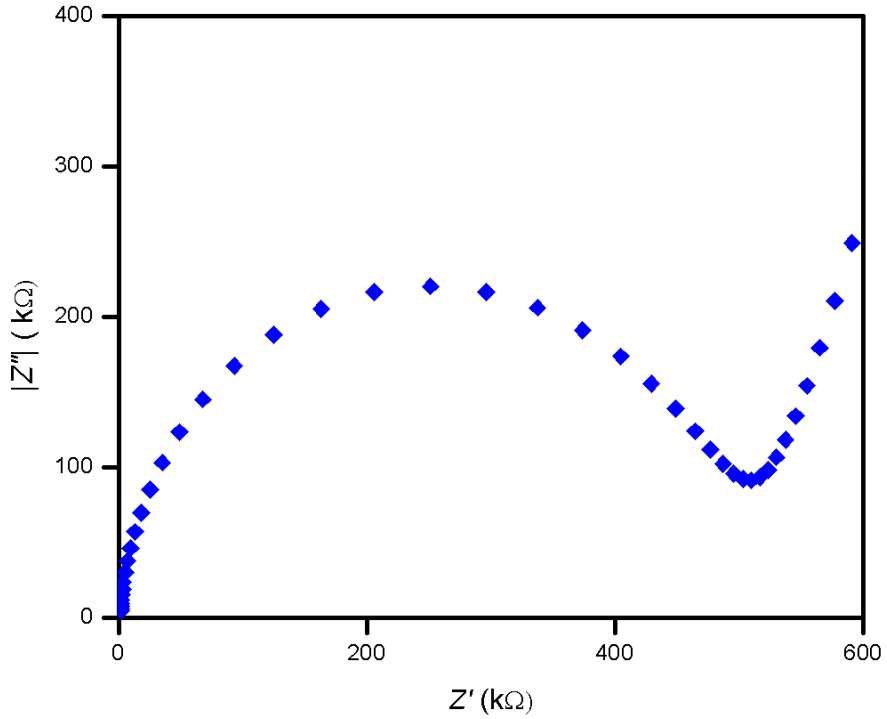

Figure 2.3 Nyquist plot of a room temperature, 2-point AC impedance measurement of a pressed pellet of MOF-177 soaked in a 1M $LiBF_4$ in 1:1 (v:v) ethylene carbonate: diethyl carbonate mixture. Conductivity is 4.0×10^{-7} S/cm.

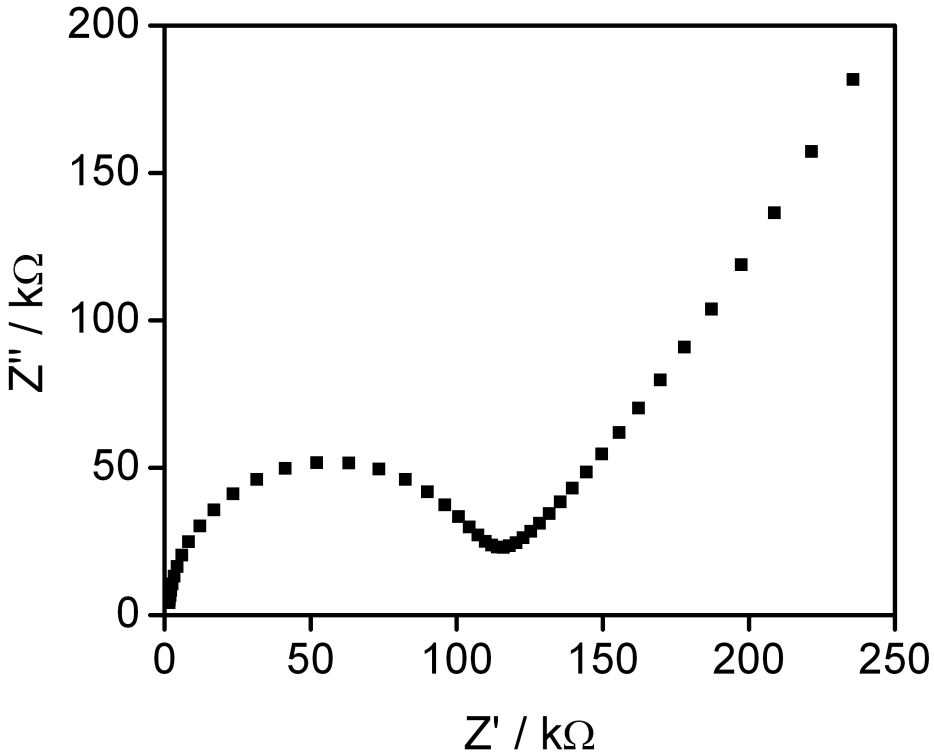

Figure 2.4 Nyquist plot of a room temperature, 2-point AC impedance measurement of a pressed pellet of Mg_2(DOBDC) soaked in a 1M $LiBF_4$ in 1:1 (v:v) ethylene carbonate: diethyl carbonate mixture.

Researchers have previously effected post-synthetic modifications of metal-organic frameworks via covalent modification of organic ligands,[11c,21] as well as through the grafting of neutral ligands onto open metal centers.[19] The structure of Mg_2(dobdc) consists of one-dimensional hexagonal channels approximately 14 Å in diameter, and lined with coordinatively-unsaturated Mg^{2+} cation sites. We hypothesized that the presence of these sites could facilitate the uptake of a lithium alkoxide, leading to higher ionic conductivity. Here, the alkoxide anions might preferentially bind the Mg^{2+} ions of the framework, pinning them in place, while leaving the Li^+ cations relatively free to move along the channels (Figure 2.5).

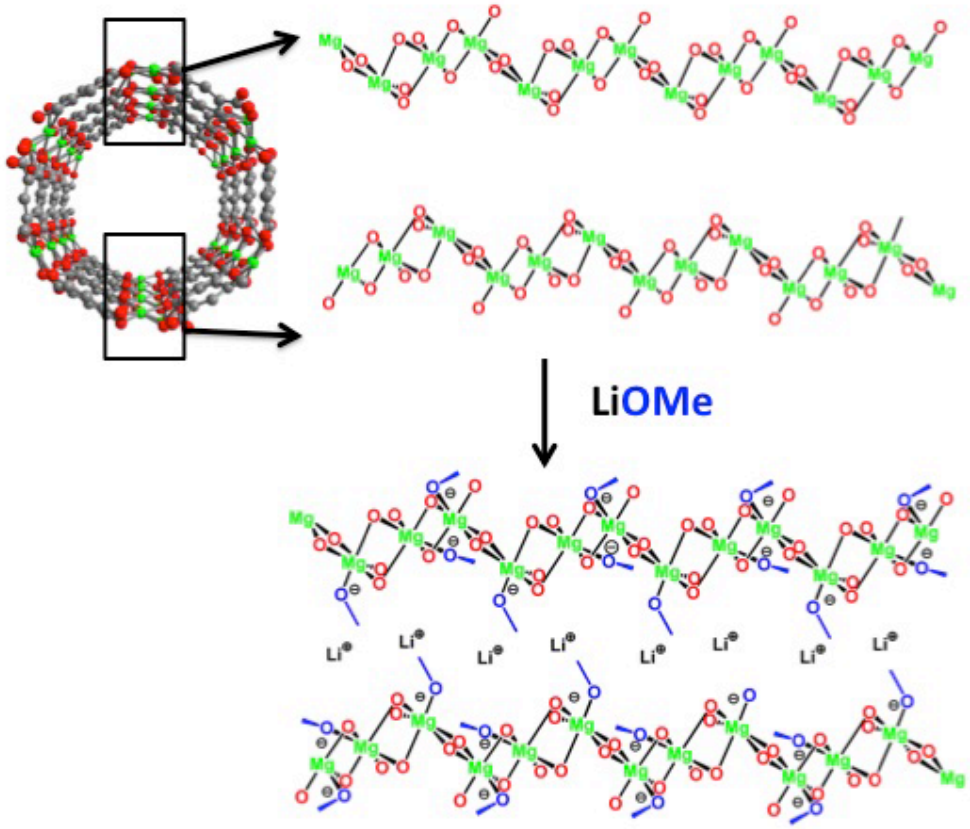

Figure 2.5 Scheme of the grafting of lithium methoxide to Mg_2(DOBDC).

Treatment of Mg_2(DOBDC) with lithium methoxide, followed by impregnation of the framework in a solution of 1M $LiBF_4$ in 1:1 (v:v) EC:DEC solution a solid material that displayed a conductivity of 1.8×10^{-5} S/cm. Variable temperature measurements of this material showed an activation energy of 0.39 eV (Figure 2.6**)**, slightly higher than the activation energy of Mg_2(DOBDC) soaked in the 1M LiBF in EC:DEC solution (0.31 eV). I reasoned that variation of the alkyl group might allow screening of the negative charge of the oxygen atom and modification of the pore content and screened grafts with other alkoxides. Indeed, modification of the Mg_2(DOBDC) with lithium isopropoxide yielded the electrolytes with the greatest conductivity, and lowest activation energies measured.

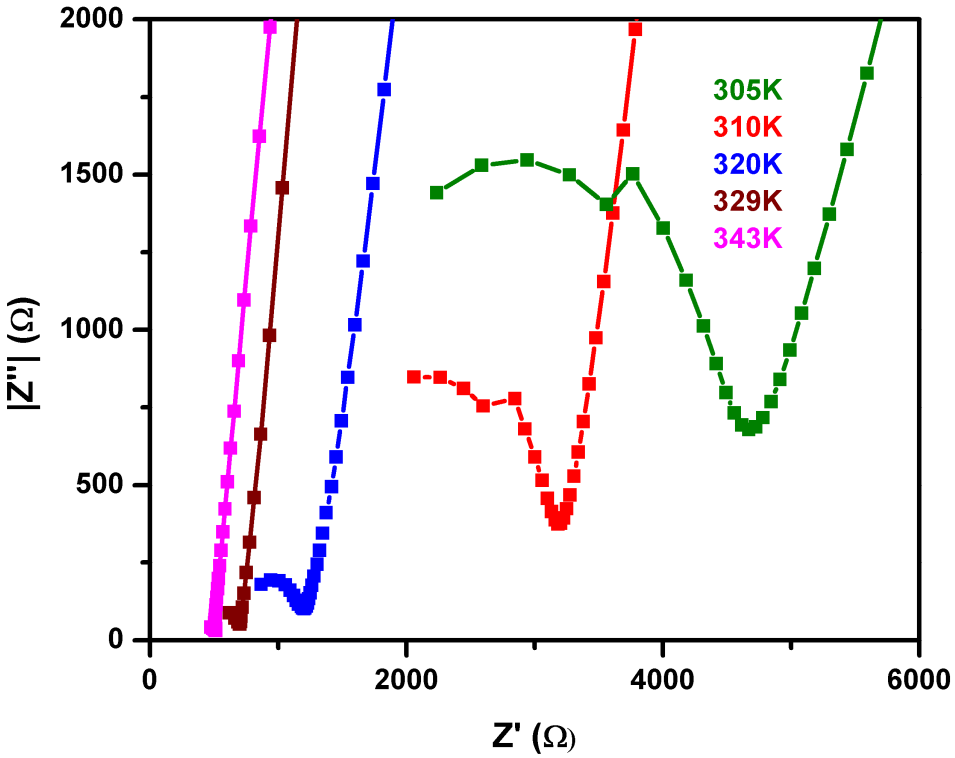

Figure 2.6 Nyquist plots of variable temperature 2-point AC impedance measurements of lithium methoxide grafted Mg_2(DOBDC)

Figure 2.7 shows a schematic of the post-synthetic modification of Mg_2(DOBDC) to obtain the most-conductive electrolyte. Mg_2(DOBDC) was activated by heating under vacuum to remove all solvent, followed by soaking for two weeks with a hot solution of Li^{i}OPr in hexanes. The solids were then washed with hexanes and dried under reduced pressure. Infrared spectra of the resulting materials revealed the emergence of aliphatic C-H stretches at 3200 cm^{-1}, a new C-O stretch at 1080 cm^{-1}, and a broadening of what I assign to be an Mg-O stretch at 450 cm^{-1} (Figure 2.8).[22] The results from elemental analyses are consistent with the formula Mg_2(DOBDC)·0.5LiO^{i}Pr. Subsequent soaking of the material in a 1 M solution of $LiBF_4$ in a 1:1 mixture of EC and DEC, resulted in uptake of 0.25 equiv of $LiBF_4$ and 2 equiv of carbonate solvent (either EC or DEC) to give a compound of formula Mg_2(DOBDC)·0.35LiO^{i}Pr·0.25$LiBF_4$·EC·DEC. Powder x-ray diffraction data for this material indicate that the framework structure is preserved throughout the impregnation process (Figure 2.9). The decrease in LiO^{i}Pr content may be due to leaching of unbound lithium alkoxide and/or exchange with $LiBF_4$. It should be noted that in concentrated solutions Li^+ cations can be solvated by as few as two carbonate molecules.[23] Within the pores of the framework, we anticipate a high density of charge carriers in close proximity to each other, allowing Li^+ cations to hop from site to site whilst remaining solvated by the carbonate molecules. The final sample was obtained as a dry, free-flowing powder that could be readily pressed into pellets.

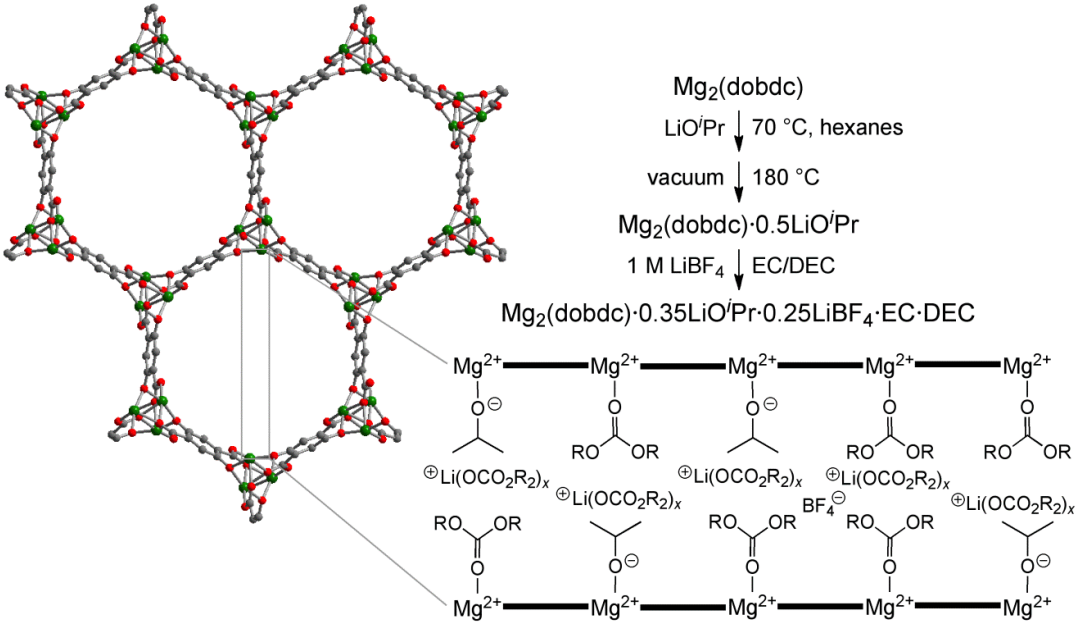

Figure 2.7 A schematic representation of the modification of $Mg_2(DOBDC)$ to obtain the solid electrolyte $Mg_2(DOBDC)\cdot 0.35LiO^iPr\cdot 0.25LiBF_4\cdot EC\cdot DEC$.

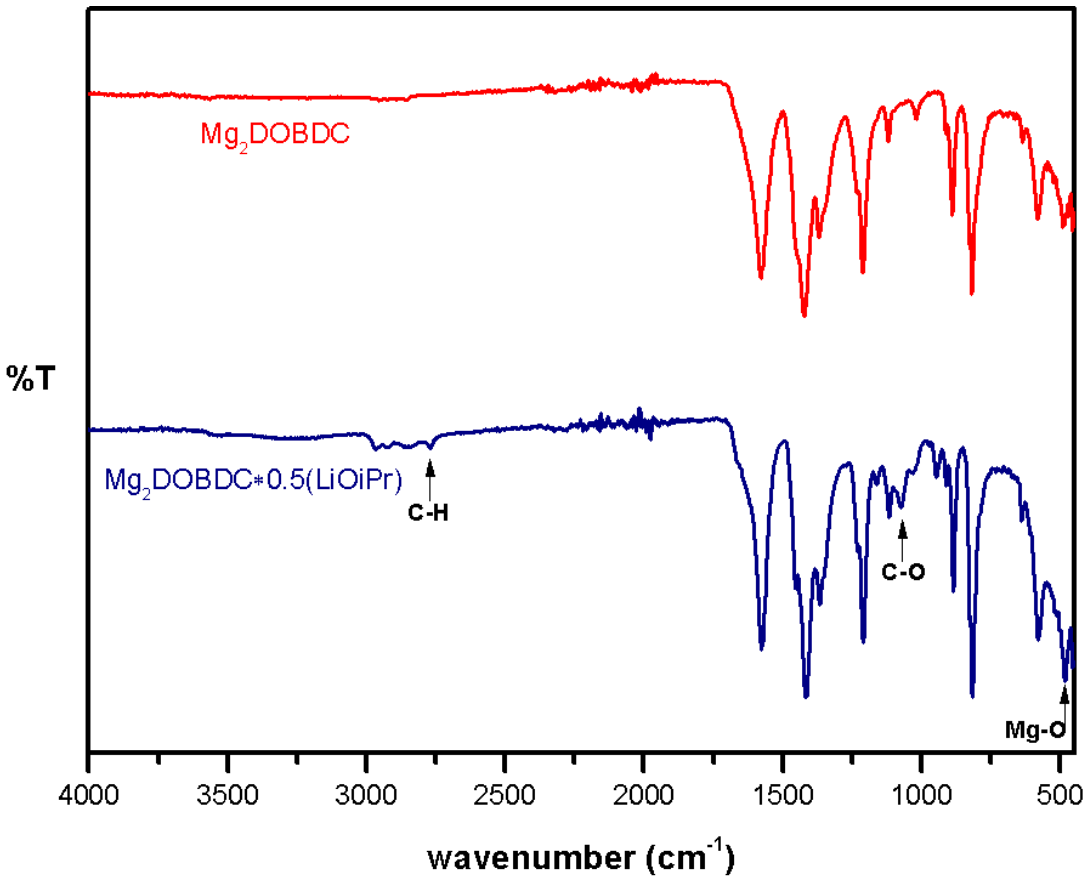

Figure 2.8 FT-IR spectra of $Mg_2(DOBDC)$ before (top, red) and after (below, blue) grafting with lithium isopropoxide.

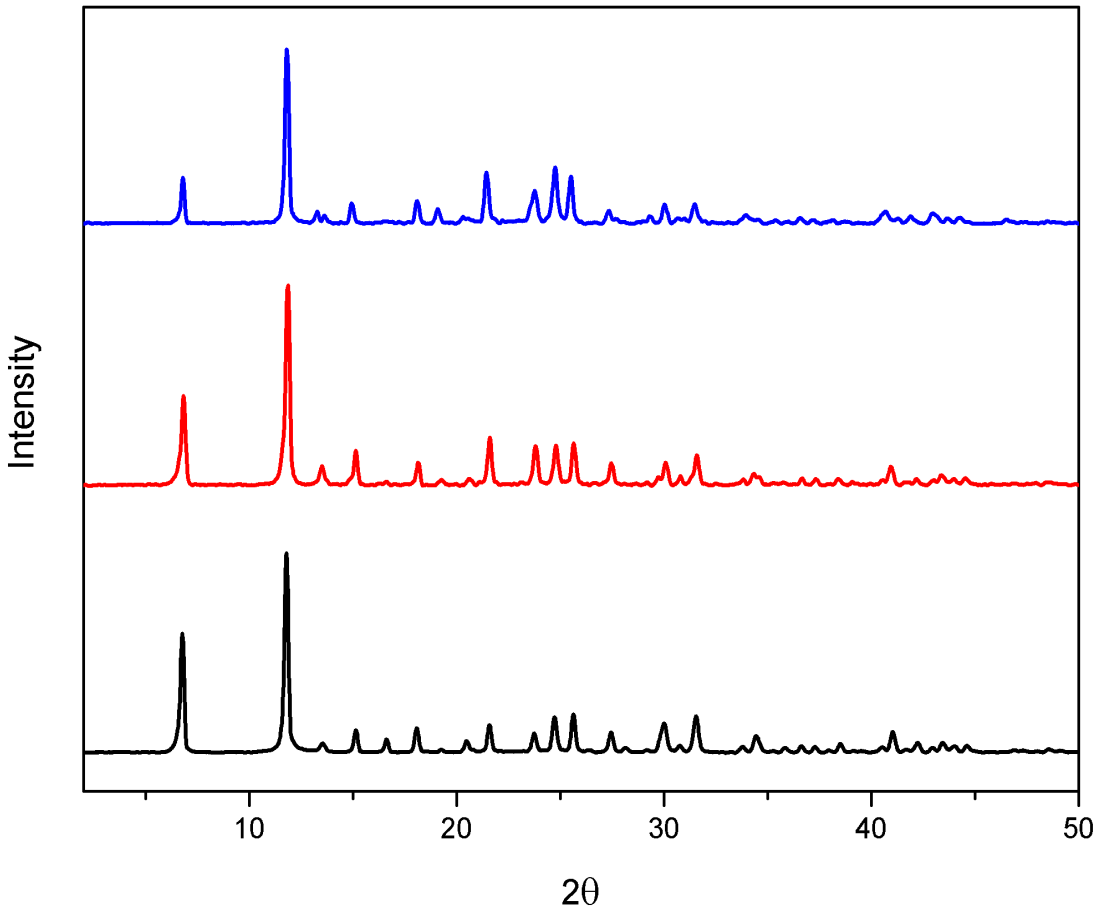

Figure 2.9 Powder x-ray diffraction patterns of Mg_2(DOBDC) as synthesized (bottom, black), post-synthetically modified (middle, red) and permeated with lithium tetrafluoroborate in carbonate solution (top, blue). Cu Kα radiation.

Figure 2.10 is a Nyquist plot of a single pellet conductivity measurement of this material. Measurements performed on pellets of this material from multiple preparations afforded room-temperature conductivities falling in the range 0.9-4.4 × 10^{-4} S/cm. These values are two orders of magnitude greater than the 1.8 × 10^{-6} S/cm measured for a pellet of Mg_2(DOBDC)·0.05$LiBF_4$·*x*EC/DEC, as obtained by simply soaking Mg_2(DOBDC) in a $LiBF_4$ electrolyte solution. Evaluation of the molar conductivities for these two materials shows that, in addition to increasing lithium electrolyte content by a factor of 6.8, the grafting increases molar conductivity by a factor of 25, leading to the 170-fold increase in conductivity (see Table 2.1). Note that it is not possible to resolve grain vs. grain boundary conduction within a pellet by examination of the Nyquist plots, since only one semicircle is observed in each data set. However, the data do not form complete, regular semicircles, indicating the presence of inhomogeneities in the conduction pathway and therefore possible multiple conduction mechanisms, albeit with similar time constants.[24]

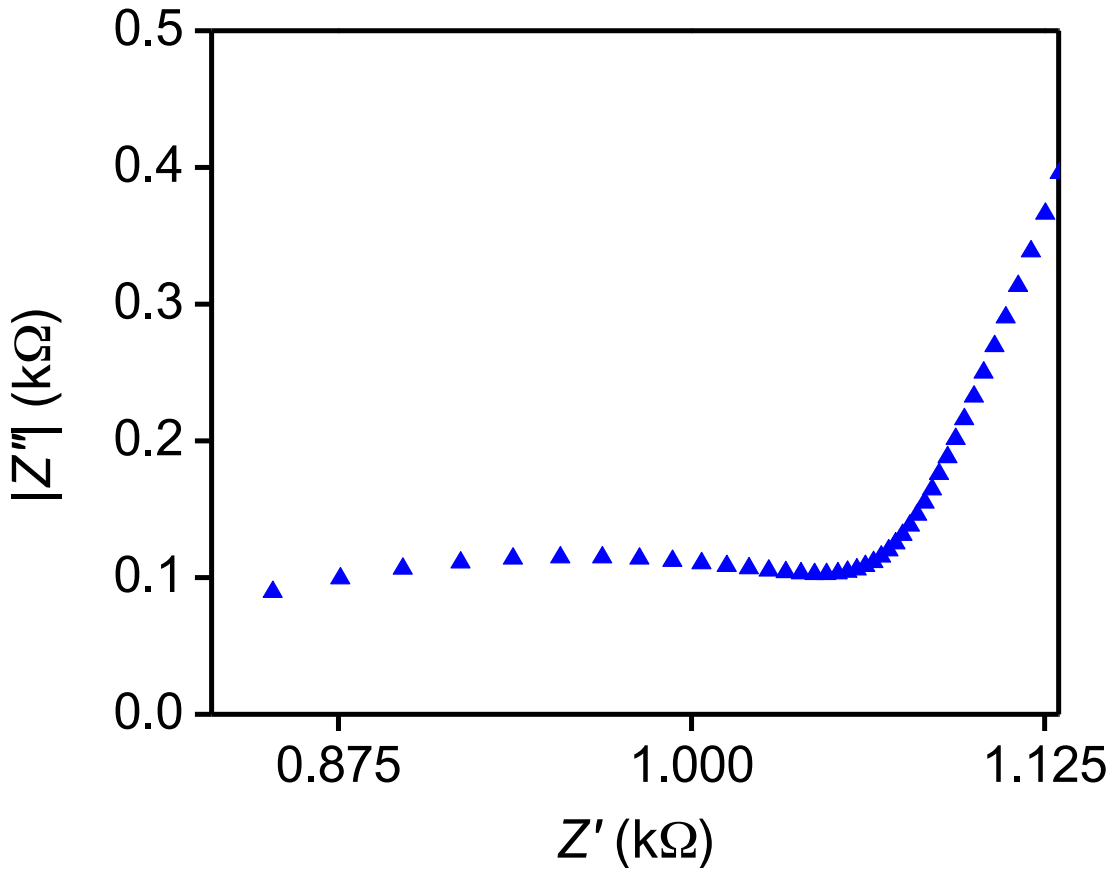

Figure 2.10 Nyquist plot of a room temperature, 2-point AC impedance measurement of a pressed pellet of Mg_2(DOBDC)·0.35LiO^{i}Pr·0.25$LiBF_4$·EC·DEC.

electrolyte loading	σ (S/cm)	c_{Li}^+ (M)	Λ_M (S·cm^{-1}M^{-1})	E_a (eV)
0.05$LiBF_4$	1.8×10^{-6}	0.19	9.6×10^{-6}	0.31
0.06LiO^{i}Pr	1.2×10^{-5}	0.23	5.2×10^{-5}	0.14
0.35LiO^{i}Pr + 0.25$LiBF_4$	3.1×10^{-4}	1.3	2.4×10^{-4}	0.15

Table 2.1 Conductivities, molar conductivities and energies of activation of Mg_2(DOBDC) based electrolytes.

Varying the temperature measurements reveal a Nernst-Einstein type activated behavior (Figure 2.11). The data indicate a low activation energy of 0.15 eV for conduction in the grafted material (Table 2.1). In contrast, a much higher activation energy of 0.31 eV is observed for the material incorporating just $LiBF_4$, suggesting a fundamental difference in the conduction mechanism. As a solid electrolyte with 10^{-4} S/cm conductivity and an activation energy of less than 0.4 eV, the new isopropoxide-grafted material can be classified as a superionic conductor.[25]

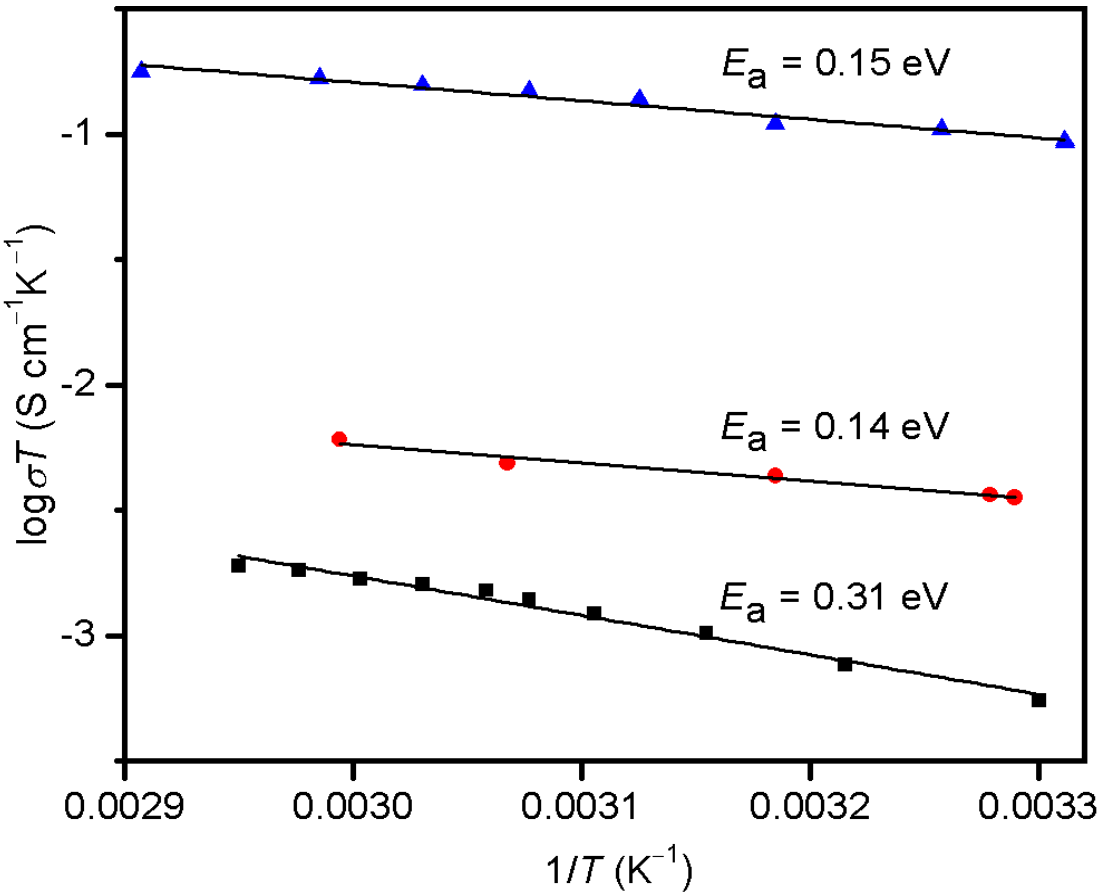

Figure 2.11 Variable temperature measurements of the used to determine energies of activation of Mg_2(DOBDC) electrolytes.

To probe the role of $LiBF_4$ in the conductivity of the metal-organic framework electrolytes, we prepared pellets of a sample of Mg_2(DOBDC) incorporating LiO^iPr and the EC/DEC solvent, but with no $LiBF_4$ added. Variation of the grafting conditions enabled preparation of Mg_2(DOBDC)·0.06LiO^iPr·xEC/DC, for which the Li^+ concentration is approximately the same as in Mg_2(DOBDC)·0.05$LiBF_4$ ·xEC/DEC. For pellets of the new isopropoxide grafted sample, a typical conductivity of 1.2×10^{-5} S/cm was obtained; however, considerable variation was observed here, with results sometimes being as low as 10^{-7} S/cm. Figure 2.12 is a Nyquist plot of a room temperature, 2-point AC impedance measurement of a pressed pellet of Mg_2(DOBDC)·0.06LiO^iPr·xEC/DC. We speculate that without the presence of additional $LiBF_4$ on the surfaces of the metal-organic framework crystallites, it may be difficult to obtain good interparticle conductivity, as well as reproducible interfacial contacts between the pressed pellet and the electrodes. This observation is consistent with other reports on the measurement of conductivities of solid electrolytes.[26] Importantly, despite the lower conductivity values, the activation energy of 0.14 eV (Table 2.1) for this sample is similar to that obtained for Mg_2(DOBDC)·0.35LiO^iPr ·0.25$LiBF_4$·EC·DEC, while the molar conductivity is five times that of Mg_2(DOBDC)·0.05$LiBF_4$ ·xEC/DEC.

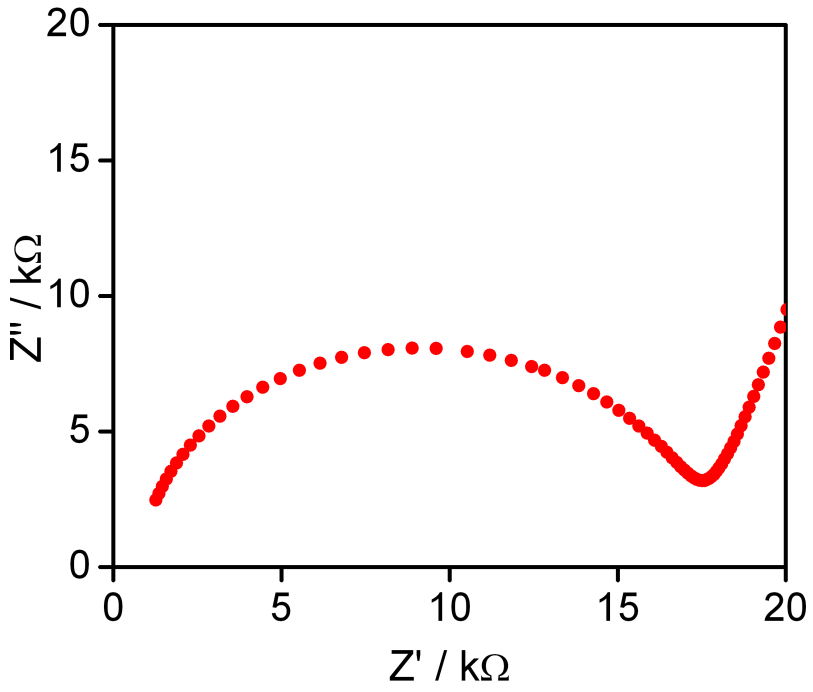

Figure 2.12 Nyquist plot of a room temperature, 2-point AC impedance measurement of a pressed pellet of $Mg_2(DOBDC)\cdot 0.06LiO^iPr\cdot xEC/DEC$.

While the impedance measurements were unable to distinguish intra- vs. interparticle conduction, a peculiarity of $Mg_2(DOBDC)$ crystallite growth provided a means of probing intraparticle conductivity. The compound can be formed as polycrystalline solid thin films in which the channel axes, along which ionic transport would be expected, are oriented normal to the film.[27] Indeed, SEM imaging showed $Mg_2(DOBDC)$ obtained to be mainly of this form (Figure 2.13), presumably grown on the surface of the 20 mL borosilicate glass vials used as reaction vessels.

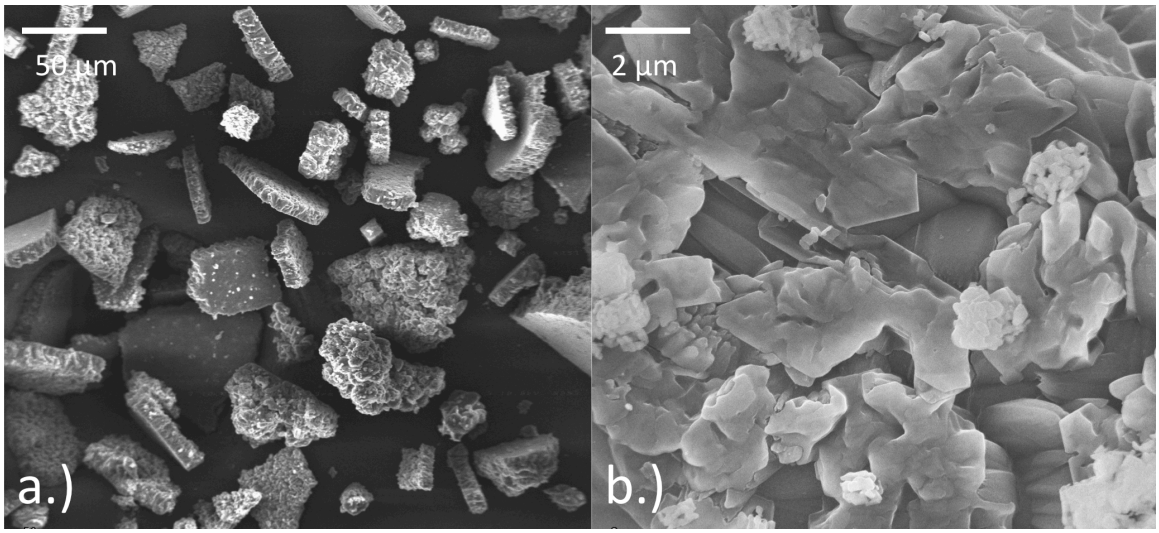

Figure 2.13 SEM micrographs of $Mg_2(DOBDC)$ (a.) on the left shows particle morphology while (b.) on the right is an image of the surface of the film. Scale bars are 50 and 2 µm, respectively.

A free-standing sheet of one of these films with the dimensions 1 mm × 2 mm × 0.4 mm was isolated and subjected to the same grafting and lithium electrolyte soaking treatment as used in preparation of the bulk solid electrolyte. Two-point AC impedance measurements (Figure 2.14) performed directly on the film revealed a conductivity of 5.5 × 10^{-5} S/cm which is of the same order of magnitude as obtained for pressed pellets of the bulk material. This result suggests that intraparticle processes rather than boundary processes dominate the conduction. It is possible that alignment of the conduction channels in the polycrystalline particles may even help to increase conductivity, since studies of lithium conductivity in polymers with anisotropic domains have revealed strong alignment and orientation effects.[28] The attainability of thin, oriented films could perhaps facilitate development of methods for processing the new solid electrolyte and integrating it within devices.

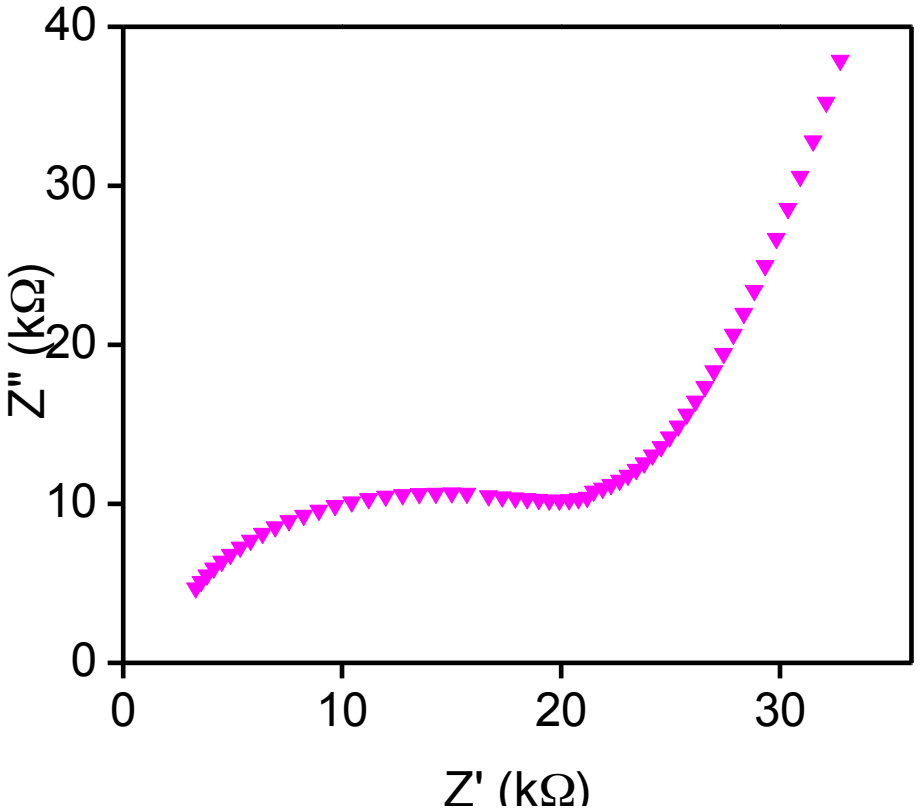

Figure 2.14 Nyquist plot of a room temperature, 2-point AC impedance measurement of a thin films of Mg_2(DOBDC)·0.35LiO^{i}Pr·0.25LiBF_4·EC·DEC.

2.4 Conclusions and Outlook

These results demonstrate a promising new approach for creating solid lithium electrolyte materials. Incorporation of a lithium alkoxide within a porous metal-organic framework with open metal centers, such as Mg_2(DOBDC), can lead to pinning of the counteranions and high ionic conductivities at ambient temperatures. The resulting

conductivity values of 10^{-4} S/cm are highly reproducible, and are at the technological limit for battery separator applications. Expansion of the framework by using elongated linkers has been demonstrated by our group[29] and allows the grafting of different anion groups and the incorporation of larger solvated multivalent cations.[30] Grafting of alkoxides to the building units of other frameworks has also been effected to make other ionically-conductive metal-organic frameworks by incorporation of the alkoxide into the inorganic building units. [31]

2.5 Acknowledgements

This research was supported by the Laboratory Directed Research and Development Program at Lawrence Berkeley National Laboratory. I thank S. Mullin, A. Teran, and S. Patel for experimental assistance and helpful discussions, and Prof. J. Newman for helpful discussions.

2.6 References

(1) (a) Nazri, G.-A.; Pistoia, G., Eds. *Lithium Batteries Science and Technology*, Kluwer Academic/Plenum, Boston, 2004. (b) Whittingham, M. S. *Chem. Rev.* **2004**, *104*, 4271.

(2) Arora, P; Zhang, Z. *Chem. Rev.* **2004**, *104,* 4419.

(3) Tarascon, J.-M.; Armand, M. *Nature* **2001**, *414*, 359.

(4) Xu, K. *Chem. Rev.* **2004**, *104,* 4303.

(5) Monroe, C.; Newman, J. *J. Electrochem. Soc.* **2005**, *152*, A396.

(6) (a) Wright, P. V. *J. Polym Sci., Phys. Ed.* **1976**, *14*, 955. (b) Armand, M. B.; Chabango, J. M.; Duclot, M. J. In *Fast Ion Transport in Solids;* Duclot M. J.; Vashishta, P.; Mundy, J. N.; Shenoy, G .K., Eds; North Holland: Amsterdam, 1979. (c) Ratner, M. A.; Shriver, D.F. *Chem. Rev.* **1988**, *88*, 109 and references therein. (d) Gadjourova, Z.; Andreev, Y.; Tunstall, D. P.; Bruce, P. G. *Nature* **2001**, *412*, 520.

(7) (a) Nagata, K. Nanno, T. *J. Power Sources* **2007**, *174*, 832. (b) Goodenough, J. B.; Kim, Y. *Chem. Mater.* **2010**, *22*, 587.

(8) (a) Eddaoudi, M.; Kim, J.; Rosi, N.; Vodak, D.; Wachter, J.; O'Keefe, M. Yaghi, O. M. *Science* **2002,** *295,* 469. (b) Matsuda, R.; Kitaura, R.; Kitagawa, S.; Kubota, Y.; Belosludov, R. V.; Kobayahi, T. C.; Sakamoto, H.; Chiba, T.; Takata, M.; Kawazoe, Y.; Mita, Y. *Nature* **2005,** *436*, 238. (c) Dincă, M.; Dailly, A.; Liu, Y.: Brown, C.M.; Neumann, D.A.; Long, J. R. *J. Am. Chem. Soc.* **2006,** *128,* 16876. (d) Sun, D.; Ma, S.; Ke, Y.; Collins, D. J.; Zhou, H.-C. *J. Am. Chem. Soc.* **2006**, *128*, 3896. (e) Kaye, S. S.; Dailly, A.; Yaghi, O. M.; Long, J. R. *J. Am. Chem. Soc.* **2007,** *129*, 14176.

(9) *(a) Allendorf, M. D.; Houk, R. J. T.; Andruszkiewicz, L.; Talin, A. A.; Pikarsky, J.; Choudhury, A.; Gall, K. A.; Hesketh, P. J. J. Am. Chem. Soc.* ***2008****, 130, 14404. (b)* Lan, A.; Li, K.; Wu, H.; Olson, D. H.; Emge, T. J.; Ki, W.; Hong, M.; Li, J. *Angew. Chem. Int. Ed.* **2009**, *48*, 2334. (c) *Lu, G.; Hupp, J. T. J. Am. Chem. Soc.* **2010**, *132*, 7832.

(10) (a) Horcajada, P.; Serre, C.; Maurin, G.; Ramsahye, N.A.; Balas, F.; Vallet-Regí, M.; Sebban, M.; Taulelle, F.; Férey, G. *J. Am. Chem. Soc.* **2008**, *130,* 6774. (b)

Rieter, W. J.; Pott, K. M.; Taylor, K. M. L.; Lin, W. *J. Am. Chem. Soc.* **2008**, *130*, 11584.

(11) (a) Seo, J.S.; Whang, D.; Le, H. Jun, S. I.; Oh, J.; Jeon, Y. J.; Kim, K. *Nature* **2000**, *404*, 982. (b) Wu, C.-D.; Hu, A.; Zhang, L.; Lin, W. *J. Am. Chem. Soc.* **2005**, *127*, 8940. (c) Cho, S.-H.; Ma, B.-Q.; Nguyen, S. T.; Hupp, J. T.; Albrecht-Schmitt, T. E. *Chem. Commun.* **2006**, 2563. (d) Horike, S.; Dincă, M.; Tamaki, K.; Long, J. R. *J. Am. Chem. Soc.* **2008**, *130*, 5854. (e) Garibay, S.; Cohen, S. M. *Inorg. Chem.* **2010**, *49*, 8086.

(12) (a) Park, Y. K.; Choi, S. B.; Kim, H.; Kim, K.; Won, B. H.; Choi, K.; Choi, J. S.; Ahn, W. S.; Won, N.; Kim, S.; Jung, D. H.; Choi, S. H.; Kim, G. H.; Cha, S. S.; Jhon, Y. H.; Yang, J. K.; Kim, J. *Angew. Chem., Int. Ed.* **2007**, *46*, 8230. (b) White, K. A.; Chengelis, D. A.; Gogick, K. A.; Stehman, J.; Rosi, N. L., Petoud, S. *J. Am. Chem. Soc.* **2009**, *131*, 18096.

(13) (a) Takaishi, S.; Hosoda, M.; Kajiwara, T.; Miyasaka, H.; Yamashita, M.; Nakanishi, Y.; Kitagawa, Y.; Yamaguchi, K.; Kobayashi, A.; Kitagawa, H. *Inorg. Chem.* **2008**, *48*, 9048. (b) Kobayashi, Y.; Jacobs, B.; Allendorf, M. D.; Long, J. R. *Chem. Mater.* **2010**, *22*, 4120. (c) Okubo, T.; Tanaka, N.; Kim, H. K.; Anma, H.; Seki, S.; Saeki, A.; Maekawa, M.; Kuroda-Sowa, T. *Dalton Trans.,* **2011**, *40,* 2218.

(14) (a) Bureekaew, S. Horike, S.; Higuchi, M.; Mizuno, M.; Kawamura, T.; Tanka, D.; Yanai, N.; Kitagawa, S. *Nat. Mater.* **2009**, *8*, 831. (b) Hurd, J. A.; Vaidhyanathan, R.; Thangadurai, V.; Ratcliffe, C. I.; Moudrakovski, I. L.; Shimizu, G. K. H. *Nat. Chem.* **2009**, *1*, 705. (c) Shigematsu, A.; Yamada, T.; Kitagawa, H. *J. Am. Chem. Soc.* **2011**, *133*, 2034. (d) Sadakiyo, M.; Yamda, T.; Kitagawa, H. *J. Am. Chem. Soc.* **2009**, *131*, 9906.

(15) (a) Férey, G.; Millange, F.; Morcette, M.; Serre, C.; Doublet, M.-L.; Grenèche, J.-M.; Tarascon, J.-M. *Angew. Chem. Int. Ed.* **2007**, *46*, 3259. (b) de Combarieu, G.; Morcrette, M.; Millange, F.; Guillou N.; Cabana, J.; Grey, C. P.; Margiolaki, I.; Férey, G.; Tarascon J.-M. *Chem. Mater.* **2009**, *21*, 1602. (c) Mulfort, K. L.; Wilson, T. M.; Wasielewski, M. R.; Hupp, J. T. *Langmuir* **2009**, *25*, 503.

(16) (a) Vitadello, M. Suarez, S.; Chung, S. H.; Fujimoto, K.; Di Noto, V.; Greenbaum, S. G.; Furukawa, T. *Electrochim. Acta.* **2003**, *48*, 2227. (b) Xi, J.; Bai, Y.; Qiu, X.; Zhu, W.; Chen, L. Tang, X. *New J. Chem.* **2005**, *29*, 454.

(17) (a) Krogh Andersen, E.; Krogh Andersen, I. G.; Metcalf-Johansen, J.; Simonsen, K. E.; Skou, E. *Solid State Ionics* **1988**, *28,* 249. (b) Ben Saad, K.; Hamzaouhi, H.; Mohamed, M. M. *Mat. Sci Eng. B.* **2007**, *139*, 226.

(18) Chae, H. K.; Siberio-Pérez, D. Y.; Kim, J.; Go, Y.; Eddaoudi, M.; Matzger, A.; O'Keefe, M.; Yaghi, O. M. *Nature* **2004**, *427*, 523.

(19) Demessence, A.; D'Alessandro, D. M.; Foo, M. L.; Long, J. R. *J. Am. Chem. Soc.* **2009**, *131*, 8784.

(20) Caskey, S. R.; Wong-Foy, A. G.; Matzger, A. J. *J. Am. Chem. Soc.* **2008**, *130*, 10870.

(21) (a) Morris, W.; Doonan, C. J.; Furukawa, H.; Banerjee, R.; Yaghi, O. M. *J. Am. Chem. Soc.* **2008**, *130*, 12626. (b) Wang, Z., Tanabe, K. K., Cohen, S.M. *Inorg. Chem.* **2009**, *48*, 296. (c) Gadzikwa, T.; Farha, O. K.; Malliakas, C. D.;

Kanatzidis, M. G.; Hupp, J. T.; Nguyen, S. T. *J. Am. Chem. Soc.* **2009**, *131*, 13613.
(22) Jung, H.S.; Lee, J.-K.; Kim, J.-Y.; Hong, K.S. *J. Colloid Interface Sci.* **2003**, *259*, 127.
(23) (a) Cazzanelli, E.; Croce, F.; Appetecchi, G. B.; Benevelli, F.; Mustarelli, P. *J. Phys Chem.* **1997***, 107*, 5740. (b) Soetens, J.-C.; Millot, C.; Maigret, B. *J. Phys. Chem. A.* **1998**, *102*, 1055.
(24) Hasbach, A.; Retter, U.; Siegler, K.; Kautek, W. *J. Electronal. Chem.* **2004**, *561*, 29.
(25) (a) Chandra S. *Superionic Solids* North-Holland, Amsterdam, 1981. (b) Colomban, P.; Novak, A. *J. Molec. Struct.* **1988**, *177*, 277.
(26) Barpanda, P.; Chotard, J.-N.; Delacourt, C.; Reynaud, M.; Filinchuk, Y.; Armand, M.; Deschamps, M.; Tarascon, J.-M. *Angew. Chem. Int. Ed.* **2011**, *50*, 2526.
(27) Bétard, A.; Zacher, D.; Fischer, R. A. *CrystEngComm* **2010**, *12*, 3768.
(28) Singh, M.; Odusanya, O.; Wilmes, G. M.; Eitouni, H. B.; Gomez, E. D.; Patel, A. J.; Chen, V. L.; Park, M. J.; Fragoui, P.; Iatrou, H.; Hadjichristidis, N.; Cookson, D.; Balsara, N. P. *Macromolecules* **2007**, *40,* 4578.
(29) McDonald, T. M.; Lee, W. R.; Mason, J. A.; Wiers, B. M.; Hong, C. S.; Long, J. R. *J. Am. Chem. Soc.* **2012**, *134*, 7056.
(30) Aubrey, M. L.; Ameloot, R.; Wiers, B. M.; Long, J. R. *Energy Environ. Sci.* **2014**, *7*, 667.
(31) Ameloot, R.; Aubrey, M.; Wiers, B. M.; Gomora-Figueroa, A. P.; Patel, S. N.; Balsara, N. P.; Long, J. R. *Chem. Eur. J.* **2013**, *19*, 5533.

Chapter 3:The Synthesis and Reduction of a Metal-Organic Framework, $K_xFe_2(BDP)_3$ (x = 0-2)

3.1 Introduction

Metal-organic frameworks are a class of materials built of inorganic clusters or chains bridged by organic linkers to form open, crystalline, three-dimensional networks that display high surface areas and permanent porosity.[1] They have been most heavily investigated for their gas sorption properties,[2-4] but also for catalysis,[5] biomedical applications,[6] sensing,[7] energy transfer,[8] and proton conductivity.[9] Although electronic conduction in metal-organic frameworks could expand their applications to areas such as electrochemical energy storage, photovoltaics, thermoelectrics, photocatalysis, and electrocatalysis, charge transport in metal-organic frameworks has only recently begun to be explored. Electronic conductivity has been demonstrated in metal-organic frameworks by incorporating electron donor units in the bridging ligand to obtain conductive π-stacked chains in the structure of the framework[10] as well as by adding organic electron acceptors to the pores of an intrinsically insulating metal-organic framework to form a network for electronic transport.[11] Another strategy to engender conductivity in metal-organic frameworks is to use the metal-ligand bond as a conduction pathway. To achieve this it is necessary to use redox-active metal ions and bridging ligands that facilitate electron transfer by forming covalent metal-ligand bonds that maximize metal-ligand orbital overlap. By selection of metal ions with accessible redox couples followed by post-synthetic oxidation or reduction, it is possible to alter the conductivity of metal-organic frameworks. The framework Cu[Ni(pyrazine-2,3-dithiolate)$_2$], utilizes a readily accessible and reversible [Ni(pyrazine-2,3-dithiolate)$_2$]$^{2-/1-}$ couple and demonstrates a thin film conductivity that rises from 10^{-8} to 10^{-4} S/cm after exposure to iodine vapor.[12]

Studies of mixed-valence bimetallic complexes demonstrate the best electronic delocalization with metals that have $d^{5/6}$ electronic configurations with octahedral geometries, bridged by nitrogen donor, π-acid ligands. This situation maximizes metal-ligand π-orbital overlap and minimizes the bond differences of the two redox states and thus reorganization energy upon electron transfer.[13] The framework, Fe(1,2,3-triazolate)$_2$, built of triazolate-bridged octahedral Fe^{2+} ions, displays a pressed pellet conductivity of 10^{-4} S/cm that increases to 10^{-3} S/cm upon exposure to iodine vapor.[14] I sought to make a framework bridged by pyrazolate bridged ferric ions that could be partially reduced to make a conductive, mixed-valence metal-organic framework. Choosing the 1,4-benzenedipyrazolate linker I was able to obtain a ferric-pyrazolate metal-organic framework, $Fe_2(BDP)_3$. The effect of reduction on the electronic structure of this system was probed by UV-VIS-NIR diffuse reflectance and FT-IR spectroscopies and indicated that $Fe_2(BDP)_3$ is a semiconductor and electronic delocalization upon reduction. FP-TRMC experiments demonstrate that $Fe_2(BDP)_3$ is as produced conductive, and that total charge mobility increases with reduction, with a peak value of μ_{tot} = 0.29 cm^2/V·s at $K_{0.8}Fe_2(BDP)_3$.

3.2 Experimental

General Considerations Unless otherwise specified, all manipulations were performed with rigorous exclusion of air and water by use of inert atmosphere (Ar/N_2) glove boxes and Schlenk techniques. Reagents were purchased from commercial vendors and used without further purification. *N,N*-dimethylformamide (DMF), methanol, and tetrahydrofuran were deoxygenated by purging with argon for 1 h and dried using a commercial solvent purification system designed by JC Meyer Solvent Systems. Inductively coupled plasma optical emission spectroscopy (ICP-OES) was performed on a Perkin Elmer Optima 7000 DV ICP-OES in the Department of Chemistry at the University of California, Berkeley. EDS spectra were taken using a JEOL JSM-6340F field emission scanning electron microscope equipped with an EDAX Falcon detector. EDS data were collected from the K K and the Fe K peaks of a 40 μm × 40 μm area for each sample at 20 kV and analyzed using the software's true standardless-quantification mode. The ratios determined from the bulk aliquots were used to estimate the degree of reduction of single crystal devices.

Sealed Tube Synthesis of $Fe_2(BDP)_3$ $Fe(acac)_3$ and H_2BDP were synthesized according to previously reported preparations.[15,16] 0.302 g (0.855 mmol) of $Fe(acac)_3$ was combined with 0.060 g (0.285 mmol) of H_2BDP and 2 ml DMF in a ½" outer diameter borosilicate tube. The reaction mixture was freeze-pump-thawed 5 times with liquid nitrogen and then flash-frozen and evacuated. The evacuated sealed tube was flame sealed and placed in an tube furnace and heated to 150 ^oC at a 0.1^oC/min ramp rate and held at that temperature for 4000 minutes. The sample was cooled to room temperature and the vial was opened. The black, microcrystalline solid was collected on a Buchner funnel and washed with *N*,*N*-DMF. This material was used for x-ray powder diffraction structure solution.

Bulk Synthesis of $Fe_2(BDP)_3$ A 100 ml Schlenk flask was charged with 6.04 g (17.1 mmol) of $Fe(acac)_3$, 1.20 g (5.71 mmol) of H_2BDP and a magnetic stir bar. 80 mL of dry, degassed DMF was added to the Schlenk flask via cannula transfer. The reaction was refluxed under nitrogen for 18 hours. The black microcrystalline precipitate was collected on a Buchner funnel. This material was heated in dimethyl sulfoxide (DMSO) at 100 °C for 8 hours, and the DMSO was decanted. The material was then washed 5 more times with heated DMSO and similarly six more times with DMF heated to 100 degrees C and six more times with methylene chloride heated to 70 °C. This washing procedure removes unreacted ligands, metal sources, polymerization products of DMF and solvents from previous washes. The material is then heated under 10 mTorr vacuum to 180 °C for 24 hours to remove guest solvent molecules. FT-IR: (solid, ATR): $\nu_{C=C}$ 1576, $\nu_{C=N}$ 1384, 1342 cm^{-1}. An aliquot of the activated sample was then soaked in DMSO, filtered, dried in air and then examined by TGA and CHN analysis. The 16% weight-loss observed at 150 °C was consistent with a formulation of $Fe_2(BDP)_3$•1.75DMSO which was in agreement with CHN analysis. Anal. Calcd. for $Fe_8C_{158}H_{138}N_{48}S_7O_7$: C, 54.23; H, 4.18; N, 19.21. Found: C, 54.73; H, 3.82; N, 18.73.

Bulk Reduction of Fe_2BDP_3 0.1M solution of potassium naphthalenide, with a 10% molar excess of naphthalene in THF was prepared immediately before use. Weighed aliquots of activated $Fe_2(BDP)_3$ were suspended in 10 ml of THF with magnetic stirring.

Measured amounts of potassium naphthalenide solution was then added to the $Fe_2(BDP)_3$ suspensions to target desired stoichiometries. The potassium naphthalenide was not added all at once, but rather in three to four portions over the course of 1-2 hours as the suspensions were stirred. The suspensions with the added potassium naphthalenide solutions were stirred overnight. The solid was then collected and repeatedly washed with tetrahydrofuran until the THF washes showed no more presence of naphthalene. PXRD measurements showed the preservation of crystallinity and potassium to iron ratios were confirmed by ICP-OES and EDX.

Low Pressure Gas Adsorption Measurements For all gas adsorption measurements 200-225 mg of $Fe_2(BDP)_3 \cdot 1.75$ DMSO was transferred to a pre-weighed glass sample tube under an atmosphere of nitrogen and capped with a Transeal. Samples were then transferred to Micromeritics ASAP 2020 gas adsorption analyzer and heated at a rate of 1 °C /min from room temperature to a final temperature of 180 °C. Samples were considered activated when the outgas rate at 150 °C was less than 2 μbar/min, which occurred near 48 hours after the start of evacuation. Evacuated tubes containing degassed samples were then transferred to a balance and weighed to determine the mass of sample. The tube was transferred to the analysis port of the instrument where the outgas rate was again determined to be less than 2 μbar/min at 180 °C. 99.999% purity gas was used for nitrogen adsorption.

Powder X-ray Diffraction Structure Solution of $Fe_2(BDP)_3$ Microcrystalline samples of solvated $Fe_2(BDP)_3$ were gently ground and deposited in an aluminum sample holder equipped with a zero-background plate. Diffraction data was collected by means of an overnight scan in the 2θ range of 5–105° with 0.02° steps using a Bruker AXS D8 Advance diffractometer equipped with Ni-filtered Cu- α radiation (λ = 1.5418 Å), a Lynxeye linear position-sensitive detector, and mounting the following optics: primary beam Soller slits (2.3°), fixed divergence slit (0.3°), receiving slit (8 mm). The nominal resolution for the set-up is 0.08° of 2θ (FWHM of the α_1 component) for the LaB_6 peak at about 2θ = 21.3°. The generator was set at 40 kV and 40 mA. In order to get higher resolution data, a powder pattern was also collected on a powder diffractometer of the Institute of Crystallography of the Italian CNR in Bari, that is equipped with a primary beam Ge(111) monochromator, Cu-Kα radiation in Debye-Scherrer geometry (glass capillary diameter: 0.5 mm), and an INEL CPS-120 position sensitive detector covering a 120° 2θ range. (The courtesy of Giuseppe Chita, IC-CNR, is acknowledged for technical assistance).

A standard peak search, followed by indexing through the Single Value Decomposition approach, as implemented in TOPAS-Academic[17] allowed the determination of approximate unit cell parameters. The space group was assigned as *Fddd* on the basis of systematic absences. The unit cell and space group were checked by a Le Bail refinement and confirmed by successful structure solution and Rietveld refinement. The structure solution of Fe2(BDP)3 was performed using the simulated annealing technique, as implemented in TOPAS. Initially, a rigid, idealized model was employed for the crystallographically independent portions of the BDP^{2-} moiety (one full and one half ligands). To build the rigid model describing BDP^{2-}, the following bond distances and angles have been adopted: a) for the benzene ring: C–C = 1.39 Å; C–H = 0.95 Å; C–C–C, C–C–H = 120°; b) C–C, C–N, N–N = 1.36 Å; C–H = 0.95 Å; internal ring angles = 108°; C–C–H = 126°; Cbenzene–Cpyrazole = 1.45 Å. After the initial

structure solution, the phenylene-pyrazole torsion angle was allowed to refine. Residual electron density in the channels was modeled as a disordered dimethylformamide (DMF) solvent molecule. The final refinement was performed using the Rietveld method, maintaining the rigid bodies introduced at the structure solution stage. The background was modeled by a polynomial function of the Chebyshev type. Peaks shapes were described by the Fundamental Parameters Approach.[18] Anisotropic peak broadening was modeled using spherical harmonics to define the peak widths. A single refined isotropic thermal parameter was assigned to the Fe atom, and this was augmented by 2.0 $Å^2$ for the atoms of the BDP^{2-} ligand and by 4.0 $Å^2$ for the atoms of the DMF molecule. Note that in the final Rietveld refinements, both collected X-ray diffraction patterns were used as independent observations of different information content and were employed simultaneously during model refinement.

Crystal data for $Fe_2(BDP)_3$ at 298 K: $Fe_2(C_{12}N_4H_8)_3(C_3H_7NO)_{0.5}$; orthorhombic, *Fddd*, a = 7.1046(2), b = 26.4943(5), c = 45.3489(9) Å, V = 8536.1(4) $Å^3$, R_{wp} = 0.026; R_p = 0.017; R_{Bragg} = 0.012. Metrical data for the solid-state structure of $Fe_2(BDP)_3$ is available free of charge from the Cambridge Crystallographic Data Centre under reference number CCDC 915106.

Synchotron PXRD and Indexing of of $K_xFe_2(BDP)_3$ Synchrotron x-ray diffraction (XRD) measurements were carried out on Beamline 1-BM-C (l = 0.6161 Å) at room temperature or 11-BM (l = 0.413751 Å) at 100 K at the Advanced Photon Source at Argonne National Laboratory. Samples of $K_xFe_2(BDP)_3$ at different levels of reduction were loaded into quartz capillaries inside a helium glove box for all XRD measurements. X-ray diffraction experiments at the University of California, Berkeley (UCB) were collected with 0.02° steps using a Bruker AXS D8 Advance diffractometer equipped with Cu-Ka radiation (l = 1.5418 Å), a Göbel mirror, a Lynxeye linear position-sensitive detector, and mounting the following optics: fixed divergence slit (0.6 mm), receiving slit (3 mm), and secondary beam Soller slits (2.5°). The generator was set at 40 kV and 40 mA.

A standard peak search, followed by indexing via the Single Value Decomposition approach, as implemented in TOPAS-Academic,[17] allowed the determination of approximate unit cell dimensions. Precise unit cell dimensions were determined by performing a structureless Le Bail refinement in TOPAS-Academic. Note that all samples were solvated.

FT-IR Spectra were recorded on a Perkin Elmer Spectrum 400 FTIR spectrophotometer equipped with an attenuated total reflectance accessory. A dinitrogen purged glove bag was attached to the attenuated total reflectance accessory to allow air- and water-free measurements of spectra.

UV−visible−NIR Diffuse Reflectance Spectra were collected using a CARY 5000 spectrophotometer interfaced with Varian Win UV software. The samples were held in a Praying Mantis air-free diffuse reflectance cell. PVDF powder was used as a non-absorbing matrix. The Kubelka−Munk conversion, $F(R)$ vs wavenumber, of the raw diffuse reflectance spectrum (R vs wavenumber) was obtained by applying the formula $F(R) = (1 - R)^2/2R$. It must be noted that this transform creates a linear relationship for the spectral intensity relative to sample concentration and assumes that the sample is infinitely diluted in the nonabsorbing matrix, that the sample layer is infinitely thick, and that the sample has a constant scattering coefficient. The K.M.

function *F(R)* is directly proportional to absorbance. Band gaps were determined by the method of Tauc.[19]

Flash Photolysis Time-Resolved Microwave Conductivity (FP-TRMC) Measurements. FP-TRMC measurements were conducted at 25 ºC under N_2 atmosphere, using $Fe_2(BDP)_3$/poly(methylmethacrylate) (PMMA) films (50/50 in wt%). The films were cast onto quartz substrates. The microwave power and frequency were set at 3mW and ~9.1 GHz, respectively. Charge carriers were generated in the films by direct excitation of MOFs using a third harmonic generation (λ = 355 nm) light pulses from a Nd: YAG laser (Spectra Physics, INDI-HG). The excitation density was tuned at 6.5×10^{15} photons cm^{-2} per pulse. The TRMC signal from a diode was recorded on a digital oscilloscope (Tektronix, TDS 3032B). To determine the quantum efficiency of charge carrier generation the $Fe_2(BDP)_3$/PMMMA films were deposited on gold interdigitated electrodes (electrode separation = 5 μm) and the photocurrent was measured upon irradiation with a 355 nm pulse. The integrated photocurrent of a standard sample of poly(9,9-dioctylfluorene) with a measured ϕ value of 2.3×10^{-4} (determined by transient absorption spectroscopic measurements) was measured. Comparison of the integrated photocurrents with the polymer standard allowed determination of the quantum efficiency of charge carrier generation in the $K_xFe_2(BDP)_3$ samples.

3.3 Results and Discussion

I obtained $Fe_2(BDP)_3$ from the reaction of ferric acetylacetonate with the ligand H_2BDP (BDP^{2-} = 1,4-benzenedipyrazolate^{2-}) with DMF at 150 ^oC to obtain a black microcrystalline powder. It is constructed of one-dimensional chains of μ^2-pyrazolate-bridged Fe^{3+} octahedra that run along the [001] direction. These chains are in turn bridged by the phenylene rings of the 1,4-benzenedipyrazolate^{2-} linker to form a three-dimensional structure with triangular channels (Figure 3.1A-B). The Fe^{3+} octahedra are distorted, with three Fe···N bond distances; 2.02Å, 1.98Å, and 1.94Å (Figure 3.1D). This material displays thermal stability up to 290 ^oC and retains crystallinity from pH = 0-14 at room temperature and from pH = 2-13 at 100 ^oC. Figure 3.1 is an image of the structure of $Fe_2(BDP)_3$ as well as the one-dimensional building unit and the synthetic scheme for its reduction described below. Table 3.1 gives selected bond distances and angles of $Fe_2(BDP)_3$.

	Distance		Angle
Fe-N1x	1.98 Å	N1x-Fe-N2	7°
Fe-N2	2.04 Å	N1x-Fe-N2’	92.5°
Fe-N1	1.94 Å	N1x-Fe-N1	81.2°
Fe···Fe (vertex to vertex)	13.25 Å	N1x-Fe-N1’	88.9°
Fe···Fe (nearest neighbor)	3.85 Å	N1-Fe-N2	91.6°
		Fe-N1x-N1x	123.1°
		Fe-N2-N1	115.6°
		Fe-N1-N2	131.0°

Table 3.1 Selected bond distances and angles of $Fe_2(BDP)_3$. Typical estimated standard deviations are 0.01 Å for bond distances and 0.1° for bond angles.

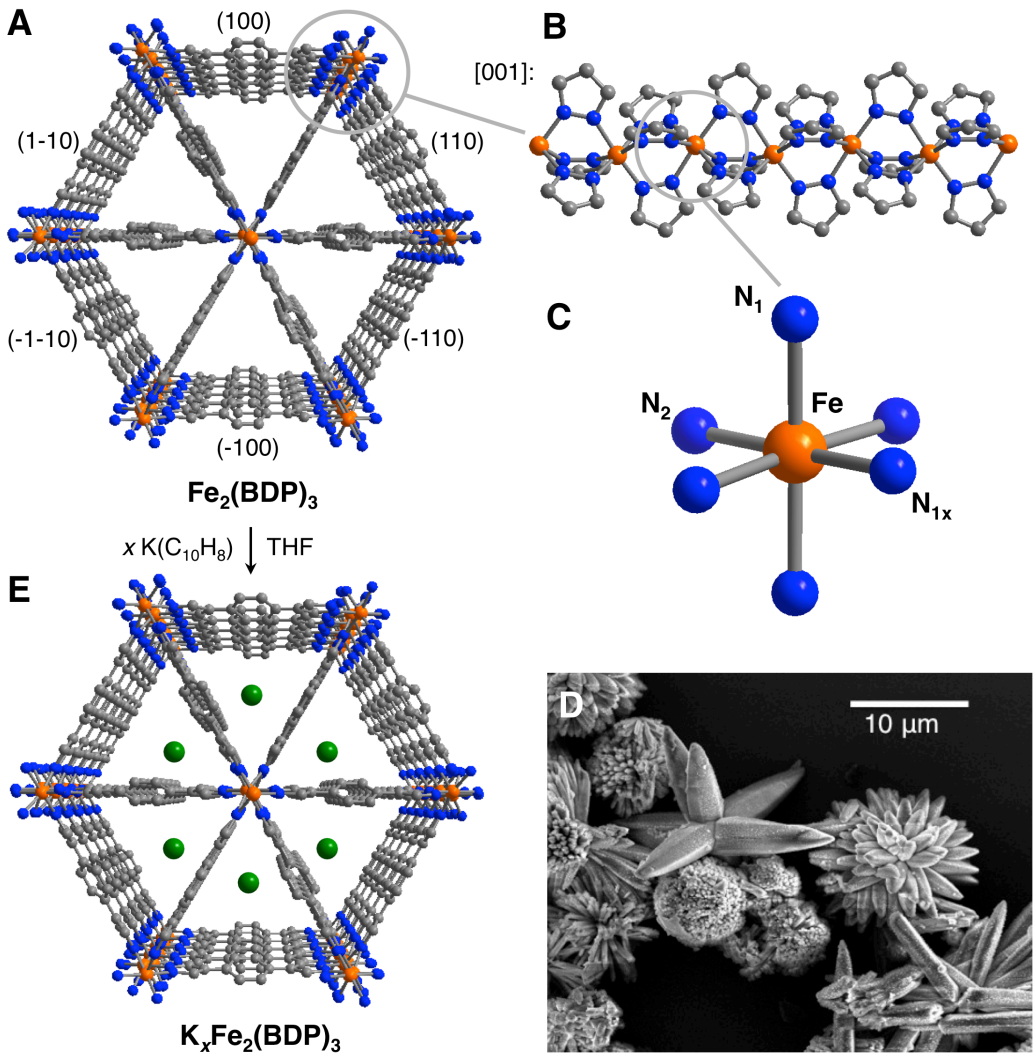

Figure 3.1 The structure of $Fe_2(BDP)_3$ (A), the one-dimensional chains of μ^2-pyrazolate-bridged ferric ions that run down the [001] direction (B), the octahedral Fe^{3+} ions with atom labels described (C), an SEM micrograph of the polydisperse microcrystallites it is obtained as (D), and a scheme for the chemical reduction of $Fe_2(BDP)_3$ with potassium naphthalenide to obtain $K_xFe_2(BDP)_3$ (E).

Pyrazolate-based metal-organic frameworks have been noted for their high chemical and thermal stability as a result of the strong metal-ligand bond due to the high pK_a of pyrazoles.[15,20,21] The chemical and thermal stability of $Fe_2(BDP)_3$, formed of a trivalent metal-ion coordinated to six pyrazolate rings in a rigid structure is even greater than previously reported pyrazolate metal-organic frameworks built of divalent ions. This framework is stable from pH =0-12 in room temperature aqueous solutions and from pH =2-10 at 100°C solutions and maintains crystallinity to 350°C in air. Figures 3.2 and 3.3 show the chemical and thermal stability of $Fe_2(BDP)_3$ in these conditions as demonstrated by powder x-ray diffraction experiments.

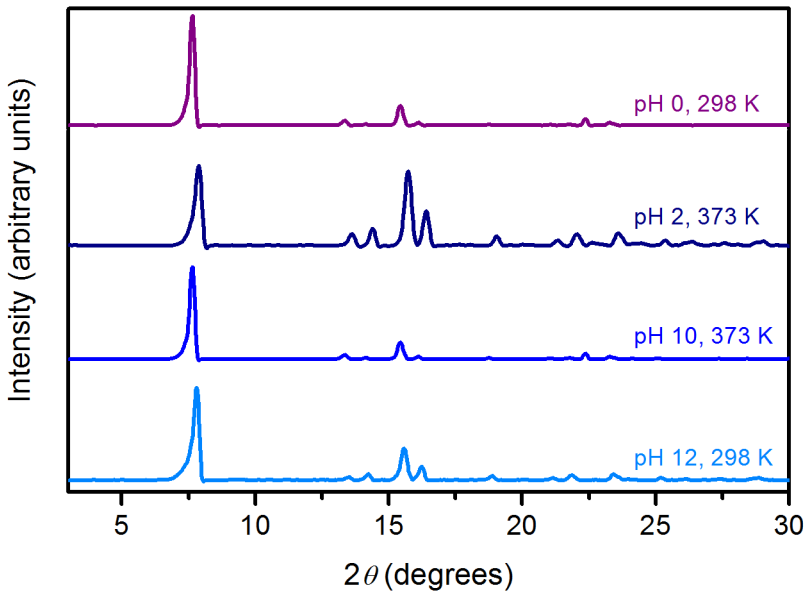

Figure 3.2 X-ray powder diffraction patterns of $Fe_2(BDP)_3$ after 14 day soaking in 10 mL of pH 0 and pH 14 water at 298 K and pH 2 and pH 10 water at 398 K. Cu Ka radiation.

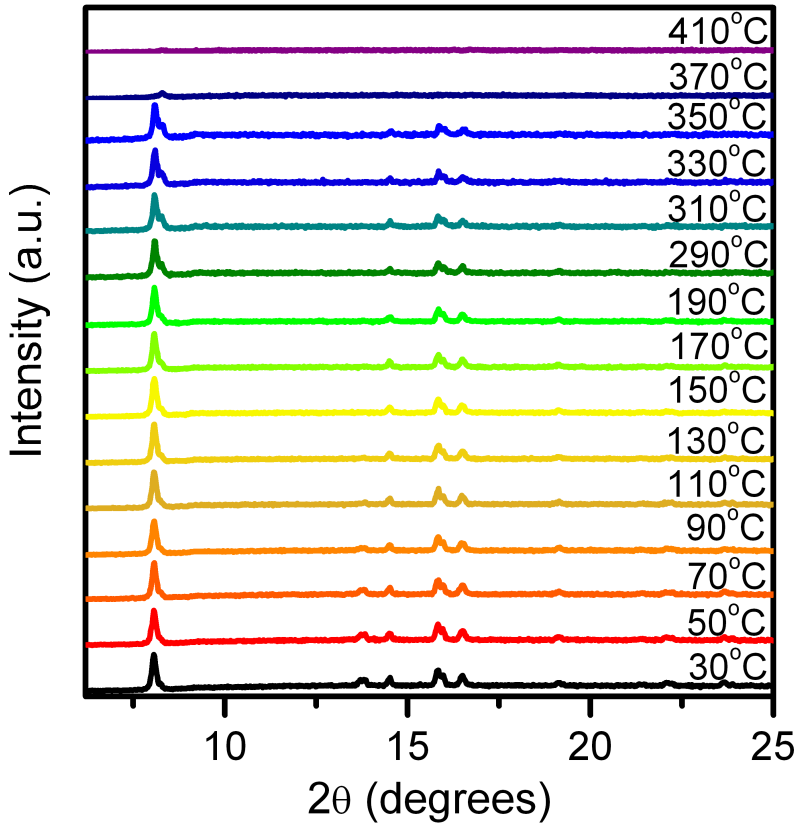

Figure 3.3 X-ray powder diffraction patterns of $Fe_2(BDP)_3$ collected at various temperatures in air.

I reasoned that I could exploit the tremendous chemical stability of $Fe_2(BDP)_3$ to effect its post-synthetic reduction. The M(OH)(BDC) framework series, built of trivalent and tetravalent metal ions are noted for the stability due to their rigid one-dimensional linkers built of high-valent metal-ions. Electrochemical reduction of the ferric framework Fe(OH)(1,4-BDC)[22] has been demonstrated, as has the chemical reduction of V(O)BDC with cobaltocenes[23,24] to obtain mixed valent V^{3+}/V^{4+} compounds. Ligand based reduction of metal-organic frameworks with lithium metal has also been claimed, although the reducing species is unclear.[25] It was envisioned that partial reduction of the Fe^{3+} ions would yield a conductive, mixed-valence metal-organic framework, where the chains of pyrazolate-bridged irons would provide a pathway for electron transfer, while the pores of the framework would accommodate stoichiometric intercalation of charge-balancing cations. I was able to reduce $Fe_2(BDP)_3$ with potassium naphthalenide to obtain the range of compositions $K_xFe_2(BDP)_3$ (x = 0-2) (see Figure 3.1E). Unit cell parameters of the reduced frameworks are given in Table 3.2, while Figure 3.4 shows the powder x-ray diffraction patterns of $K_xFe_2(BDP)_3$. BET fits of 77 K N_2 adsoption isotherms of activated $Fe_2(BDP)_3$ reveal a surface area of 1230 m^2/g which decreases to 610 m^2/g and 478 m^2/g for activated samples of $K_{0.9}Fe_2(BDP)_3$ and $K_{1.1}Fe_2(BDP)_3$, respectively. This decrease in surface area is presumably due to the filling of the pores with potassium ions and solvent molecules not removed by activation.

x in $K_xFe_2(BDP)_3$	*a (Å)*	*b (Å)*	*c (Å)*	*V (Å)*
0	45.406(1)	26.4739(7)	7.0974(2)	8531.5(3)
0.2	45.643(8)	26.423(4)	7.0644(2)	8520(2)
0.4	45.635(6)	26.413(3)	7.0644(8)	8515(2)
0.8	45.524(6)	26.402(3)	7.0557(7)	8480(2)
0.9	45.524(6)	26.412(6)	7.103(1)	8591(3)
1.1	45.5143(7)	26.5386(4)	7.0935(1)	8568.2(2)
1.3	45.426(4)	26.438(2)	7.0547(6)	8473(1)
1.4	45.75(1)	26.431(6)	7.089(1)	8574(4)
1.7	45.344(6)	26.364(4)	7.0584(10)	8438(2)
2.0	45.799(9)	26.602(3)	7.064(1)	8607(2)

Table 3.2 Unit cell parameters of $K_xFe_2(BDP)_3$ from synchrotron radiation powder diffraction experiments.

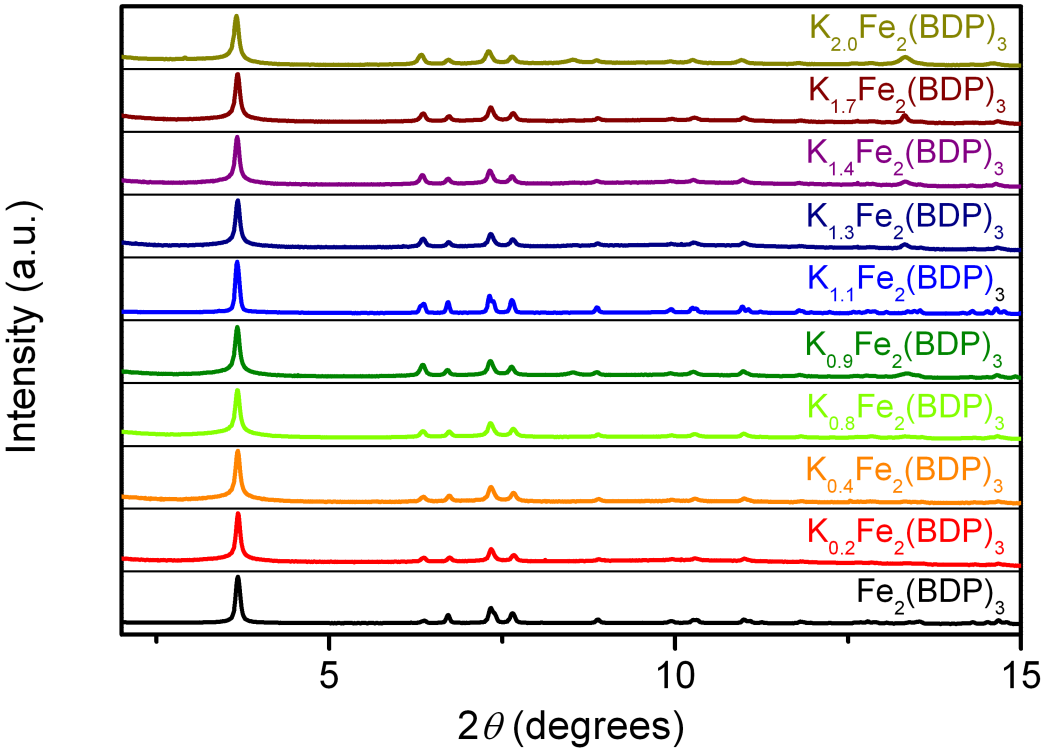

Figure 3.4 Powder x-ray diffraction patterns of $K_xFe_2(BDP)_3$ (x = 0, 0.2, 0.4, 0.8, 0.9, 1.1, 1.3, 1.4, 1.7, 2.0)

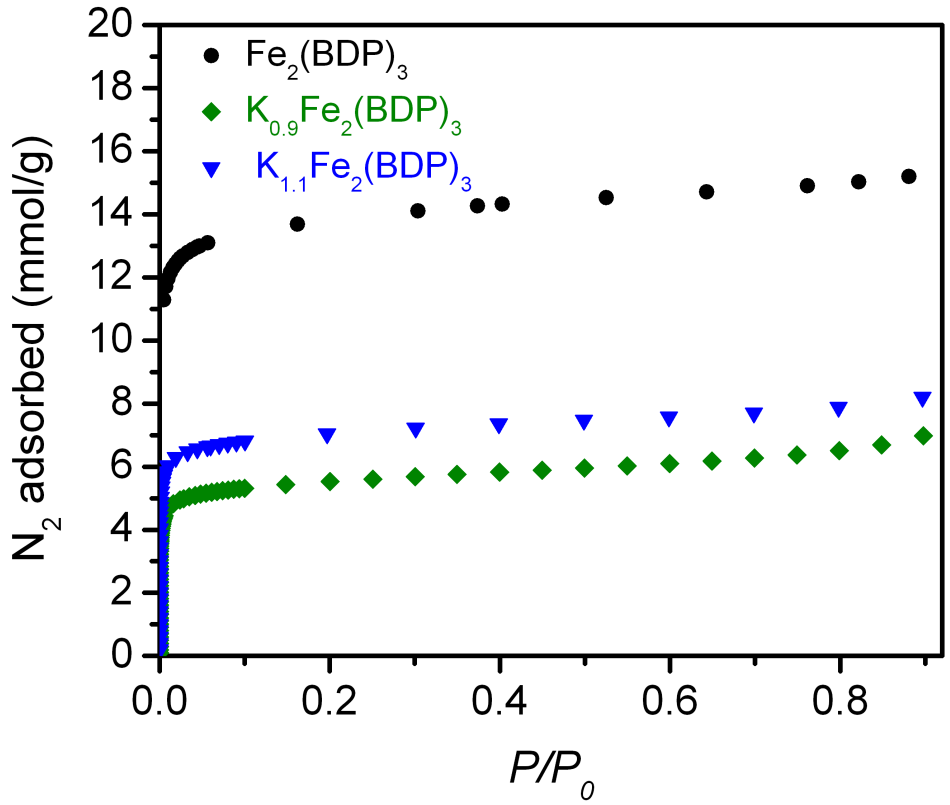

Figure 3.5 77K N_2 adsorption isotherms of $Fe_2(BDP)_3$, $K_{0.9}Fe_2(BDP)_3$ and $K_{1.1}Fe_2(BDP)_3$.

UV-Vis-NIR diffuse reflectance measurements of $Fe_2(BDP)_3$ show a broad absorption above 1.2 eV (Figure 3.6) Tauc plot analysis reveals a direct optical band gap of 1.19 eV that is maintained as the material is reduced to $K_{0.8}Fe_2(BDP)_3$. At $K_{0.9}Fe_2(BDP)_3$, the absorption band above 1.2eV is strongly diminished, and the material becomes reflective to photons with energies greater than 1.3 eV. For $K_{1.1\text{-}1.7}Fe_2(BDP)_3$, the band edge is clearly present, with calculated band gaps shifted to 1.40 - 1.49 eV and at $K_{2.0}Fe_2(BDP)_3$ the band edge shifts to 2.08 eV. A strong and broad band between 0.5 and 1.0 eV becomes clearly present upon reduction of $Fe_2(BDP)_3$ to $K_{0.8}Fe_2(BDP)_3$. This feature has the strongest relative intensity at $K_{0.94}Fe_2(BDP)_3$ with a peak energy of 0.52eV and disappears as the material is reduced to $K_{2.0}Fe_2(BDP)_3$. Because this feature is not seen in the spectra of $Fe_2(BDP)_3$ and $K_{2.0}Fe_2(BDP)_3$ but emerges at intermediate levels of reduction, it is assigned to intervalence charge transfer. Similar broad bands of similar energies are assigned to intervalence charge transfer transitions in conductive mixed-valence charge transfer salts.[26] It should be noted that oxidized polypyrrole[27] and polythiophene[2i] films show similar spectral features that are attributed to the growth of intra-band polaron and bipolaron states.

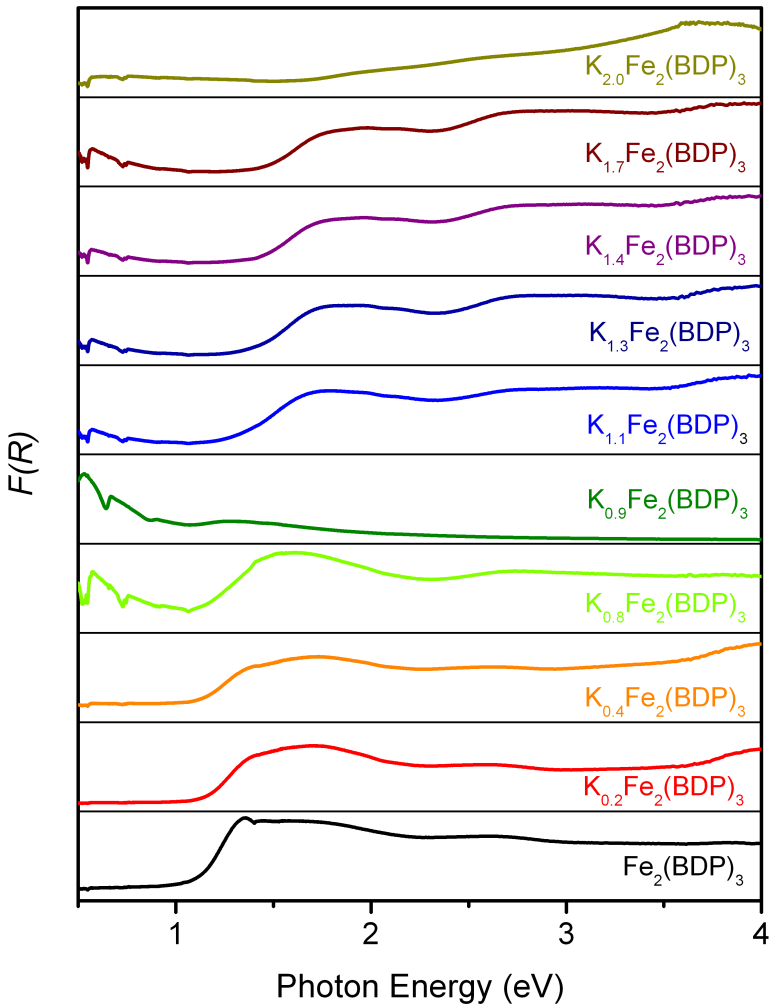

Figure 3.6 UV-Vis-NIR diffuse reflectance spectra of $K_xFe_2(BDP)_3$ (x = 0, 0.2, 0.4, 0.8, 0.9, 1.1, 1.3, 1.4, 1.7, 2.0).

Mid-IR spectroscopy shows the emergence of a broad band in the region 2500-450 cm^{-1} upon reduction. The intensity and width of this feature increases with reduction to $K_{0.94}Fe_2(BDP)_3$, and then decreases upon further reduction (Figure 3.7). Similar bands in the Mid-IR are shown by conductive mixed-valence polymers of pyrazine-bridged Fe^{2+}, Ru^{2+}, and Os^{2+} porphyrinates,[29] mixed-valence charge transfer salts,[30] and doped polyacetylene.[31] In those systems these Mid-IR features are attributed to low energy transitions between delocalized states.

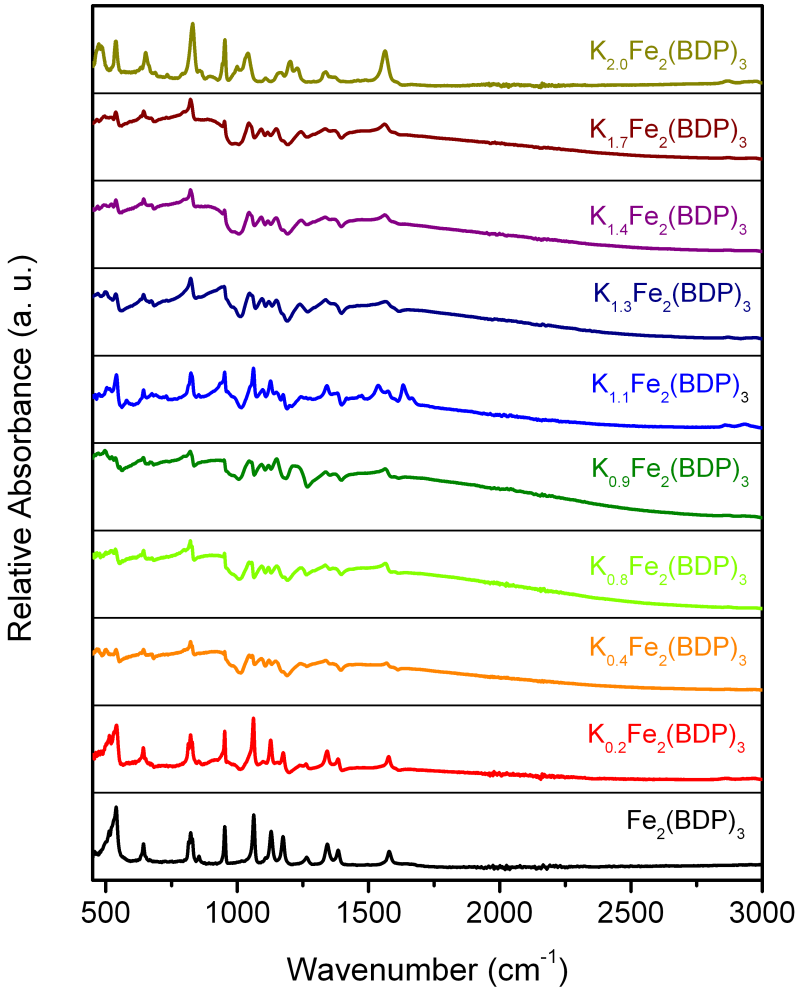

Figure 3.7 FT-IR absorbance spectra of $K_xFe_2(BDP)_3$ (x = 0, 0.2, 0.4, 0.8, 0.9, 1.1, 1.3, 1.4, 1.7, 2.0).

Because measurements of polycrystalline samples include interparticle and contact resistances, FP-TRMC was used to gain insight into the intrinsic charge transport characteristics of $Fe_2(BDP)_3$ before and after reduction. FP-TRMC is a contactless probe of charge mobility, not limited by interfacial resistances, grain boundaries and crystal anisotropies.[32] These measurements show that $Fe_2(BDP)_3$ is itself conductive with a total charge mobility μ_{tot} of 0.02 $cm^2/V{\cdot}s$. After reduction, the total charge mobility increases, with the highest mobility, 0.29 $cm^2/V{\cdot}s$, displayed at $K_{0.80}Fe_2(BDP)_3$. By $K_{2.0}Fe_2(BDP)_3$, the total charge mobility decreases to 0.07 $cm^2/V{\cdot}s$. Fig. 3A shows the conductivity transients and calculated total charge mobilities of the five stoichiometries of

$K_xFe_2(BDP)_3$ measured (x = 0, 0.2, 0.4, 0.8, 2.0). This measurement demonstrates that $Fe_2(BDP)_3$ is, as synthesized, a semiconductor, which shows an increase in mobility upon doping, indicative of *n*-type conduction. The FP-TRMC total charge mobilities of $K_xFe_2(BDP)_3$ rival or surpass those of organic polymers such as polyphenylenevinylenes (0.01−0.1 $cm^2/V{\cdot}s$)[33] and polythiophenes (0.015−0.075 $cm^2/V{\cdot}s$)[34] and organic molecular conductors such as rubrene (0.05 $cm^2/V{\cdot}s$).[35]

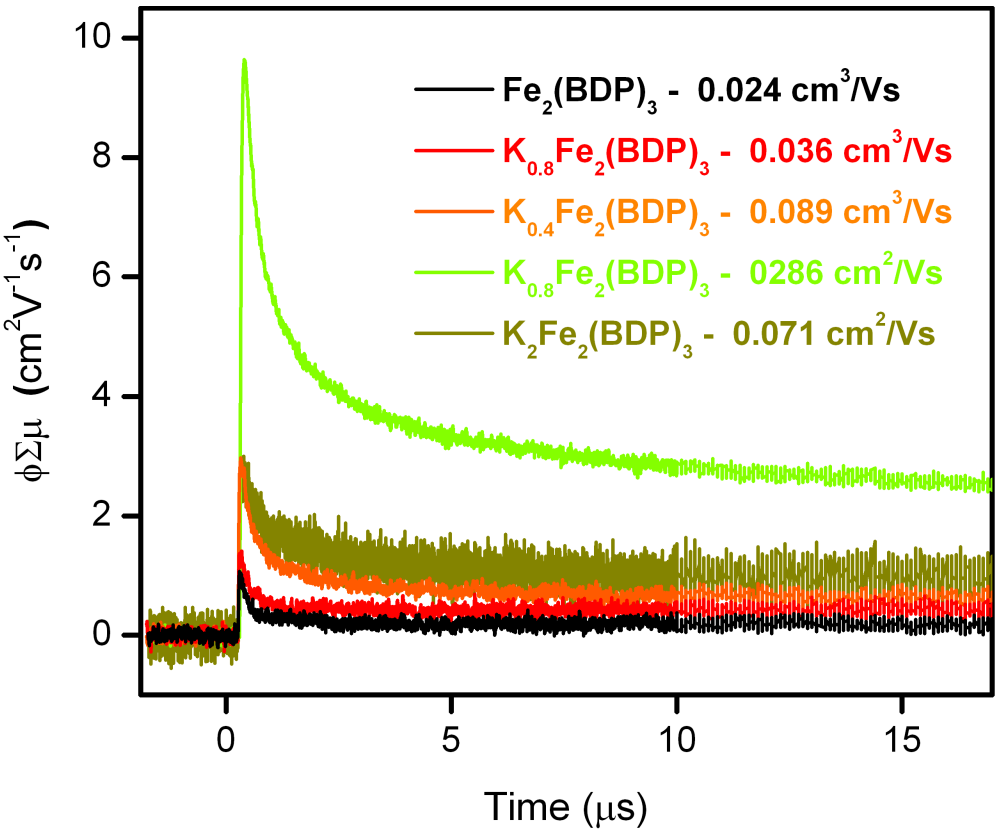

Figure 3.8 Conductivity transients observed by FP-TRMC upon excitation at 355 nm with 6.5 × 10^{15} photons cm^{-2} per pulse for $K_xFe_2(BDP)_3$ (x = 0, 0.2, 0.4, 0.8, 2.0) and their calculated total charge mobilities.

3.4 Conclusions and Outlook

$Fe_2(BDP)_3$ is a highly stable porous metal-organic framework, that can be stoichiometrically reduced by chemical reagents such as potassium naphthalenide. Optical measurements reveal that the material is an intrinsic semiconductor and 4-point pressed pellet measurements demonstrate ohmic conductivity after reduction. This result demonstrates tunable, intrinsic charge mobility in a pyrazolate bridged metal organic framework. It may be possible to obtain this material with other trivalent metals such as Ti^{3+}, Co^{3+} and V^{3+}. In the case of Ti^{3+} and Co^{3+} oxidative intercalation of a charge balancing anion could create a conductive mixed-valence solid, whereas the V^{3+} analogue of this material could also be chemically reduced. Given the more diffuse orbitals of the earlier V^{2+} and V^{3+} ions, this material could display improved charge transport properties.

3.5 Acknowledgements

This work was supported by the National Science Foundation through the grant "Conductive Metal-Organic Frameworks" (Award No. DMR-1309066) and a grant from the Go KRICT Project for Future Technology of the Korea Research Institute of Chemical Technology (KRICT). I thank Lucy E. Darago and Jarad Mason for help and valuable discussions, Dr. Greg Halder for help with the diffraction data collection at 1-BM-C and 17-BM at the Advanced Photon Source, the staff at 11-BM-B for assisting with mail-in diffraction samples at the Advanced Photon Source, and Dr. Trudy Bolin and Dr. Michael Pape for use of the helium glovebox in Sector 9 of the Advanced Photon Source. Use of the Advanced Photon Source at Argonne National Laboratory was supported by the U. S. Department of Energy, Office of Science, Office of Basic Energy Sciences, under Contract No. DE-AC02-06CH11357.

3.6 References

(1) Long, J. R.; Yaghi O. M. *Chem. Soc. Rev.* **2009**, *38*, 1213.
(2) Sculley, J.; Yang, D.; Zhou, H.-C. *Energy and Environmental Science* **2011**, *4*, 2721.
(3) Eddaoudi, M.; Kim, J.; Rosi, N.; Vodak, D.; Wachter, J.; O'Keeffe, M.; Yaghi, O. M. *Science* **2002**, *295*, 469.
(4) Matsuda, R.; Kitaura, R.; Kitagawa, S.; Kubota, Y.; Belosludov, R. V.; Kobayashi, T. C.; Sakamoto, H.; Chiba, T.; Takata, M.; Kawazoe, Y.; Mita, Y. *Nature* **2005**, *436*, 238.
(5) Seo, J. S.; Whang, D.; Lee, H.; Jun, S. I.; Oh, J.; Jeon, Y. J.; Kim, K. *Nature* **2000**, *404*, 982.
(6) McKinaly, A.C.; Morris, R. E.; Horcajada, P.; Férey, G.; Gref, R.; Couvreur, P.; Serre, C. *Agnew. Chem. Int. Ed.* **2010**, *49*, 6260.
(7) Lu, G.; Hupp, J. T. *J. Amer. Chem. Soc.* **2010**, *132,* 7832.
(8) Kent, C. A.; Liu, D.; Ma, L.; Papanikolas, J. M.; Meyer, T. J.; Lin, W. *J. Amer. Chem. Soc.* **2011**, *133*, 12940.
(9) Sadakiyo, M.; Yamada, T.; Kitagawa, H. *J. Am. Chem. Soc*. **2014**, *136*, 13166.
(10) Narayan, T. C. ; Miyaki, T.; Seki, S.; Dincă, M. *J. Amer. Chem. Soc.* **2012**, *134,* 12933.
(11) Talin, A.A.; Centrone, A.; Ford, A. C.; Foster, M. E.; Stavila, V.; Haney, P.; Kinney, R. A.; Szalai, V.; El Gabaly, F.; Yoon, H.P.; Léonard, F.; Allendorf, M. D. *Science* **2013**, *343*, 64.
(12) Kobayashi, Y.; Jacobs, B.; Allendorf, M. D.; Long, J. R. *Chem. Mater.* **2010**, *22*, 4120.
(13) (a.) Creutz C. *Prog. Inorg. Chem.* **1983**, *30*, 1. (b.) Richardson, D. E.; Taube, H. *Coord. Chem. Rev.* **1984**, *60*, 107. (c.) Crutchley, R. J. *Adv. Inorg. Chem.* **1994**, *41*, 273.
(14) Gándara, F.; Uribe-Romo, F. J.; Britt, D. K.; Furukawa, H.; Lei, L.; Cheng, R.; Duan, X.; O'Keefe, M.; Yaghi, O. M. *Chem. Eur. J.* **2012**, *18*, 10595.
(15) Choi, H. J.; Dincă, M.; Dailly A.; Long, J. R. *Energy Environ. Sci.*, **2010**, *3*, 117.

(16) Chaudhari, M.K.; Dehury, S. J.; Dhar, S. S.; Bora, U.; Choudary, B. M.,; Mannepalli, L. K. Process for Making Metal Acetylacetonates. US Patent No.7,282,573 B2, October 16, 2007.
(17) Coelho, A. *TOPAS-Academic*, version 4.1; Coelho Software: Brisbane, 2007.
(18) Cheary, R. W.; Coelho, A. A. *J. Appl. Crystallogr.* **1998**, *31*, 851.
(19) Tauc, J.; Grigorovici, R; Vancu, A. *Phys. Status Solidi* **1966**, *15*, 627.
(20) Colombo, V.; Galli, S.; Choi, H. J.; Han, G. D.; Maspero, A.; Palmisano, G.; Masciocchi, N.; Long, J. R. *Chem. Sci.* **2011**, *2*, 1311.
(21) Galli, S.; Masciocchi, N.; Colombo, V.; Maspero, A.; Palmisano, G.; Lopez-Garzon, F. J.; Domingo García, M.; Fernandez-Morales, I.; Barea, E.; Navarro, J. A. R. *Chem. Mater*. **2010**, *22*, 1664.
(22) Férey, G.; Millange, F.;, M.; Serre, C.; Doublet, M.-L.; Grenèche, J.-M.; Tarascon, J.-M. *Angew. Chem. Int. Ed.* **2007**, *46*, 3259.
(23) Meilikhov, M.; Yusenko, K.; Torisis, A.; Jee, B.; Mellot-Draznieks, C.; Pöppl, A.; Fischer, R. A. *Dalton Trans.* **2010***, 39*, 10990.
(24) Meilikhov, M.; Yusenko, K.; Fischer, R. A. *Dalton Trans.* **2010***, 39*, 10990.
(25) Mulfort, K.L; Hupp, J. T. *J. Am. Chem. Soc.* **2007**, *129*, 9604.
(26) Torrance, J. B. ; Scott, B. A. ; Welber, B.; Kauffman, F. B. Seiden, P. E. *Phys. Rev. B* **19**, 730 (1979).
(27) Brédas, J. L.; Scott, J. C.; Yakushi, K.; Street, G. B. *Phys. Rev. B.* **1984**, *30*, 1023.
(28) Chung, T.-C.; Kaufman, J. H.; Heeger, A. J.; Wudl, F. *Phys. Rev. B* **1984**, *30*, 702.
(29) Collman, J. P.; McDevitt, J. T.; Leidner, C. R.; Yee, G. T.; Torrance, J. B.; Little, W. A. *J. Am. Chem. Soc.* **1987**, *109*, 4606.
(30) Tanner, D. B.; Jacobsen, C. S.; Garito, A. F.; Heeger, A. J. *Phys. Rev. B* **1976**, *13*, 3381.
(31) Fincher, Jr, C. R.; Ozaki, M.; Heeger, A. J.; MacDiarmid, A. G. *Phys. Rev. B* **1979**, *19*, 4140.
(32) Saeki, A.; Koizumi, Y.; Aida, T.; Seki, S. *Acc. Chem. Res.* **2012**, ***45***, 1193.
(33) Krebs, F. C.; Jørgensen, M. *Macromolecules* **2003**, *36*, 4374.
(34) Saeki, A.; Seki, S.; Koizumi, Y.; Sunagawa, T.; Ushida, K.; Tagawa, S. *J. Phys. Chem. B* **2005**, *109*, 10015.
(35) Saeki, A.; Seki, S.; Takenobu, T.; Iwasa, Y.; Tagawa, S. *Adv. Mater*. **2008**, *20*, 920.

Chapter 4: Electron Mobility as a Function of Reduction in the Conductive Metal-Organic Framework, $K_xFe_2(BDP)_3$ (x = 0-2) as studied by Single Crystal Transport Measurements, Mössbauer Spectroscopy, and Solid State Slow Scan Rate Cyclic Voltammetry.

4.1 Introduction.

Measurements of electronic conductivity in three-dimensional metal-organic frameworks have been limited to polycrystalline thin films and pressed pellets.[1-3] In such measurements, the intrinsic resistance of the material cannot be separated from interparticle and grain boundary resistances. Contactless microwave conductivity measurements performed on metal-organic frameworks[4] provide a good probe of intrinsic charge transport, but cannot directly give the sign of charge carriers. Single-crystal field-effect transistor (FET) measurements allow the determination of the mobility and sign of charge carriers and can be fabricated to resemble useful device architectures. FET measurements have been performed on organic,[5,6] metallophthalocyanine,[7] and fullerene[8] single crystals as well as on single-walled carbon nanotubes[9] and individual inorganic nanowires.[10] However, for organic-inorganic hybrid systems, FET investigations have been primarily done on thin films of systems such as lead-iodide perovskites.[11] The rigid, open structures of metal-organic frameworks offer the possibility of topotactic reduction or oxidation of these materials via solution processes with concomitant counterion insertion to precisely alter transport properties. From a technological standpoint, this could allow new strategies for device fabrication and implementation not feasible with materials such as inorganic solids, polymers and molecular conductors that pack densely in the solid state. Herein I demonstrate single crystal 4-point direct current conductivity measurements of $Fe_2(BDP)_3$ as well as single-crystal field-effect transistor mobility measurements of $K_xFe_2(BDP)_3$ as a function of x, the degree of reduction. $Fe_2(BDP)_3$ is demonstrated to be a semiconductor as produced with ambipolar charge transport. Upon reduction, $K_xFe_2(BDP)_3$ displays *n*-type conduction, with an increase in conductivity over 4 orders of magnitude and a peak electron mobility of 0.84 $cm^2/V{\cdot}s$. Mössbauer spectroscopy and slow-scan cyclic voltammetry demonstrate the high degree of electronic delocalization in $K_xFe_2(BDP)_3$.

4.2 Experimental

General Considerations Unless otherwise specified, all manipulations were performed with rigorous exclusion of air and water by use of inert atmosphere (Ar/N_2) glove boxes and Schlenk techniques. *N,N*-dimethylformamide, acetonitrile, methanol, and tetrahydrofuran were deoxygenated by purging with argon for 1 h and dried using a commercial solvent purification system designed by JC Meyer Solvent Systems. Reagents were purchased from commercial vendors and solvents were dried with an

activated alumina column. EDS spectra were taken using a JEOL JSM-6340F field emission scanning electron microscope equipped with an EDAX Falcon detector. EDS data were collected from the K K and the Fe K peaks of a 40 μm × 40 μm area for each sample at 20 kV and analyzed using the software's true standardless-quantification mode.

Microcrystals of $Fe_2(BDP)_3$ for device fabrication were prepared in a sealed tube reaction as is described in Chapter 3.

Bulk $Fe_2(BDP)_3$ was synthesized and reduced as described in Chapter 3.

Single Crystal FET and 4-Point Device Fabrication and Measurements $Fe_2(BDP)_3$ microcrystals were suspended in a 0.1 weight percent dispersion in acetonitrile. Microcrystals were micro-manipulated between prefabricated electrodes on FET substrates (200 nm oxide). Loaded devices were placed into a FEI Strata 235 dual beam focused ion beam and examined via the SEM in the system. To increase the electrical contact area and physical stability of the crystal on the device, EBID (electron beam induced deposition) was used to place Pt/C pads at the interface of crystal and electrode on each side. Note that while this process was conducted within a FIB, only the SEM capabilities were used to avoid any potential ion beam damage. The exposure times were limited to a maximum of 60 seconds at a time to limit potential migration of the deposited Pt away from the intended area. Once several bonds were created, many devices were robust enough for solution-based reduction and subsequent electrical measurements performed on 2636A Dual Channel Keithley SourceMeter in a probe station,

Sequential Reduction and Measurement of Single-Crystal $Fe_2(BDP)_3$ FETs After initial measurements were performed on unreduced single-crystal devices, the FETs on microelectrode arrays were brought into a dinitrogen glove box and placed into a 100 ml borosilicate glass jar with 50 ml of THF and 300 mg of $Fe_2(BDP)_3$. The chip was surrounded with pierced aluminum foil, taking care not to contact the foil with the chips. The foil housing the microelectrode arrays served to prevent mechanical abrasion of the chips while allowing access to the reductant solution. c. 20 ml of a freshly prepared 0.07M potassium naphthalenide solution was added to the jar. The jar was capped and agitated by hand for one hour and then let to sit overnight. The chips were then removed and rinsed 5x with THF. An aliquot of the bulk $Fe_2(BDP)_3$ sample was then removed and analyzed by EDS. To protect the devices from oxidation while transferring to the probe station, two drops of a polystyrene in toluene solution were added to the chips, and let dry in the dinitrogen glovebox. This coating procedure was repeated twice and the sample was removed from the glovebox and transferred to the probe station. In the probe station, the probes pierced the polystyrene coating through to the contact pads of the microelectrode array. After measurement the chips were brought back into the dinitrogen glove box and soaked in toluene for twenty minutes to dissolve the protective polystyrene coating. The chips were then rinsed gently two times with toluene and two times with THF and then set to dry. They were again placed in a pierced aluminum foil protective covering and into the jar with excess $Fe_2(BDP)_3$ sample, and the procedure for stepwise reduction, protection and measurement of the devices was repeated.

EDS EDS spectra were taken using a JEOL JSM-6340F field emission scanning electron microscope equipped with an EDAX Falcon detector. EDS data were collected from the K K and the Fe K peaks of a 40 μm × 40 μm area for each sample at 20 kV and analyzed using the software's true standardless-quantification mode.

Mössbauer The Mössbauer spectra were obtained at 290 K with a SEE Mössbauer spectrometer equipped with a Co-57 in Rh source over the velocity range of ±12 mm/s. The isomer shifts are given relative to *a*-iron at 290 K. In an argon glove box, absorbers were prepared by intimately grinding a mixture of the sample with boron nitride powder and packing the mixture into a 1" diameter polypropylene washer, that was sealed with three layers of packing tape before transferring to the spectrometer. In the spectrometer the sample was stored in a helium atmosphere to prevent oxidation.

Electrochemical Measurements In an argon glovebox, cyclic voltammetry was conducted in a custom built PFA T-cell with titanium current collectors. Potassium metal polished to a mirror finish was used at the reference and counter electrodes. The working electrode was prepared by dropcasting a slurry of 60 wt% $Fe_2(bdp)_3$, 30 wt% Super P (Fischer) and 10 wt% PvdF (Aldrich) suspended in THF onto carbon cloth (Fuel Cell Earth). The electrode was desolvated at 180 ºC for approximately 2 hours, then loaded into the PFA cell. Electrodes were separated by a quartz fiber separator saturated with a 0.1 M solution of KTFSI (STREM) in anhydrous propylene carbonate (Aldrich). Cells were set to relax at open circuit potential to a limiting condition of 0.1 mV/h prior to measurement. Slow scan cyclic voltammetry was performed on a Bio-Logic VMP-3 multipotentiostat. Cyclic voltammograms were collected with an IR drop correction determined via single point potentiostatic ac impedance measurement at 10 mV ac and 0 V versus open circuit. Quasi-equilibrium conditions were observed for sweep rates of 0.1 mV/s and slower for the material $K_xFe_2(bdp)_3$ for the range $0 \leq x \leq 1.95$.

4.3 Results and Discussion

To perform single crystal transport measurements, dispersions of $Fe_2(BDP)_3$ were dropcast onto FET-ready Si substrates (200 nm SiO_2 top layer) prefabricated with interdigitated microelectrode arrays. $Fe_2(BDP)_3$ forms as a polydisperse mixture of acicular microcrystals, the smallest being less than 100 nm, and the largest being greater than 20 μm (Fig. 1D). The cross section of the crystals is a hexagon with sides defined by the (110), (100), (1-10), (-1-10), (-100), and (-110) planes. The long axis of the crystals run in the [001] direction, down which the μ^2-pyrazolate-bridged ferric ions run and through which conduction is expected. By dropcasting dispersions of $Fe_2(BDP)_3$ in a volatile solvent onto an interdigitated electrode, it is possible to form electrical contacts between the lead of an interdigitated microelectrode array and single crystals of $Fe_2(BDP)_3$. Figure 4.1 is an optical micrograph of a microcrystal of $Fe_2(BDP)_3$ bridging multiple leads of a microelectrode array in a configuration useful for device fabrication. Using an electron beam in the presence of a gaseous Pt precursor, Pt/C composite contacts were deposited at the interface between large single microcrystals of $Fe_2(BDP)_3$ and the patterned microelectrodes to improve mechanical stability and increase the area of the contacts. One such device is shown in Figure 4.2 In this manner, it was possible to perform a variable temperature four-point conductivity measurement on a singe crystal, the results of which are demonstrated in Figure 4.3. The 300 K conductivity of this crystal was 9.6×10^{-3} S/cm, with a high temperature (300 K - 225 K) activation energy $E_a = 25 \pm 5$ meV and a low temperature (200 K - 80 K) $E_a = 102 \pm 3$ meV.

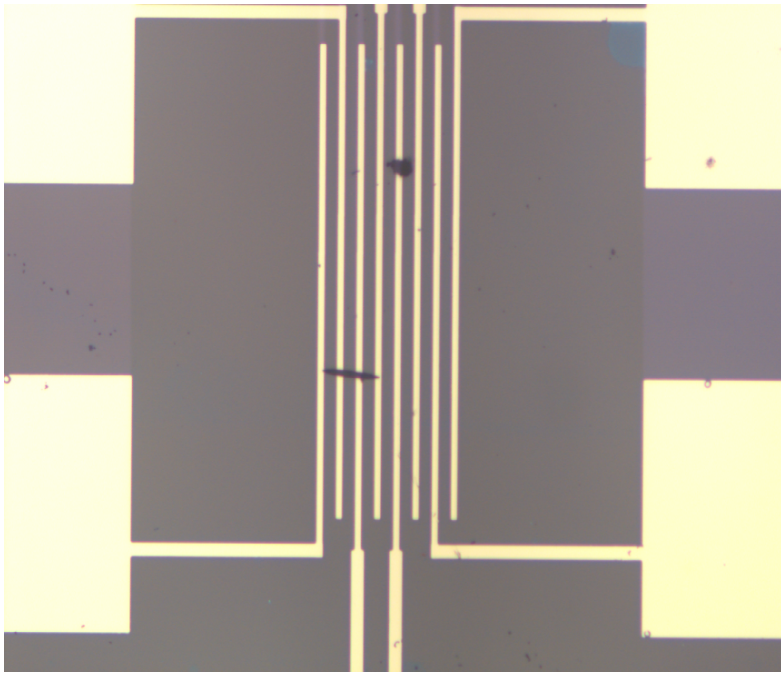

Figure 4.1. Optical micrograph of a $Fe_2(BDP)_3$ single crystal bridging the microelectrode leads of an interdigitated microelectrode array.

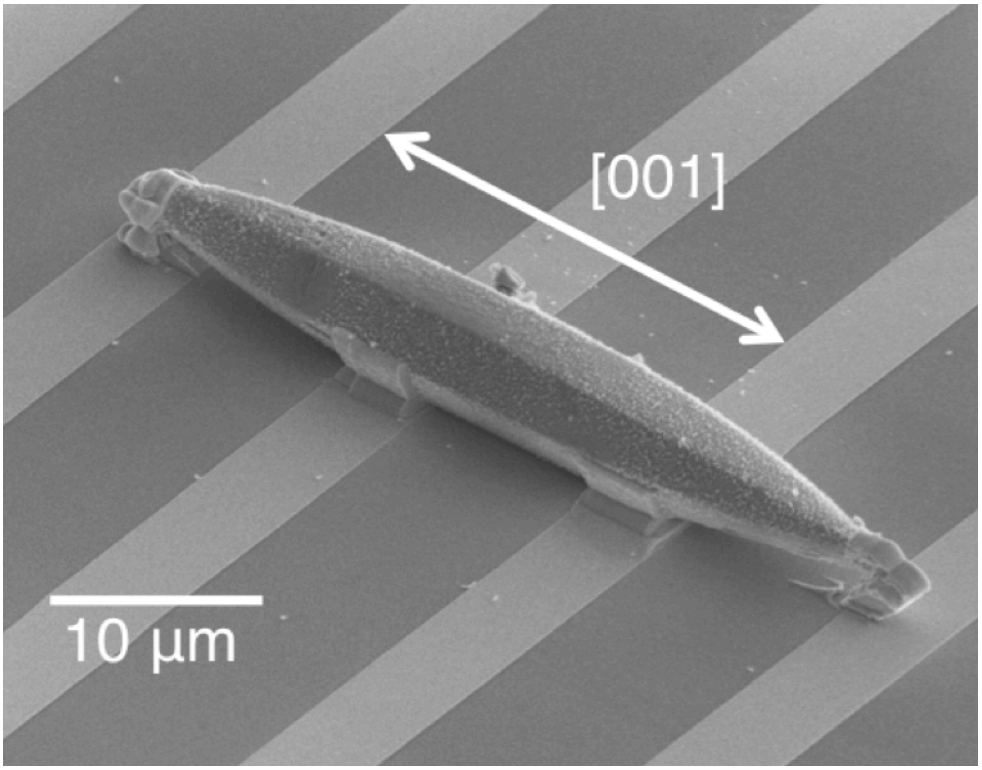

Figure 4.2 Single crystal of $Fe_2(BDP)_3$ with 4 Pt-bonded contacts to the leads of an interdigitated electrode. The [001] direction along the length of the crystal is indicated.

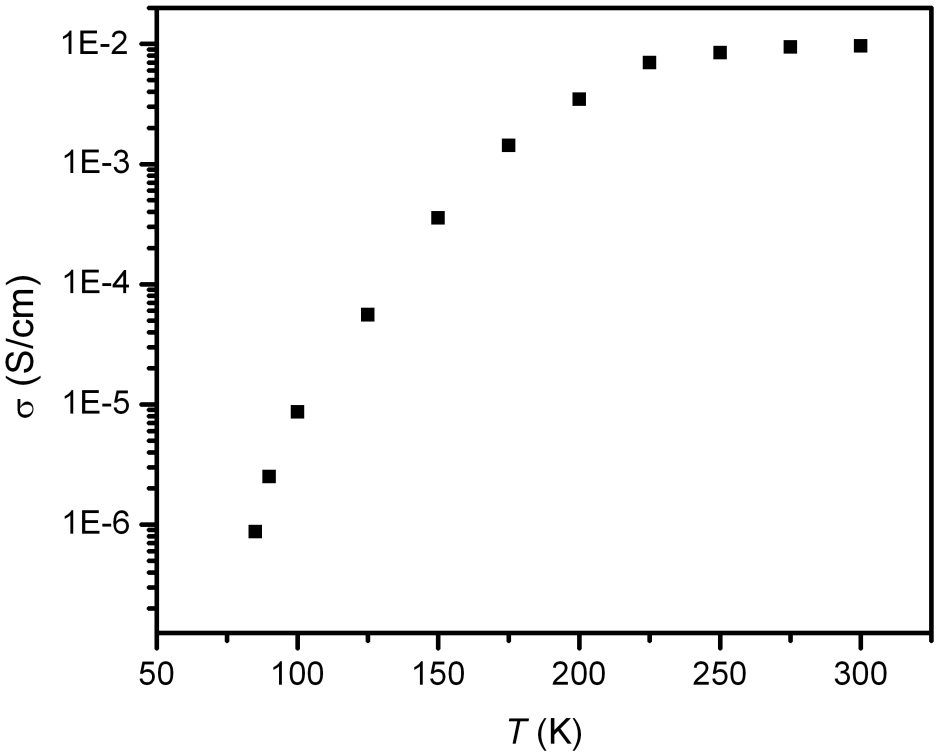

Figure 4.3 Variable temperature 4-point conductivity measurement of a single crystal of $Fe_2(BDP)_3$.

FET devices were fabricated by bonding single crystals of $Fe_2(BDP)_3$ to leads of the interdigitated microelectrodes to form source and drain contacts. Applying a voltage to the silicon substrate allowed the application of a gating voltage, while the 200 nm SiO_2 layer served as a dielectric. Multiple FET devices were fabricated and transconductance measurements were performed on each device. Figure 4.4 is a scanning electron micrograph of a two-point device bonded to an interdigitated electrode.

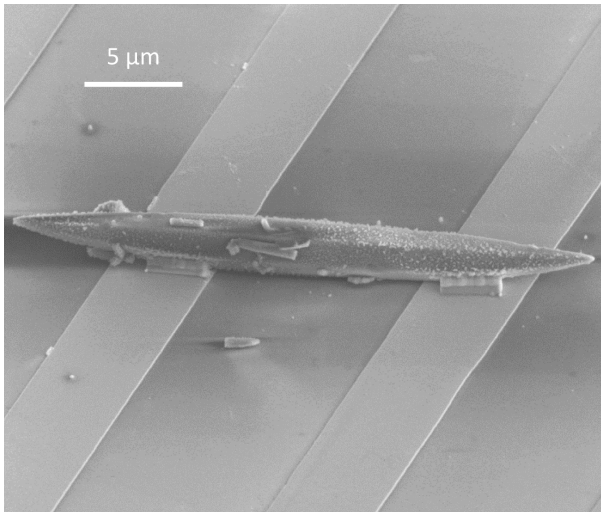

Figure 4.4 Scanning electron micrograph of a 2-point single crystal $Fe_2(BDP)_3$ device.

To achieve controlled reduction of the single crystal devices, under inert atmosphere the arrays with bonded $Fe_2(BDP)_3$ single-crystal FETs were placed in a vessel with THF and bulk $Fe_2(BDP)_3$ sample. Potassium naphthalenide in THF was added to the vessel in an amount to reduce the bulk Fe2(BDP)3 to the target stoichiometry, along with the bonded microcrystal. In this manner the stoichiometry of the reduction was controlled by the ratio of the added potassium naphthalenide to the amount of bulk $Fe_2(BDP)_3$ in the vessel. Figure 4.5 is a schematic for this process. In this way, the bulk $Fe_2(BDP)_3$ and the microcrystals bonded to the microelectrode array were fractionally reduced in steps and the transport properties of the FET devices were measured after each step of reduction. The ratios determined from the bulk aliquots were used to estimate the degree of reduction of single crystal devices.

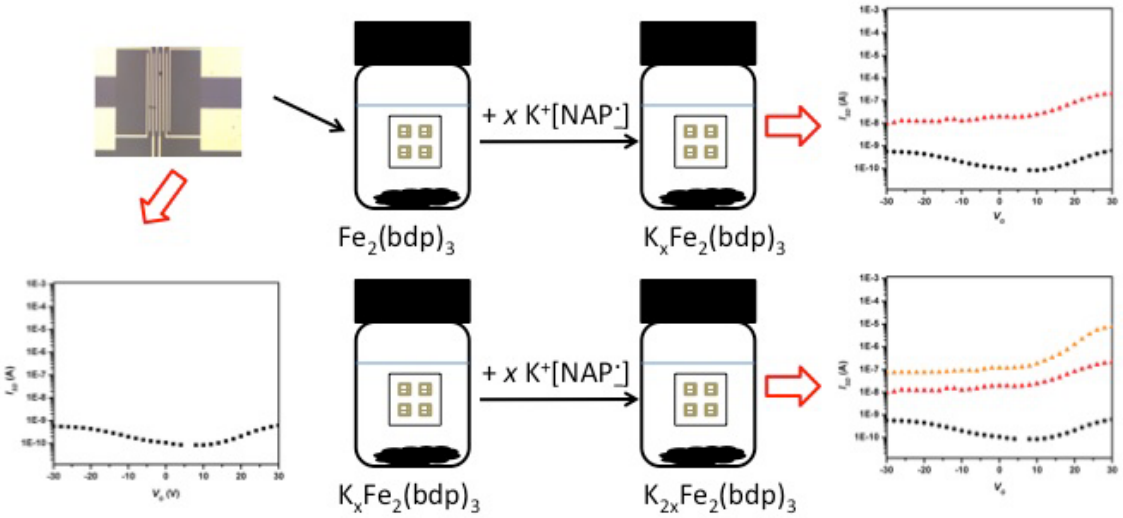

Figure 4.5. Schematic for incremental doping and transcurrent measurement of a single-crystal field effect transistor device.

While not all devices survived these manipulations, it was possible to perform measurements up to $K_{0.78}Fe_2(BDP)_3$ on multiple devices and up to $K_{1.96}Fe_2(BDP)_3$ on a single device. This particular device's transcurrents as a function of gate voltage and degree of reduction are shown in Figure 4.6.

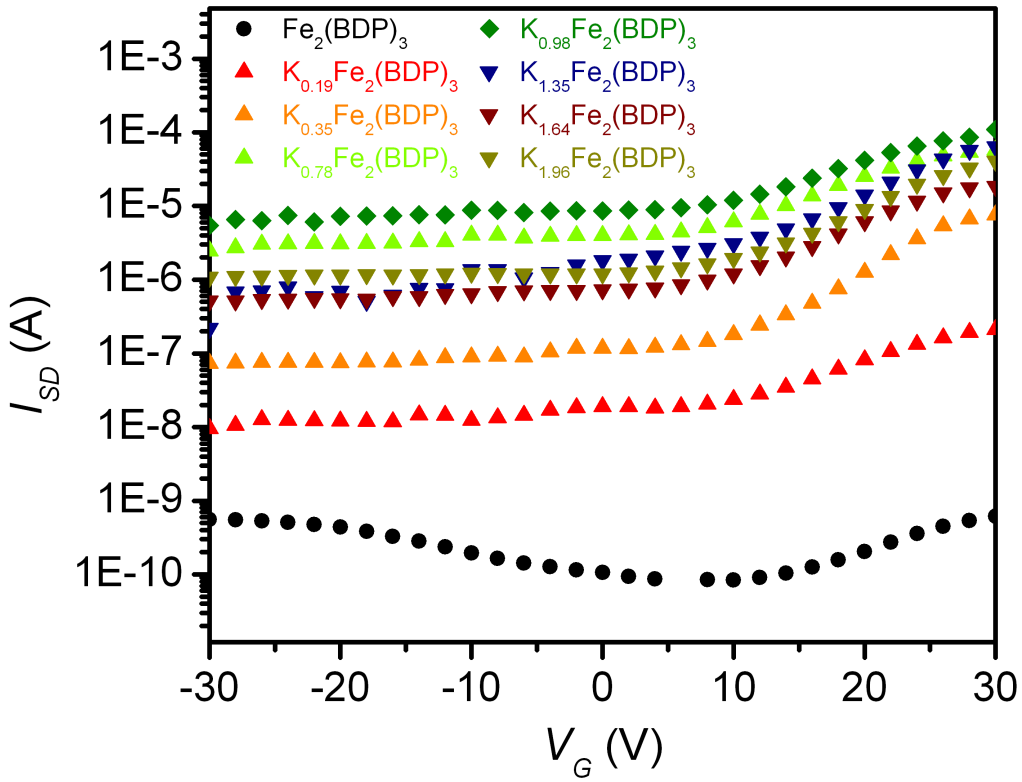

Figure 4.6. Transcurrents as a function of gating voltage for a single crystal of $K_xFe_2(BDP)_3$ for multiple stoichiometries (x = 0, 0.19, 0.35, 0.78, 0.98, 1.35, 1.68, 1.98)

Upon reduction, the two-point DC conductivity of this device rises from 3.5×10^{-7} S/cm to a peak value of 0.025 S/cm at a stoichiometry of $K_{0.98}Fe_2(BDP)_3$. Figures 4.7 and 4.8 are I-V curves of this device for the $K_0Fe_2(BDP)_3$ and $K_{0.98}Fe_2(BDP)_3$ stoichiometries.

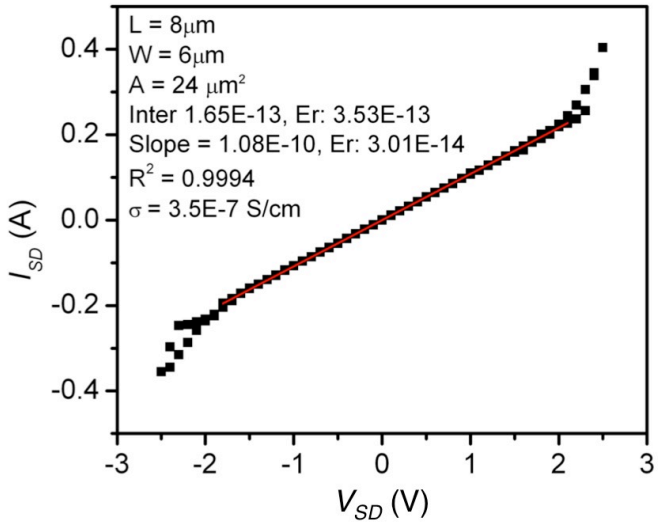

Figure 4.7 IV-curve of a two-point DC measurement of a $K_xFe_2(BDP)_3$ single crystal used in the FET measurements shown in **Figure 4.6** at the stoichiometry x = 0.

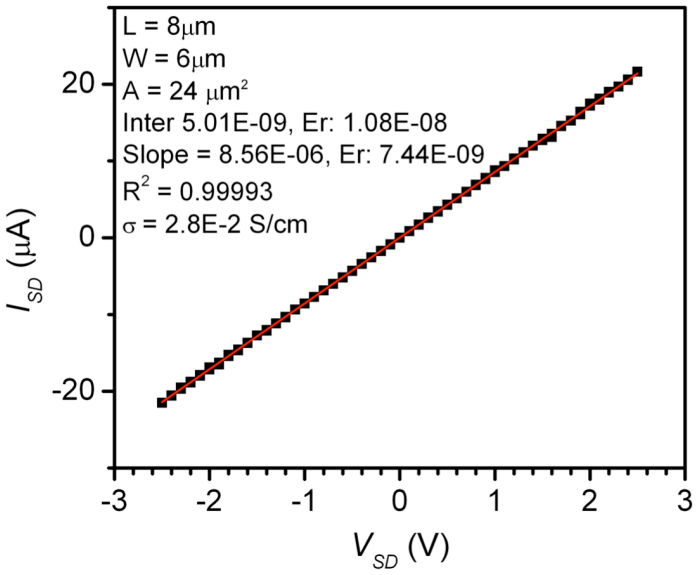

Fiure 4.8. IV-curve of a two-point DC measurement of a $K_{0.98}Fe_2(BDP)_3$ single crystal used in the FET measurements shown in **Figure 4.6** at the stoichiometry $x = 0.98$.

After reduction, transcurrents increase with positive voltage-gating, indicative of *n*-type conduction (Figure 4.6). The ambipolar transport of the unreduced $Fe_2(BDP)_3$ could be due to low lying acceptor states that are eliminated as the framework is reduced. In the devices measured, transcurrents increase as a function of reduction until $K_{0.98}Fe_2(BDP)_3$, and decrease upon further reduction. The average electron and hole mobilities of all measured devices as a function of reduction are shown in Figure 4.9. A peak mobility of μ_e = 0.84 $cm^2/V{\cdot}s$ is observed for $K_{0.98}Fe_2(BDP)_3$. The field-effect mobilities for $K_{x\geq0.35}Fe_2(BDP)_3$ are in the higher range of reported values for conjugated organic *p*-type polymers such as polyhexathiophene[12] and within the range of reported field-effect electron mobilities of *n*-type polymers[13] and amorphous silicon.[14] In Fe2(BDP)3 the iron sites are located at the 16g Wyckoff sites in the *Fddd* space group. This allows the calculation of the Fe···Fe distance, 3.56Å in $K_{0.8}Fe_2(BDP)_3$ at 295 K given its lattice parameters of a = 45.722(3) Å, b = 26.388(4) Å, c = 7.0815(6) Å. It is possible to apply time-energy uncertainty to estimate the value of the minimum mobility necessary for a band treatment in a one-dimensional conductor, given an intersite spacing, a:

$$\mu_{min} = \frac{\pi a^2 e}{3h} \qquad (1)$$

where h is Planck's constant, 6.626×10^{-34} J·s, and e is the charge of an electron, 1.602×10^{-19} C.[15] Using the site spacing of a = 3.56 Å yields minimum mobility, μ_{min} = 0.3 $cm^2/V{\cdot}s$. The measured average FET mobility μ_{FET} of $K_{0.78}Fe_2(BDP)_3$ is 0.4 $cm^2/V{\cdot}s$ and the FP-TRMC mobility μ_{tot} of $K_{0.8}Fe_2(BDP)_3$ is 0.29 $cm^2/V{\cdot}s$, suggesting that for $2.0 > x \geq 0.78$ in $K_xFe_2(BDP)_3$, the conduction electrons can be treated as being at least partially delocalized over the iron-pyrazolate chains.

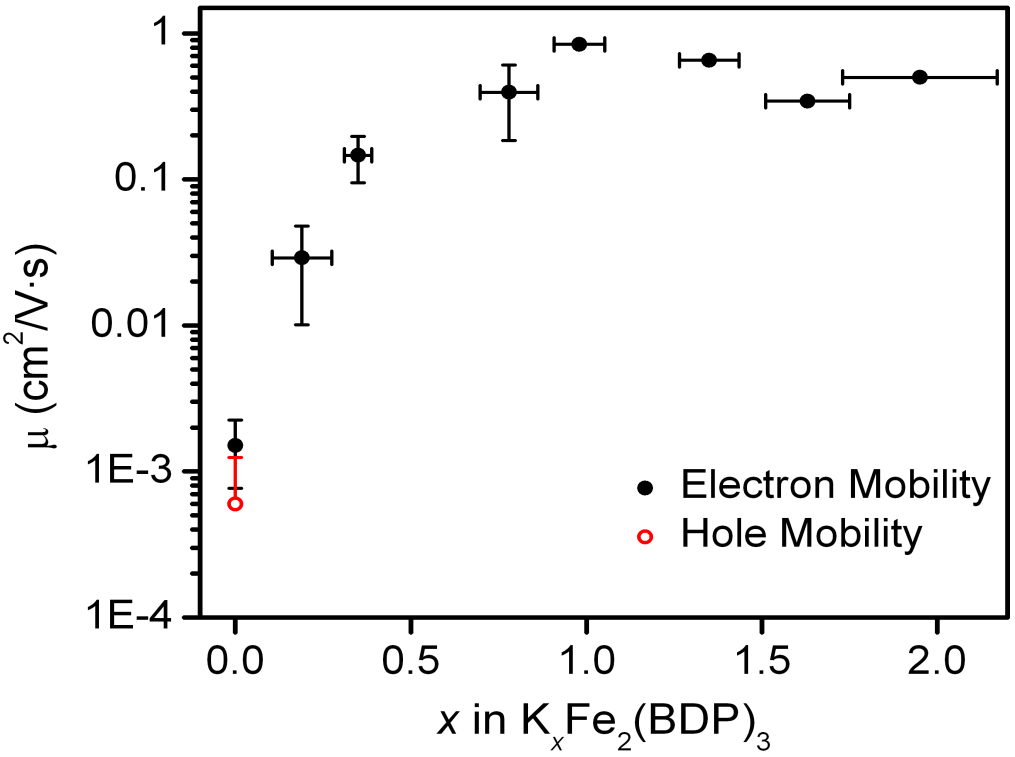

Figure 4.9 Hole and electron FET mobilities of single crystal $Fe_2(BDP)_3$ devices measured as a function of reduction.

Two-point DC conductivity measurements of $Fe_2(BDP)_3$ single crystals show an average 2×10^4 increase in conductivity upon reduction to $K_{0.98}Fe_2(BDP)_3$. Multiplying the four-point DC conductivity of $Fe_2(BDP)_3$ by this value allows an estimation of the four-point conductivity of a $K_{0.98}Fe_2(BDP)_3$ crystal as $\sim 2 \times 10^2$ S/cm. The relation $\sigma = n_e \mu_e e$ yields a charge carrier density $n_e \sim 10^{21}$ e/cm^3, a value comparable to that estimated by dividing the potassium content per unit cell by the unit cell volume of $K_{0.9}Fe_2(BDP)_3$, 8.9×10^{20} e/cm^3. This indicates that at near half-reduction, electrons from reduction are delocalized over the framework as conduction electrons.

The 290 K Mössbauer spectrum of $Fe_2(BDP)_3$ shows a major Fe^{3+} component with an isomer shift of 0.063(1) mm/s relative to 290 K *a*-iron and a quadrupole splitting of 0.973(1) mm/s, with a relative area of 93% and a minor high-spin Fe^{3+} component with an isomer shift of 0.54(2) mm/s and a quadrupole splitting of 1.03(3) mm/s, with a relative area of 7%. The spectra of $K_{0.2 \le x \le 1.7}Fe_2(BDP)_3$ are composed of three doublets, two consistent with the components of $Fe_2(BDP)_3$ as well as a high-spin Fe^{2+} doublet. The spectrum of $K_{2.0}Fe_2(BDP)_3$ is composed of a high-spin Fe^{3+} doublet and a high-spin Fe^{2+} doublet. Fig. 4.10 shows the 290 K Mössbauer spectra of $Fe_2(BDP)_3$, $K_{0.80}Fe_2(BDP)_3$, $K_{0.94}Fe_2(BDP)_3$, and $K_2Fe_2(BDP)_3$. In $K_xFe_2(BDP)_3$ the high spin Fe^{2+} component is not clearly present for $x < 0.9$. For $x \ge 0.9$, the relative area of the high-spin Fe^{2+} component increases from 11 to 46 % as x increases from 0.9 to 2. This indicates that upon reduction of the framework, a significant fraction of the electrons from reduction are not localized on the iron ions on the Mössbauer time scale (10^{-8} s).

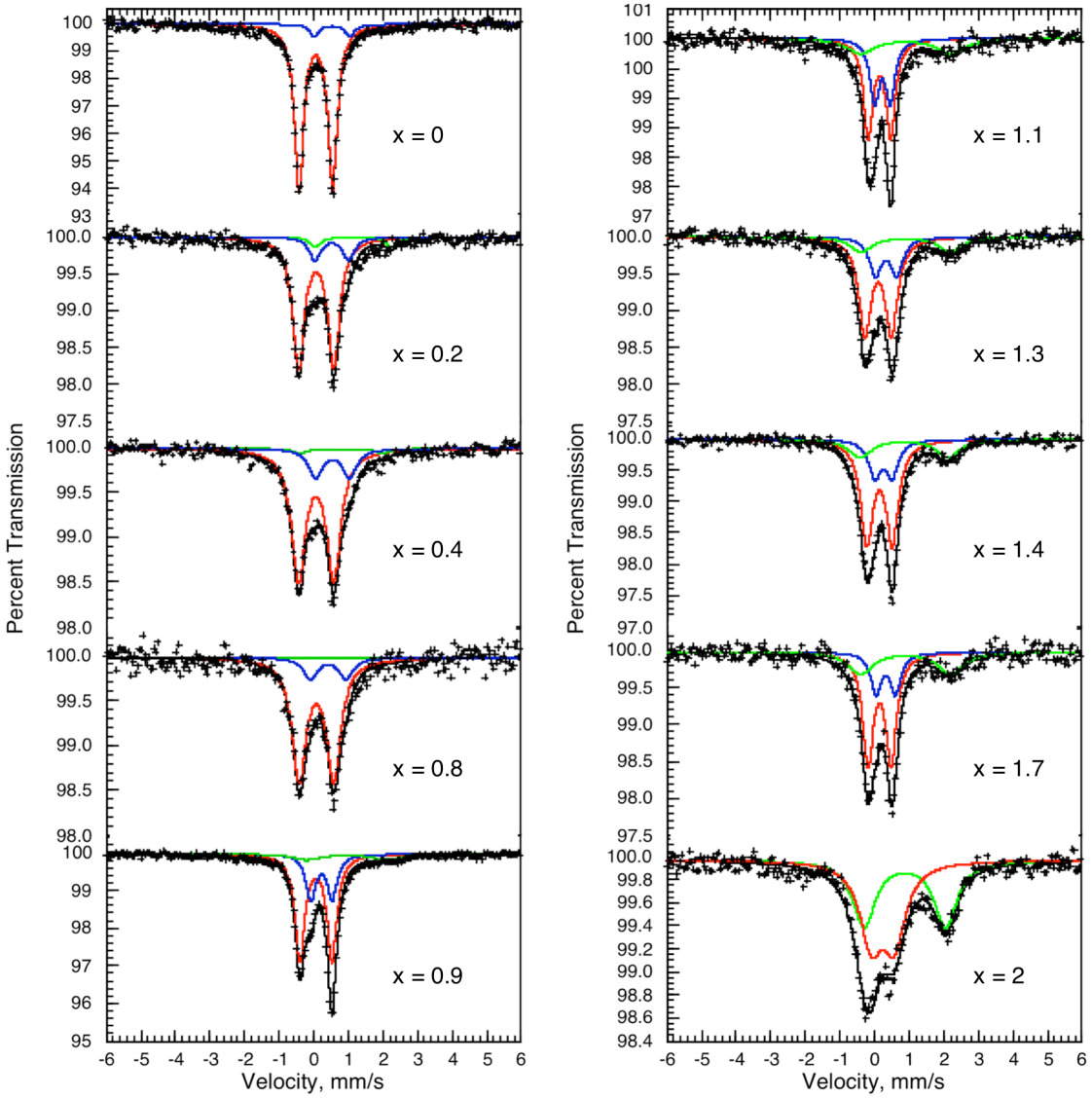

Figure 4.10 Mössbauer spectra measured at 290 K of $K_xFe_2(BDP)_3$ (x = 0, 0.80, 0.94, 2.0). and fits The red and blue doublets are assigned to Fe^{3+} and minor H.S. Fe^{3+} components, and the green doublet is assigned to H.S. Fe^{2+}. The black crosses are data points.

Table 4.1 The 290 K Mössbauer Spectral Parameters of $K_xFe_2(bdp)_3$.

-

x	δ_1,[a] mm/s	Δ_{Q1},[b] mm/s	Γ_1,[c] mm/s	RA_1[d]	δ_2,[a] mm/s	Δ_{Q2},[b] mm/s	Γ_2,[c] mm/s	RA_2[d]
0	0.063(1)	0.973(3)	0.319(4)	0.927(7)	0.54(2)	1.03(3)	0.319(4)	0.073(7)
0.2	0.072(3)	1.016(6)	0.408(9)	0.79(2)	0.530(2)	0.97(2)	0.408(9)	0.14(2)
0.4	0.071(5)	1.023(7)	0.49(1)	0.80(2)	0.550(3)	1.02(2)	0.49(3)	0.16(1)
0.8	0.08	1.0	0.49(2)	0.84(3)	0.42	1.03(8)	0.49(2)	0.150(5)
0.9	0.068(2)	0.930(4)	0.339(3)	0.630(6)	0.227(5)	0.62(1)	0.339(3)	0.267(6)
1.1	0.12(1)	0.71(3)	0.346(8)	0.34(4)	0.200(8)	0.52(2)	0.346(8)	0.56(4)
1.3	0.110(7)	0.76(2)	0.43(2)	0.59	0.34(2)	0.61(3)	0.43(2)	0.23
1.4	0.151(6)	0.73(1)	0.430(8)	0.59	0.26(2)	0.50(3)	0.430(8)	0.21
1.7	0.150(6)	0.67(1)	0.37(2)	0.55	0.33(2)	0.56(3)	0.37(2)	0.2
2.0	0.24(1)	0.66(2)	0.78(3)	0.54(1)				

x	δ_3,[a] mm/s	Δ_{Q3},[b] mm/s	Γ_3,[c] mm/s	RA_3[d]
0				
0.2	1.15	2.2	0.408(9)	0.06(1)
0.4	1.15	2.2	0.49(1)	0.04(1)
0.8	1.2	2.2	0.49(2)	0.01
0.9	0.95	2.3	1.0	0.107(6)
1.1	0.7	2.9	0.8(1)	0.1
1.3	0.9(1)	2.6(1)	0.8	0.180(3)
1.4	0.85(5)	2.53(6)	0.81	0.200(2)
1.7	0.9	2.60(9)	0.84	0.250(4)
2.0	0.88(2)	2.35(3)	0.78(3)	0.46(1)

[a]δ The isomer shifts are referred to *a*-iron at 295 K. [b]Δ_{Qi} are the quadrupole splittings of the red (1), blue (2), and green (3) doublets as shown in Figure 4.10, [c]Γ_i is the full line width at half maximum of the doublet i. The line widths Γ_1 and Γ_2 were constrained to be equal. [d]RA_i is the relative area of the doublet i. [e]The statistical errors are given in parentheses. The absence of error indicates that the parameter was constrained to the value given. The actual errors are approximately twice as large.

Slow scan, solid state cyclic voltammetry gives further insight into the behavior of $Fe_2(BDP)_3$ upon reduction and the degree of electronic delocalization in $K_xFe_2(BDP)_3$. At a 0.015 mV/s scan rate (Figure 4.11), two reductive waves are observed at 2.447 V and 1.639 V (vs. $K^{0/+}$), with respective integrations of -390 mC and -590 mC. The ratios between the integrations indicate the first wave is a reduction to the stoichiometry of $K_{0.8}Fe_2(BDP)_3$. A shoulder near 1.60 V is visible on the second, lower voltage reductive wave. This feature disappears at faster scan rates (Figure 4.12). In the oxidative scan two waves are observed; the first lower voltage wave is composed of peaks at 1.726 V, and 1.846 V with a shoulder at 1.812 V and a single higher voltage, broad wave with a peak current at 2.474V. The integrations of the two oxidative waves are respectively +580 mC and +400 mC, their sum equal to the integrations of the corresponding reductive waves, demonstrating that these redox processes are reversible. The lower voltage peaks in the oxidative scans also coalesce at higher scan rates. The peak splittings can be attributed to a reorganization of the potassium ions and Fe^{2+} sites in the framework, while the hysteresis between reductive and oxidative scans reflects the changes in the chemical environment as this reorganization occurs, a process that becomes increasingly resolved at slower scan rates. Taking the peak separation between the first two reductive peaks, ΔE = 0.80 V, it is possible to calculate a comproportionation constant $K_c = 2 \times 10^{14}$. This value, in the upper range seen for Class III molecular mixed-valence compounds,[16] is consistent with the strong degree of electronic delocalization in $K_{0.8\leq x<2}Fe_2(BDP)_3$, as shown by the results of Mössbauer spectroscopy and FET electron mobility measurements as well as the intervalence charge transfer absorptions, Mid-IR spectral features, and FP-TRMC total charge carrier mobilities described in Chapter 3.

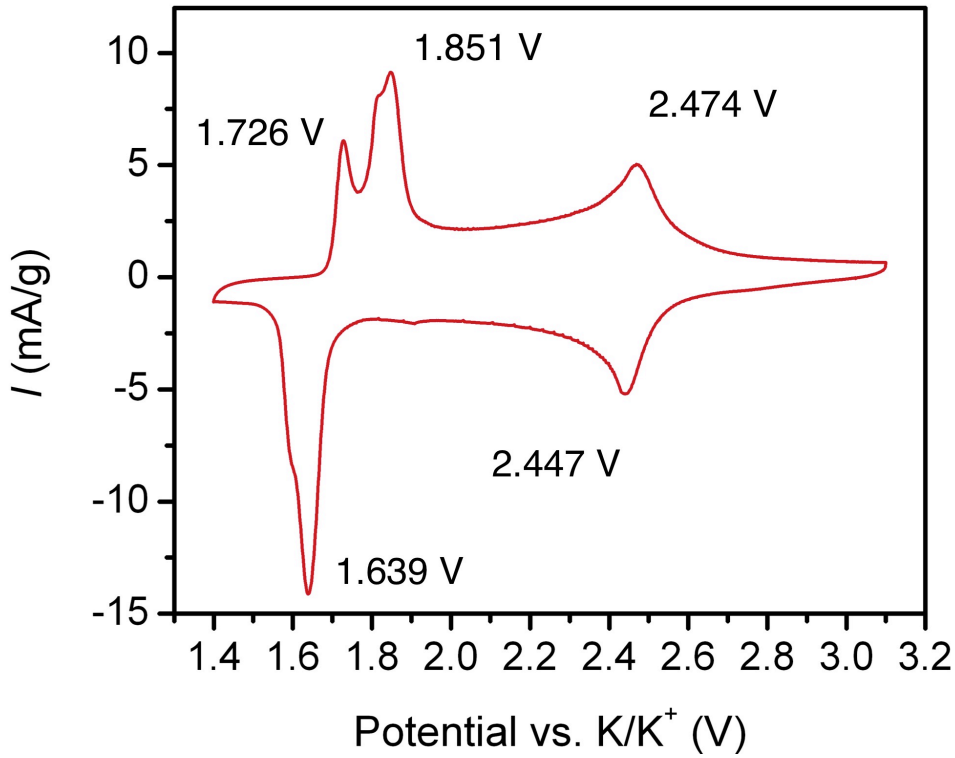

Figure 4.11 Solid state cyclic voltammogram of $Fe_2(BDP)_3$ at a 0.015 mV/s scan rate with a 0.2M KTFSI in propylene carbonate electrolyte.

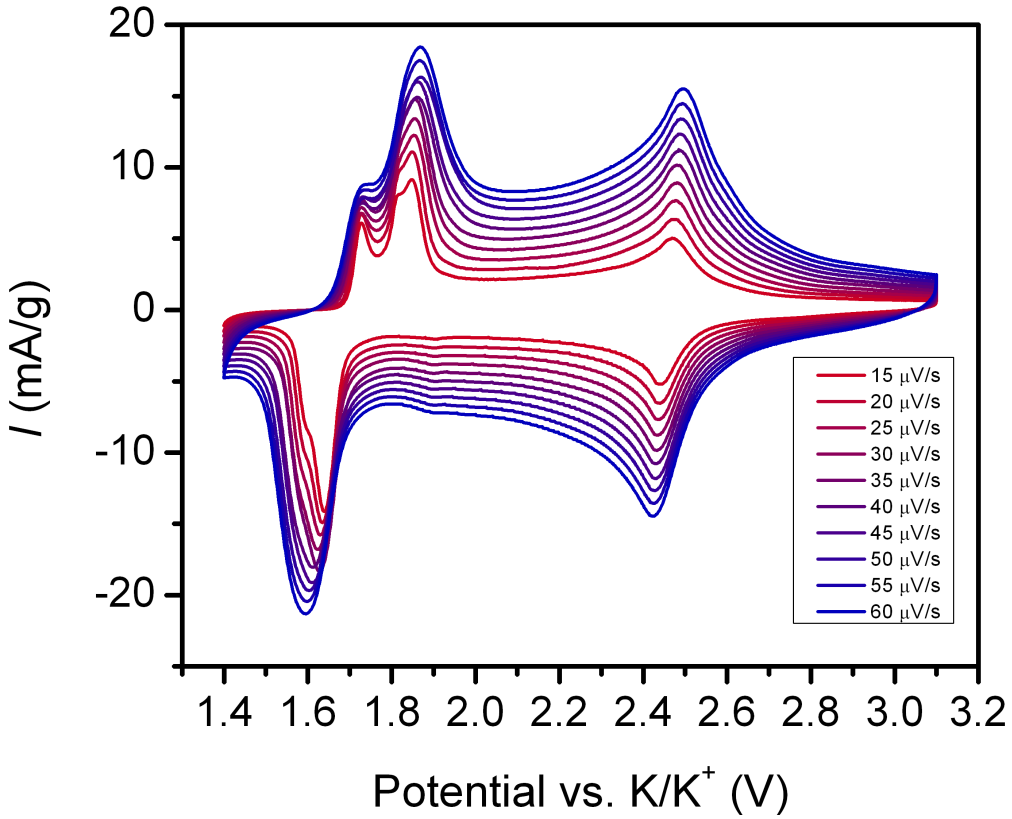

Figure 4.12 Solid state cyclic voltammogram of $Fe_2(BDP)_3$ at a 0.015 mV/s -0.06 mV/s scan rates with a 0.2M KTFSI in propylene carbonate electrolyte.

4.4 Conclusions and Outlook

A strategy to measure the changes in charge transport properties on single crystals of metal-organic frameworks as a function of reduction where successfully implemented here. This approach could be implemented with other redox-active metal-organic frameworks. Single crystal measurements of the unreduced framework show ohmic conductivities that drastically increase upon reduction. $Fe_2(BDP)_3$ shows ambipolar charge transport that becomes *n*-type upon reduction, with high field effect mobilities. Mössbauer spectroscopy and slow scan solid state cyclic voltammetry corroborate the high degree of electronic delocalization of $K_xFe_2(BDP)_3$.

4.5 Acknowledgements

This work was supported by the National Science Foundation through the grant "Conductive Metal-Organic Frameworks" (Award No. DMR-1309066) and a grant from the Go KRICT Project for Future Technology of the Korea Research Institute of Chemical Technology (KRICT).

4.6 References

(1) Talin, A.A.; Centrone, A.; Ford, A. C.; Foster, M.E.; Stavila, V.; Haney, P.; Kinney, R. A.; Szalai, V. ; El Gabaly, F.; Yoon, H.P.; Léonard, F.; Allendorf, M. D. *Science* **2013**, *343*, 64.

(2) Kobayashi, Y.; Jacobs, B.; Allendorf, M. D.; Long, J. R. *Chem. Mater.* **2010**, *22*, 4120.

(3) Gándara, F.; Uribe-Romo, F. J.; Britt, D. K.; Furukawa, H.; Lei, L.; Cheng, R.; Duan, X.; O'Keefe, M.; Yaghi, O. M. *Chem. Eur. J.* **2012**, *18*, 10595.

(4) Narayan, T. C. ; Miyaki, T.; Seki, S.; Dincă, M. *J. Amer. Chem. Soc.* **2012**, *134,* 12933.

(5) Pozdorov, V.; Menard, E.; Borissov, A.; Kiryukhin, V.; Rogers, J. A.; Gershenson. M. E. *Phys. Rev. Lett.* **2004**, *93*, 086602.

(6) Molinari, A. S.; Alves, H.; Chen, Z.; Faccheti, A.; Mopurgo, A. F. *J. Amer. Chem. Soc.*, **2009**, *131*, 2462.

(7) de Boer, R. W. I.; Stassen, A. F.; Craciun, M. F.; Mulder, C. L.; Molinari, A.; Rogge, S.; Morpurgo, A. F. *Appl. Phys. Lett.* **2005**, *86*, 262109.

(8) Li, H.; Tee, B. C.-K.; Cha, J. J.; Cui, Y.; Chung, J. W.; Lee, S. Y.; Bao, Z. *J. Amer. Chem. Soc.* **2012**, *134*, 2760.

(9) Tans, S. J.; Verschueren, A. R. M.; Dekker, C. *Nature* **1998,** *393*, 49.

(10) Duan, X.; Huang, Y.; Cui, Y.; Wang, J.; Lieber, C. M. *Nature* **2001**, *409*, 66.

(11) Kagan, C. R.; Mitzi, D. B.; Dmitrakopoulos, C. D. *Science* **1999**, *286*, 945.

(12) Sirringhaus, H.; Brown, P. J.; Friend, R. H.; Nielsen, M. M.; Bechgaard, K.; Langeveld-Voss, B. M. W;. Spiering, A. J. H.; Janssen, R. A. J.; Meijer, E. W.; Herwig, P.; de Leeuw, D. M. *Nature* **1999**, *401*, 685.

(13) Yan, H.; Chen, Z.; Zheng, Y.; Newman, C.; Quinn, J. R.; Dötz, F.; Kastler, M.; Facchetti, A. *Nature*, **2009**, *457*, 679.

(14) Kanicki, J.; Libsch, F. R.; Griffith, J.; Polastre, R. Performance of thin hydrogenated amorphous silicon thin-film transistors. *J. Appl. Phys.* **1991**, *69*, 2339.

(15) Bright, A.; Chaikin, P. M.; McGhie, A. R. *Phys. Rev. B* **1974**, *10*, 3560.

(16) McWhinnie, S. L. W.; Jones, C. J.; McCleverty, J. A.; Collison, D.; F. E. Mabbs, *J. Chem. Soc., Chem. Commun.* **1990**, 940.

Chapter 5: Fe_2(DSBDC), a Chalcogenide-Containing Metal-Organic Framework Displaying High Charge Mobility.

5.1 Introduction

One-dimensional inorganic chains built of metal ions with oxo-donor bonds are a common structural motif in metal-organic frameworks.[1] Two reported metal-organic frameworks built of one-dimensional oxo-bridged chains also display interesting electrochemical and charge-transfer properties that suggest avenues for engendering long-range charge transport in metal-organic frameworks. $FeF_{0.8}(OH)_{0.2}$(BDC), a ferric framework built from linear chains of *trans*-vertex sharing iron octahedra reversibly intercalates lithium ions electrochemically.[2] However, Mössbauer spectroscopy and computational studies suggest a high degree of localization in this framework. Increasing the connectivity of the inorganic polyhedra from vertex-sharing to edge-sharing would provide more bridging orbitals and result in closer metal-metal separation. The M_2(DOBDC) structure type is built of one-dimensional helical chains of edge-sharing octahedra.[1,3] It is possible to remove coordinated solvent upon heating and evacuation and adsorb dioxygen in the ferrous Fe_2(DOBDC). Upon coordination of dioxygen there is an electron transfer from the Fe^{2+} ion to the dioxygen to form a superoxide below 211 K. Above 211 K electron transfer from an adjacent Fe^{2+} to form a bound peroxide, demonstrating electron transfer between metal-centers upon partial oxidation.[4]

The vast majority of metal-organic frameworks are made of redox-inactive, hard Lewis acids such as Mg^{2+}, Zn^{2+}, Ln^{3+}, Zr^{4+} and hard Lewis base oxo-donor ligands, and as such form metal-ligand bonds of a predominately ionic character.[5] Chalcogen donors have a closer match in electronegativity with the transition metal orbitals, as well as more diffuse, directional orbitals that could form bonds of greater covalency improving electronic communication between redox-active metal ions.[6-9] Indeed, non-porous coordination solids with sulfur ligands that display charge transport properties have been reported.[10,11] However, the strong, irreversible metal-sulfur bond presents a challenges in obtaining crystalline materials multitopic ligands with only sulfur donor atoms .[12] One strategy to deal with this challenge is the use of heterodonor ligands, were the ligand molecule contains both hard and soft-donors capable of coordinating the same metal. The previously reported compound H_4DSBDC[13] ($DSBDC^{4-}$ = 2,5-disulfido-1,4-benzenedicarboxylate^{4-}) is analogous to H_4DOBDC, with thiophenol groups replacing the phenols. By reacting this ligand with ferrous chloride I was able to obtain a framework, Fe_2(DSBDC)(*N,N*-DMF)$_2$, **1**, that is isostructural to Fe_2(DOBDC). FP-TRMC measurements demonstrated that this framework displays intrinsic charge mobility while 2-point pressed pellet AC impedance measurements confirm the electronic conductivity of this material and show an increase in conductivity upon oxidation, indicative of *p*-type conduction.

5.2 Experimental

General Considerations *N,N*-dimethylformamide and acetonitrile were deoxygenated by sparging with argon for 1 h and dried using a commercial solvent purification system designed by JC Meyer Solvent Systems. Anhydrous methanol was purchased from Sigma Aldrich and was deoxygenated by sparging with argon with dinitrogen for one hour. Infrared spectra were collected on a Perkin Elmer Spectrum FT-IR/FT-FIR spectrometer equipped with a Pike Technologies GladiATR attenuated total reflectance (ATR) accessory. Single crystal diffraction measurements were performed on a Bruker Platinum 200 instrument at the Advanced Light Source at the Lawrence Berkeley National Laboratory. Carbon, hydrogen, and nitrogen analyses were obtained from the Microanalytical Laboratory of the University of California, Berkeley. UV-visible-NIR diffuse reflectance spectra were collected using a CARY 5000 spectrophotometer interfaced with Varian Win UV software.

Fe_2DOBDC was prepared as previously reported.[4]

H_4DSBDC was synthesized according to a previously reported procedure.[13]

Fe_2DSBDC (1) Single crystal: In a dinitrogen glove box, a half-sealed ½" borosilicate tube was charged with 0.027 g (0.057 mmol) of $FeCl_2$ and 0.023 g (0.01 mmol) of H_4DSBDC, 1 g of *N,N*-dimethylformamide and 1 g of methanol. A rubber tube-sealer adaptor was then attached to the open end of the borosilicate tubing. The sample was then removed from the glove box, connected to a Schlenk line and freeze-pump-thawed 5 times with liquid nitrogen. The tube was then evacuated flash frozen and flame sealed to 6" length. The sealed tube was then placed in a tube furnace and ramped to 120°C at 0.1°C/min and held at that temperature for 4000 minutes. The temperature was brought down to room temperature at 1°C/min.

Bulk Synthesis of 1 A 250 ml Schlenk flask was charged with a magnetic stir bar, 0.4780 g (3.77 mmol) of $FeCl_2$ and 0.3996 g (1.72 mmol) of H_4DSBDC. 105 ml *N,N*-dimethylformamide and 125 ml methanol was added to the flask and attached to a Schlenk line. The flask was then attached to a reflux condenser and heated to 120°C for 12 hours. The reaction mixture was cooled to room temperature and the supernatant removed by cannula filtration. The reaction flask was evacuated until the product was dry. An aliquot of this material was then flame sealed in a capillary to confirm its phase purity. FT-IR (cm^{-1}): 2925 (w) 2857 (w) 1655 (w) 1534 (s) 1357 (s) 1304 (w) 1345 (m) 1146 (w) 1086 (s) 1061 (w) 889 (w) 841 (s) 793 (m) 675 (w) 633 (m) 572 (m) 559 (m) 529 (w). Anal. Calcd for $Fe_2C_{14}H_{16}N_2O_6S_2$: C, 34.73; H, 3.33; N, 5.79; S, 13.25. Found: C, 34.90; H, 3.64; N, 6.06; S, 12.99.

Single Crystal Structure Solution of 1 Single crystals of **1** were obtained from the above sealed tube reaction. A suitable crystal was selected and coated with Paratone-N oil and then mounted on Kaptan loops. Crystals were frozen at a temperature of 100 K by an Oxford Cryosystems Cryostream using N_2 and kept at that temperature during data collection. Data was collected at Beamline 11.3.1 at the Advanced Light Source, Lawrence Berkeley National Laboratory using synchrotron radiation (λ = 0.8856). Using Olex2,[14] the structure was solved with the ShelXT[15] structure solution program using Direct Methods and refined with the ShelXL[15] refinement package using Least Squares minimization.

2-point AC Impedance Spectroscopy In an argon-filled glove box, ac impedance spectroscopy measurements were made using a homemade test cell on thermostatted pressed samples using a Solartron 1260 frequency response analyzer connected to a Solartron 1296 dielectric interface and blocking stainless steel electrodes. SMART (v1.1.1) software was used as control software. Measurements were made over a frequency range of 1 MHz to 1 Hz using a 100 mV (peak voltage) applied ac signal. Ten measurements were made in every frequency decade with 1 s integration times at each frequency.

Flash Photolysis Time-Resolved Microwave Conductivity Measurements FP-TRMC measurements were conducted at 25 ºC under N_2 atmosphere, using **1**/poly(methylmethacrylate) (PMMA) films (50/50 in wt%). The films were cast onto quartz substrates. The microwave power and frequency were set at 3mW and ~9.1 GHz, respectively. Charge carriers were generated in the films by direct excitation of MOFs using a third harmonic generation (λ = 355 nm) light pulses from a Nd: YAG laser (Spectra Physics, INDI-HG). The excitation density was tuned at 6.5×10^{15} photons cm^{-2} per pulse. A resonant cavity was used to obtain high sensitivity in the measurement of transient conductivity. The TRMC signal from a diode was recorded on a digital oscilloscope (Tektronix, TDS 3032B). To determine the quantum efficiency of charge carrier generation the **1**/PMMA films were deposited on gold interdigitated electrodes (electrode separation = 5 μm) and the photocurrent was measured upon irradiation with a 355 nm pulse. The integrated photocurrent of a standard sample of poly(9,9-dioctylfluorene) with a measured ϕ value of 2.3 x 10^{-4} (determined by transient absorption spectroscopic measurements) was measured. Comparison of the integrated photocurrents with the polymer standard allowed determination of the quantum efficiency of charge carrier generation in the samples of **1**.

5.3 Discussion and Results

Diffraction quality single crystals of **1** were obtained from a sealed tube reaction. Figure 5.1 shows the structure of **1**. It is built of infinite one-dimensional helical chains of vertex sharing Fe^{2+} ions as shown in Figure 5.2. The Fe^{2+} ions are bridged by the sulfur atom of the thiophenolate group and one of the oxygen atoms from the carboxylate group. This compound is isostructural to Fe_2(DOBDC), the structure of which is shown in Figure 5.3 Table 5.1 shows crystallographic data for **1**. While the crystals were large enough to obtain crystal structures through single-crystal x-ray diffraction experiments, they were not large enough for single crystal conductivity measurements. It was possible to obtain bulk powder of **1**, allowing interrogation of this material's charge transport characteristics by pressed pellet measurements and FP-TRMC experiments. Attempts to evacuate guest solvent and obtain surface area measurement of this material were unsuccessful.

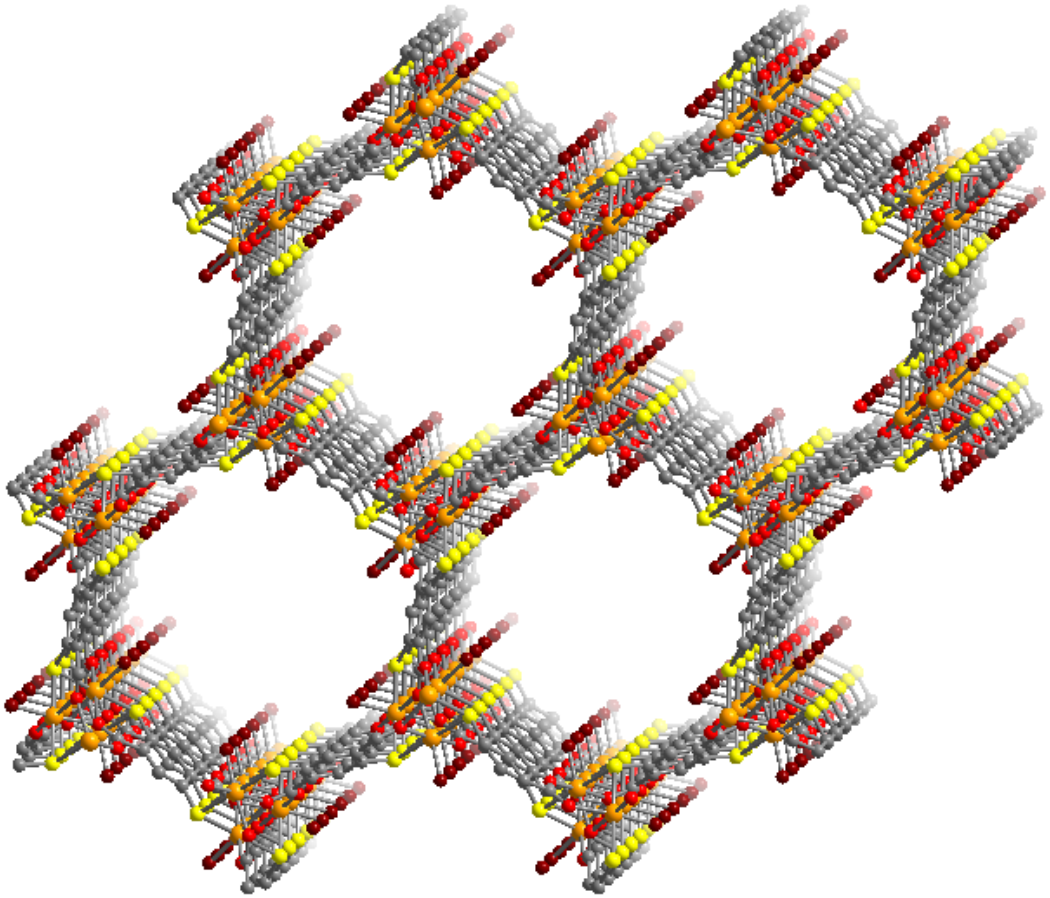

Figure 5.1 A ball and stick representation of **1**. Orange, yellow, gray spheres represent iron, sulfur, and carbon atoms. Red and burgundy spheres represent oxygen atoms from the $DSBDC^{4-}$ linker and coordinated *N,N*-DMF molecules, respectively. Hydrogen atoms and non-oxygen solvent molecules have been omitted for clarity.

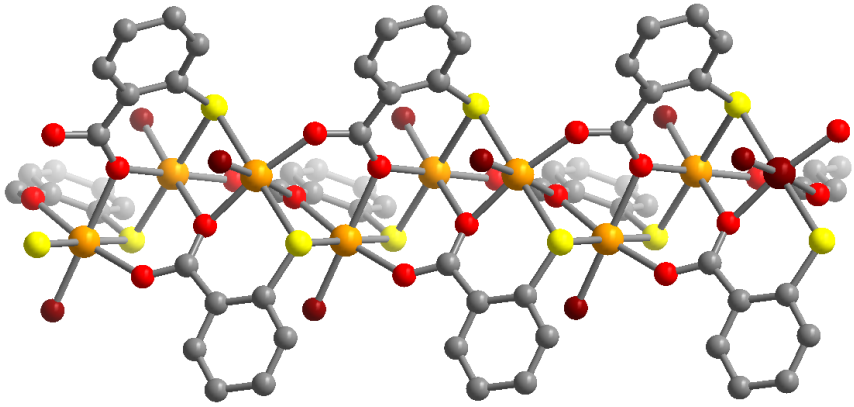

Figure 5.2 A ball and stick representation of a section of the one-dimensional chains of **1**. Orange, yellow, gray spheres represent iron, sulfur, and carbon atoms. Red and burgundy spheres represent oxygen atoms from the $DSBDC^{4-}$ linker and coordinated *N,N*-DMF molecules, respectively. Hydrogen atoms and non-oxygen solvent molecules have been omitted for clarity.

Table 5.1 Crystal data and structure refinement for **1.**

	1 - $Fe_2(DSBDC)(N,N\text{-}DMF)_2$
Empirical formula	$C_{10.5}H_9Fe_{1.5}N_{1.5}O_{4.5}S_{1.5}$
Formula weight	360.05
Temperature/K	100 K
Crystal system	Trigonal
Space group	R-3
a/Å	27.428(3)
b/Å	27.428(3)
c/Å	7.2075(8)
α/°	90
β/°	90
γ/°	120
Volume/$Å^3$	4695.8(12)
Z	12
$\rho_{calc}g/cm^3$	1.528
μ/mm^{-1}	2.931
F(000)	2178.0
Crystal size/mm^3	150 × 15 × 15
Radiation	Synchotron (λ = 0.8856)
2Θ range for data collection/°	6.412 to 85.856
Index ranges	$-42 \leq h \leq 42$, $-40 \leq k \leq 42$, $-10 \leq l \leq 11$
Reflections collected	25010
Independent reflections	3994 [R_{int} = 0.0471, R_{sigma} = 0.0356]
Data/restraints/parameters	3994/63/194
Goodness-of-fit on F^2	1.066
Final R indexes [I>=2σ (I)]	R_1 = 0.0418, wR_2 = 0.1297
Final R indexes [all data]	R_1 = 0.0649, wR_2 = 0.1446
Largest diff. peak/hole / e $Å^{-3}$	0.90/-0.52

[a] $R_1 = \Sigma||F_o|-|F_c||/\Sigma|F_o|$, $wR_2 = \{\Sigma[w(F_o^2-F_c^2)^2]/\Sigma[w(F_o^2)^2]\}^{1/2}$

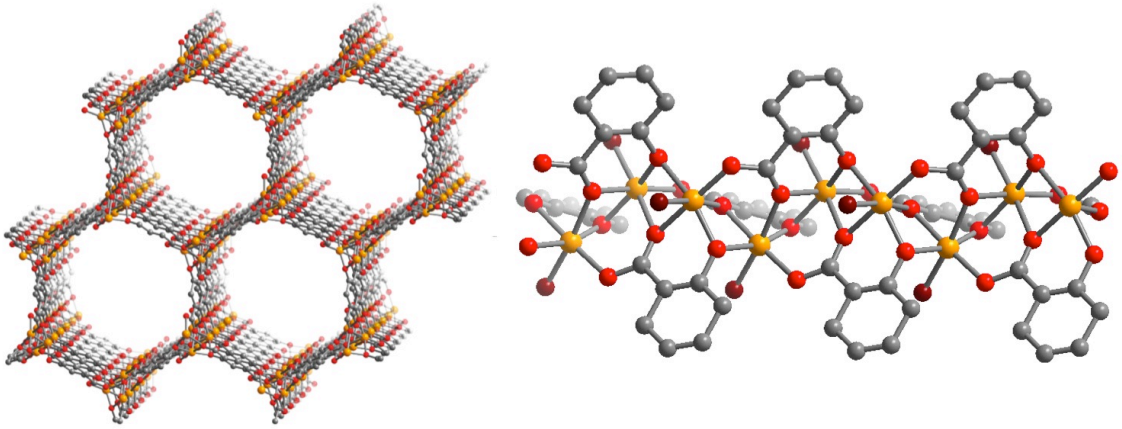

Figure 5.3 A ball and stick representation of (left) a section of Fe_2(DOBDC) structure and (right) a portion of its one-dimensional chains. Orange, yellow, gray spheres represent iron, sulfur, and carbon atoms. Red and burgundy spheres represent oxygen atoms from the $DOBDC^{4-}$ linker and coordinated *N,N*-DMF molecules, respectively. Hydrogen atoms and non-oxygen solvent molecules have been omitted for clarity.

Two-point AC impedance spectroscopy of pressed pellets of Fe_2(DOBDC) showed no conductivity above that of the resolution of the impedance analyzer (10^{-12} S/cm). Pressed pellets of **1** are, however, conductive. Figure 5.4 is a Nyquist plot of a 2-point AC impedance spectroscopy measurement. Because the impedance spectra touches the real axis, the stainless steel electrodes were not blocking to the charge carriers in this material, indicating electronic conduction.[16] The conductivity of this pellet is 6.0×10^{-10} S/cm. The observation of conductivity in **1** as opposed to Fe_2(DOBDC) indicates that the incorporation of bridging sulfur atom ligands is an effective strategy to engender conductivity in metal-organic frameworks. Upon oxidation with one equivalent of ferrocinium hexafluorophosphate for every two irons in **1** in acetonitrile solvent, the pressed pellet conductivity increases to 4.0×10^{-8} S/cm, indicative of *p*-type conduction. It should be noted that the plot of the unoxidized material is a depressed semicircle indicative of inhomogeneites in the conduction pathways such as different crystallites of different quality, different crystal face contacts, and different interparticle resistivities as well as electrode/crystallite interfaces. The Nqyuist plot of **1** after oxidation shows at least two apparent semicircles suggesting two conduction pathways that are being resolved, such as bulk conduction and interparticle conduction, or the electrode pellet interfacial charge transfer and interparticle charge transfer.

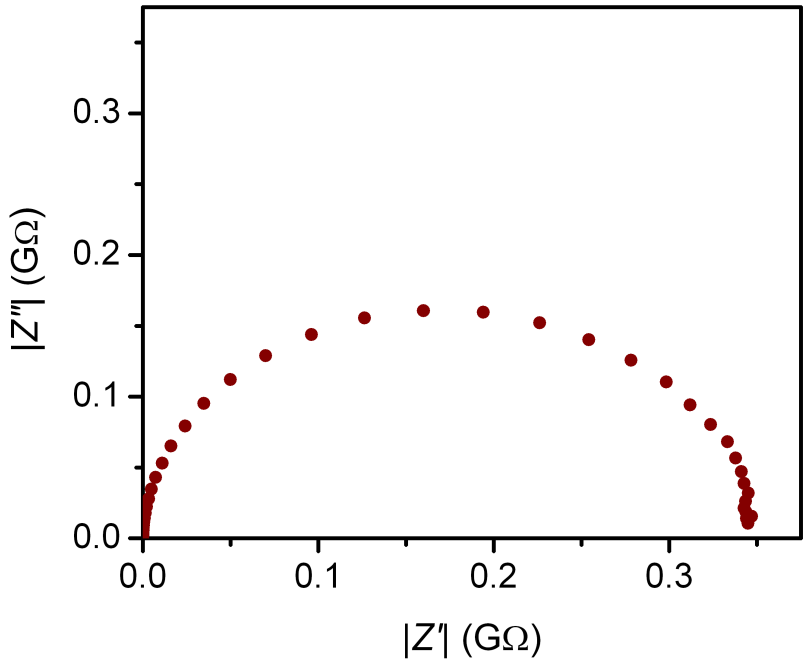

Figure 5.4 Nyquist plot of 2-point AC impedance spectra of a pressed pellet of **1**.

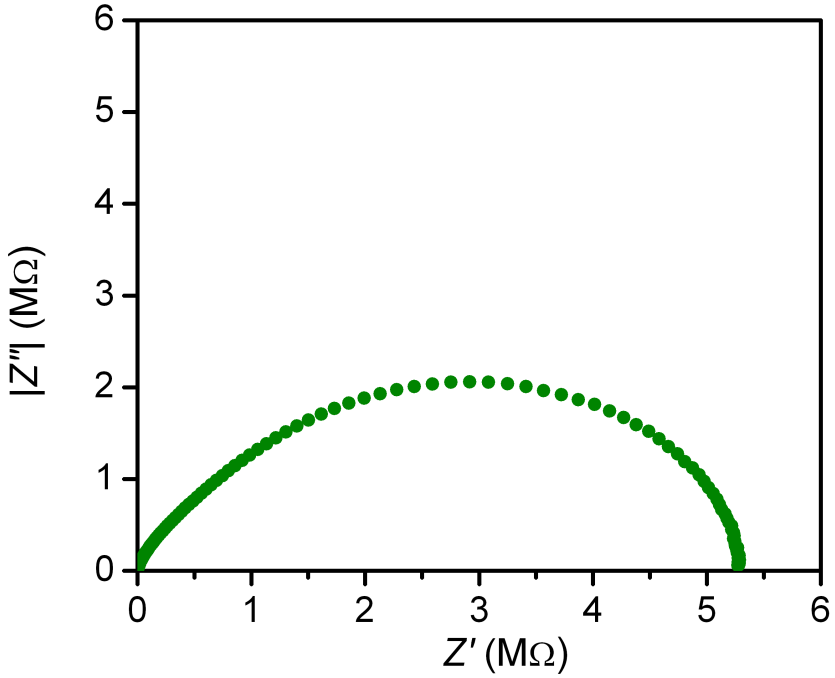

Figure 5.5 Nyquist plot of 2-point AC impedance spectra of a pressed pellet of **1** oxidized with $FeCp_2PF_6$.

Because pressed pellet conductivity measurements are limited by sample inhomogeneties and interfacial impedances, FP-TRMC[17] was used to gain further insight into the charge transport of **1**. The peak transient mobility of **1**, $\phi\Sigma\mu = 5.6 \times 10^{-5}$ cm^2/V·s divided by the estimated quantum efficiency of charge carrier generation, $\phi = 3.5 \times 10^{-4}$ indicates that the total charge mobility is 0.17 cm^2/V·s, in the range of conductive polymers such as

polyphenylenevinylenes (μ = 0.01−0.1 $cm^2/V{\cdot}s$)[18] and polythiophenes (0.015−0.075 $cm^2/V{\cdot}s$)[19]

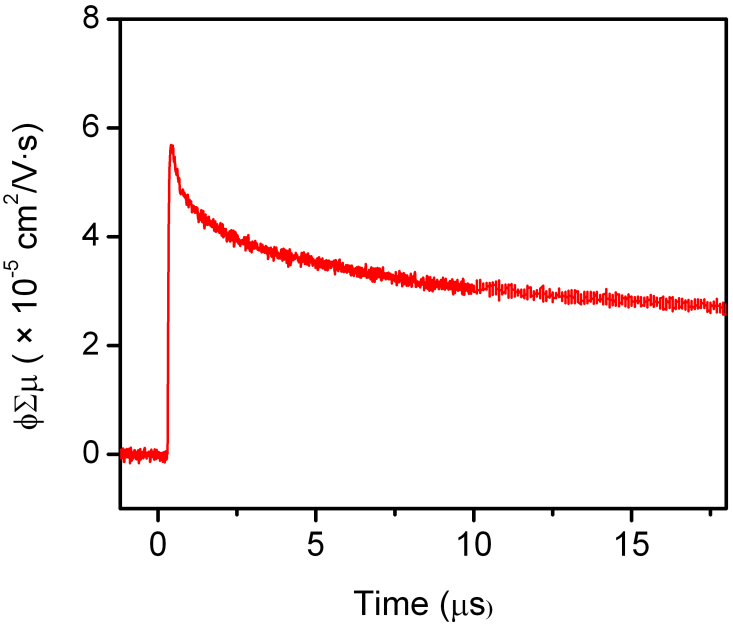

Figure 5.6 Conductivity transients of **1** observed by FP-TRMC upon excitation at 355 nm with 6.5×10^{15} photons cm^{-2} per pulse.

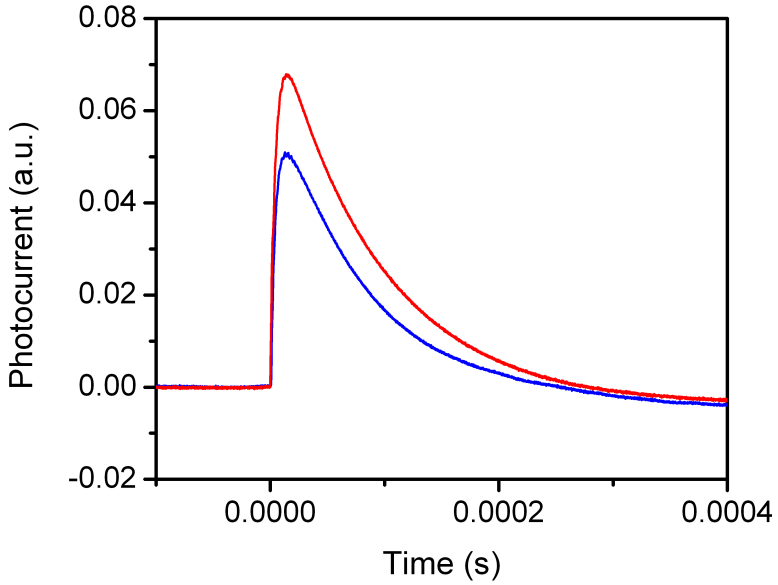

Figure 5.7 Photocurrents of **1** (red) and poly-9,9-dioctylfluorene (blue) after excitation with a 355 nm laser pulse.

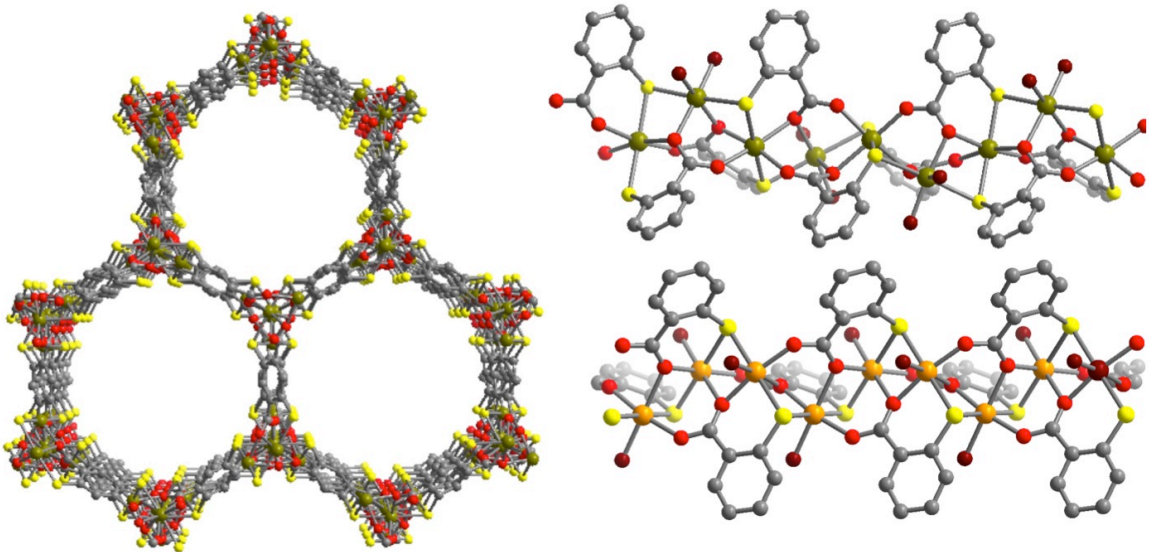

Figure 5.8 Left: View of Mn_2(DSBDC) down its pores. Right: One-dimensional chains of Mn_2(DSBDC) (top) and one-dimensional chains of **1** (bottom). Gray, yellow, red, and burgundy spheres are carbon, sulfur, oxygen atoms from the organic linker and oxygen atoms from solvent ligands. The chartreuse spheres are Mn^{2+} ions, and the orange spheres are Fe^{2+} ions. Hydrogen atoms and non-oxygen atoms of the solvent molecules are omitted for clarity.

One reported metal-organic framework is $Mn_2(DSBDC)_2$[20] This framework has a structure similar to both Fe_2(DOBDC) and **1** (as well as $Mn_2(DOBDC)_2$[3c]) with a honeycomb structure with hexagonal channels and is built of one-dimensional chains of edge sharing octahedra. Figure 5.8 shows the structure of Mn_2(DSBDC) as well as sections of the one-dimensional chains that comprise **1** for comparison. Unlike **1** and Fe_2(DOBDC), Mn_2(DSBDC) has two independent Mn^{2+} ions that are bridged by sulfur and oxygen atoms of the ligand. One Mn^{2+} ion has two solvent molecules that can be exchanged, the other has no coordinating solvent. As synthesized, the material is coordinated by DMF, which can be exchanged with methanol and then activated. FP-TRMC measurements of this material shows a total charge mobility of 0.02 $cm^2/V•s$ that decreases upon activation to 0.01 $cm^2/V•s$. In **1**, equivalent Fe^{2+} ions are spaced 3.19 Å apart from each other, whereas in Mn_2(DSBDC) the nearest neighbor Mn···Mn distance is 3.34 Å and 6.20 Å between nearest equivalent Mn^{2+} ions. Additionally, Fe···S distances in **1** are closer, 2.44 Å and 2.45 Å, in comparison to 2.49 Å and 2.63 Å in Mn_2DSBDC. The closer sulfur-metal distances and nearest neighbor metal-metal distances may help to improve electron transfer. Furthermore, a d^5/d^6 couple in a pseudo-octahedral coordination environment should make hole/electron transfer more energetically favorable[21] than the d^4/d^5 couple associated with electron transfer in a Mn^{2+} based material. One notable feature of the conductivity transient decay curve in Figure 5.6 is the lack of a clearly resolvable knee. A knee is clearly observed in the conductivity transients of Mn_2(DSBDC) and is attributed to conduction through the 1,4-benzenedithiolate moiety. That this feature is lacking in the FP-TRMC conductivity transients of **1** may indicate that the Fe-S-Fe chain is far more dominant than charge transfer through 1,4-benzenedithiol moiety.

5.4 Outlook and Conclusions

This work demonstrates the successful incorporation of bridging chalcogenides in a metal-organic framework to engender intrinsic charge transport in a metal-organic framework. An obvious extension of this work would be to form metal-organic frameworks with ligands with even more electropositive chalcogenide donors such as selenium or tellurium. An isoreticular analogue of the M_2(DOBDC) has been reported M_2(*m*-DOBDC) with the ligand 2,3-dihydroxy-1,4-benzenedicarboxylic acid, where the hydroxyl groups are *meta* to each other.[22] Similar changes in ligand symmetry to the H_4DSBDC ligand may further tune electronic properties. The M_2(DOBDC) structure type can be expanded isoreticularly.[23,24] The expanded Mg(DOBPDC) (DOBPDC^{4-} = 4,4′-dioxido-3,3′-biphenyldicarboxylate^{4-}) is reported to be more stable than Mg_2(DOBDC).[24] It is possible that a similarly expanded analogue may be more amenable to activation than **1**, giving a permanently microporous, conductive metal-organic framework.

5.5 Acknowledgements

I gratefully acknowledge KRICT grant and the National Science Foundation for funding, Miguel Gonzalez and Rodi Gavosta-Torres for crystallographic and experimental assistance, as well as Prof. Mircea Dinca, Lei Sun, and Michael Aubrey for lively and helpful discussions.

5.6 References

(1) Rosi, N. L.; Kim, J.; Eddaoudi, M.; Chen, B.; O'Keeffe, M.; Yaghi, O. M. *J. Am. Chem. Soc.* **2005**, *127*, 1504.
(2) Férey, G.; Millange, F.; Morcette, M.; Serre, C.; Doublet, M.-L.; Grenèche, J.-M.; Tarascon, J.-M. *Angew. Chem. Int. Ed.* **2007**, *46*, 3259.
(3) (a.) Dietzel, P. D. C.; Morita, Y.; Blom, R.; Fjellvåg, H. *Angew. Chem., Int. Ed.* **2005**, *44*, 6354. (b.)Dietzel, P. D. C.; Panella, B.; Hirscher, M.; Blom, R.; Fjellvåg, H. *Chem. Commun*. **2006**, 959. (c.) Zhou, W.; Wu, J.; Yildirim, T. J. Am. Chem. Soc. **2008**, *130*, 15268. (d.) Caskey, S. R.; Wong-Foy, A. G.; Matzger, A. J. *J. Am. Chem. Soc.* **2008**, *130*, 10870. (e.) Bhattacharjee, S.; Choi, J.; Yang, S.; Choi, S. B.; Kim, J.; Ahn, W. *J. Nanosci. Nanotechnol.* **2010**, *10*, 135. (f.) R. Sanz, R.; Martínez, F.; Orcajo, G.; Wojtas, L.; Briones, D. *Dalton Trans.* **2013**, *42*, 2392
(4) Bloch, E. D.; Murray, L. J.; Queen, W. L.; Chavan, S.; Maximoff, S. N.; Bigi, J. P.; Krishna, R.; Peterson, V. K.; Grandjean, F.; Long, G. J.; Smit, B.; Bordiga, S.; Brown, C. M.; Long, J. R. *J. Am. Chem. Soc.* **2011**, *133*, 14814.
(5) Hendon, C. H.; Tiana, D.; Walsh, A. Phys. Chem. Chem. Phys. 2012, 14, 13120.
(6) Warmbier, R.; Quandt, A.; Seifert, G. *J. Phys. Chem. C* **2014**, 140523084022000.
(7) Zagorodniy, K.; Seifert, G.; Hermann, H. *Appl. Phys. Lett.* **2010**, *97*, 251905.
(8) Zaanen, J.; Sawatzky, G. A.; Allen, J. W. *Phys. Rev. Lett.* **1985**, *55*, 418.
(9) Holliday, B. J.; Swager, T. M. *Chem. Commun*. **2005**, 23.

(10) Turner, D. L.; Vaid, T. P.; Stephens, P. W.; Stone, K. H.; DiPasquale, A. G.; Rheingold, A. L. *J. Am. Chem. Soc.* **2008**, *130*, 14.
(11) Amo-Ochoa, P. ; Castillo, O.; Alexandre, S. S.; Welte, L.; de Pablo, P. J.; Rodriguez-Tapiador, M. I.; Gomez-Herrero J.; Zamora, F. *Inorg. Chem.* **2009,** *48*, 7931.
(12) Mensforth, E.J.; Hill, M. R.; Baten, S. R. *Inorg. Chim. Acta* **2013**, *403*, 9.
(13) Field, L.; Engelhardt, P. R. *J. Org. Chem.* **1970**, *35*, 3647.
(14) Dolomanov, O.V., Bourhis, L.J., Gildea, R.J, Howard, J.A.K. & Puschmann, H. (2009), *J. Appl. Cryst.* 42, 339.
(15) Sheldrick, G.M. (2008). *Acta Cryst*. A64, 112-122.
(16) Barsukov, E.; MacDonald, R. J. *Impedance Spectroscopy: Theory, Experiment, and Applications, 2nd Ed.* Springer, Berlin 2004.
(17) (a.) Saeki, A.; Koizumi, Y., Aidia, T.; Seki, S. *Acc. Chem. Res.* **2012**, *45*, 1193. (b.) Saeki, A.; Seki, S.; Koizumi, Y.; Tagawa, S. *J. Photochem. Photobiol. A*, **2007**, *186*, 158. (c.) Saeki, A.; Seki, S.; Sunagawa, T.; Ushida, K.; Tagawa S. *Philos. Mag.* **2006**, *86*, 1261.
(18) Krebs, F. C.; Jørgensen, M. *Macromolecules* **2003**, *36*, 4374.
(19) Saeki, A.; Seki, S.; Koizumi, Y.; Sunagawa, T.; Ushida, K.; Tagawa, S. *J. Phys. Chem. B* **2005**, *109*, 10015.
(20) Sun, L.; Miyakai, T.; Seki, S. Dinca, M. *J. Am. Chem. Soc.* **2013**, *135*, 8185.
(21) (a.) Creutz C. *Prog. Inorg. Chem.* **1983**, *30*, 1. (b.) Richardson, D. E.; Taube, H. *Coord. Chem. Rev.* **1984**, *60*, 107. (c.) Crutchley, R. J. *Adv. Inorg. Chem.* **1994**, *41*, 273.
(22) Kapelewski, M. T.; Geier, S. J.; Hudson, M. R.; Stuk, D.; Mason, J. A.; Nelson, J. N.; Xiao, D. J.; Hulvey, Z.; Gilmour, E.; FitzGerald, S. A.; Head-Gordon, M.; Brown, C. M.; Long, J. R. *J. Am. Chem. Soc.* **2014**, *136*, 12119-12129.
(23) Deng, H.; Grunder, S.; Cordova, K. E.; Valente, C.; Furukawa, H.; Hmadeh, M.; Gańdara, F.; Whalley, A. C.; Liu, Z.; Asahina, S.; Kazumori, H.; O'Keeffe, M.; Terasaki, O.; Stoddart, J. F.; Yaghi, O. M. *Science* **2012**, *336*, 1018.
(24) McDonald, T. M.; Lee, W. R.; Mason, J. A.; Wiers, B. M.; Hong, C. S.; Long, J. R. *J. Am. Chem. Soc.* **2012**, *134*, 7056.

Appendix A: Novel Pyrazole Ligands and Pyrazolate Frameworks with Divalent, Tetrahedral Metal Ions.

A.1 Introduction

Metal-organic frameworks built from pyrazolate based ligands have shown applicability in a range of applications electronic conductivity discusses in this work as well to hydrogen storage[1,2] and gas separations.[3] The high pK_a of pyrazoles gives strong-metal ligand bonds[4] and some of these frameworks display high thermal and chemical stabilities.[5] One metal-organic framework, Co(BDP) (BDP = 1,4-benzenedipyrazolate$^{2=}$), displays a stepped isotherm due to framework flexibility.[1,6] Its zinc analogue, Zn(BDP) is also reported.[1] By alteration of the ligand it may be possible to tune the gas sorption, flexibility and stability properties of these materials. Herein, I demonstrate the synthesis of five novel dipyrazole ligands and five novel pyrazolate frameworks.

A.2 Experimental

Physical measurements. Infrared spectra were collected on a Perkin Elmer Spectrum FT-IR/FT-FIR spectrometer equipped with a Pike Technologies GladiATR attenuated total reflectance (ATR) accessory. Carbon, hydrogen, and nitrogen analyses were obtained from the Microanalytical Laboratory of the University of California, Berkeley. Mass spectra were obtained from the QB3/Chemistry Mass Spectrometry Facility at UC Berkeley. ^{1}H and ^{13}C NMR spectra were recorded at ambient temperature on Bruker AVQ-400 spectrometers, and all chemical shifts are given in relation to residual solvent peaks. The following abbreviations are used for spin multiplicity: *s* = singlet, *d* = doublet, *t*= triplet, *q*= quartet, *m* = multiplet, *br* = broad. Unless otherwise specified all reagents and solvents were purchased from commercial vendors and used without further purification. 1,4-dibromo-2,5-dimethoxybenzene was synthesized as previously reported.[7]

1-(tetrahydro-2*H*-pyran-4-yl)-4-(4,4,5,5-tetramethyl-1,3,2-dioxaborolan-2-yl)-1*H*-pyrazole (1). A 250mL round bottom flask was charged with a stir bar and 2.766 g (14.3 mmol) of 4-(4,4,5,5-tetramethyl-1,3,2-dioxaborolan-2-yl)-1*H*-pyrazole. 140 mL of toluene was added and the reaction mixture was stirred until all the pyrazole dissolved. 1.925 mL (21.3 mmol) of 2,3-dihydropyran was added to the reaction mixture and the flask was attached to a reflux condenser and purged with nitrogen. Via syringe 0.064g (0.56 mmol) of trifluoroacetic acid dissolved in 1.429 mL toluene was added to the reaction mixture. The mixture was heated at 85 °C under nitrogen atmosphere overnight. When all starting material had disappeared, the reaction mixture was removed from heat and solvent was removed by rotary evaporation yielding a brown oil. The oil was taken up into 2 mL of methylene chloride and chromatographed over a silica gel column (1:2 (v:v) ethyl acetate:hexanes). The elution solvent was removed by rotary evaporation to yield 3.742g (94.4%) of white flaky crystals. IR (ATR, cm^{-1}): 3090, 2975, 2940, 2860, 1555, 1465, 1445, 1410, 1380, 1370, 1315, 1295, 1255, 1215, 1200, 1165, 1140, 1110, 1085, 1060, 1045, 1015, 1005, 985, 935, 875, 855, 830, 800, 765, 710, 690, 665, 615, 595, 580, 550, 520, 510, 460. ^{1}H-NMR (400 MHz, DMSO-*d*6): δ 7.928 (s, 1H), 7.816 (s,

1H), 5.344 (dd, *J* = 6.8 Hz and 2.4 Hz, 1H), 4.032 (dd, *J* = 9.6 Hz and 2.8 Hz, 1H), 3.682 (td, *J* = 10.4 Hz and 3.2 Hz, 1H), 2.063(m, 3H) 1.656 (m, 3H), 1.300 (s, 12H) ^{13}C-NMR (400 MHz, $CDCl_3$): δ 145.64, 134.97, 87.54, 83.52, 67.91, 30.71, 25.15, 25.00, 24.91, 22.54. Anal. Calcd for $C_{14}H_{23}N_2O_3B$: C, 60.45; H, 8.33; N, 10.07. Found: C, 60.39; H, 8.47; N, 9.93. MS (EI) m/z 278 (M^+) MS (EIHR) for $C_{14}H_{23}N_2O_3B$, calcd (found) *m/z*: 278.1802 (278.1805)

2,6-bis(1-(tetrahydro-2H-pyran-2-yl)-1*H*-pyrazol-4-yl)naphthalene (2). A 250 mL oven dried round bottom flask was charged with a stir bar, 0.937 g (3.27 mmol) 2,6-dibromonaphthalene, 2.000 g (7.190 mmol) 1-(tetrahydro-2*H*-pyran-4-yl)-4-(4,4,5,5-tetramethyl-1,3,2-dioxaborolan-2-yl)-1*H*-pyrazole, 0.264 g (0.23mmol) tetrakis(triphenyl-phosphine) palladium(0) and 2.546 g (7.814 mmol) cesium carbonate, purged with nitrogen and attached to a condenser. 100 mL of a degassed 1:1 (v:v) mixture of *p*-dioxane and water was added to the reaction vessel and the mixture was stirred and heated to 85 °C under an nitrogen atmosphere for 2d. The reaction mixture was removed from heat and solvent was removed by rotary evaporation to yield a grey-brown residue. The residue was taken up in 150 mL of methylene chloride and washed with 200 mL deionized water. The aqueous layer was extracted with methylene chloride (2x 200 mL) and the combined organics were dried over $MgSO_4$. The solvent was removed by rotary evaporation to yield a brownish residue that was taken up into methylene chloride chromatographed over silica gel (5:1 (v:v) ethyl acetate: hexanes). The elution solvent was removed by rotary evaporation to yield 0.771g (55.1%) of a flaky white solid. IR (ATR, cm^{-1}): 3110, 2940, 2855, 1730, 1615, 1555, 1505, 1450, 1440, 1430, 1395, 1375, 1350, 1285, 1260, 1210, 1180, 1140, 1120, 1080, 1055, 1040, 1015, 975, 940, 910, 900, 875, 855, 820, 785, 755, 720, 695, 685, 655, 625, 540, 520, 495, 475, 460. ^{1}H-NMR (400 MHz, $CDCl_3$): δ 7.9533 (s, 2H), 7.903 (s, 2H), 7.809 (d, *J* = 8.4 Hz, 2H), 7.611 (d, *J* =8.6 Hz, 2H), 7.381 (d, J =7.2 Hz, 2H), 5.436 (dd, *J* = 9.2 Hz and 2.8 H, 2H), 4.102 (dd, *J* = 11.2 Hz and 2.4 Hz, 2H), 3.739 (td, *J* = 11 Hz and 2.4 Hz, 2H), 2.146 (m, 6H), 1.694 (m, 6H) . ^{13}C-NMR (400 MHz, $CDCl_3$): δ137.52, 132.79, 129.71, 128.49, 125.19, 124.87, 123.64, 123.53, 88.03, 68.05, 30.77, 25.17, 22.6. Anal. Calcd. For $C_{26}H_{28}N_4O_2$: C, 72.87; H, 6.59; N, 13.07. Found C, 72.86; H, 6.75; N, 13.07. MS (EI) m/z 428 (M^+)

2,6-di(*1H*-pyrazol-4-yl)naphthalene (H_2NDP) (3). A 250 mL single neck round bottom flask was charged with 0.669 g (1.56 mmol) 2,6-bis(1-(tetrahydro-2*H*-pyran-2-yl)-1*H*-pyrazol-4-yl)naphthalene and a stir bar. 100 mL of ethanol and 15mL of concentrated hydrochloric acid were added to the flask that was then attached to a condenser and refluxed overnight under dinitrogen atmosphere. The solid product was washed repeatedly with deionized water until the filtrate was neutral to yield 0.287g of an off-white solid (70.6% yield.) IR (ATR, cm^{-1}): 3300-2400 (br) 1610, 1565, 1500, 1510, 1435, 1375, 1350, 1295, 1255, 1230, 1185, 1160, 1140, 1090, 1030, 960, 880, 850, 810, 685, 650, 620, 545, 480, 470 ^{1}H-NMR (400 MHz, DMSO-d_6): δ 13.016 (br s, 2H), 8.472 (br s, 2H), 8.082 (s, 2H), 7.846 (d, *J* = 8.8 Hz, 2H), 7.781 (d, *J* = 8.4 Hz, 2H). ^{13}C-NMR (400 MHz, DMSO-d_6): δ 135.95, 132.11, 129.49, 127.98, 124.90, 122.49, 121.36 MS (EI) m/z 260 (M^+) MS (EIHR) for $C_{16}H_{12}N_4^+$ calcd(found): 260.1062(260.1054).

9,10-bis(1-(tetrahydro-2H-pyran-2-yl)-1*H*-pyrazol-4-yl)anthracene (4). A 250 mL oven dried round bottom flask was charged with a stir bar, 1.098g (3.270 mmol) 9,10-dibromoanthracene, 2.000g (7.190 mmol) 1-(tetrahydro-2H-pyran-4-yl)-4-(4,4,5,5-

tetramethyl-1,3,2-dioxaborolan-2-yl)-1H-pyrazole, 0.305g (0.26mmol) tetrakis(triphenyl-phosphine) palladium(0) and 2.546g (7.814 mmol) cesium carbonate, purged with nitrogen and attached to a condenser. 100 mL of a degassed 1:1 (v:v) mixture of *p*-dioxane and water was added to the reaction vessel and the mixture was stirred and heated to 85 °C under an nitrogen atmosphere for 2d. The reaction mixture was removed from heat and solvent was removed by rotary evaporation to yield a brown residue. The residue was taken up in 150 mL of methylene chloride and washed with 200 ml deionized water. The aqueous layer was extracted with methylene chloride (2x 200 ml) and the combined organics were filtered and dried over $MgSO_4$. The solvent was removed by rotary evaporation to yield a yellow residue that was crystallized from acetone and hexanes to yield 0.696 (44.5%) pale beige needles. IR (ATR, cm^{-1}): 3085, 2940, 2855, 1620, 1570, 1465, 1440, 1380, 1340, 1320, 1300, 1285, 1270, 1250, 1200, 1180, 1145, 1135, 1080, 1060, 1040, 1020, 1010, 975, 935, 910, 875, 845, 820, 770, 675, 650, 605, 550, 520, 460 ^{1}H-NMR (400 MHz, $CDCl_3$): δ 7.969 (q, *J* = 3.2 Hz, 4H), 7.829 (s, 2H) 7.766 (s, 2H), 7.380 (q, *J* =3.2 Hz, 4H), 5.586 (dd, *J* = 8.6 Hz and 3.6 Hz, 2H), 4.181 (dd, *J* =11.6 Hz and 3.2 Hz, 2H), 3.815 (td, *J* =11.2 Hz and 2.8 Hz, 2H), 2.218 (m, 6H), 1.747 (m, 6H) ^{13}C-NMR (400 MHz, $CDCl_3$): δ 141.97, 131.11, 129.09, 128.01, 127.05, 126.82, 125.45, 118.32, 88.12, 68.24, 30.85, 25.21. MS (EI) m/z 478 (M^+).

9,10-di(1*H*-pyrazol-4-yl)anthracene (H_2ADP) (5). A 250 mL single neck round bottom flask was charged with 0.353 g (0.738 mmol) of 9,10-bis(1-(tetrahydro-2*H*-pyran-2-yl)-1*H*-pyrazol-4-yl)anthracene and a stir bar. 70 mL of methanol and 5mL of concentrated hydrochloric acid were added to the flask. The flask was attached to a condenser and refluxed overnight. 100 mL of deionized water was added to the reaction mixture and the product was collected over a Buchner funnel and washed with sodium carbonate solution until the wash was neutral. The yellow product was dried overnight on a vacuum line. Yield: 0.179g (78.2%). IR (ATR, cm^{-1}): 3300-2800 (br), 1620, 1575, 1510, 1435, 1410, 1370, 1320, 1260, 1200, 1155, 1135, 1065, 1045, 1025, 1010, 945, 910, 880, 855, 825, 770, 735, 670, 650, 615, 510 ^{1}H-NMR (400 MHz, DMSO-*d*6): δ 13.345 (s, 2H), 8.006 (s, 2H), 7.869 (q, *J* =2.4 Hz, 4H), 7.698 (s, 2H), 7.440 (q, *J* =4 Hz, 4H). ^{13}C-NMR (400 MHz, DMSO-d_6): δ 140.48, 130.45, 128.19, 126.59, 125.30, 115.64. MS (EI) m/z 310 (M^+) MS (EIHR) for $C_{20}H_{16}N_4^+$, calcd (found) *m/z*: 310.1218(310.1212)

1,4-bis(1-(tetrahydro-2H-pyran-2-yl)-1*H*-pyrazol-4-yl)-2,3,5,6-tetramethyl-benzene (6). A 250 mL oven dried round bottom flask was charged with a magnetic stir bar, 0.496g (1.28 mmol) 1,4-diiodo-2,3,5,6-tetramethylbenznene, 0.755 g (2.72 mmol) 1-(tetrahydro-2H-pyran-4-yl)-4-(4,4,5,5-tetramethyl-1,3,2-dioxaborolan-2-yl)-1H-pyrazole, 0.123g (0.11 mmol) tetrakis(triphenyl-phosphine) palladium(0) and 1.534 g (15.4 mmol) potassium carbonate and 0.070 g lithium chloride (1.65 mmol), purged with nitrogen and attached to a condenser. 100 mL of a degassed 1:1 (v:v) mixture of *p*-dioxane and water was added to the reaction vessel and the mixture was stirred and heated to 80 °C under an nitrogen atmosphere for 2 days when thin layer chromatrography showed the disappearance of the diiodotetramethylbenzene starting material. The reaction mixture was removed from heat and a flaky white solid precipitated that was collected by gravity filtration. The organics were extracted with methylene chloride (3 x 100 mL). The organic layer was dried under rotary evaporation was combined with the precipitate from the reaction mixture and together recrystallized from toluene. The white product was dried in a vacuum dessicator. Yield = 0.220 g (39%). IR (ATR, cm^{-1}): 3036(w), 2930(m),

2845(m), 1752 (w), 1434 (s), 1378 (s), 1347 (w), 1263 (m), 1199 (s), 1178 (m), 1070 (s), 1035 (s), 962 (s), 958 (m), 942 (w), 910 (s), 872 (s), 843 (w), 821 (w), 790 (w), 742 (m), 691 (w), 612 (w), 549 (w), 512 (s). ^{1}H-NMR (400 MHz, $CDCl_3$): δ 7.461 (s, 2H) 7.434 (s, 2H), 5.46 (br. d, *J* =4.8 Hz, 2 Hz), 4.115 (br. d., *J* = 5.6 Hz, 2H), (br. t., *J* = 10.4, 2H), 2.625- 2.057 (br. m., 6 H), 1.897-1.637 (br. m., 6H). ^{13}C-NMR (400 MHz, $CDCl_3$): δ 140.46, 134.98, 128.63, 127.11, 121.78, 87.33, 68.20, 30.67, 25.16, 22.74, 18.72 Anal. Calcd for $C_{26}H_{34}N_4O_2$: C, 71.86; H, 7.89; N, 12.89. Found: C, 71.55; H, 7.75; N, 12.50. MS (EI) m/z = 434 (M^+). MS (EIHR) for $C_{26}H_{34}N_4O_2^+$, calcd (found) *m/z*: 434.2686(434.2682).

1,4-bis(1*H*-pyrazol-4-yl)-2,3,5,6-tetramethylbenzene (H_2TMBDP) (7). A 100 mL single neck round bottom flask was charged with 0.200 g (0.46 mmol) of $(THP)_2$-TMBDP, a magnetic stir bar, 25 ml of methanol and 37 wt% aqueous HCl and attached to a reflux condenser. Under N_2 atmosphere the reaction mixture was refluxed for 18 hours. The reaction mixture was then left to cool to room temperature and 50 mL of a 0.6M aqueous $KHCO_3$ solution was added. The white precipitate was collected and dried in a vacuum dessicator. Yield = 0.122 g (99.5%). IR (ATR, cm^{-1}): 3300-2500 (br), 1577 (w), 1493 (m), 1459 (m), 1414 (w), 1365 (w), 1349 (m), 1263 (w), 1210 (s), 1149 (m), 1039 (s), 954 (m), 854 (m), 809 (w), 764 (s), 705 (w), 613 (m). ^{1}H-NMR (400 MHz, DMSO-*d*6): δ 12.91 (br. s., 2H), 7.453 (s, 4H), 1.947 (s, 12H). ^{13}C-NMR (400 MHz, DMSO-*d*6): δ 132.60, 131.92, 119.54, 18.28. MS (EI) m/z = 266 (M^+). MS (EIHR) for $C_{16}H_{18}N_4^+$, calcd (found) *m/z*: 266.1531 (266.1535).

1,4-bis(1-(tetrahydro-2H-pyran-2-yl)-1*H*-pyrazol-4-yl)-2,5-dimethoxybenzene (8). A 250 mL oven dried round bottom flask was charged with a magnetic stir bar, 1.665 g (4.31 mmol) 1,4-dibromo-2,5-dimethoxybenzene 3.341 g (12.0 mmol) 1-(tetrahydro-2H-pyran-4-yl)-4-(4,4,5,5-tetramethyl-1,3,2-dioxaborolan-2-yl)-1H-pyrazole, 0.458 g (0.37 mmol) tetrakis(triphenyl-phosphine) palladium(0). 140 mL of a degassed 1:1 (v:v) mixture of *p*-dioxane and 2M aq. Na_2CO_3 was added to the reaction vessel and the mixture was stirred and heated to reflux under an nitrogen atmosphere for 20 hours. The reaction mixture was filtered and extracted with methylene chloride (200 mL x 2). The organics were washed with brine (100 ml) and the aqueous layer was back extracted with methylene chloride (100 ml x 2). The combined organics were dried over $MgSO_4$ and solvent was removed by rotary evaporation to obtain a brown oil. The residue was purified by column chromatography (SiO_2, 1:1 (v:v) ethyl acetate:hexanes). The fractions containing the desired product were dried by rotary evaporation to yield an off-white powder. Yield = 1.50 g (61%). IR (ATR, cm^{-1}): 3124 (w), 3098 (w), 2938(m), 2922 (m), 2836 (m), 1684 (w) 1575 (m) 1498 (s), 1464 (s), 1458 (m) 1438 (s) 1422 (s), 1375 (vs), 1356 (m), 1315 (m), 1275 (s), 1257 (m), 1209 (s), 1198 (s), 1126 (w) 1079 (s), 1058 (m) 1040 (vs), 1020 (m), 983 (s) 965 (w) 938 (w), 910 (m) 879 (w), 855 (s), 818 (m), 791 (m), 762 (s), 722 (w), 704 (w), 694 (w), 659 (w), 627 (m), 555 (w), 540 (w). MS (EI) m/z = 438 (M^+).

1,4-bis(1*H*-pyrazol-4-yl)-2,5-dimethoxybenznene (H_2-*p*-DMEOBDP) (9). In a 100 ml round bottom flask, 1.472 g (3.36 mmol) of **(7)** was suspended in 50 mL of absolute ethanol and 2 mL of 37 wt% aqueous HCl and refluxed under N_2. Within one half hour the solids dissolved and after another hour solid precipitated. The reaction mixture was then allowed to cool and was neutralized with a saturated $NaHCO_3$ solution. The solid, white product was collected by filtration and dried in a vacuum dessicator.

Yield 0.910 g (100%). MS (EI) m/z = 270 (M^+). MS (EIHR) for $C_{14}H_{14}N_4O_2^+$, calcd (found) *m/z*: 270.1117(270.116).

2,5-bis(1*H*-pyrazol-4-yl)-*p*-benzoquinone (H_2-*p*-BQDP) (10). 0.441 g (1.01 mmol) of **8** was suspended in 10 ml of acetonitrile and 5 ml of dimethylsulfoxide in a 100 ml round bottom flask with a stir bar. 1.650 g of ceric ammonium nitrate (3.010 mmol) in 10 mL of deionized water was added and the reaction mixture was heated to reflux for one hour. Then 5 mL of 37 wt% aqueous HCl was added to the reaction mixture which was then refluxed for 2 hours. The reaction mixture was removed from heat and allowed to cool to room temperature. The reaction mixture was brought to a pH=8 with the addition of saturated $NaHCO_3$ solution and the orange precipitate was collected by filtration. Yield 0.153 g (64%). ^{1}H-NMR (400 MHz, DMSO-*d*6): δ 8.302 (s, 2H), 7.139 (s, 1H) ^{13}C-NMR (400 MHz, DMSO-*d*6): δ 187.24, 137.45, 126.27, 112.85. MS (EI) m/z = 270 (M^+).

Cobalt(2,6-naphthalenedipyrazolate) (11) single crystal synthesis. A 0.7cm OD borosilicate tube was charged with 34 mg (0.12 mmol) $Co(NO_3)_2$•$6H_2O$,15 mg ($5.8x10^{-5}$ mol) of 2,6-naphthalenedipyrazole and 0.4 ml DMF. The tube was freeze-pump-thawed seven times and then flash frozen, evacuated and flame sealed to final length of 8 cm. The sealed tube was placed in an oven an heated to 140^{o}C at a ramp rate of 0.2 °C min^{-1}. The temperature was held for 4000 minutes and then brought to room temperature was a cooling rate of 1 °C min^{-1}.

X-ray Structure Determination of (11). A single crystal of **11** was coated in Paratone-N oil, attached to a Kapton loop, quickly transferred to a Bruker Platinum 200 Instrument at the Advanced Light Source at the Lawrence Berkeley National Laboratory. Preliminary cell data were collected to give a unit cell consistent with the tetragonal Laue group, and the unit cell parameters were later refined against all data. A full hemisphere of data was collected. Data were integrated and corrected for Lorentz and polarization effects using SAINT 7.34[8] and were corrected for absorption effects using SADABS 2.10.[9] The structure was solved by direct and Patterson methods and expanded through successive difference Fourier maps. It was refined against all data using the SHELXTL 5.0[10] software package. A Flack parameter of 0.46(7) suggested twinning, and a twin component was therefore included with the twinning law of 0 1 0 1 0 0 0 0 –1. Thermal parameters for all non-hydrogen atoms on the framework skeleton were refined anisotropically. Application of the SQUEEZE routine in the PLATON[11] software package was applied to remove intensities from disordered solvent molecules in the framework pores.

Cobalt(1,4-tetramethylbenzenedipyrazolate) (12) single crystal synthesis. A 0.7cm OD borosilicate tube was charged with 34 mg (0.12 mmol) cobalt triflate,15 mg ($5.84x10^{-5}$ mol) of **7** and 0.4 ml *N,N*-diethylformamide. The tube was freeze-pump-thawed seven times and then flash frozen, evacuated and flame. The sealed tube was placed in an oven an heated to 150^{o}C at a ramp rate of 0.1 °C min^{-1}. The temperature was held for 4000 minutes and then brought to room temperature was a cooling rate of 1 °C min^{-1} to obtain purple single crystals.

Zinc(1,4-tetramethylbenzenedipyrazolate) (13) single crystal synthesis. A 0.7cm OD borosilicate tube was charged with 45 mg (0.13 mmol) zinc triflate, 20 mg ($7.1x10^{-5}$ mol) of **7** and 0.4 ml *N,N*-diethylformamide. The tube was freeze-pump-thawed seven times and then flash frozen, evacuated and flame sealed. The sealed tube was

placed in an oven an heated to 150°C at a ramp rate of 0.1 °C min^{-1}. The temperature was held for 4000 minutes and then brought to room temperature was a cooling rate of 1 °C min^{-1} to obtain white single crystals.

Cobalt(2,5-*p*-dimethoxybenzenedipyrazolate) (14) single crystal synthesis. A 0.7cm OD borosilicate tube was charged with 44 mg (0.13 mmol) cobalt triflate, 20 mg (7.4 x 10^{-5} mol) of **9** and 0.4 ml *N,N*-diethylformamide. The tube was freeze-pump-thawed seven times and then flash frozen, evacuated and flame sealed. The sealed tube was placed in an oven an heated to 150°C at a ramp rate of 0.1 °C min^{-1}. The temperature was held for 4000 minutes and then brought to room temperature was a cooling rate of 1 °C min^{-1}. Pink crystals suitable for single-crystal X-ray diffraction experiments were isolated.

Cobalt(2,5-*p*-dihydroxybenzenedipyrazolate) (15) single crystal synthesis. A 0.7cm OD borosilicate tube was charged with 44 mg (0.13 mmol) cobalt triflate, 17 mg (7.1 x10^{-5} mol) of **10** and 0.4 ml *N,N*-diethylformamide. The tube was freeze-pump-thawed seven times and then flash frozen, evacuated and flame sealed. The sealed tube was placed in an oven an heated to 150°C at a ramp rate of 0.1 °C min^{-1}. The temperature was held for 4000 minutes and then brought to room temperature was a cooling rate of 1 °C min^{-1}. Purple crystals suitable for single-crystal X-ray diffraction experiments were isolated.

Single-Crystal X-ray Diffraction for (12), (13), (14) and (15). X-ray diffraction analyses were performed on single crystals coated with Paratone-N oil and mounted on MiTeGen loops. Crystals were frozen at a temperature of 100 K by an Oxford Cryosystems Cryostream 700 plus. Data were collected at Beamline 11.3.1 at the Advanced Light Source, Lawrence Berkeley National Laboratory using synchrotron radiation (λ = 0.7749 Å for **12** and **14**, λ = 0.8856 Å for **13** and λ = 1.0332 Å for **15**) with a Bruker AXS APEX II CCD detector on a D85 diffractometer. Raw data were integrated and corrected for Lorentz and polarization effects using Bruker AXS SAINT software.[8] Absorption corrections were applied using SADABS.[9] Space group assignments were determined by examination of systematic absences, E-statistics, and successive refinement of the structures. The structure was solved by direct and Patterson methods and expanded through successive difference Fourier maps. It was refined against all data using the SHELXTL 5.0[10] software package. SHELXL[12] was operated in the OLEX2[13] interface. None of the crystals showed significant decay during data collection. Thermal parameters were refined anisotropically for all non-hydrogen atoms. Hydrogen atoms were placed in ideal positions and refined using a riding model for all structures. A solvent mask was applied[14] as implemented in OLEX2 for **12** and **13** to account for unassigned electron density within the pores.

A.3 Results and Discussion

The ligands **3** and **5** were synthesized by Suzuki coupling reactions between a tetrahydropyran-protected pyrazole pinacol boronate ester and the corresponding aromatic dibromide followed by deprotection**. (**Scheme A.1). Suzuki coupling reactions followed by deprotection were also used to obtain **7** and **9**. Oxidative demethylation by ceric ammonium nitrate[15] was used to obtain **10** (Scheme A.2).

Solvothermal reaction of these ligands with cobalt and zinc salts in sealed tubes yielded three new frameworks - cobalt(2,6-naphthalenedipyrazolate) (**11**), cobalt(2,3,5,6-1,4-benzenedipyrazolate) (**12**) and zinc(2,3,5,6-tetramethylbenzene-1,4-dipyrazolate) (**6**). Table A.1 gives the crystallographic metrics of these three structures. All structures show the same general connectivity and topology as Co(BDP).

Table A.1 Crystal parameters and structure refinement data of **11**, **12** and **13**.

	(11)	**(12)**	**(13)**
Crystal System	Tetragonal	Tetragonal	Tetragonal
Space Group	$P4_3$	$P4_3$	$P4_3$
a,b,c (Å)	15.4754(3), 15.4754(3), 13.5298(4)	13.2837(4), 13.2837(4), 12.9365(5)	13.2756(10), 13.2756(10), 13.1203(14)
α, β, γ (°)	90	90	90
V, (Å^3)	3240.22(13)	2282.73(16)	2312.3(4)
Z	8	8	8
R1[a], wR2[b] (I>2σ(I))	0.0983, 0.2937	0.0419, 0.1197	0.0641,0.1551
R1[a], wR2[b] (all data)	0.0985, 0.2944	0.0484, 0.1234	0.1183, 0.1725

[a] $R_1 = \Sigma||F_o|-|F_c||/\Sigma|F_o|$, $wR_2 = \{\Sigma[w(F_o^2-F_c^2)^2]/\Sigma[w(F_o^2)^2]\}^{1/2}$

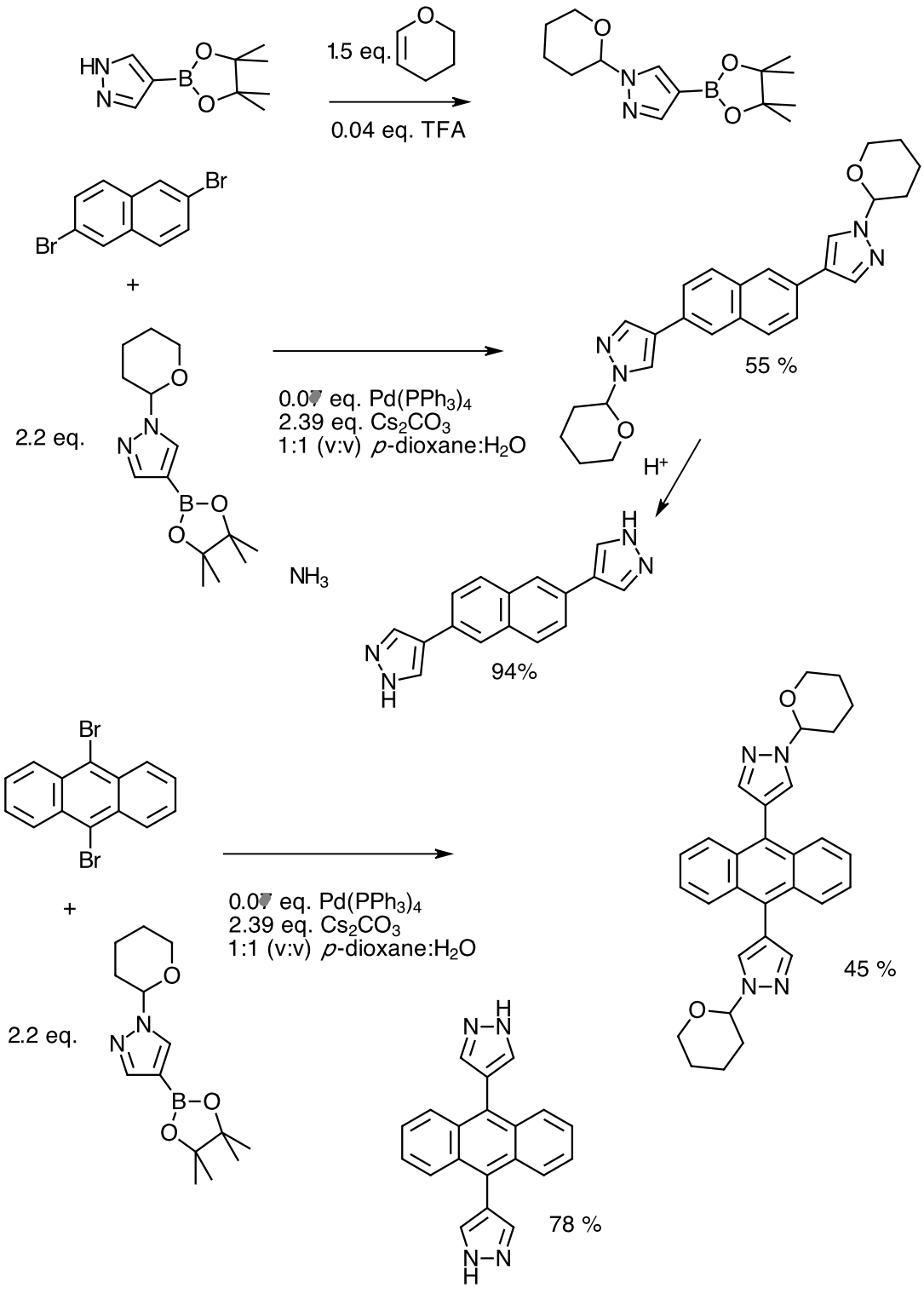

Scheme A.1 Protection of pyrazole pinacolatoborate and the synthesis of **3** and **5**.

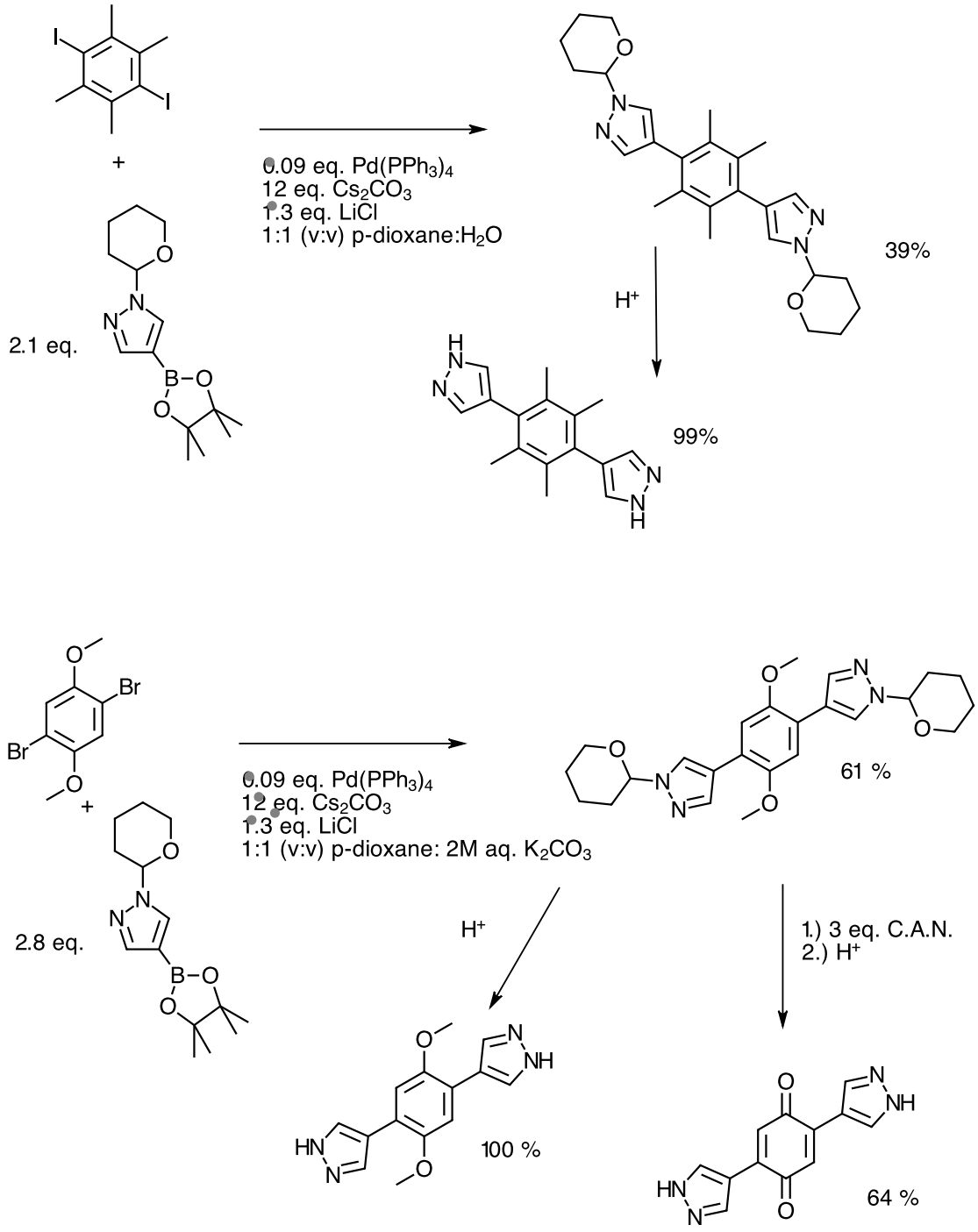

Scheme A.2 The synthesis of the ligands **7**, **9** and **10**.

The structure of **4** shown in Figure A.2 consists of one-dimensional chains of Co(II) ions (Co···Co 3.4776(28) Å) each coordinated by a distorted tetrahedron of nitrogen atoms from four separate NDP^{2-} ligands (Co···N =1.954(7), 1.970(8), 1.976(8), and 2.001(8)). Pairs of Co^{2+} atoms are bridged by pyrazolate ligands in a motif demonstrated in Co(BDP) as well as homoleptic Co(II) pyrazolates.[15] The structure forms a 15x15 $Å^2$ channel interconnected by smaller slit-like openings between the ligands.

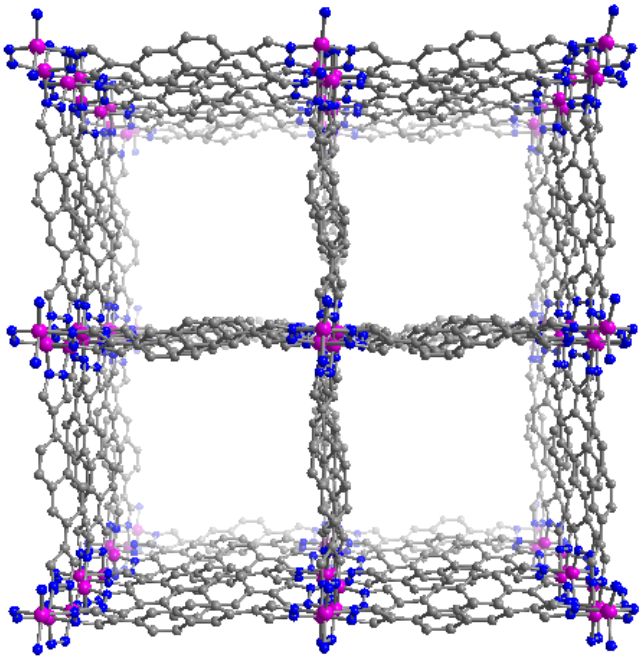

Figure A.1 View down the *c*-axis of **11**

12 and **13** are isostructural compounds shown in Figures A.4 and A.5 These compounds show the same structure type and connectivity of Co(BDP) and **11**, in both of these frameworks the central benzene ring is disordered. The metal-ligand tetrahedral in these structures are distorted (Co···N bond lengths in **12** are 1.985(5), 1.982(5), 1.961(5), and 1.968(5) Å and Zn···N bond lengths are 1.937(14), 1.941(13), 1.975(16), and 1.977(18) Å in **13**). The nearest metal-metal distances of **12** and **13**, Co···Co and Zn···Zn respectively, are 3.431(2) Å and 3.493(7) Å.

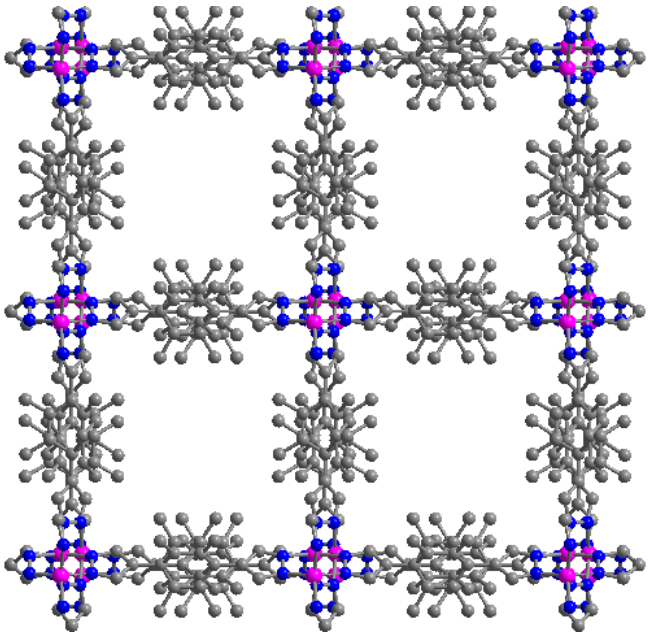

Figure A.2 View down the *c*-axis of **12**. Gray, blue and purple spheres represent carbon, nitrogen and zinc atoms respectively. Hydrogen atoms are omitted for clarity.

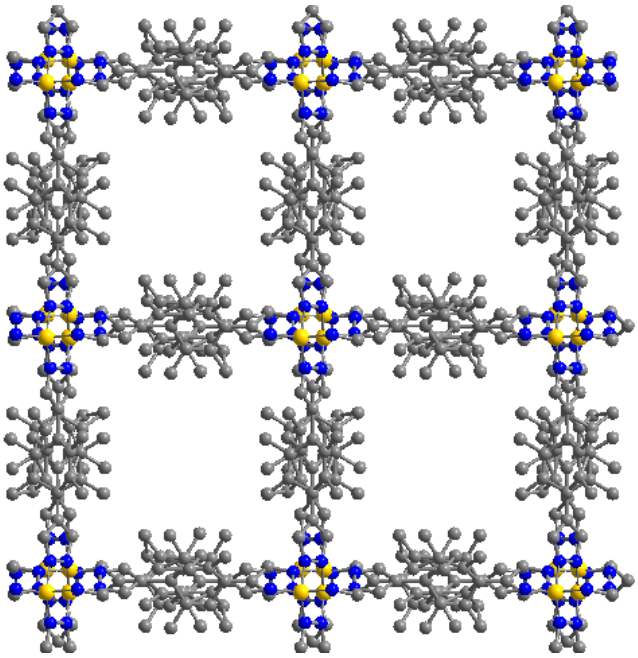

Figure A.3 View down the *c*-axis of **13**. Gray, blue and yellow spheres represent carbon, nitrogen and zinc atoms respectively. Hydrogen atoms are omitted for clarity.

Table A.2 gives the crystal and refinement parameters of **14** and **15**. As shown in Figure A.4, **14** is partially closed, with ordered solvent molecules. It is the only crystal structure described in this appendix that is not tetragonal. It has the same connectivity of Co(BDP), **11, 12** and **13**. The nearest Co···Co distance is 3.429(6) Å and the cobalt nitrogen bond lengths are 1.971(3), 1.998(2), 1.970(2), and 1.971(3) Å.

Table A.2 Crystal parameters and structure refinement data of **14** and **15**.

	(14)	**(15)**
Crystal System	Triclinic	Tetragonal
Space Group	P-1	$P4_2/n$
a,b,c (Å)	6.7728(2), 12.9081(4), 13.2237(4)	18.7932(8) 18.7932(8) 7.1228(4)
α, β, γ (°)	60.9740(15) 89.845(2) 84.271(2)	90
V, (Å^3)	1004.43(5)	2515.4(3)
Z	12	32
R1[a], wR2[b] (I>2σ(I))	0.0423, 0.0801	0.0597, 0.1567
R1[a], wR2[b] (all data)	0.0591, 0.0873	0.0790, 0.1708

[a] $R_1 = \Sigma||F_o|-|F_c||/\Sigma|F_o|$, $wR_2 = \{\Sigma[w(F_o^2-F_c^2)^2]/\Sigma[w(F_o^2)^2]\}^{1/2}$

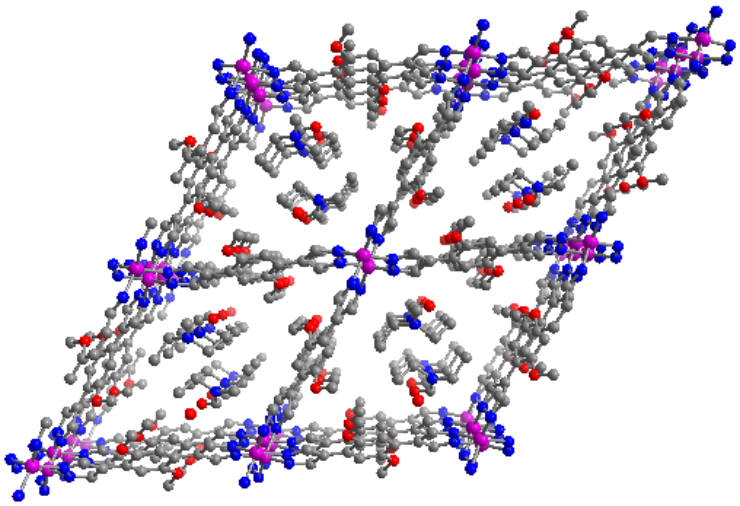

Figure A.4 View down the *c*-axis of **14**. Gray, blue, red and purple spheres represent carbon, nitrogen, oxygen and cobalt atoms respectively. Hydrogen atoms are omitted for clarity.

Figure A.5 shows the structure of **15**. In this structure the Co^{2+} ions are collinear with Co···Co bond distance 3.5614(14) Å. The metal-nitrogen tetrahedral have two Co-N bond lengths, 1.971(6) Å and 1.969(6) Å. The ligand C···O bond distance is 1.3702(92) Å

consistent with the typical lengths of s a single C-O bond and the distance between the ligand oxygen the nearest guest solvent oxygen is 2.6670(93) Å, consistent with a OH···O hydrogen bond.[16] This indicates that in the synthesis the ligand was reduced *in situ*. Whereas **14** is partially closed, this **15** assembles in an open structure, perhaps due to the greater uptake of guest solvent molecules that pack into the pores due to the ability of the ligand to act as a hydrogen bond donor, forcing the framework open.

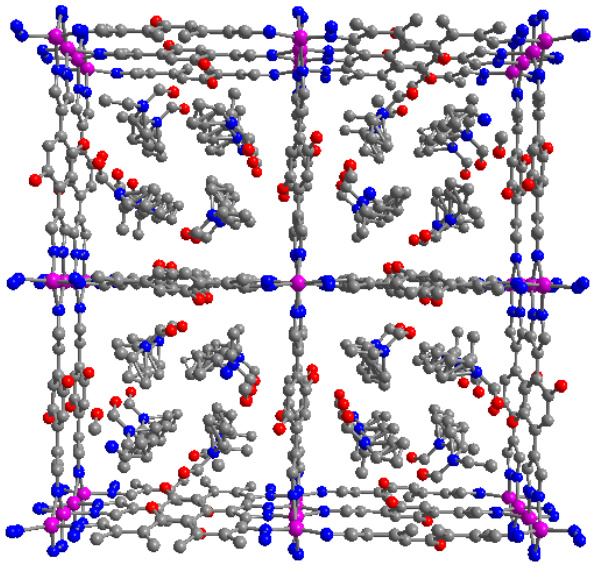

Figure A.5 View down the *c*-axis of **15**. Gray, blue, red and purple spheres represent carbon, nitrogen, oxygen and cobalt atoms respectively. Hydrogen atoms are omitted for clarity.

A.4 Conclusions and Future Work

This work discloses the synthesis five novel pyrazole ligands and five novel frameworks and with the same connectivity and structure type of a previously reported metal-organic framework Co(BDP). Gas sorption measurements may show what effects the ligand alterations have on the gas sorption properties and framework flexibility.

A.5 Acknowledgements

This work was funded by the National Science Foundation and the Korean Research Institute of Chemical Technology. I gratefully acknowledge Kenji Sumida and Miguel Gonzalez for his help in crystal structure collection and determination.

A.6 References

(1) Choi, H. J.; Dincă, M.; Long, J. R. *J. Am. Chem. Soc.* **2008**, *130*, 7848.
(2) Choi, H. J.; Dinca, M.; Dailly, A.; Long, J. R. *Energy Environ. Sci.* **2010**, *3*, 117.
(3) Colombo, V.; Montoro, C.; Maspero, A.; Palmisano, Masciocchi, N.; Galli, S.; Navarro, J. A. R. *J. Am. Chem. Soc.* **2012**, *134*, 12830.
(4) Ardiozza, G. A.; LaMonica, G. *Prog. Inorg. Chem.* **1997,** *46,* 151.

(5) Colombo, V.; Galli, S.; Choi, H. J.; Han, G. D.; Maspero, A.; Palmisano, G.; Masciocchi, N.; Long, J. R. *Chem. Sci.* **2011**, *2*, 1311.
(6) Salles, F.; Maurin, G.; Serre, C.; Llewellyn, P. L.; Knofel, C.; Choi, H. J.; Filinchuk, Y.; Oliviero, L.; Vimont, A.; Long, J. R.; Ferey, G. *J. Am. Chem. Soc.* **2010**, *132*, 13782.
(7) López-Alvarado, P.; Avedaño, C.; Menéndez, J. C. *Synth. Comm.* **2002**, *32*, 3233.
(8) SAINT v7.34 Software for the Integration of CCD Detector System; Bruker Analytical X-ray Systems: Madison, WI, 2001.
(9) Sheldrick, G.M. SADABS v2.10, Program for adsorption corrections; Institute for Inorganic Chemistry University of Göttingen: Göttingen, Germany, 1996; R. H. Blessing, *Acta Crystallogr., Sect. A*. **1995,** 51, 33.
(10) Sheldrick, G.M. SHELXTL 5.0, Program for solution and refinement of crystal structures; University of Göttingen: Göttingen,Germany, 1997.
(11) Sluis, P.; Spek, A. L. *Acta Crystallogr., Sect. A*. **1990**, *46,*194.
(12) Sheldrick, G.M. (2008). *Acta Cryst*. A64, 112.
(13) Dolomanov, O.V., Bourhis, L.J., Gildea, R.J, Howard, J.A.K. & Puschmann, H. (2009), *J. Appl. Cryst.* 42, 339.
(14) Peyton, J.; Callery, P. S.; Shulgin, A. T.; Castagnoli, N. *J. Org. Chem.* **1976**, *41*, 3627.
(15) Masciocchi, N.; Ardizzoi, G. A.; Brenna, S.; LaMonica, G.; Maspero, A.; Galli, S.; Sironi, A. *Inorg. Chem.* **2002**, *23*, 6080.
(16) Wallwork, S. C. *Acta. Cryst.* **1962**, *15*, 758.